UNIVERSITY OF SOUTHAMPTON

Using surface waves to image melt migration pathways and storage beneath the northern East African Rift

by

Emma L. Chambers

ORCID 0000-0001-6969-2920

A thesis submitted for the degree of
Doctor of Philosophy

in the
Faculty of Environmental and Life Sciences
Ocean and Earth Science

June 2020

Thesis: Chambers, Emma L. (2020) "Using surface waves to image melt migration pathways and storage beneath the northern East African Rift", University of Southampton, Faculty of Environmental and Life Sciences, Ocean and Earth Science, PhD Thesis, 0-191.

Data: Chambers, Emma L., Harmon, Nicholas., Keir, Derek., Rychert, Catherine. A. and Gallacher, Ryan. (2020) "A joint inversion of Rayleigh waves from ambient noise tomography and teleseisms to image melt and seismic structure in the northern East African Rift. Journal of Geophysical Research: Solid Earth". DOI: https://doi.org/10.5258/SOTON/D1408

All Raw data are freely available from the IRIS Data Management Center (IRISDMC; https://service.iris.edu/fdsnws/dataselect/1/)

UNIVERSITY OF SOUTHAMPTON

ABSTRACT

FACULTY OF ENVIRONMENTAL AND LIFE SCIENCES
OCEAN AND EARTH SCIENCE

Doctor of Philosophy

USING SURFACE WAVES TO IMAGE MELT MIGRATION PATHWAYS AND STORAGE BENEATH THE NORTHERN EAST AFRICAN RIFT

by Emma L. Chambers

Continental rifting is thought to develop from a combination of mechanical stretching and magma assisted rifting. The northern East African Rift is a unique location where we can observe subaerially the initial stages of rifting through to incipient seafloor spreading, as well as the spatial extent of extensional processes away from the rift valley. Multiple models have been proposed to understand the evolution of lithospheric stretching and magmatism in the northern East African Rift, however previous seismic studies are not directly comparable for areas on and off rift due to variations in method, resolution, and scale. It is vital for our understanding of magma assisted rifting processes to have one model that allows comparisons laterally and in depth, a goal that can be achieved in this environment. Here, I invert surface waves from ambient noise and teleseismic Rayleigh waves extracted from 269 seismic stations present between 1999 and 2017 to image the Earth's velocity structure beneath the northern East African Rift System from 5 – 210 km depth. I then use Love waves from ambient noise data to investigate radial anisotropy at crustal depths to determine crustal layering and the depth and shape of magma storage. Shear velocities are everywhere slow in the mantle, with velocities in the rift slow enough ($<4.10 \pm 0.04$ km/s) to require pervasive partial melt. At asthenospheric depths slow velocity anomalies (<4.15 km/s ± 0.04 km/s, 80 – 130 km depth) are not directly beneath melt-rich crustal regions, suggesting mantle melt is ephemeral and/or melt migrates laterally during ascent. Furthermore, the anomalies are segmented along rift, existing in areas that have not undergone significant crustal thinning (segments ~110 x 80 km wide, ~60 – 120 km deep), suggesting segmented melt supply starts prior to significant plate deformation. Off rift a fast lid is present at depths of 60 - 80 km but is obscured within the rift suggesting melt is infiltrating the lithosphere. At crustal depths velocities are laterally heterogenous and some of the changes can be attributed to variations in crustal thickness. However, velocities beneath the Main Ethiopian Rift (MER) and the off rift Ethiopian Plateau are slow enough to require melt which I interpret as ongoing magmatic emplacement both on and off rift. The MER is significantly slower than Afar suggesting crustal thickness may be a factor in melt residence time. Anisotropy is required from 5 – 30 km depth suggesting the crust is inherently layered. Effective medium theory suggests thin compositional layering of felsic and mafic intrusions can account for anisotropy up to 4%, however to reconcile the highest observed anisotropy (7%) and lowest velocities we require 2 - 4% partial melt oriented in sills. Along rift, horizontally aligned radial anisotropy ($V_{SH} > V_{SV}$) gets progressively weaker northwards until $V_{SV} > V_{SH}$, suggesting melt reorients from sills to dykes as rifting progresses. This thesis indicates there can be significant melt accumulation in the crust both on and off rift. Furthermore, melt supply starts early in the breakup process which in turn informs our understanding of how magma assists rifting.

Contents

List of Figures

List of Tables

Acronyms

ANT	Ambient Noise Tomography
EAMS	Erta Ale Magmatic Segment
EAR	East African Rift
EARS	East African Rift System
Hz	Hertz
IRIS DMC	Incorporated Research Institutions for Seismology Data Management Center
LAB	Lithosphere Asthenosphere Boundary
LLSVP	Large Low Shear Velocity Province
LPO	Lattice Preferred Orientation
Ma	Million years ago
MAR	Mid Atlantic Ridge
MER	Main Ethiopian Rift
NCF	Noise Correlation Functions
nEAR	northern East African Rift
OMP	Oriented Melt Pockets
PTL	Periodic Thin Layering
SAC	Seismic Analysis Code
SNR	Signal to Noise Ratio
SOD	Standing Order for Data
SPO	Shape Preferred Orientation
TGD	Tendaho Goba'ad discontinuity
TRAILS	Turkana Rift Arrays to Investigate Lithospheric Structure
V_{SH}	Horizontally polarised shear velocity
V_{SV}	Vertically polarised shear velocity
VTI	Vertical Transverse Isotropy
YTVL	Yerer-Tullu Wellel Volcanotectonic Lineament

Declaration of Authorship

I, Emma L. Chambers, declare that this thesis entitled *Using surface waves to image melt migration pathways and storage beneath the northern East African Rift* and the work presented in it are my own and has been generated by me as the result of my own original research.

I confirm that:

1. This work was done wholly or mainly while in candidature for a research degree at this University;
2. Where any part of this thesis has previously been submitted for a degree or any other qualification at this University or any other institution, this has been clearly stated;
3. Where I have consulted the published work of others, this is always clearly attributed;
4. Where I have quoted from the work of others, the source is always given. With the exception of such quotations, this thesis is entirely my own work;
5. I have acknowledged all main sources of help;
6. Where the thesis is based on work done by myself jointly with others, I have made clear exactly what was done by others and what I have contributed myself;
7. Parts of this work have been published as:
    - Chapter 3 has been published as: Chambers, E. L., Harmon, N., Keir, D., and Rychert, C. A. (2019). Using Ambient Noise to Image the Northern East African Rift. Geochemistry, Geophysics, Geosystems, 20:2091–2109. *Author contributions*: ELC processed data and wrote the paper. DK helped write the paper. NH provided codes and helped with methods and to write the paper. CAR helped write the paper.
    - Chapter 4 has been submitted for publication in *Journal of Geophysical Research: Solid Earth* with the title 'A joint inversion of Rayleigh waves from ambient noise tomography and teleseisms to image melt and seismic structure in the northern East African Rift,' and authors: Chambers, E. L., Harmon, N., Keir, D., Rychert, C. A. and Gallacher, R. *Author contributions*: ELC processed data and wrote the paper. NH provided codes and helped write the paper. DK helped write the paper. CAR helped write the paper. RG processed half of teleseismic data and discussed methods.
    - Chapter 5 is in prep: Chambers, E. L., Harmon, N., Keir, D., and Rychert, C. A. in prep. *Author contributions*: ELC processed data and wrote the paper. NH provided codes and helped with methods and to write the paper. DK helped write the paper. CAR helped write the paper.

.

Signed:

Date:

Publications

Journal Publications arising from this Thesis

Chambers, E. L., Harmon, N., Keir, D., and Rychert, C. A. (2019). Using Ambient Noise to Image the Northern East African Rift. *Geochemistry, Geophysics, Geosystems,* 20:2091–2109.

Chambers, E. L., Harmon, N., Keir, D., Rychert, C. A. and Gallacher, R. (in review). A joint inversion of Rayleigh waves from ambient noise tomography and teleseisms to image melt and seismic structure in the northern East African Rift. *Journal of Geophysical Research: Solid Earth.*

Chambers, E. L., Harmon, N., Keir, D., and Rychert, C. A. (in prep). Variations in melt emplacement beneath the northern East African Rift from radial anisotropy. *Earth and Planetary science Letters.*

Other Journal Publications arising during this Thesis

Ahmed A., Doubre, C., Leroy, S., Keir, D., Pagli, C., Hammond, J.O.S., Atalay, A., Bes de Berc, M., Grunberg, M., Vergne, J., Pestourie, R., Mamo, S., Kibert, B., Cubas, N., Lavayssiere, A., Janowski, M., Lengline, O., La Rosa, A., **Chambers E. L.,** Illsley-Kemp, F. (in review). Crustal Structure Variations beneath the Western Afar Margin from Receiver Functions. *Tectonophysics*

Davy, R. G., **Chambers, E. L.,** Harmon, N., Minshull, T. A., Bayrakci, G. Klaeschen, D. (in prep). Determining the shear velocity structure from Rayleigh wave dispersion at the Deep Galicia margin using ambient noise cross-correlation.

Chambers, E. L., Ebinger, C., Keir, D., Harmon, N., (in prep). Investigating melt storage using ambient noise and radial anisotropy in Kenya and Tanzania.

Acknowledgements

Firstly I would like to thank my primary supervisor Dr. Derek Keir, for his guidance and support during my PhD at Southampton. For his patience answering questions and always having time to discuss ideas for a new interpretation or project. I would also like to thank my supervisor Dr. Nicholas Harmon for discussions on codes and continuous jokes, along with Dr. Catherine Rychert for significant improvements to manuscripts and discussions of geophysical concepts. I am also immensely grateful to Prof. Cynthia Ebinger for hosting me for a 3 month placement in her lab with Sarah Jaye Oliva. The opportunity allowed me to explore areas outside of my thesis and develop myself as a researcher.

The support and discussions with the Southampton postdocs have been invaluable and I would particularly like to thank Sai, Tim, and Petros. I would also like to thank the Ethiopia and Seismicity groups. Special mentions to Aude Lavayssiere, Melanie Siegburg and Emma Watts, the Ethiopian girls, and to Finn Illsley-Kemp, Dan Possee and Ben Chichester. Thanks guys for great memories over a coffee and a chat, running round conferences, or fieldwork in Afar. I would also like to thank Ryan Gallacher for his belief that I could complete a PhD so many years ago as a young undergraduate. His enthusiasm has been invaluable and it has been great to work together.

I would also like to thank Derek and Cindy again for giving me the opportunity to carry out all aspects of fieldwork in Ethiopia and Kenya. The experience and memories from these trips will be with me forever. I would also like to thank everyone I had the opportunity to meet and work with, with a special mention to Atalay Ayele and everyone at the IGSSA for making me so welcome. I thank IRIS and SEIS-UK for the training and access to data throughout my PhD. This work would not have happened without these resources and was further supported by NERC studentship NE/L002531/1.

To my office who have put up with me muttering to my computer, kept me sustained with home baking and included me in all things palaeo, thank you. I am also grateful for the support of friends with special mentions to Lydia and Emily and my massive family, Sarah, Gareth, Liam, Fiona, Joanne and Callum. A particular mention to my mum who was always at the other end of the phone if I needed her, Gareth for his continued support, and Liz for whenever I needed a relax in London.

Finally I would like to thank James and Astrid. Astrid for her cuddles, attitude and keeping me grounded by bringing in the occasional bird. And James, who despite everything has stayed by my side being positive and encouraging about every aspect of my work. This includes support when I decided to go away for 4 months on placement and fieldwork immediately after getting married! I love you and couldn't have done this without you.

In memory of Kevin Chambers and Margaret Chambers

Chapter 1

Introduction

1.1 Thesis Motivation

Continents rift through a combination of tectonic and magmatic forces (Buck, 2004)(Figure 1.1). Tectonic processes do not provide enough force to rift thick continental lithosphere, instead requiring emplacement of magma to rift with lower forces (Buck, 2006; Mackenzie et al., 2005). In magma-rich extensional settings magma is thought to intrude the more ductile lower lithosphere which then feed dykes that intrude higher into the lithosphere and crust. The addition of hot magma reduces plate strength from heat transfer, allowing further magmatic intrusions to shallower levels with melt buoyant to at least mid-crustal levels (Buck, 2004; Keir et al., 2006a)(Figure 1.1). Plate extension is typically associated with decompression melting of the asthenosphere, usually focused beneath the extending rift (Bastow and Keir, 2011). Most studies attempt to address processes governing production and the role of melt by localising extension to the rift (Ebinger and Casey, 2001; Keir et al., 2005). However, there is debate as to the distribution of melt storage and migration pathways during rifting, and how these change through time during the rifting to breakup process (Hutchison et al., 2015; Magee et al., 2016; White et al., 2008). In addition, it is unclear whether melt is isolated to the rift or can migrate off rift.

Beneath a magmatic rift such as the northern East African Rift (EAR), elevated mantle potential temperatures, melt focusing and active upwelling all are likely to contribute to melt production and migration. The expected distribution of melt from each process is different. For elevated mantle potential temperatures, melt production and intrusion would be expected to be distributed evenly along the rift (e.g., White and Mckenzie (1989)). Melt focussing would result in melt ponding at regions that have a step change in lithospheric thickness (e.g., Hammond et al. (2014)). In contrast active upwelling would generate melting in segmented regions on and off axis from the rift (Figure 1.5)(e.g. Wang et al., 2009; Gallacher et al., 2016).

To better understand the processes responsible for rifting the upper lithosphere, knowledge of the crustal structure both on and off the rift is required. The rift flanks give an insight into the original crustal structure, while variations within the rift give clues to the importance of melt at different stages of rifting. While multiple velocity models have been generated for the region, they are not directly comparable for areas on and off rift due to variations in method, resolution, and scale. In order to facilitate direct comparisons between regions and thereby interpret evolution of rifting processes in space and time, we require a complete and self-consistent model for the northern EAR. Furthermore, while the rifts have been extensively studied, the magmatic and tectonic processes occurring beneath the rift flanks, such as the Ethiopian Plateau, have been understudied due to a lack of seismic data. This has now been partially rectified with the addition of the YY plateau network (Keranen, 2013) which we exploit for the first time to produce absolute shear wave velocity maps.

In this thesis I utilise Rayleigh and Love surface waves obtained from ambient noise and teleseisms recorded on seismometers from multiple seismic networks distributed throughout Ethiopia, Yemen, Djibouti and Eritrea. I use the surface waves to produce an absolute shear wave velocity model of the crust and upper mantle of the northern East African Rift down to 210 km depth enabling analysis of variations in crustal and upper mantle velocity structure in depth and at the progressive stages of rift evolution. In addition, to further explore melt pathways I measure radial anisotropy in order to assess the role fluids play in rifting on and off the rift.

1.2 Research Questions

In this thesis I aim to address the following research questions:

1. **What is the seismic structure of the crust within the northern East African Rift System and how does it inform our understanding of continental rifting in melt rich environments?** At the surface we can observe volcanoes (e.g. Siegburg et al., 2018), and within the mantle studies suggest there is a component of partial melt (e.g. Bastow et al., 2011; Civiero et al., 2015, 2016; Gallacher et al., 2016; Ferguson et al., 2013). What is less well known is how the two systems connect through the uppermost mantle and crust. Seismic imaging has been performed in different areas of the rift, however, variations in method, resolution, and scale among the methods make direct comparisons on and off rift challenging.

2. **At what stage does segmentation of the melt zone occur in the breakup process and how does melt migrate into the lithosphere?** At fully established ocean ridges segmentation is observed within the mantle of the melt zone. Segmentation of melt is also observed beneath the northern EAR (e.g. Hammond et al., 2013; Wang et al., 2009) but due to limited resolution it hasn't been established if segmentation is present beneath all areas of the rift (including those at the earliest stages of rifting) and whether segmentation changes as rifting progresses. It is also not widely known how melt in the asthenosphere migrates to the surface. Fluids are known to reside within the rift axis and in areas of geothermal activity and volcanism (Keir et al., 2009a), but it is not clear how and where fluids reside at different depths during rifting, how they move in the lithosphere and if they are present at all stages of rifting. Furthermore, recent geophysical studies suggest there

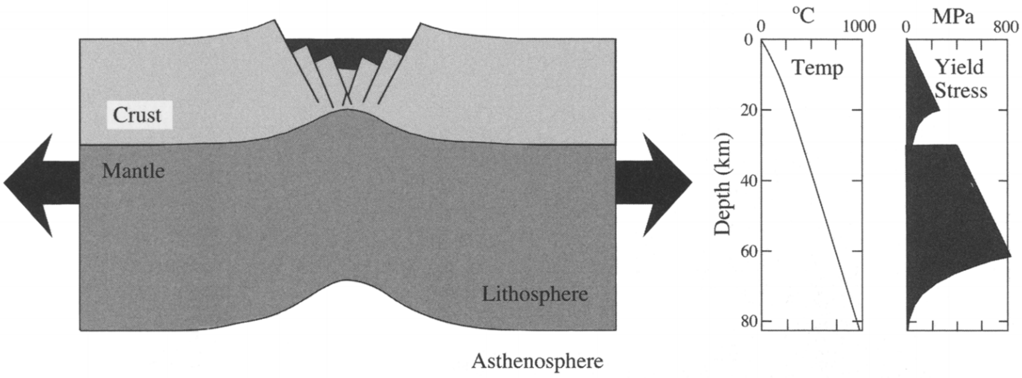

(a) Tectonic Stretching

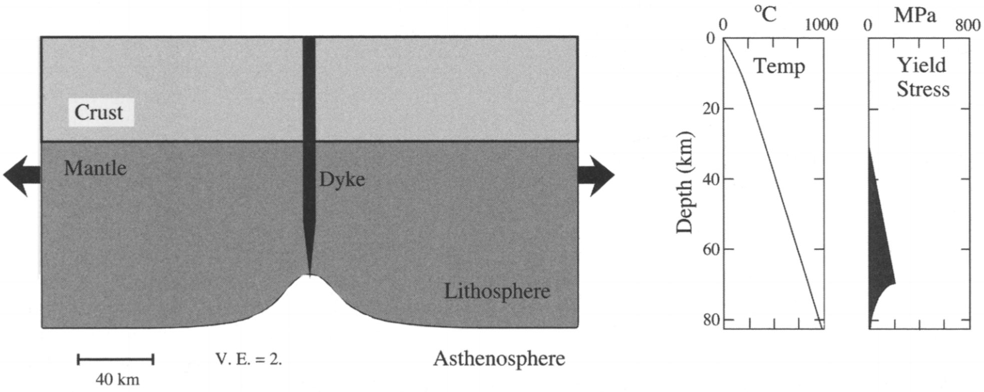

(b) Magmatic Extension

Figure 1.1: Models for extension of rheologically layered lithosphere. The top panel shows mechanical stretching in which strain is accommodated by large offset faults. in brittle layers and by ductile deformation in weaker layers. Bottom panel shows magmatic extension that includes the effects if magmatic intrusion and subsequent heating. The strain localisation and strength reduction of the lithosphere is enhanced by melt intrusion. From Buck (2006).

is partial melt located off rift beneath the Ethiopian Plateau, however the cause and exact location of this melt is debated.

3. **What is the shape of melt within the crust and how does this change with progressive rifting?** Isotropic tomography models can give an indication on the location of melt within the crust (answered in question 1), but not its shape. Where and how magma is stored in the crust has important implications for the strength of the crust as the presence of partial melt and heat weakens the surrounding crust. The depth of magma storage is a key factor for magmatic evolution, transforming mafic melts from the mantle to more felsic compositions observed in the crust. In addition, the depth of storage, location and geometry of partial melt presents another control on mineralization, important for economic resources. Yet, in many rifts globally the depths and geometry of magmatic emplacement both past and present remains difficult to constrain. Previous studies of anisotropy in the East African Rift suggest melt is stored as sills in the lower crust and as dykes in the upper crust (e.g. Keir et al., 2005; Kendall et al., 2006; Bastow et al., 2010;

Hammond et al., 2014), however these models are not comparable in scale or method and have not been carried out off rift beneath the Ethiopian Plateau.

1.3 Key Processes

While investigating the controls on rifting and the nature of the magmatic plumbing system it is apparent that there are multiple processes controlling the system. In the next section I discuss some of the crucial processes that underline the work of this thesis.

1.3.1 Driving Forces of Rifting

The driving forces for continental rifting are thought to occur from a range of sources such as distant plate forces (subduction), edge driven flow from cratons (King and Ritsema, 2000), mantle convection causing traction on the overriding plate, and from asthenospheric upwelling such as small scale convection and mantle plumes (Ebinger, 2005; Kendall et al., 2006)(Figure 1.3). The simplest model for rifting involves mechanical stretching where strain is accommodated by large offset border faults requiring large stresses to rupture the plate (McKenzie, 1978). In contrast, in the magma assisted rifting model, plume-lithosphere interactions of dyke intrusions can heat the lithosphere sufficiently to initiate further magma production and require less strain to rupture the weakened lithosphere (Buck, 2004, 2006)(Figure 1.1). In the northern part of the East African Rift System (EARS) where rifting is more mature, strain is mainly accommodated by magmatic extension in the rift, whereas in the southern EAR, extension is accommodated by mechanical extension along large border faults with little magmatic rifting (Ebinger and Casey, 2001; Keranen et al., 2004).

The initiation of rifting for the EARS is thought to coincide with a mantle plume interacting with the plate to initiate rifting from diverging mantle flow. However, it is not known whether the structure persists to the present day, with considerable debate as to the nature of this plume, or indeed plumes. Multiple studies have imaged the mantle but have varying degrees of agreement on the number of upwellings. The three main possibilities, which I discuss in greater detail below, include 1) a single upwelling from the African superplume (Nyblade, 2011), 2) two smaller plumes beneath Afar and Kenya respectively (Pik et al., 2006) and 3) multiple small scale plumes which are potentially associated with the African superplume (Civiero et al., 2016, 2019) (Figure 1.4).

1.3.1.1 African Superplume

The African superplume is one of two Large Low Shear Velocity Provinces (LLSVP) that extend to the core mantle boundary. The second LLSVP is located beneath the Pacific, antipodal to the African Superplume. The LLSVPs were originally called Jason (Pacific) and Tuzo (African) after the researchers who first proposed and imaged mantle plumes (Wilson, 1963; Morgan, 1971; Wilson, 1973). As their name suggests, the superplumes are large areas that are observed as low shear velocity features in tomographic images. The composition of such features is debated but it has been suggested they are piles of reworked subducted ocean crust (Niu, 2018). The

African superplume extends from the core mantle boundary beneath southern Africa in a north-northeastward direction (Ritsema et al., 1999; Hansen et al., 2012)(Figure 1.2), up to at least mid-mantle depths beneath Kenya and Ethiopia (Nyblade, 2011; Ritsema et al., 1999; Furman et al., 2006; Simmons et al., 2012; Hansen et al., 2012) though some studies suggest the upper part of the superplume may have moved from beneath Kenya and Ethiopia, southwards towards Tanzania (Weeraratne et al., 2003). The mantle beneath the northern EARS is anomalously hot (Ferguson et al., 2013; Rooney et al., 2012a) which has been attributed in some studies as an effect of the thermal and/or chemical anomaly of the African superplume. Shear velocities are also slow in the upper mantle of East Africa (observed to be 9 - 16 % slower than ambient mantle) which have been similarly interpreted (Nyblade, 2011; Ritsema et al., 1999; Simmons et al., 2012). The timing of the impingement of the plume beneath the EAR coincides with the distribution and timing of magmatism (Ebinger and Sleep, 1998) as well as uplift across East Africa (Ebinger and Casey, 2001; Furman et al., 2006; Sembroni et al., 2016b; Gani et al., 2007; Pik et al., 2003; Daradich et al., 2003; Hassan et al., 2020). Similarities in the geochemical composition of mafic magmatism in both Afar and northern Kenya provide further support for the African superplume (Nelson et al., 2012).

1.3.1.2 Multiple Plumes

Variations in the geochemical and petrological signatures led Pik et al. (2006) to propose two deep mantle plumes, one beneath Afar and the other Kenya. High ^{3}He/^{4}He ratios in Oligocene flood basalts and Sr and Nd estimations, suggest the Afar plume is linked to a deep source whereas the composition of the Kenyan plume has a shallower origin making them chemically distinct (Pik et al., 2006; Rogers et al., 2000; George et al., 1998). Further geochemical studies have suggested four or more distinct plumes or “plumelets” due to variations in the chemical compositions that have been suggested to arise from the African superplume (Meshesha and Shinjo, 2008). Similarly, petrological studies suggest all melt derives from one parental source (Siegburg et al., 2018; Hutchison et al., 2018), either the Afar plume or the African superplume, despite variation in magmatic composition at individual volcanoes.

1.3.1.3 Multiple Mantle Upwellings

Further debate on the number of plumes comes from tomographic imaging of P and S waves which show variation in the number of plumes beneath the EARS including potential plumes beneath Tanzania, Kenya, the Main Ethiopian Rift (MER), Afar and the Arabian Peninsula (e.g. Emry et al., 2019; Weeraratne et al., 2003; Bastow et al., 2005, 2008; Gallacher et al., 2016; Civiero et al., 2015; French and Romanowicz, 2015; Petrunin et al., 2020; Koptev et al., 2018). However, many studies interpret the multiple upwellings as evidence that the mantle plume that initiated rifting in Afar is no longer present (e.g. Hammond et al., 2013; Rychert et al., 2012; Gallacher et al., 2016). Emry et al. (2019) suggest several distinct secondary plumes that rise from the mantle transition zone and migrate towards areas of thinner lithosphere beneath Kenya, Afar and the MER. With increasingly enhanced resolution at shallower depths the more segmented low velocity regions are imaged, whereas at greater depths and coarser resolution, these features merge into one structure, the African superplume.

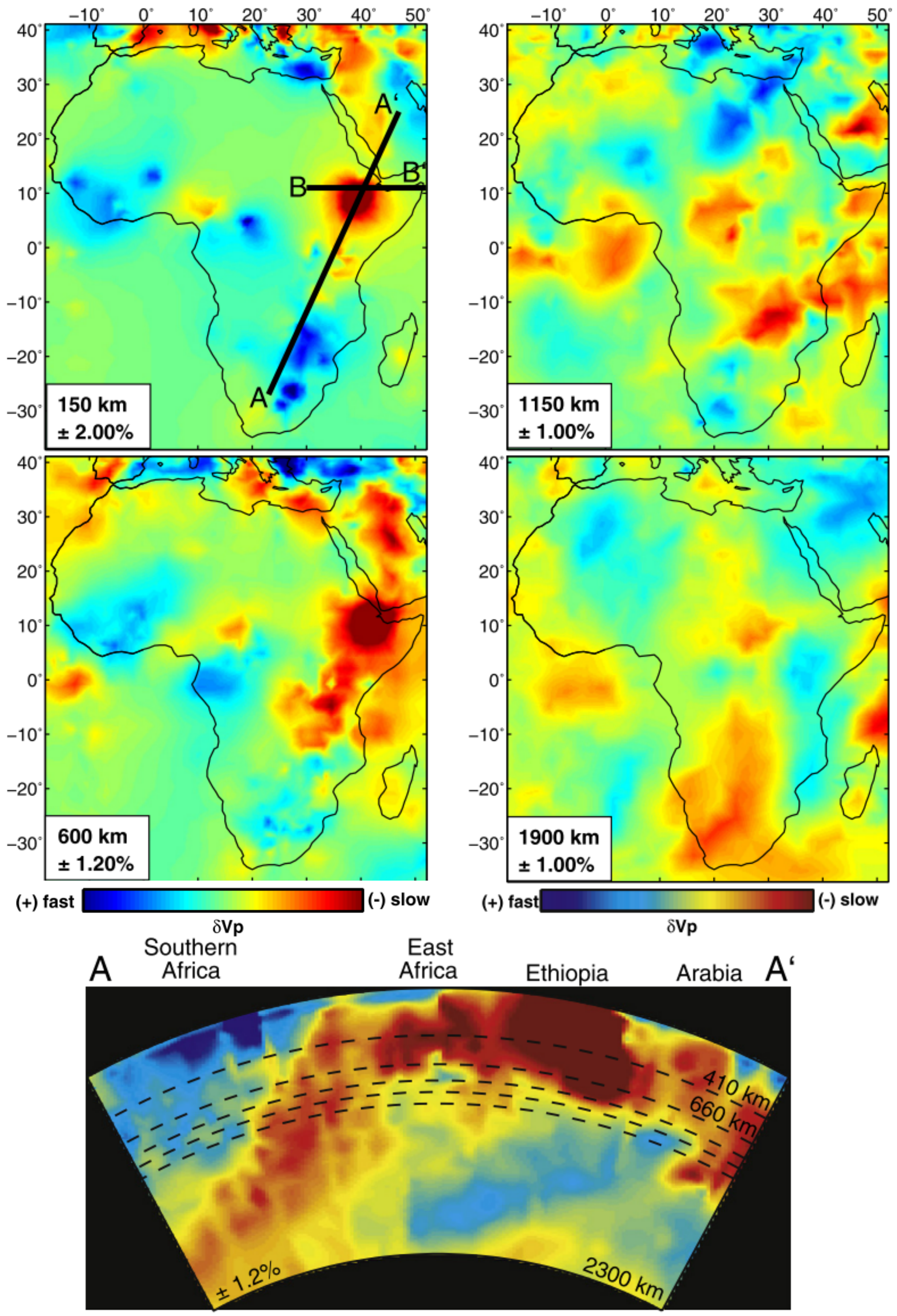

FIGURE 1.2: P-wave tomography maps using body waves and relative arrival time tomography of the African superplume in the mantle from 150 - 2300 km depth. Red colours are slow velocity and blues faster velocity. The plume rises from the core mantle boundary beneath southern Africa, rising to upper mantle depths beneath Ethiopia. From Hansen et al. (2012).

1.3.1.4 Large Scale Mantle Convection and Gravitational Potential Energy

While it is likely a plume was needed to initiate rifting in a strong plate, models are divided regarding whether large scale mantle convection is required (Lithgow-Bertelloni and Silver, 1998; Ghosh et al., 2008) or if gravitational potential energy gradients are sufficient to sustain present day rifting (Stamps et al., 2014, 2015). Recent studies of lithospheric buoyancy forces from variations in lithospheric density driven buoyancy, suggest stress is spread across the entire plate rather than being forced by upwellings and basal drag (Stamps et al., 2014; Ghosh et al., 2009). These models are sufficient to explain present day rifting rates without convection (Stamps et al., 2014; Ghosh et al., 2009). Although basal flow and horizontal mantle tractions overestimate observed motions (Stamps et al., 2014, 2015; Ghosh et al., 2008), dynamic plate uplift of East Africa from mantle upwellings or a plume are required to accommodate the extension (Stamps et al., 2015; Ghosh et al., 2008). Furthermore, modelling of dynamic topography suggests full scale mantle convection from the African superswell is driving plate motions, though most intense motions are at the core mantle boundary (Lithgow-Bertelloni and Silver, 1998). The upwelling provides support for the uplifted topography of the region, with the Ethiopian Plateau requiring dynamic support for its current elevation (Lithgow-Bertelloni and Silver, 1998; Sembroni et al., 2016a). If the plate was previously modified by magmatic intrusion (Gao et al., 1997), faulting from previous orogenies (van Wijk, 2005), or undergone thermal erosion from asthenospheric upwellings (Maguire et al., 2018), lithospheric strength may be reduced and the plume model not required for initial rifting and uplift (Stamps et al., 2014, 2015).

A recent study further explores convection focussed to the upper mantle (Lees et al., 2020) using numerical modelling to investigate melt distribution between two boundary layers. The pattern that emerges is a spoke pattern planform with rising upwelling plume hubs connected by "spokes." If the lithosphere is sufficiently thin ($<$80 km) and water content high ($>$100 ppm) then both the hub and spoke will generate melt. Measures of gravity, topography and volcanism in Africa map well to areas the model predicts will contain melt and thus upper mantle convection could be the current driver for melt generation (Lees et al., 2020).

1.3.2 Asthenospheric Flow, Melt Generation and Migration

Magma assisted rifting requires a component of melt. This melt is often imaged as low velocity segments at asthenospheric depths beneath oceanic rifts (e.g. Wang et al., 2009; Gallacher et al., 2016). Typically melt after it has been produced will rise vertically due to buoyancy effects and then flow along the base of the lithosphere towards areas of thinner lithosphere, usually the rift axis (Magde and Sparks, 1997; Sparks et al., 1993; Splegelman and Reynolds, 1999). As plates separate from further intrusion and rifting effects discussed above, mantle rises to replace the extracted melt leading to decompression melting and further increasing melt flow by dynamic upwelling (Magde and Sparks, 1997; Buck and Su, 1989; Buck, 2004; Wang et al., 2009). Furthermore as the lithosphere thins mantle will also rise leading to similar processes (Buck, 2004). While ascent is typically thought to be vertical unless a boundary is met, studies

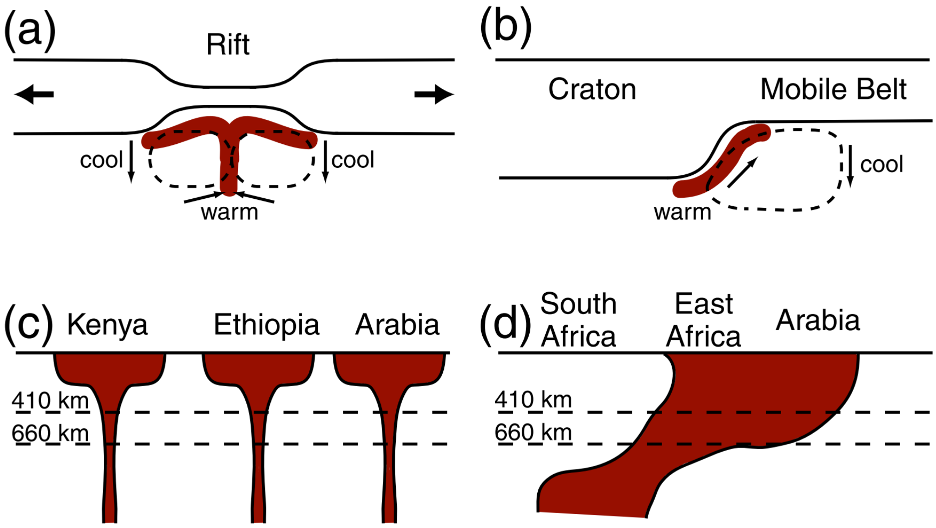

FIGURE 1.3: Models of rifting for the East African Rift System. Cartoons illustrate different geodynamic models that have been proposed , including (a) small-scale convection induced by lithospheric stretching, (b) small-scale convection resulting from edge-flow, (c) plume models, and (d) superplume model. From Hansen et al. (2012).

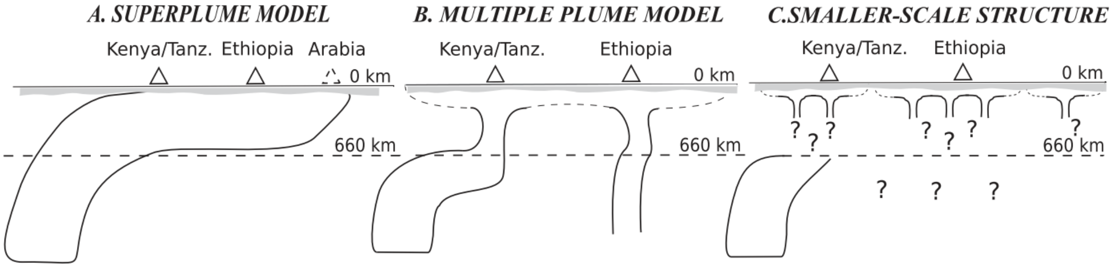

FIGURE 1.4: Cartoon of the three main models for mantle plumes beneath the East African Rift from Civiero et al. (2015). The models vary from one plume of the African Superplume (a), to two large upwelling plumes, one beneath Ethiopia and the other Kenya (b) and multiple small-scale upwellings with no clear link to depth (c).

have suggested melt could migrate laterally from upwelling and buoyancy driven flow (Dick, 1989; Spiegelman and McKenzie, 1987; Spiegelman, 1996). In more developed mid ocean ridge systems melt is focussed to the axis forcing excess melt to migrate laterally along the axis due to rheological and density contrasts at the Moho (Garmany, 1989) (e.g. the East Pacific Rise (Varga et al., 2008), Gulf of California (Wang et al., 2009) and the Mid Atlantic Ridge (Braun and Sohn, 2003; Ghods and Arkani-Hamed, 2000).

Melt migration can occur off rift due to tectonic processes such as plate flexure, extension or pre-existing zones of weakness (Pilet et al., 2016), and by melt focussing from a wide melt zone (Ghods and Arkani-Hamed, 2000). Furthermore, melt in plume-rift settings can migrate from the plume to an area of thinner lithosphere, typically the rift axis (Braun and Sohn, 2003). Lateral melt migration has been suggested within the EARS from off axis lateral flow of plume material west towards the Cameroon volcanic line and south to the Comoros Islands (Ebinger and Sleep, 1998). This hypothesis suggests plume material flows into areas of thin lithosphere beneath the Mesozoic–Palaeogene rifts and passive margins of Africa and Arabia. In Afar, geodetic observations and models of coupled but spatially distant zones of subsidence and uplift provides strong evidence for lateral melt migration near the base of the crust over length scales of ∼80 km along rift during the Dabbahu dyking event (2005 – 2009) (Grandin et al., 2012; Wright et al., 2012).

At mid ocean ridges melt organises itself into discrete magmatic segments beneath the axis that are ∼50 - 200 km in length (e.g. Gallacher et al., 2016; Wang et al., 2009) in the upper mantle, typically at the lithosphere-asthenosphere-boundary. These are imaged as zones of slow velocity within the mantle. Beneath more mature ocean rifts, zones of segmented slow velocity have been observed in areas such as the Gulf of California, the Red Sea Rift and the Mid Atlantic Ridge (MAR) (Lekic et al., 2011; Ligi et al., 2012; Wang et al., 2009)(Figure 1.5). Segmentation varies with spreading rate, being more abundant at slow spreading ridges (e.g. the MAR) than fast spreading ridges (Magde and Sparks, 1997). The processes that generate segmentation of the melt zone beneath oceanic rifts are debated with hypothesis ranging from plumes (Civiero et al., 2015, 2019), to buoyancy-driven active upwelling (Gallacher et al., 2016; Magde and Sparks, 1997; Ligi et al., 2012) and decompression melting (Rychert et al., 2012; Bastow et al., 2008), though all processes require an increase in melt production (Buck and Su, 1989; Eilon and Abers, 2017; Nielsen and Hopper, 2004; Wang et al., 2009)(Figure 1.5).

1.4 The East African Rift System

The EARS is made up of several rifts extending over 4000 km, from the Afar triple junction in the north, to Mozambique and Madagascar in the south (e.g. Ebinger et al. 1997). While most rift systems are beneath the oceans making them difficult to analyse, the EARS is fully subaerial making it unique, and allowing unprecedented observations of the mechanisms of rifting, from continental breakup to incipient seafloor spreading. The EARS is breaking apart by a combination of tectonic and magmatic forces whose contributions vary along its length. In the northern and eastern branches, magmatic rifting is considered to be the main driver for extension. In contrast, the western branch, which extends through Tanzania, Uganda and the Democratic Republic of Congo, is dominated by mechanical rifting, though magmatism is present but focussed to discrete areas. The eastern and western branches reconnect in southern Tanzania and the Malawi rift, extending south to Mozambique, the southeastern branch of the EARS. In addition, the rift further splits to produce the southwestern branch, extending west into Zimbabwe and as far as Botswana in the Okavango rift (Figure 1.7).

1.4.1 Geological History of the EARS

1.4.1.1 Volcanism

Volcanism is widespread along the EARS with more volcanism present in the north than in the south (red triangles Figure 1.8). In the northern EAR volcanism initiated 45 Ma and continues to present (e.g. Rooney et al. 2014; Barnie et al. 2016; Siegburg et al. 2018). The largest volcanic event was the emplacement of the Ethiopian flood basalt province, with the main eruptions occurring 31 - 29 Ma (Hofmann et al., 1997; Ukstins et al., 2002; Rooney et al., 2012a)

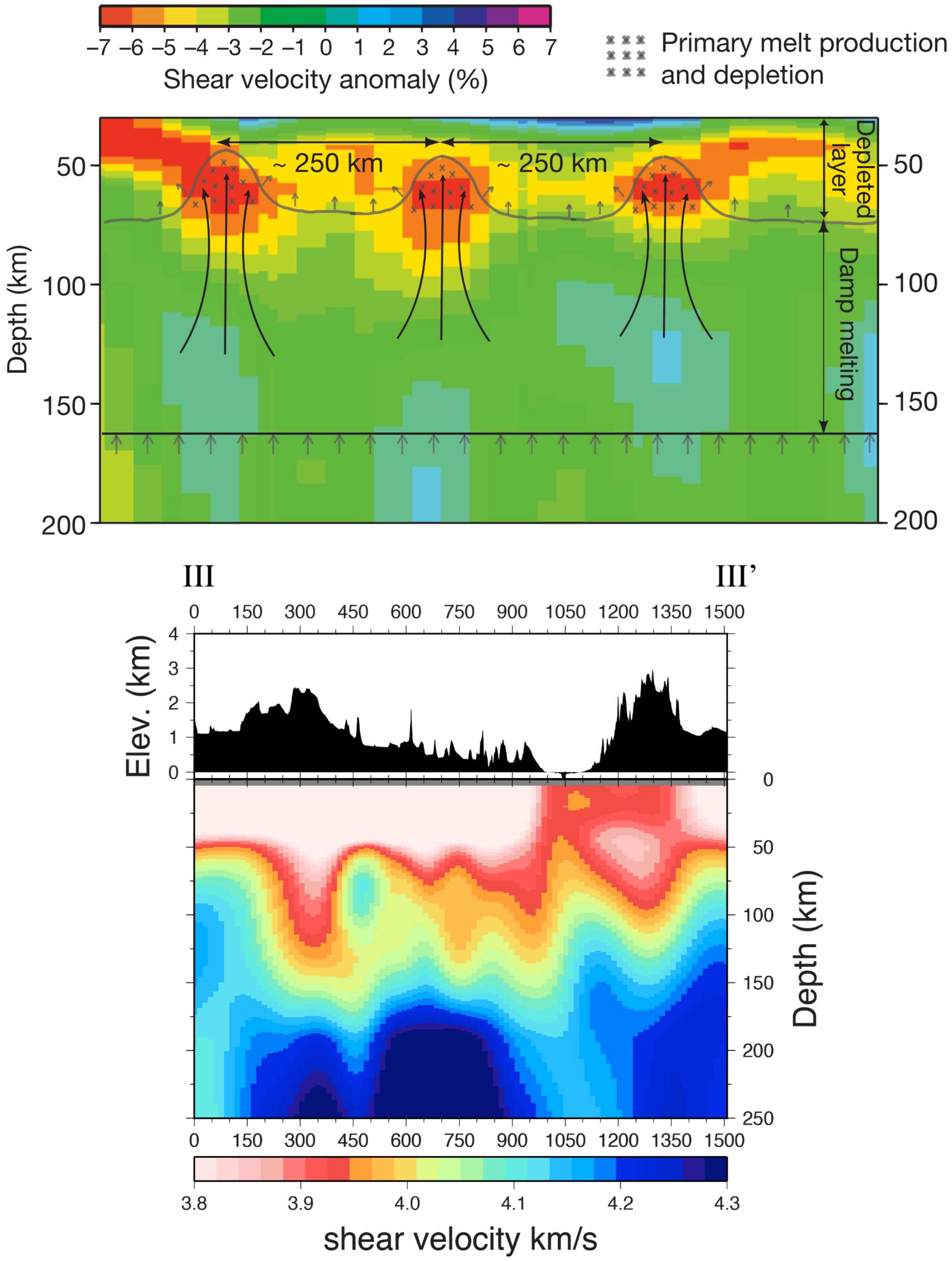

Figure 1.5: Images of segmentation beneath the Gulf of California and the northern East Africa Rift. Upper panel: Schematic interpretation of mantle velocities beneath the Gulf of California generated from Rayleigh-wave tomography. Low shear wave velocity anomalies (red) are interpreted as concentrated melt and active upwelling forming segmentation beneath the rift. From Wang et al. (2009). Lower Panel: Segmented slow velocities beneath the Central MER, Northern MER and Afar regions with a further segment beneath Yemen generated by Teleseismic Rayleigh-wave tomography. From Gallacher et al. (2016).

linked to the impingement of a mantle plume. The flood basalts are ~2 km thick and cover an area ~600,000 km^2 extending across Yemen and Ethiopia (Rooney, 2017; White and Mckenzie, 1989). The Ethiopian Plateau continued to have sporadic volcanism with alkali shield volcanoes emplaced above the flood basalts from 22 - 11 Ma (e.g. Mt. Choke and Mt. Guguftu) (Beccaluva et al., 2009; Kieffer et al., 2004). Within the Eastern branch, volcanism initiated 23 Ma (Ebinger et al., 1989a,b; Chorowicz, 2005, and references therein) whereas the western branch has significantly less volcanic activity which is isolated to volcanic provinces, where volcanism began in the late Miocene ~7.25 Ma (Ebinger et al., 1989a; Chorowicz, 2005). In the Tanganyika rift, the central basin started to subside between 12 and 9 Ma, the northern basin between 8 and 7 Ma, and the southern basin between 2 and 4 Ma (Chorowicz, 2005). The Rungwe volcanic province started rifting 8.6 Ma and the Malawi rift started to subside during the late Miocene at 8-9 Ma (Ebinger et al., 1989a).

Volcanic activity today in Ethiopia is largely focused within the ~70 km long and 20 km wide en-echelon magmatic segments of the rift axis (Ebinger and Casey, 2001; Hayward and Ebinger, 1996; Wolfenden et al., 2004; Barnie et al., 2016; Rooney et al., 2014; Siegburg et al., 2018). The volcanic segments in Afar and the Main Ethiopian Rift (MER) are the main focus of present day extension, while prior to the Pleistocene, extension was focussed at the border faults (Ebinger and Casey, 2001; Wolfenden et al., 2004, 2005). One of the most obvious signs of volcanic activity is the presence of the Erta Ale lava lake in the Danakil depression, a very active volcano (e.g. Moore et al., 2019). In November 2010 the Erta Ale lava lake erupted (Field et al., 2012) with a further eruption in January 2017 (Moore et al., 2019; Xu et al., 2017). Within the Dabbahu-Manda Hararo segment, a dyking event occurred from 2005 - 2010 with 14 intrusions into the crust with the initial dyke intrusion ~60 km long (Wright et al., 2006; Ebinger et al., 2008; Belachew et al., 2011).

Not all volcanic activity is constrained to the rift with studies finding evidence for ongoing lower crustal intrusions and magmatic activity off rift (e.g. Mackenzie et al., 2005; Maguire et al., 2006; Hautot et al., 2006; Whaler and Hautot, 2006). Mt Kenya and Kilimanjaro are two examples of off axis volcanoes which have potentially formed by reactivation of Precambrian zones of weakness away from the rift valley, though the source of off axis volcanism is still debated (Bosworth, 1987; Chorowicz, 2005). S-wave studies beneath the Ethiopian Plateau, YTVL and Nabro find slow velocities (Chambers et al., 2019; Kim et al., 2012) coupled with high conductivity bodies beneath the YTVL which have been interpreted as melt zones (Didana et al., 2014; Samrock et al., 2015, 2018; Whaler and Hautot, 2006). In June 2011 Nabro volcano located on the eastern margin of the Danakil depression in Eritrea erupted, killing 7 people (Goitom et al., 2015; Hamlyn et al., 2014) and generating ash clouds reaching 17 km (Clarisse et al., 2014). In addition, southwest of Lake Tana on the Ethiopian Plateau there is evidence for Quaternary volcanism (Conticelli et al., 1999) and at the Yerer-Tullu Wellel Volcanotectonic Lineament (YTVL), a 700 km long, 80 km wide corridor of faults and volcanoes trending east-west (e.g. (Rooney, 2017)). Geothermal features are also widespread in Ethiopia with the majority located along the centre of the rift and on the Ethiopian Plateau but are absent on the Somalian plateau (Keir et al., 2009a; Korostelev et al., 2015) (Figure 1.6).

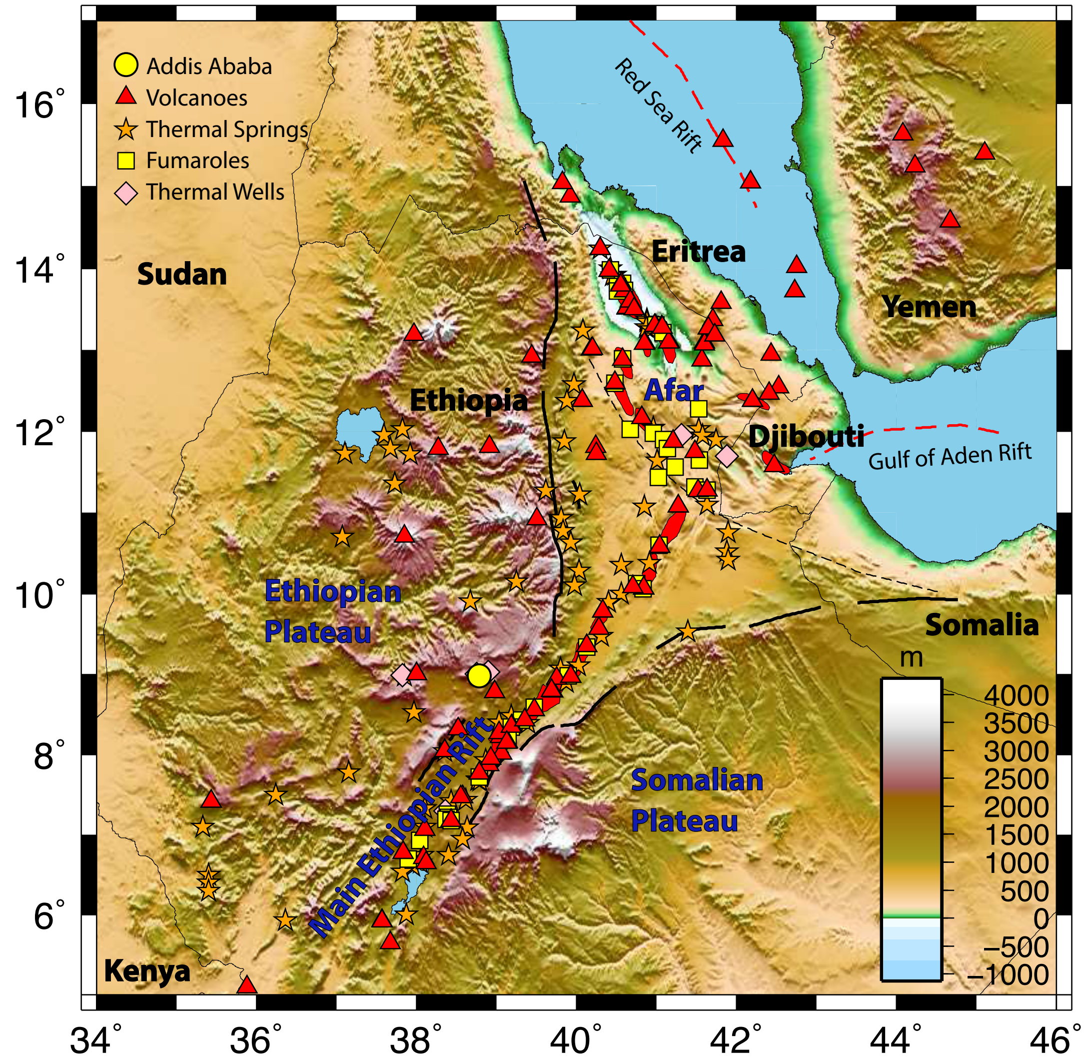

FIGURE 1.6: Map of volcanoes and known thermal springs, thermal wells and fumaroles in Ethiopia and the surrounding regions. Geothermal features from Keir et al. (2009a).

1.4.2 Current Rift Development

1.4.2.1 Surface Segmentation

Segmentation of the rift has been observed at varying depths and length scales beneath the EARS and rifts as a whole (e.g. Wang et al., 2009; Magde and Sparks, 1997; Bastow et al., 2005; Gallacher et al., 2016; Civiero et al., 2015; Lekic et al., 2011). At the surface, segmentation of faults and the magmatic system varies in length scale between oceanic and continental rifts. In continental rift sectors the rift is bounded by border faults >50 km in length, in contrast to oceanic basins which are bounded by faults of ∼10 km length (Ebinger et al., 1989b; Hayward and Ebinger, 1996). At the early stages of rifting, rift segments generally form along pre-existing lithospheric weaknesses which were created during previous tectonic activity. The segments later interconnect to form a continuous rift system (Corti, 2012; Nelson et al., 1992; Zwaan and Schreurs, 2017). In the EAR this transition from long offset border faults to shorter segments is observed in Ethiopia where faults in the MER are ∼50 km long in contrast to Afar where they are

$\leqslant$15 km (Hayward and Ebinger, 1996). In areas that are magmatically rifting the faults bound regions of active volcanism which are contained within the surface magmatic segment (Ebinger and Casey, 2001).

1.4.2.2 Extension and Seismicity

The MER and Afar depression are the product of divergence of the Nubian, Somalian and Arabian plates forming the Afar triple junction. The plates are separated by three rifts: The Red Sea rift (Nubian, Arabian plates), The Gulf of Aden rift (Somalian, Arabian plates) and the MER (Somalian, Nubian plates). Rifting of the Red Sea and Gulf of Aden initiated approximately coeval with the main flood basalt emplacement (Bosworth et al., 2005; Hofmann et al., 1997; Pik et al., 1998; Wolfenden et al., 2004) while the MER started rifting later at 20 Ma in the South, and 11 Ma in the north (Kazmin et al., 1978; Wolfenden et al., 2004). The Tendaho Goba'ad discontinuity (TGD) separates the east-west extension in the northern-most MER from the northeast-southwest extension in Afar (Tesfaye et al., 2003).

Extension broadly decreases from north to south along the rift with the fastest full spreading rates of 18 mm/yr. for the Red Sea rift (McClusky et al., 2010; Vigny et al., 2006), 16 mm/yr. for the Gulf of Aden Rift (Vigny et al., 2006; Jestin et al., 1994), and 6 mm/yr. for the MER (Jestin et al., 1994; Casey et al., 2006; Saria et al., 2014)(Figure 1.8). Further south in Mozambique extension decreases to ∼1 mm/yr. (Stamps et al., 2018; Saria et al., 2014). Similarly to the Northern branch, the Eastern branch is characterised by a southward decrease in extension rate, in contrast to the Western branch where extension rate increases southward (Stamps et al., 2018; Saria et al., 2014).

Seismicity is present in much of the rift system, broadly following each surface magmatic segment of the rift axis (e.g. Keir et al., 2006a; Illsley-Kemp et al., 2017; Lavayssière et al., 2019). Focal mechanisms suggest the seismicity is linked to extensional faulting perpendicular to the local rift axis (Craig et al., 2011)(Figure 1.8). There is more seismic activity on the less magmatic branches of the EAR (except Afar where extension rates are largest), with the Western branch more seismically active than the Eastern branch potentially due to stronger crust beneath the Western branch allowing accumulation of elastic strain (Chen and Molnar, 1983). In contrast, the Eastern branch is characterised by more magmatic rifting and slower extension rates (Calais et al., 2008) though there is evidence for diffuse seismicity at the northern Tanzania Divergence (Craig et al., 2011; Albaric et al., 2014).

While seismicity in the EARS is typically low magnitude (Mw <5), large intraplate events can occur such as the Mw 6.5 Botswana earthquake in 2017 (e.g. Moorkamp et al., 2019; Kolawole et al., 2017). The Botswana earthquake is part of the southwestern Branch of the EARS, the youngest area of extension of the rift, in the Okavango rift zone. Seismic velocity and resistivity models of Botswana provide little evidence for mantle upwelling, instead suggesting mechanical stretching is the dominant force in this part of the rift (Moorkamp et al., 2019).

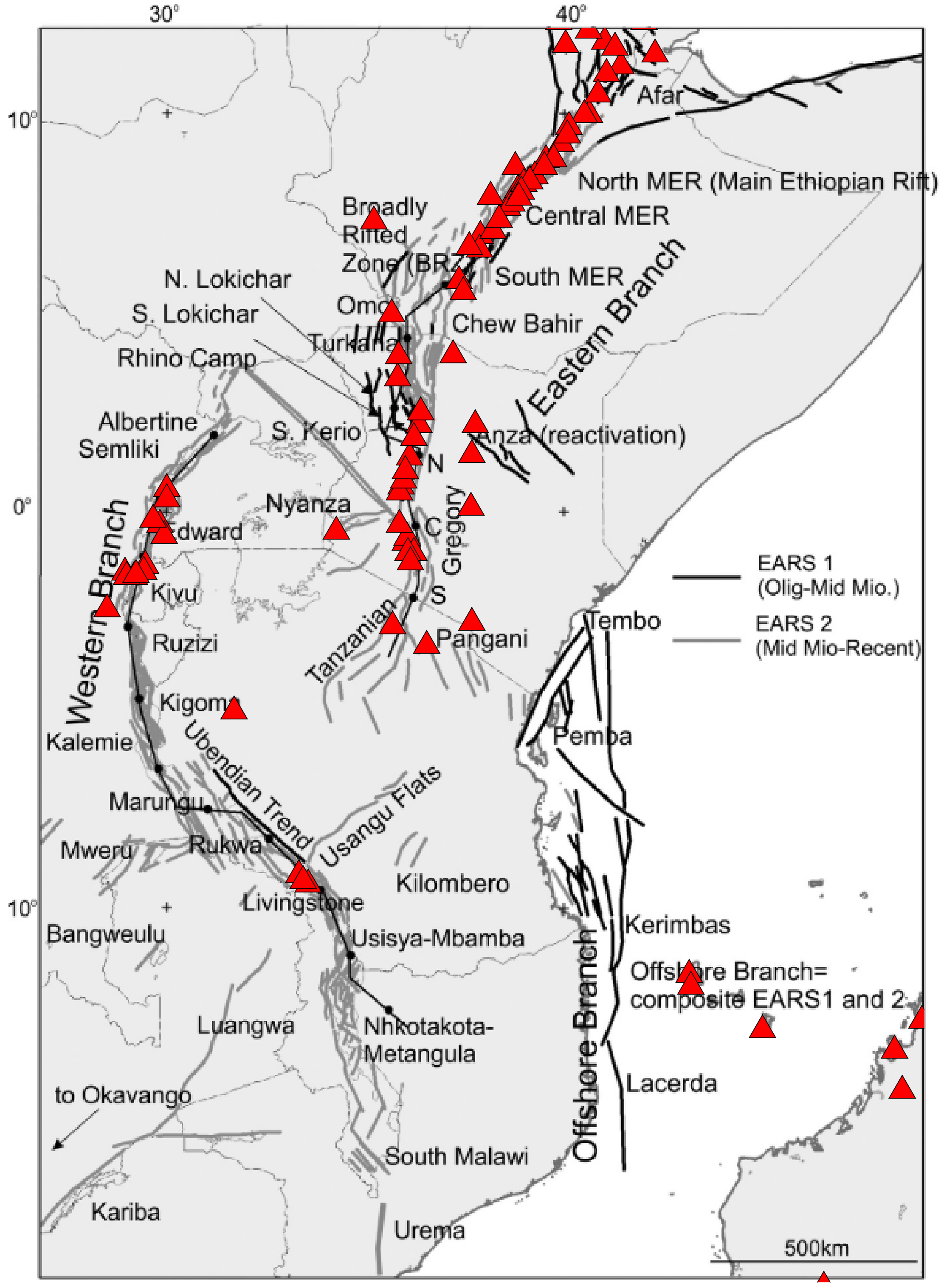

Figure 1.7: EARS faults and key basins of the EARS with volcanoes marked as red triangles showing most magmatic rifting is located on the Eastern and northern Branches with less magmatism on the Western and Southern branches. Adapted from Macgregor (2015).

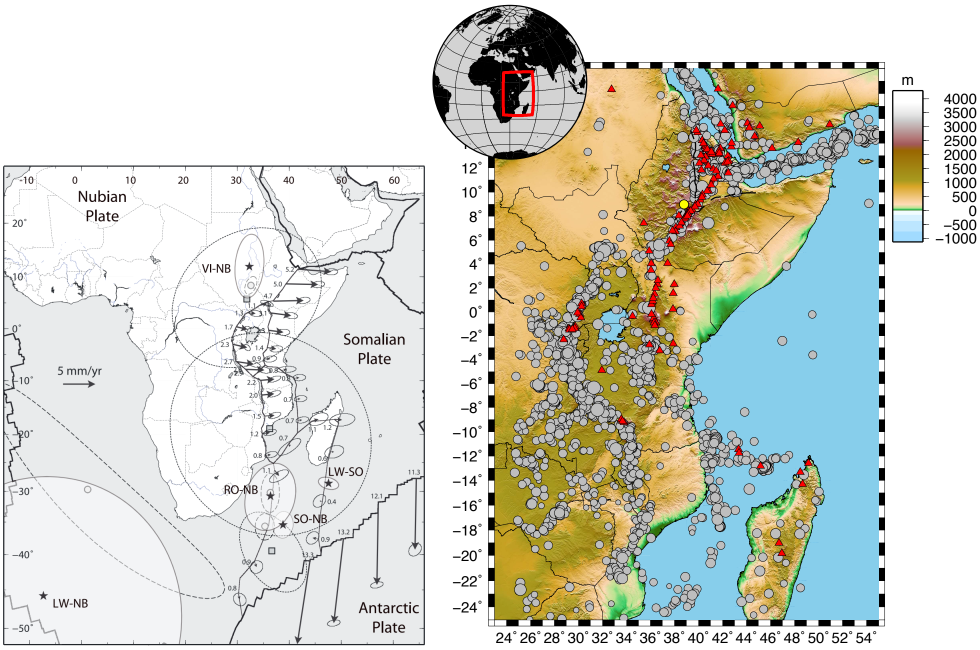

FIGURE 1.8: Extension and seismicity maps of the EARS. Left panel shows extension in East Africa based on a fixed Nubian plate from GPS studies. From Saria et al. (2014). Right panel shows seismicity as grey circle scaled according to magnitude (>3) from 2000 - 2020. Earthquakes are from the NEIC catalogue. Volcanoes marked as red triangles and Addis Ababa yellow circle. Earthquakes highlight all rift segments of the EARS but there is a significant difference in the amount of seismicity between each segment.

1.5 Seismic Structure of the EARS

Seismological studies of the EARS have been used to determine variations in velocity, crustal and plate thickness, temperature and composition. These parameters vary laterally and with depth along the EARS. In particular tomographic studies of the northern EAR have been used to image velocity variations within the rift and attribute them to changes in composition, temperature, melt and anisotropy within the crust and mantle. Below I summarise some of the key findings along the rift from the asthenosphere to the crust.

1.5.1 Asthenospheric Structure

At regional scales surface waves have been used to constrain crustal thickness and lithospheric thickness (Pasyanos and Nyblade, 2007; Fishwick, 2010; Fishwick and Bastow, 2011) providing enhanced resolution for the African continent when compared to global models. Surface waves studies of the upper mantle beneath Africa image fast velocity regions beneath the cratons and slow velocities elsewhere including beneath the EARS (Ritsema et al., 1999; Debayle et al., 2001; Pasyanos and Nyblade, 2007; Lebedev and Van Der Hilst, 2008; Priestley et al., 2008; Fishwick, 2010). P and S wave tomography studies of the mantle identify low velocities beneath the EARS with a broad significantly slower velocity zone beneath Ethiopia at depths of 75 - 400 km, including the MER, Afar and beneath the YTVL (Bastow et al., 2005, 2008; Benoit et al., 2006). Teleseismic Rayleigh wave tomography find similar results with evidence for segmentation in the mantle beneath the rift (Figure 1.9)(Gallacher et al., 2016). The velocities beneath the rift are slow enough to require elevated temperatures and partial melt to explain the observations (e.g. Bastow et al., 2008; Gallacher et al., 2016), in contrast to areas off rift where velocities, while slow compared to global averages, can be accounted for by elevated mantle temperatures beneath the area (Gallacher et al., 2016). The broad slow velocity zone has therefore been interpreted as zones of mantle upwelling (Civiero et al., 2015; Gallacher et al., 2016; Civiero et al., 2016) with a connection to the African superplume (Emry et al., 2019; Civiero et al., 2015; Bastow et al., 2005). Furthermore, Pn tomography found evidence for melt accumulation in the asthenosphere at the Lithosphere-Asthenosphere-Boundary (LAB) with melt channelised from the segmented upwelling zones to the rift axis (Corbeau et al., 2014).

1.5.2 Lithosphere Asthenosphere Boundary (LAB)

The lithosphere asthenosphere boundary (LAB) is the change between the lithosphere and the asthenosphere, and marks the base of tectonic plates. The nature of this interface is strongly debated with the most common definition that it represents the boundary at which the thermal layer switches from purely conductive in the lithosphere to convective in the asthenosphere (Fischer et al., 2010; Sleep, 2005; Rychert and Shearer, 2009)(Figure 1.10). Temperature differences modify the strength of the lithosphere with cold mantle increasing viscosity in the lithosphere. However, temperature gradually increases with depth, not fully explaining the variations in observations between the asthenosphere and lithosphere (Eaton et al., 2009; Fischer et al., 2010). Beneath the EAR, temperatures at the LAB are estimated to be between 1350 and $1490°C$ from modelling and geochemistry studies (e.g. Ferguson et al., 2013; Rooney, 2019; Armitage et al., 2015). Other factors that can vary the definition and depth of the LAB are grain size, mineral composition, volatile enrichment, water content and partial melting which all change the viscosity (Figure 1.10).

In seismic data the LAB is typically characterised as a seismic velocity decrease from the lithosphere to the asthenosphere. In tomographic studies this is often a broad fast zone overlying a slow velocity region. S-to-P receiver functions find a sharp change in the velocity contrast indicating a compositional or thermal change in the plate structure (Fischer et al., 2010; Eaton et al., 2009; Lavayssière et al., 2018; Rychert and Shearer, 2009). The LAB increases with depth from oceanic to continental plates, but thickness of the crust, lithosphere cratons and deepest LAB have not been observed to be related (Fishwick, 2010). The oceanic LAB is interpreted as a compositional boundary between dry and hydrated peridotite with the water content reduced by melting at mid ocean ridges (Hirth and Kohlstedt, 1996). In contrast, beneath continental cratons cold mantle remains attached to the base of the craton for billions of years with a gradual transition from cold lithosphere to warm asthenosphere making a transitional boundary for the LAB (Fischer et al., 2010; Pearson et al., 1995; Shapiro et al., 1999). In addition, partial melt can play a significant role in reducing the viscosity and velocity of the lithosphere, even at small fractions and particularly if the melt is aligned (Takei and Holtzman, 2009; Kohlstedt and Holtzman, 2009). However, the magnitude of the effect depends on the melt distribution and orientation (Hammond and Kendall, 2016; Hammond and Humphreys, 2000b; Takei, 2017). The velocity change has also been attributed to anisotropy from preferentially oriented melt

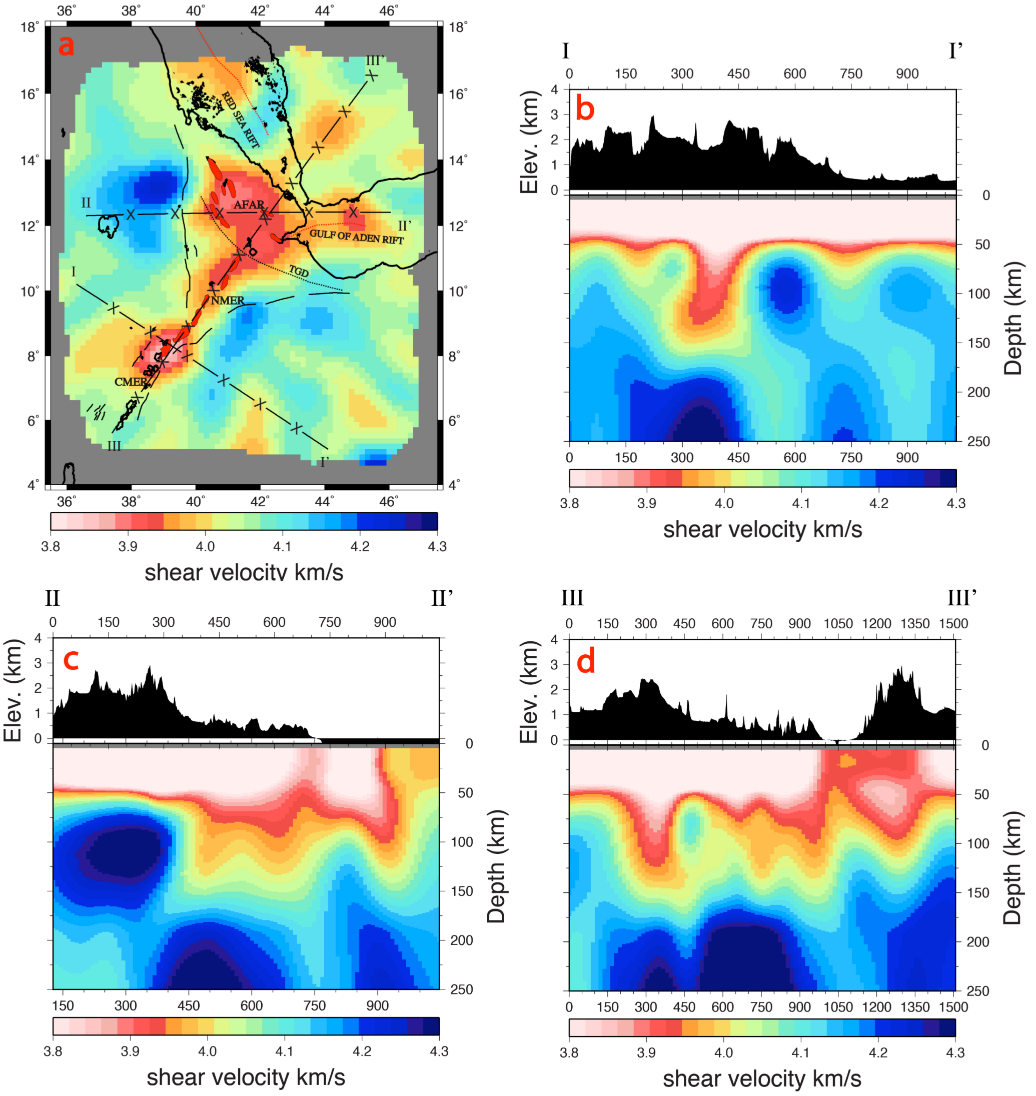

FIGURE 1.9: Depth averaged 3D shear velocity model slice and transects from Gallacher et al. (2016). (a) 40-132 km averaged depth slice shows that the Gulf of Aden and Afar form a continuous low velocity (<4.00 km/s) region. Higher velocities (>4.00 km/s) separate low velocities between the Northern MER (3.90–4.00 km/s) and a focused low velocity (3.80–3.95 km/s) along the Central MER. The Tendaho-Goba'ad Discontinuity (TGD), shown as a black dotted line, marks the boundary between the Northern MER and Afar. The magmatic segments for Afar, Central MER and Northern MER are shown shaded in red. (b) The I-I transect shows a focused low velocity (3.80–4.00 km/s) beneath the Central MER. (c) The II-II transect shows low velocities beneath Afar (3.80–4.00 km/s) and the Gulf of Aden (3.80-4.00 km/s). (d) The III-III transect shows an ∼200km long low velocity (3.80–4.00 km/s) beneath the Central MER and an ∼300 km long low velocity (3.90–4.00 km/s) beneath the Northern MER and Afar. The spacing between the low velocities is 150 km. Crustal velocities <3.8 km/s are saturated at 3.8 km/s.

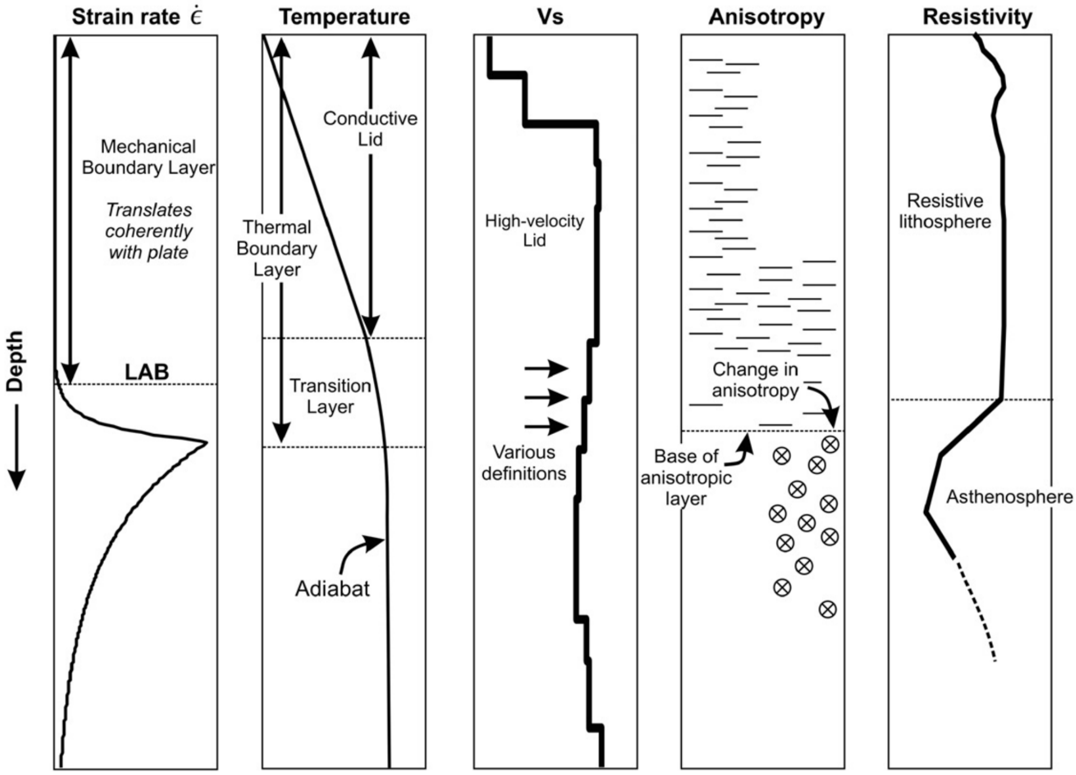

Figure 1.10: Definitions of the LAB by common observations (Eaton et al., 2009). Each definition has a different depth, or range of depths, for the LAB. Consequently, the mechanism, or combination of mechanisms, defining the LAB remain unclear and the boundary can be sharp or transitional.

pockets or aligned olivine or orthopyroxene (Gaherty et al., 1999; Levin and Park, 2000; Takei and Holtzman, 2009)(Figure 1.10).

The EARS has variable lithospheric thickness in excess of 200 km in the southern extent of the rift where deep cratonic roots are located, becoming thinner further north to <80 km depth (Figure 1.11). In the northern EAR, LAB depths have been interpreted from S-to-P receiver functions, surface wave tomography and a joint inversion between Rayleigh wave velocities and receiver functions (Fishwick, 2010; Rychert et al., 2012; Lavayssière et al., 2018; Dugda et al., 2007). The LAB is thought to lie at 60 - 80 km depth beneath the Ethiopian Plateau, and thinned from ∼30 Myrs of magmatism. The depth of the LAB beneath the rift is debated (Dugda et al., 2007; Lavayssière et al., 2018; Rychert et al., 2012; Fishwick and Bastow, 2011)(Figure 1.11). Beneath Afar the LAB resides at a maximum depth of 50 km (Dugda et al., 2007; Fishwick, 2010), while S-to-P receiver functions suggest the LAB is not present (Rychert et al., 2012) or obscured by melt (Lavayssière et al., 2018).

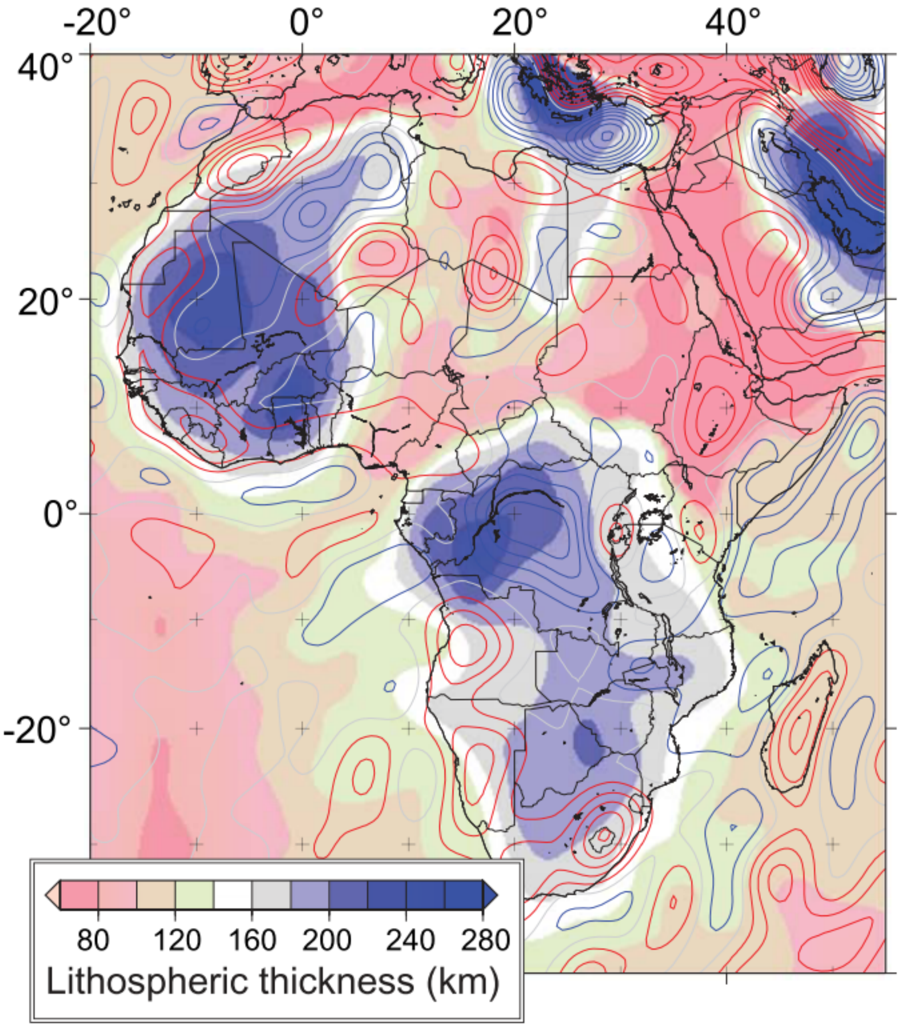

FIGURE 1.11: Map of lithospheric thickness from Fishwick and Bastow (2011). Generated from the tomographic model of Fishwick (2010) where the velocities were converted to temperature using the empirical parameterisation of Priestley and McKenzie (2006) and fitted to geotherms.

1.5.3 Upper Mantle Structure

Beneath Africa, tomographic studies find variable velocities in the upper mantle. Those beneath the EAR are typically slow, whereas the mantle velocity structure beneath cratonic areas is significantly faster (Emry et al., 2019; Fishwick and Bastow, 2011; Grijalva et al., 2018; Hansen et al., 2012). In the southern and western sections of the EAR, faster velocities indicative of deeper cratonic roots and normal temperature mantle were observed with slow velocities isolated to areas of recent volcanism (Emry et al., 2019; Hansen et al., 2012). Beneath the more magmatically active northern and eastern branches of the EARS shear wave velocities are slow when compared to global average models (e.g. ak135)(Kennett et al., 1995) and in places slow enough to require melt (e.g. the MER and Afar) (Bastow et al., 2005, 2008; Gallacher et al., 2016). Beneath Ethiopia velocities are slow everywhere including off rift (Bastow et al., 2005; Gallacher et al., 2016; Bastow et al., 2008). The velocities off rift can be accounted for by elevated temperatures whereas those within the rift require a component of partial melt (Gallacher et al., 2016).

At upper mantle depths (<100 km) beneath the magmatic northern and eastern branches of the EARS, low velocity zones are segmented along axis beneath the rift valley, at length scales of hundreds of kilometres (e.g. Bastow et al., 2005; Emry et al., 2019; Hammond et al., 2013; Gallacher et al., 2016; Civiero et al., 2015, 2016). Tomographic images of Afar have found segmented slow velocities beneath the rift axis that become more localised and focussed in the crust suggesting segmented asthenospheric upwellings feed the discrete magmatic segments (Hammond et al., 2013). Segmentation of the asthenosphere is observed beneath the MER and Afar from body wave and surface wave tomography in the mantle (Bastow et al., 2005, 2008; Gallacher et al., 2016) providing further evidence for multiple upwellings generating segmentation in the mantle. At Moho depths Pn tomography has observed segmentation of slow velocity zones interpreted as partial melt beneath the magmatic segments and off-axis suggesting the segments and intrusions can be fed by off-axis delivery of melt (Stork et al., 2013).

1.5.3.1 Temperatures

The mantle is slower than expected for a mantle peridotite everywhere beneath Ethiopia, suggesting mantle temperatures are elevated in this region (e.g. Bastow et al., 2005, 2008; Chambers et al., 2019; Fishwick, 2010; Gallacher et al., 2016; Stork et al., 2013). Geodynamic modelling and mantle flow models suggest mantle potential temperatures range from normal (Pinzuti et al., 2013; Rychert et al., 2012) to moderately elevated by 100 - $170°C$ above ambient mantle ($\sim 1350°C$) (e.g. Armitage et al., 2015; Rychert et al., 2012). Geochemical analysis and modelling of REE compositions of recent lava flows find similar results (Rooney et al., 2012a; Ferguson et al., 2013; Rooney et al., 2012b; Beccaluva et al., 2009). The temperature is not thought to vary significantly between the rift valley and off rift beneath the plateau (Rooney et al., 2012a; Ferguson et al., 2013). Beneath the rift axis, where regional studies find the slowest velocities, a combination of slightly elevated temperature and melt are required after accounting for variations in composition (e.g. Armitage et al., 2015; Bastow et al., 2005; Chambers et al., 2019; Gallacher et al., 2016; Hammond et al., 2013). Relatively high REE concentrations suggest temperatures are elevated enough to initiate melt generation beneath the rift with moderately high pressures and temperatures ($\sim 1450°C$) at depths of 53 – 120 km. The maximum starting depths for initiation are 88 - 120 km (Ferguson et al., 2013; Rooney et al., 2005).

Absolute crustal temperatures are harder to determine due to velocity variations and geochemical analyses being influenced by a range of intertwined factors such as composition, residence time and presence of fluids (Karakas and Dufek, 2015; Rooney et al., 2017). It is likely temperatures in the crust of the rift are elevated due to the presence of dyke intrusions and partial melt (Karakas and Dufek, 2015), which have been used in studies modelling gravity and seismic velocity in areas of highly intruded crust (Cornwell et al., 2006; Bastow et al., 2005; Rooney et al., 2007)

1.5.4 Crustal structure

The crust of the EAR is highly variable in terms of composition and thickness. In general the crust is thickest beneath the plateaus with more continental velocity structure observed, whereas the rift valleys have thinned crust and evidence for modification by magmatism (e.g.

Mackenzie et al., 2005; Maguire et al., 2006; Ogden et al., 2019; Hammond et al., 2011). First-arrival travel-time tomography and passive source P-wave models observe high P-wave velocity anomalies (>6.5 km/s) located beneath the surface magmatic segments at mid crustal depths suggested to be cooled mafic intrusions (Keranen et al., 2004; Daly et al., 2008; Dugda et al., 2005). Slow S-wave velocities are observed at similar depths beneath the MER, Afar and areas of the Ethiopian Plateau (Keranen et al., 2009). The slow S-wave velocities coupled with high Vp/Vs ratios beneath the axis and off rift provides evidence for melt at mid to lower crustal levels (Keranen et al., 2009; Dugda et al., 2005). Ambient noise studies have provided further information on the phase, group and shear velocities beneath the rift which are sensitive to fluids (Kim et al., 2012; Korostelev et al., 2015). Kim et al. (2012) analysed crustal structure within rift segments of the northern and central sections of the MER extracting group velocities before inverting for absolute shear velocity (Figure 1.12). They found two slow velocity zones interpreted as areas of magmatic activity beneath the magmatic segments controlled by faulting, in addition to magmatism at the rift flanks beneath the YTVL. This observation is similar to geochemistry and receiver function studies within Ethiopia that suggest slow velocity zones in the lower crust supply melt for the surface magmatic segments (Hammond et al., 2013; Rooney et al., 2005; Kendall et al., 2006). Korostelev et al. (2015) focussed on the Afar rift, producing phase velocity maps but not inverting for shear velocity (Figure 1.13). They observed slow velocities interpreted as extensive magmatic modification of the crust, including beneath the rift flanks, which map to known sources of volcanism and geothermal activity. Both studies find evidence for a complex magmatic plumbing system in the crust (Kim et al., 2012; Korostelev et al., 2015) (Figure 1.13 and Figure 1.12).

1.5.4.1 Crustal Thickness

Crustal thickness has been modified by rifting and volcanism beneath the EAR and is consequently highly variable. Regional topographic models of Africa suggest irregular thickness with the thickest crust beneath the flood basalt province of Ethiopia and the cratons of southern Africa (Pasyanos and Nyblade, 2007; Globig et al., 2016; Prodehl et al., 1997). Northwestern Africa contains thinner crust and beneath the Afar triple junction (Globig et al., 2016; Pasyanos and Nyblade, 2007) (Figure 1.14). The EARS has variable Moho depths along its length with the Turkana depression in southern Ethiopia and Northern Kenya a region of thinner crust (∼35 km) separating the thicker crust of the northern branch and western and eastern branches of the rift system (Globig et al., 2016)(Figure 1.14). The western part of the Ethiopian Plateau and the Somalian Plateau are 30 - 40 km thick and considered to be representative of pre-rifted unmodified crust (Figure 1.14) (Globig et al., 2016; Ogden et al., 2019; Hammond et al., 2011). The western edge of the Ethiopian Plateau is 30 – 35 km thick (Ogden et al., 2019; Globig et al., 2016) and considered the least modified by the flood basalt emplacement. The Somalian Plateau on the western edge had minor modification during the flood basalt emplacement but is otherwise unmodified crust that is 35 - 40 km thick (Mackenzie et al., 2005; Stuart et al., 2006) (Figure 1.14). In contrast the eastern part of the Ethiopian Plateau has been affected by the flood basalt intrusions and has thicker crust ranging from 40 - 45 km thick (Mackenzie et al., 2005; Ogden et al., 2019; Stuart et al., 2006) (Figure 1.14). The Arabian Peninsula and Yemen have crustal thickness estimates of ∼35 km, similar to those of the Somalian Plateau and the western part of the Ethiopian Plateau (Ahmed et al., 2013).

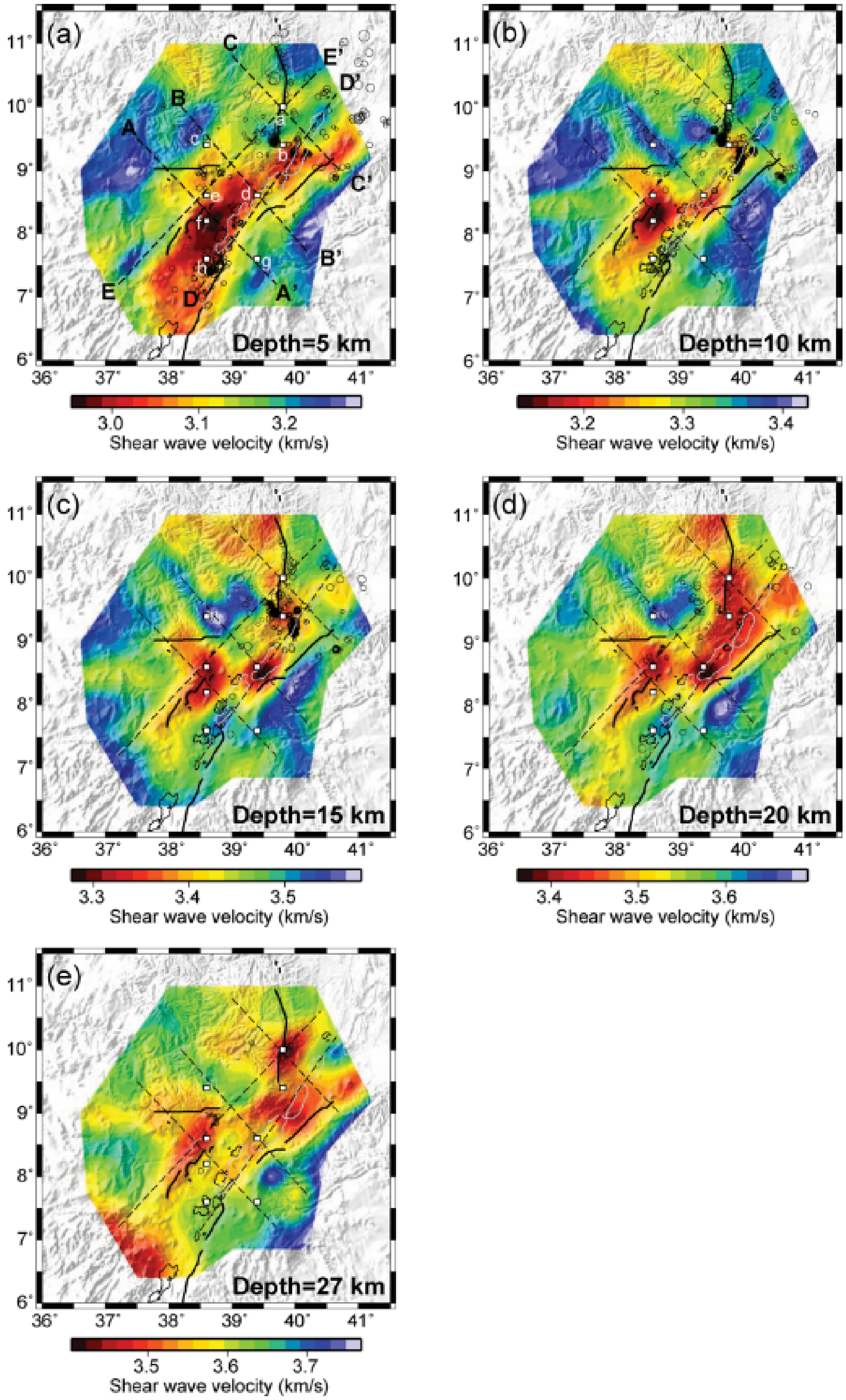

FIGURE 1.12: Shear velocity maps of the MER using ambient noise tomography at depths of 5, 10, 15, 20 and 27 km depth. Depth is indicated in the lower right corner of each map. Earthquake epicentres from Keir et al. (2006b) within ±2.5 km of the depth of each model slice are shown with open circles. The slowest velocities are constrained to the rift with moderate velocities beneath the Western border fault and the Yerer-Tullu Wellel volcanotectonic lineament. From Kim et al. (2012).

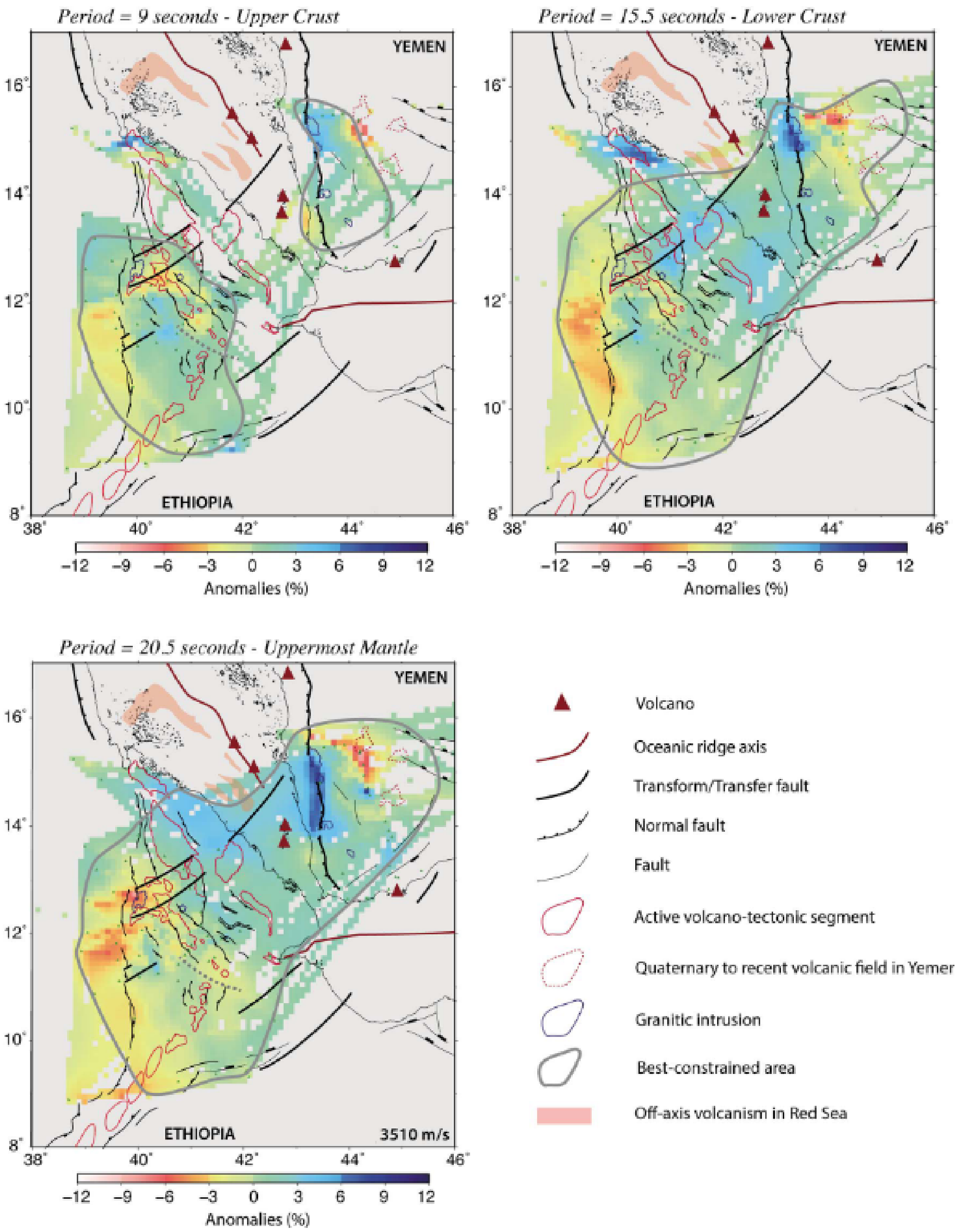

Figure 1.13: Phase velocity maps (percent with respect to average) for Afar and Yemen using ambient noise tomography at 9, 13.5 and 20.5 seconds period. The average velocity for each period is in the bottom right of each map (m/s). The solid grey line delimitates the best constrained area. Note slow velocities beneath the Ethiopian Plateau at all periods and slow velocities in northern Afar for the shortest period only. At longer periods phase velocity is fast within northern Afar. From Korostelev et al. (2015).

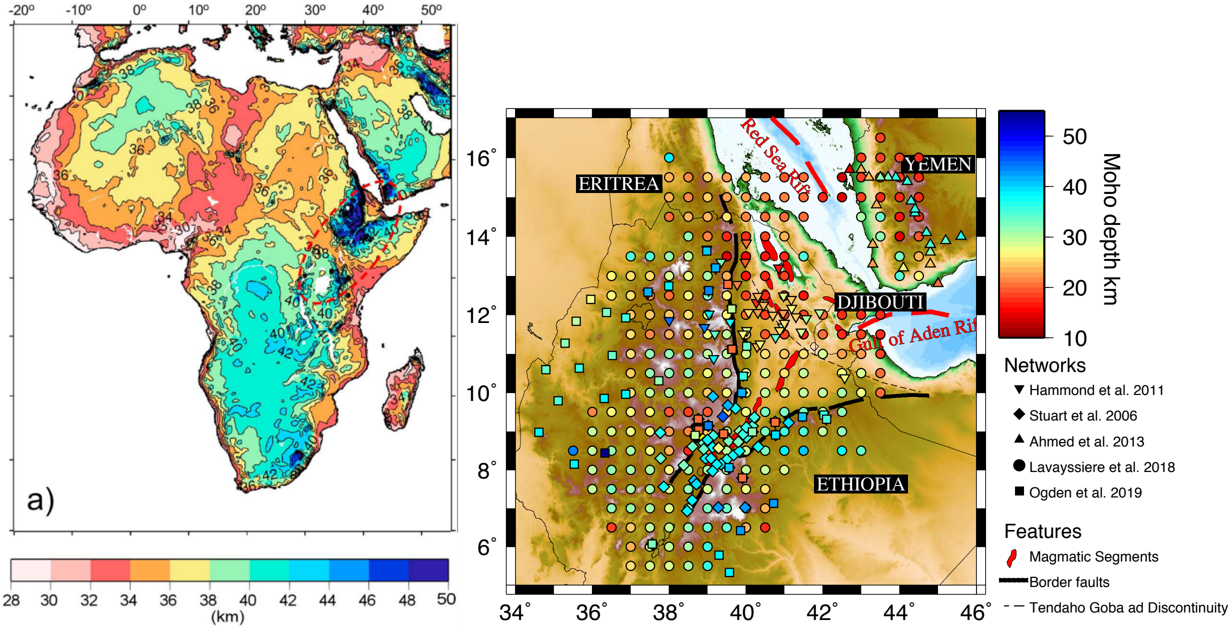

Figure 1.14: Maps of Moho depth. Left Panel, Moho depth across Africa based on integrated modelling of elevation, geoid data and thermal analysis. From Globig et al. (2016). Right panel, receiver function Moho depths from studies including H/ϰ stacking and S-to-P receiver functions. Results from Stuart et al. (2006); Hammond et al. (2011); Ahmed et al. (2013); Lavayssière et al. (2018); Ogden et al. (2019).

The rift is mostly thinner than the plateaus with the exception of areas in the southern MER where crustal thicknesses range from 30 – 38 km thick (Figure 1.14). The thicker crust has been interpreted as evidence for lower crustal intrusions into the lower crust (Hammond et al., 2011; Maguire et al., 2006; Stuart et al., 2006). In Afar crustal thickness ranges from <16 - 26 km, a result of crustal thinning from progressive rifting (Dugda et al., 2005; Hammond et al., 2011; Lavayssière et al., 2018). The Danakil depression has the thinnest crust and at its lowest point is 120 m below sea level despite being subaerial (Bastow and Keir, 2011; Keir et al., 2013). While there are varying crustal thicknesses no area in the MER or Afar has progressed to full seafloor spreading. Crustal thicknesses are too thick and the composition is not reflective of Mid Ocean Ridge Basalt (MORB), a characteristic of rifts that have progressed to full seafloor spreading.

Studies constraining crustal thickness have also analysed the ratio of P-wave to S-wave velocities (Vp/Vs ratio) in the region which can estimate the likely average composition of the plate. Receiver function studies find Vp/Vs ratios of 1.7 - 1.8 beneath the Ethiopian Plateau in areas not affected by flood basalt volcanism which are suggested to indicate the crustal structure prior to rifting (Ogden et al., 2019; Hammond et al., 2011; Hammond, 2014). Vp/Vs values increase to 1.9 beneath the flood basalts on the Ethiopian Plateau reflecting the more mafic composition (Hammond et al., 2011; Ogden et al., 2019) and 1.95 beneath the rift where there have been significant intrusions (Hammond et al., 2011; Stuart et al., 2006). In areas of Afar the Vp/Vs ratio exceeds 2.0 indicating pervasive partial melt(Hammond et al., 2011; Hammond, 2014).

1.6 Anisotropy

Anisotropy provides another diagnostic of rifting processes, allowing determination of mantle flow and orientation of layers and melt. Seismic anisotropy is produced in a variety of ways from lattice preferred orientation (LPO) of minerals in the crust and mantle, as oriented melt pockets (OMP), or as periodic thin layering (PTL) of contrasting materials (Kendall, 2000; Backus, 1962). In the upper mantle LPO of olivine is the primary mechanism for seismic anisotropy, aligning in the direction of flow. Furthermore, rift parallel lithospheric anisotropy in regions with known melt is generally interpreted as aligned partial melt generated by melt focusing along the LAB (Holtzman and Kendall, 2010; Holtzman, 2016). Within the upper crust, aligned micro-cracks vertically orientated parallel to the direction of maximum horizontal stress are thought to be the main driver (Crampin, 1994). PTL of materials with contrasting velocities (e.g. volcanics and sediments) can generate long-wavelength anisotropy (Backus, 1962). If the layering is horizontal, the medium will act like a homogeneous hexagonally symmetric material with a vertical symmetry axis. This is commonly referred to as vertical transverse isotropy (VTI), but the terms polar or radial anisotropy are also used to describe such symmetry (Kendall et al., 2006). OMP generate anisotropy which can be used to interpret melt fraction and the shape of melt inclusions (Kendall, 1994, 2000; Kendall et al., 2006). Thin disk-like melt pockets generate more anisotropy than long tube-shaped inclusions in general (Kendall, 2000; Hammond et al., 2014, 2013). In areas that are actively upwelling from buoyancy effects and elevated mantle potential temperatures, anisotropy would likely record vertical mantle flow beneath the rift.

Measuring anisotropy can be used to determine melt alignment and direction of flow. Shear wave splitting is one method used to measure anisotropy. When a shear wave encounters an anisotropic medium it splits into two orthogonal shear waves oriented in the fast and slow directions with the delay times between the two quantifying the amount of splitting (e.g. Kendall et al., 2006; Hammond et al., 2010). Body wave studies have good lateral resolution but are limited to regions with seismic stations (Kendall et al., 2005). Surface waves are also affected by seismic anisotropy with azimuthal variations in the surface wave phase velocities and discrepancies between the Love and Rayleigh wave shear velocities (Kendall et al., 2006; Kirkwood and Crampin, 1981; Bastow et al., 2010). The dispersive nature of surface waves leads to good resolution of anisotropy variation with depth, but has poor horizontal resolution due to long wavelengths (Kendall et al., 2006) so should be combined with body waves and measures of SKS splitting to provide good vertical and horizontal resolution giving a better idea about length scales of anisotropy (Bastow et al., 2010, 2007). The speeds of horizontally propagating Love (SH) and Rayleigh (SV) waves vary similarly with azimuth for LPO and OMP induced anisotropy, but their relative change is distinctive for each mechanism.

Within the EARS measurements of anisotropy at depth observe a dominant northeast southwest anisotropic fast direction suggesting LPO from broad flow dominates the uppermantle rather than a plume (Hammond et al., 2014; Kendall et al., 2006; Bastow et al., 2010) (Figure 1.15). At upper mantle depths SKS splitting have produced results that are, in general, rift parallel which is similar for most rifts with the notable exception of the Baikal rift where fast polarisation directions are rift perpendicular, potentially due to cooler rifting temperatures (Gao et al., 1997; Kendall et al., 2006, 2005; Ayele et al., 2004; Bagley and Nyblade, 2013). SKS measurements in Kenya, Ethiopia and Djibouti, have been correlated with the amount of melt production (Ayele et al., 2004; Bagley and Nyblade, 2013). Further south in Tanzania and Kenya the magnitude of splitting and anisotropy is smaller where the rift is younger (Gao et al., 1997; Walker et al., 2004). The shallow source of anisotropy coupled with increased splitting results in more magmatic regions and alignment with magmatic segments suggests that within the EAR and certainly sections at later stage rifting, anisotropy is controlled by OMP (Kendall et al., 2006; Gallacher et al., 2016; Hammond et al., 2014) down to depths of at least 75 km. Furthermore splitting at stations within the magmatic segments show much larger anisotropy (∼6%) than those in the rift valley but outside the segments (∼3%) (Kendall et al., 2005, 2006). Outside the rift the splitting is further reduced in the Ethiopian Plateau. Overall anisotropy cannot be explained by the direction of absolute plate motion as Africa is almost stationary in a hotspot reference frame with both the Nubian and Somalian plates moving in a northwesterly direction which is not observed in the anisotropy (Calais et al., 2006; Kendall et al., 2006; Bastow et al., 2010). Away from the rift fossil anisotropy with fast direction northeast - southwest are persevered in the lithosphere (Hammond et al., 2014; Walker et al., 2004). At crustal depths most anisotropy is horizontally aligned except beneath recent areas of volcanism where it is vertical (Hammond et al., 2014). In addition, at depths <10 km periodic thin layering of seismically fast and slow material is present (Bastow et al., 2010).

1.7 Thesis Outline

The focus of this thesis is to investigate how rifting modifies plate structure at various stages of rifting. Methods for the ambient noise, teleseismic surface waves, joint inversion and radial anisotropy are presented in Chapter 2 with details of the networks used. Chapter 3 details the crust and uppermost mantle velocity structure from ambient noise tomography. Chapter 4 focuses on a joint inversion between the ambient noise detailed in Chapter 3 and phase velocities from teleseismic Rayleigh waves. This was to investigate upper mantle segmentation beneath the rift at greater resolution. Chapter 5 investigates flow of melt and crustal fabric using radial anisotropy from the ambient noise dataset.

Author's note: Chapters 3, 4 & 5 have been written as stand-alone research papers. Each of these chapters contains a review of the tectonic setting and methods used and consequently there may be some degree of repetition between these chapters.

Chapter 2 Methods

In this chapter I summarise the methods used in Chapters 3, 4 & 5. First I detail the seismic data used in this thesis which was all available from the IRIS DMC. I then discuss the ambient noise tomography technique using DISPER80 (Saito, 1988) to generate absolute shear velocities. After this I discuss the techniques used to produce shear velocities from Rayleigh surface wave tomography of teleseisms. I then progress to discussing the joint inversion between the two methods. I then finish with the methods for the radial and azimuthal anisotropy.

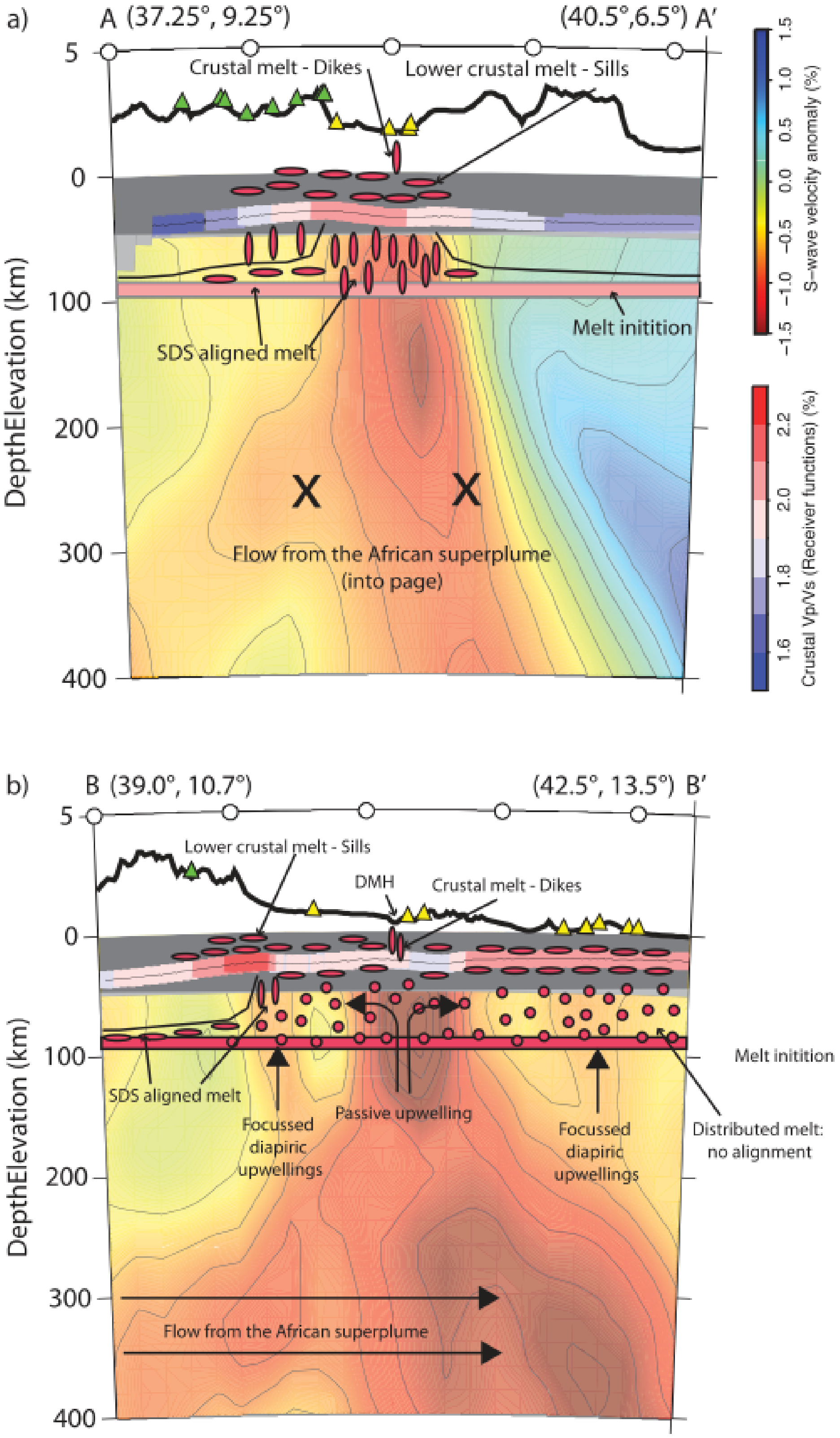

FIGURE 1.15: Model of anisotropy in Ethiopia from Hammond et al. (2014) using S-wave tomography with annotations on top. Panels are of a) the MER and b) Afar. Topography (thick black line), crustal thickness, and bulk crustal VP/VS (multicoloured line) are also displayed from Hammond et al. (2011). The thin black line shows interpreted lithospheric thickness after Rychert et al. (2012). Red ellipses show aligned melt and red circles show melt with little alignment. The pink band shows the region of melt initiation Rychert et al. (2012); Hammond et al. (2010); Ferguson et al. (2013)[Hammond et al., 2010; Rychert et al., 2012; Ferguson et al., 2013]. Triangles show Holocene (yellow) and older (green) volcanoes.

Chapter 3 Using Ambient Noise to Image the Northern East African rift

In this chapter I present results from ambient noise tomography for the northern East African Rift. The results show the mantle is everywhere slow beneath the region requiring moderately elevated temperatures and a component of partial melt. Melt focussing occurs beneath the MER due to large changes in crustal thickness across the narrow MER. In contrast melt within Afar is more dispersed due to the wide rift. In addition, I found evidence for melt beneath the Ethiopian Plateau at uppermost mantle to mid crustal depths suggesting ongoing melt emplacement is occurring off-rift.

Chapter 4 A joint inversion of Rayleigh waves from ambient noise tomography and teleseisms to image melt and seismic structure in the northern East African Rift

In this chapter I perform a joint inversion between phase velocities obtained from the ambient noise in Chapter 3 combined with those from teleseismic Rayleigh surface waves. The rationale was to enhance resolution at Moho depths and produce one absolute 3-D shear velocity model of the crust and mantle. This enables interpretation of spatial variations in processes beneath different sectors of the rift and adjacent flanks. This work also enables further constraints on the controls of melt beneath the Ethiopian Plateau by establishing maximum depths of melt and lateral connectivity to the rift.

Chapter 5 Variations in melt emplacement beneath the northern East African Rift from radial anisotropy

In this chapter I generate maps of radial anisotropy from the Love and Rayleigh wave components of surface waves. The focus was to look for layering in the crust which could be indicative of magma storage in sill or dyke structures associated with the magmatic plumbing system. This in turn was related to the shear velocity observations in the upper, mid and lower crust.

Chapter 6 Conclusions

Here I summarise the findings of the thesis and how they address the science questions and hypotheses which I set out to address. I also outline the outstanding questions and potential future research that could be undertaken to investigate further.

Chapter 2

Methods

In this chapter I discuss the methods used to produce this thesis. I first discuss the data used and collection procedures. I then focus on the use of ambient noise for tomographic imaging (used in Chapter 3) and progress to using Rayleigh waves from teleseisms to image the velocity structure deeper in the Earth (Chapter 4). Following this I discuss the methods I used to perform a joint inversion between the phase velocities obtained from the ambient noise and teleseisms (Chapter 4). Due to the complexities in relating velocity to Earth structure I include a section accounting for temperature effects from the emplacement of a flood basalt (Chapter 3 and Chapter 4). Finally, I discuss the methods for the radial anisotropy used in Chapter 5.

2.1 Data Collection

The data used for this thesis were all readily available from the Incorporated Research Institutions for Seismology, Data Management Centre (IRIS DMC) or from SEIS-UK (RiftVolc dataset) (Brisbourne, 2012). I also had the opportunity to participate in fieldwork during my PhD in order to gather data from seismometers for 3 projects deployed in Ethiopia and Kenya. The first fieldwork was in September 2017 where I participated in 2 field campaigns lasting 1 month in total. For the RiftVolc project I was part of a team to retrieve data and remove the seismometers as the final stage of the seismic fieldwork. The Afar17-18 fieldwork involved deploying seismometers and servicing existing instruments. The data will be available to future students to analyse, in addition to the existing receiver function analysis to assess crustal thickness variations from the Ethiopian Plateau into the rift (co-author on paper submitted to Tectonophysics. Ahmed et al. Crustal Structure Variations beneath the Western Afar Margin from Receiver Functions). The data collected from the Ethiopian fieldwork was for the RiftVolc project and was incorporated into the datasets used in this thesis (Chapter 4). The Kenyan fieldwork for the TRAILS project (Turkana Rift Arrays to Investigate Lithospheric Structure in Kenya), took place in January 2019 where I lead a field team to deploy 21 seismometers. Data from the TRAILS project will be available for future PhD students to work with. Participating in these projects has allowed me to engage in all areas of seismic fieldwork.

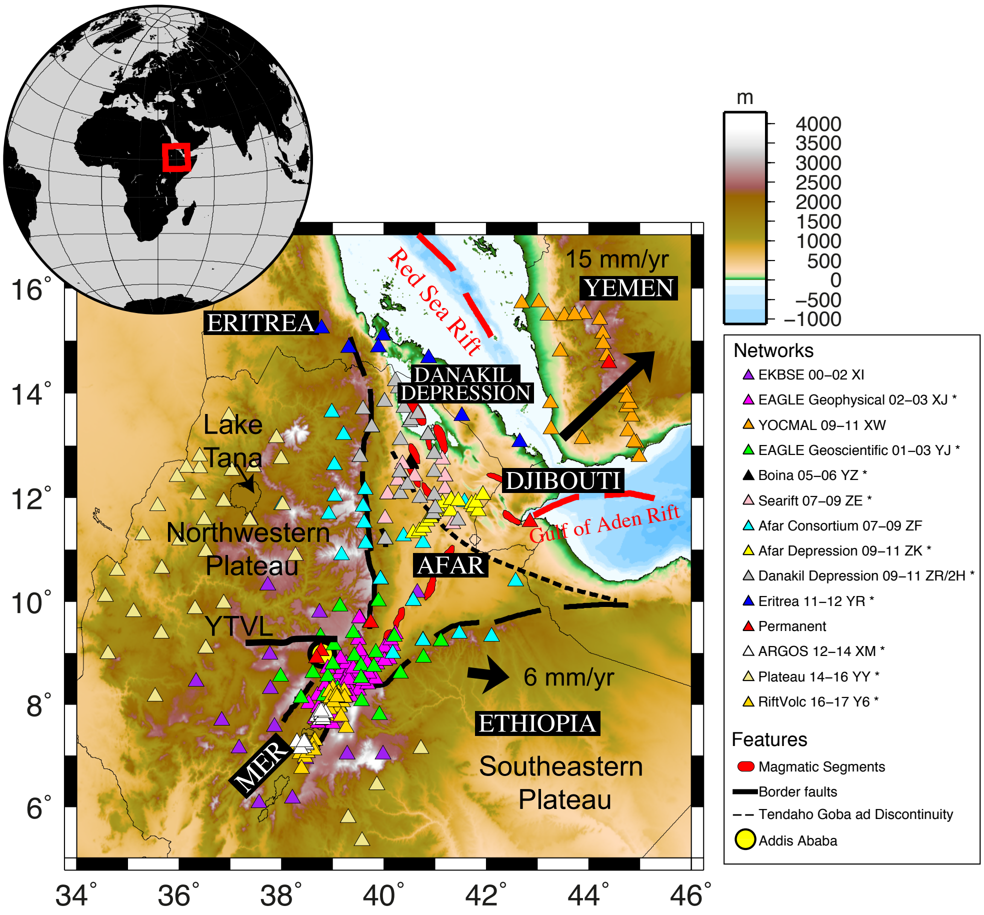

Figure 2.1: Map of all seismic stations used in this thesis. Thick black lines show border faults, red polygons magmatic segments and dashed lines the Tendaho-Goba'ad discontinuity (TGD). Stations are triangles coloured to their project deployment. Networks with * have not been used for ambient noise prior to this work. Black arrows depict plate motions relative to the Nubian plate and Addis Ababa is marked by a yellow circle.

2.1.1 Networks

In this thesis I have used multiple seismic networks present in Ethiopia, Djibouti, Eritrea, and Yemen which are all available for download from the IRIS DMC. In the table below (Table 2.1) I detail all the networks used in this study, and show their locations in Figure 2.1. There is good coverage in northern Afar, the MER and Ethiopian Plateau. In eastern Ethiopia including central and east Afar and the Somalian Plateau, the coverage is sparser. Furthermore, there are no ocean bottom seismometers in the Red Sea or Gulf of Aden reducing coverage in these regions.

All networks detailed below are used for the ambient noise study, except the RiftVolc network where station separation was not sufficient for the required 2 x wavelength when cross correlating the signals (Chapter 3). For teleseismic events all networks were used (Chapter 4). In total 274 seismic stations operating from 1999 – 2017, with the majority of the stations equipped with broadband instruments, were used in this thesis. The networks were present at various intervals and not continuous for the whole period. Only stations present at the same time were used for cross correlation of ambient noise.

Network Name	Network Code	Start Date	End Date	No. Stations	Available From
Permanent Stations (FURI, ATD, AAUS, DESE, ANKE)	IU, G, AF	1999, 1993, 2006, 2009	Present	5	IRIS DMC
Ethiopia Kenya Broadband Seismic Experiment	XI	25/02/2000	13/05/2002	28	IRIS DMC
EAGLE Geoscientific	YJ	22/10/2001	30/01/2003	31	IRIS DMC
EAGLE Geophysical	XJ	04/10/2002	10/02/2003	55	IRIS DMC
BOINA	YZ	18/10/2005	09/02/2007	9	IRIS DMC
Searift	ZE	11/03/2007	18/10/2009	19	IRIS DMC
Afar Consortium	ZF	04/10/2007	21/10/2009	32	IRIS DMC
Afar Depression	ZK	31/12/2009	17/05/2011	18	IRIS DMC
Danakil Depression/Afar0911	ZR/2H	07/10/2009	20/02/2013	23	IRIS DMC
Young Conjugate Margins Lab in the Gulf of Aden (YOCMAL)	XW	27/03/2009	19/05/2011	79/23	IRIS DMC
Eritrea	YR/5H	16/06/2011	14/10/2012	7	IRIS DMC
Aluto and Regional Geophysical Observation Study SEIS-UK (ARGOS)	XM	08/01/2012	01/02/2014	21	IRIS DMC
Exploring extensional tectonics beyond the Ethiopian Rift (Plateau)	YY	18/03/2014	26/02/2016	33	IRIS DMC
Rift valley volcanism past present and future (RiftVolc)	Y6	10/02/2016	05/10/2017	41	IRIS DMC/SEIS-UK

TABLE 2.1: A table of each seismic network used in this thesis and when it was operational.

2.1.2 Earthquakes

For Chapter 4 I extracted the Rayleigh waves from teleseismic events. The earthquakes were recorded on 3-component broadband seismometers and I used the vertical component to extract the Rayleigh waves. All teleseisms were downloaded from the IRIS DMC with magnitudes >5.5 and epicentral distances of 25 - 150° from 1999 - 2017. The range is extended from the typical 30 - 150° range to account for the large aperture of our stations which is greater than 5° between the furthest spaced stations. The range is chosen to ensure the Rayleigh wave does not arrive at the station from the opposite direction at a similar time. The teleseisms were windowed around the surface wave and manually inspected to ensure the surface wave was distinguishable from the body wave. In addition, the signal to noise ratio, group velocity dispersion curve and wave energy were inspected for each event at every station. For an event to be included the seismograms required a SNR of greater than 3, a continuous group velocity dispersion curve, and peak energy between the approximate frequencies of interest (0.01 Hz to 0.07 Hz). A further requirement was for more than 7 good seismograms per event as this is the minimum station coverage resulting in a stable answer in the two plane wave inversion described below. In total, 1053 teleseismic events were recorded that met all the specified criteria (Figure 2.2), an increase of 484 above the 569 recorded by Gallacher et al. (2016).

2.2 Ambient Noise Tomography

Ambient noise refers to the background vibrations of the Earth. This may be generated by a series of sources including the Earth's hum, primary microseism, secondary microseism and local noise sources e.g. weather (Figure 2.3). For the purposes of tomographic studies, seismologists are primarily interested in the primary and secondary microseism which are generated by ocean waves. Noise sources at shorter periods such as anthropogenic noise, are highly attenuating becoming incoherent at distances greater than several kilometres, which for most seismic surveys is too small. The primary microseism (peaking at ∼15 s period (Bensen et al., 2007)) is generated by ocean waves interacting with shallow bathymetry, typically at coast lines (Hasselmann, 1963; Traer et al., 2012). The secondary microseism (∼7.5 s period) is generated by the interaction of ocean gravity waves, often generated by storms, which produce a pressure wave that carries energy to the seafloor (Bensen et al., 2007; Hillers et al., 2012). This vibration is then carried through the Earth and detected by seismometers. The secondary microseism is more energetic that the primary microseism resulting in double the frequency recorded (Longuet-Higgins, 1950). On a seismometer the recorded microseisms look like the background "jitter" that was traditionally discarded in favour of impulsive sources such as earthquakes and explosions.

The primary and secondary microseism depend on variations in bathymetry in addition to the ocean swell, which is itself affected by changes in weather patterns. As such the distribution of the noise sources is not equal everywhere on the Earth as shown in Figure 2.4 and have a strong seasonal dependence (Hillers et al., 2012). The strongest noise sources occur during the autumn and winter months associated with increased storm activity in the northern hemisphere. In contrast, during the summer months the Southern Ocean and South Pacific are the dominant noise sources. In addition, the distribution of land sources is not equal around the Earth creating

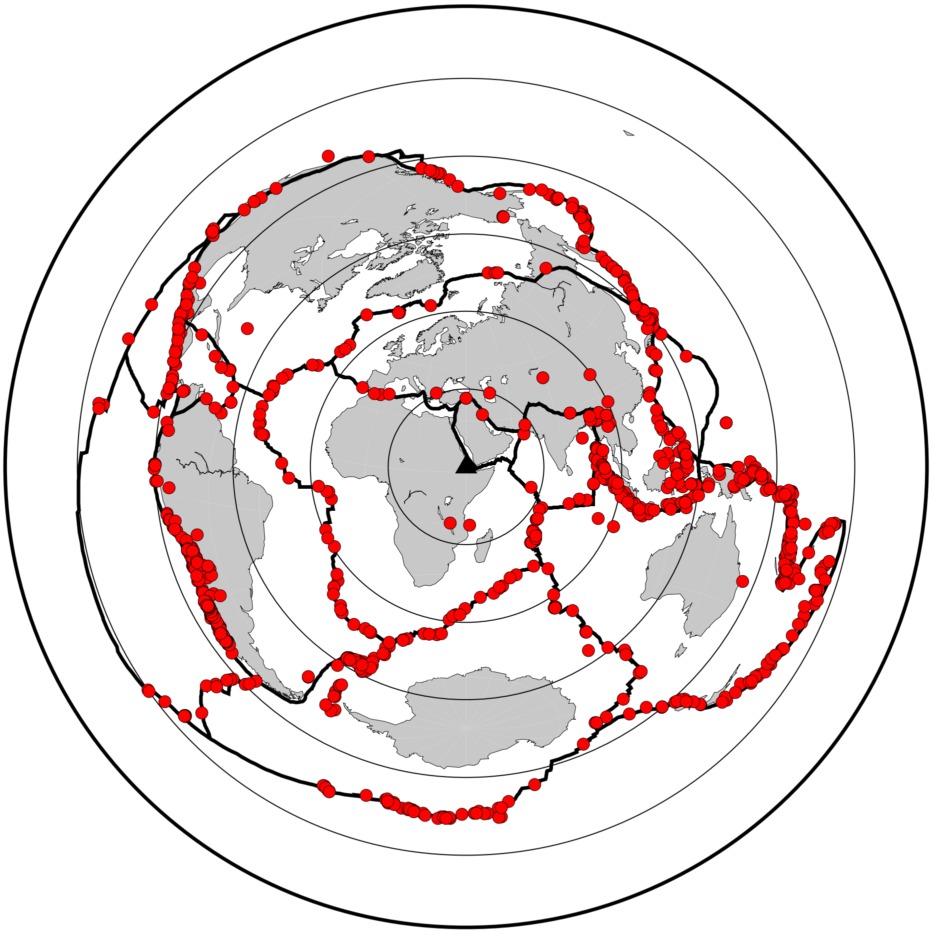

FIGURE 2.2: All 1053 teleseismic events used in Chapter 4 displayed as red circles after quality control had been undertaken. Earthquakes have magnitude >5.5 and epicentral distances between 25 - 150°.

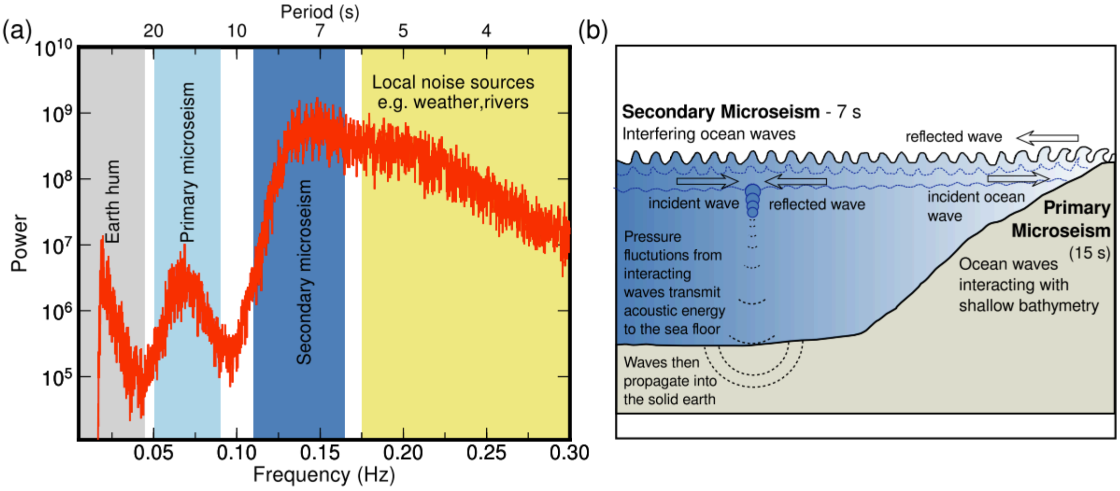

FIGURE 2.3: The ambient noise wave field. a) The power spectrum of the noise wave field. The source frequency bands are denoted by the coloured bands. b) Figure illustrating generation mechanisms for the primary and secondary microseism noise sources which are the frequency bands of interest for tomographic imaging. Adapted from Green (2016).

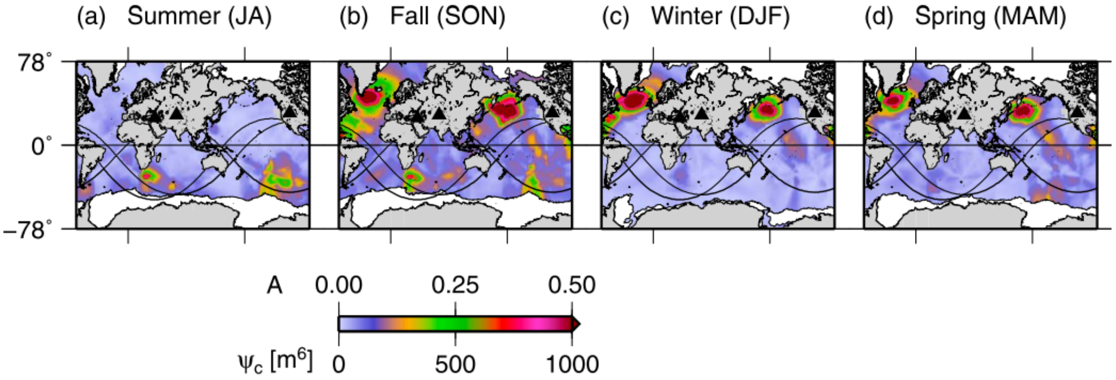

FIGURE 2.4: The observed global excitation patterns can serve as a template for future investigations of global microseism hot spot activity. Each pixel is occupied by the maximum A, Ψ_c value measured during the respective season. Seasons are associated with the northern hemisphere. Letter combinations indicate months: JA, July, August; SON, September, October, November; DJF, December, January, February; and MAM, March, April, May. From Hillers et al. (2012).

further variations in the noise field. The primary microseism noise is therefore more dominant in the northern hemisphere than the southern hemisphere.

The ambient noise wave field can be assessed by spectral analysis of the continuous cross correlations between stations within the Ethiopian network. Euler et al. (2014) backprojected the frequency-slowness power spectrum from stations of the Ethiopian Kenya Broadband Seismic experiment and found the North Atlantic between Greenland and Iceland and the Southern Ocean were the most significant sources of P waves, which map well to regions of the largest wave height forecasts (Figure 2.5). Due to the uneven distribution of noise sources there is some directionality bias with the fast direction observed in a north-northwest to south-southeast direction.

2.2.1 Why Use Ambient Noise?

The realisation that the noise that had obstructed impulsive signals could be used to observe Earth's seismic structure has allowed for rapid developments in tomographic imaging (e.g. Weaver, 2005; Shapiro et al., 2005). Ambient noise can be used to determine the Green's function between two stations. The Green's function is the seismic response of a medium to an impulsive point source and gives an indication of the velocity structure between the two stations. One station effectively acts as the source while the second station is the recorder. By cross correlating the signals, an approximation of the time dependent Green's function is obtained giving us information about the seismic structure between the two stations. The period of the noise determines the depth range possible to image, with the general rule, the shorter the period the shallower the depth range (Boschi and Weemstra, 2015).

Some of the key benefits include the ability to perform this technique anywhere on Earth where there is a recording station. Resolution is not restricted to the nonuniform distribution of earthquakes and other impulsive sources and the technique is also non-destructive unlike explosive sources. When ambient noise is used for tomographic imaging, in many instances the resolution will be enhanced due to the increase in sources (Weaver, 2005). This is particularly true for networks deployed for short periods that may not record many earthquakes (Shapiro et al., 2005).

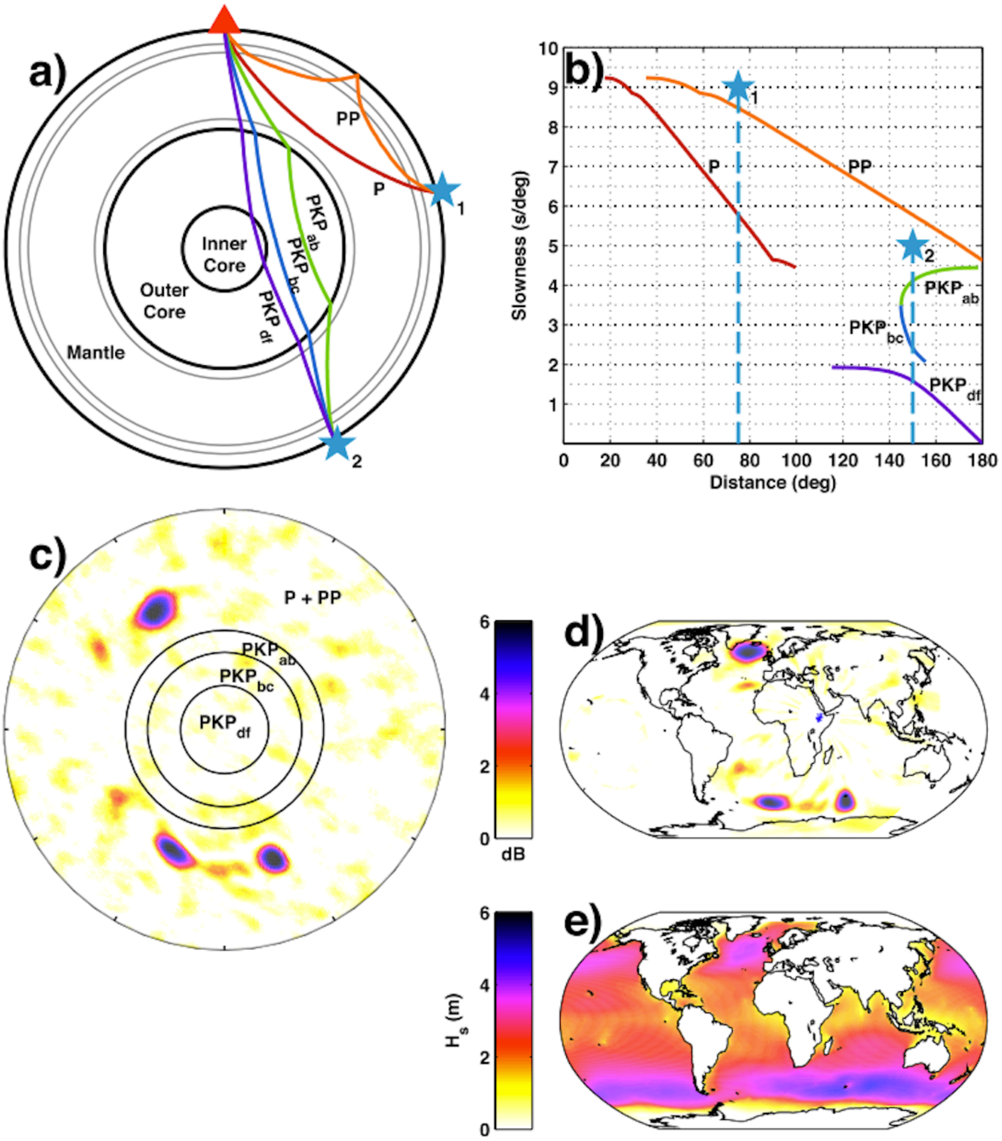

Figure 2.5: Plot illustrating the method of backprojecting body wave seismic noise recorded by the Ethiopia Kenya Broadband Seismic Experiment array to estimate source locations. (a) Example ray paths of microseismic body wave phases expected to have the highest amplitudes (Gerstoft et al., 2008). (b) Plot of the slowness versus distance relationship of those seismic phases for a surface source propagating through the 1-D earth model ak135 (Kennett et al., 1995). The overlap in slowness of P & PP introduces a distance ambiguity for waves recorded in the slowness range of 4.5–9.25 s deg^{-1}. For example, waves travelling through the array at 7.5 s deg^{-1} may be interpreted as P waves from a source 50° from the array and PP waves from a source at a 100° distance range. (c) Slowness spectrum for the noise correlations averaged across the 5–7.5 s period band. The spectrum is divided by concentric black rings at 2.0, 3.5 and 4.5 s deg^{-1} corresponding to the slowness ranges of the different seismic phases shown. The spectrum is normalised to give 0 dB at the median value. (d) P & PKPbc backprojection of the slowness spectrum using the slowness–distance curves. (e) Significant wave height hindcasts (Tolman, 2009) averaged from February 2000 to May 2002 (the Ethiopia array deployment duration) show that the backprojected seismic noise recorded by the Ethiopia array is strongest where there is substantial ocean wave activity. Taken from Euler et al. (2014).

In addition, as this technique focusses on the use of surface waves it is particularly sensitive to imaging fluids. This leads to a range of applications including groundwater imaging, oil exploration, monitoring of water tables, CO_2 storage, nuclear waste disposal, geothermal monitoring and glacier retreat to name a few (Weaver, 2005). As the cross correlations are quick to compute the technique can be used to monitor a structure in real time provided the data is continually transmitting (Mordret et al., 2016).

There are some problems with using ambient noise and they arise with the assumptions made, primarily that all noise sources are equally distributed which is inherently untrue as discussed above. Furthermore, the Noise Correlation Function (NCF) provides useful data for a limited frequency range, and continuous time series are required over a long time period (Dalton et al., 2011). The reason the data must be acquired over a long time period is because the measurement can be influenced by seasonal variations changing the seismic velocity by several percent (Sens-Schönfelder and Wegler, 2006). Hydrological conditions can change the seismic velocities generating variations between rainy and dry seasons. If this is the case then the effects must be removed to ensure an accurate tomography model is produced. Stacking the data over several years will aid this process returning an average between the two conditions. Having tested the dataset in this thesis I find no evidence for seasonal variations which is likely due to the arid nature of the Afar region and the use of data over a 18-year period.

2.2.2 Data Download

The data used for the ambient noise tomography was all freely available from the IRIS Data Management Center (IRIS DMC) (http://service.iris.edu/fdsnws/dataselect/1/) or from SEIS-UK (RiftVolc dataset)(Brisbourne, 2012) (Table 2.1). Each seismic network was downloaded separately using Standing Order for Data (SOD). The program sends a request to the IRIS DMC for the given network and list of stations. You also specify the output file type, in this case Seismic Analysis Code (SAC), and pre-process the data before the file is downloaded to your computer, saving time and space between processing steps. In the following sections I discuss the full methods for the Ambient Noise Tomography (ANT) from pre-processing steps to producing absolute shear velocity maps.

2.2.3 Initial Pre-Processing

The pre-processing, cross correlations and linear stacking of the data follow the methods of Bensen et al. (2007); Harmon et al. (2007, 2008) and Harmon and Rychert (2016). Continuous data from 269 stations were downloaded in 24-hour sections and resampled to 1 Hz. Due to the scale of our study region, $\sim$1100 km$^{\mathbf{2}}$, downsampling to 1 Hz will not affect the resolution of the final images when smoothing, grid size and station separation are taken into account. If the final aim was to image the internal plumbing structure of individual volcanoes, the sample rate should not be downsampled as dramatically. In addition, only records with a complete day's recording were used. Within the SOD code, the instrument response, mean and trend are removed from the data. A bandpass filter was also applied between 0.005 - 0.45 Hz before being saved in SAC format.

2.2.4 Cross Correlations and Stacking

The next step involved using adapted MATLAB scripts of Harmon et al. (2007) and Harmon et al. (2008). The data had a second bandpass filter applied between 0.005 - 0.4 Hz and a Tukey window applied at the ends of the files to prevent edge effects when Fourier transforming the data. The data were then normalised by their respective magnitude to create a single broadband NCF. The normalised time-series is then spectrally whitened to maximise the broadband period range of the signal. The procedure broadens the frequency band of the single station records by inversely weighting the complex spectrum by a smooth version of the amplitude spectrum. The pre-processing was done so as to maximise the noise signal that is obtained during cross correlation.

The cross correlation $C_{fg}(\tau)$ of two functions $f(t)$ and $g(t)$ is defined as:

$$C_{fg}(\tau) = f(t) \otimes g(t) = \int_{-\infty}^{\infty} f^*(t)g(t+\tau)dt \tag{2.1}$$

For discretely sampled signals with N time samples, $f(t) \otimes g(t)$ can be interpreted as the dot product of the Nx1 vector f with a time-shifted copy of the Nx1 vector g. For our purposes the time-series are cross-correlated in the frequency domain by performing a fast Fourier transform on $f(t)$ and $g(t)$, and using the relation:

$$C(\omega) = 2\pi F^*(\omega) * G(\omega) \tag{2.2}$$

where ω is the angular frequency. As the stations are mainly broadband I cross correlated all the components (z, n and e) but focus on the z (vertical) components which are used to obtain the Rayleigh wave component. This produced a two sided NCF for all possible station pairs on each day. (For information on obtaining the Love wave component see Section §2.6 where I discuss anisotropy). Each day required >10 operational stations, stations to be greater than 2x wavelength apart and each station pair was required to have concurrently running stations with >10 days of continuous recording (Figure 2.6). For studies with less stations and cross correlations the threshold of 10 operational stations required each day can be reduced as with the >10 days of continuous recording. To increase the SNR and gain more cross correlations it would also be worth splitting the data into hour long chunks, cross correlating these, stacking for each day before stacking all together.

The NCFs were asymmetric due to the distribution of noise sources. In order to overcome this, I sum the two sides of the cross correlations and average them to make a symmetric noise correlation function. This enables the noise source to be treated as symmetric. Every day file for each cross correlation pair was then stacked. Increasing the number of stacked days improves the signal-to-noise ratio, boosting the Rayleigh wave signal in the NCF. The final NCF display a clear wave with a move-out phase velocity of ~3 km/s corresponding to the Rayleigh wave. All cross correlation functions were visually inspected before being included resulting in a total of 6716 NCF once quality control parameters were applied (Figure 2.7).

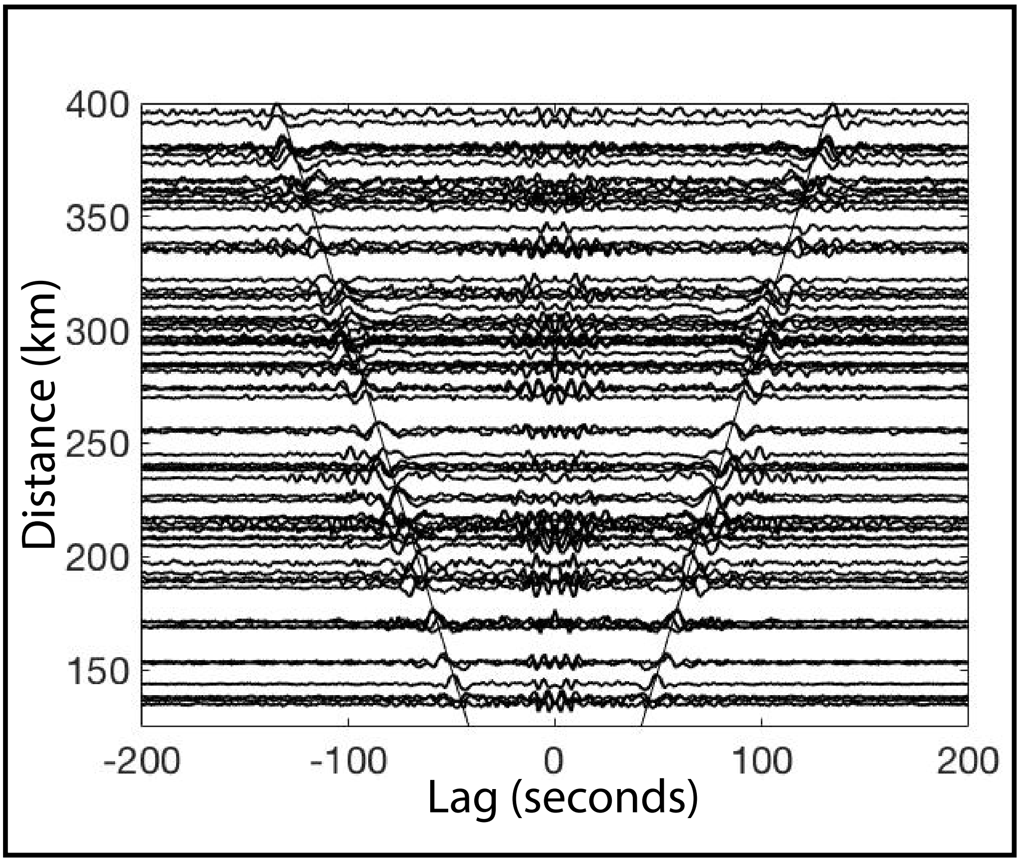

Figure 2.6: Example Noise Correlation Functions as a function of distance and lag.

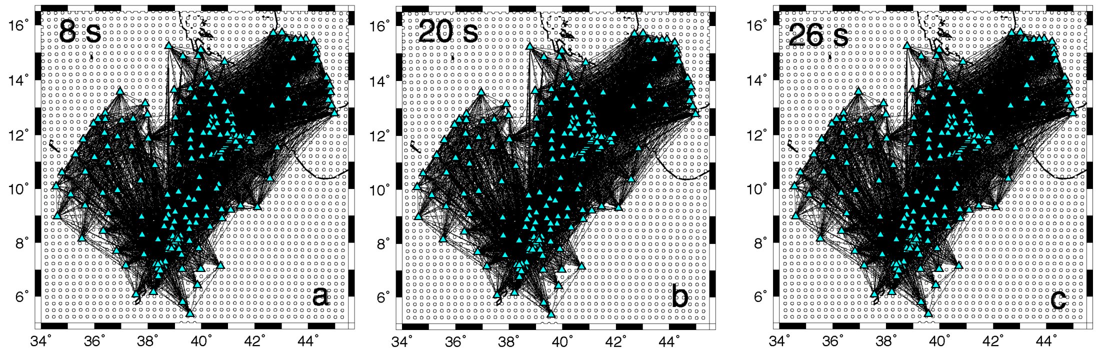

Figure 2.7: Ray paths (black lines) at 8, 20 and 26 seconds for all possible seismometer pairs (stations shown as blue triangles) overlain on a nodal grid of 0.25°.

2.2.5 The Tomographic Inversion Process for Phase Velocity

Here I discuss the method behind the tomographic inversion to obtain phase velocity. Phase velocity V_p is the rate at which the phase of a wave propagates in space and can be defined as:

$$V_p = \frac{\lambda}{T} = \frac{\omega}{k} \tag{2.3}$$

where λ is the wavelength, T is the time period, ω is the angular frequency and k is wavenumber. Group velocity V_g is the velocity at which the overall envelope of the wave's amplitude travels through space. It is defined as:

$$V_g = \frac{\partial \omega}{\partial k} \tag{2.4}$$

Group and Phase velocity are linked by the formula:

$$V_g = V_p - \lambda \frac{\partial V_p}{\partial \lambda} = V_p + k \frac{\partial V_p}{\partial k}. \tag{2.5}$$

Both measurements vary with frequency and are dispersive. The reason for using phase velocity rather than group velocity is that phase velocity is measured as the peak amplitude of a spike whereas for group velocity peak of a wave envelope is less precisely defined than the phase and is limited to a shorter depth range than phase velocity (Boschi et al., 2013). In addition, a wider time window is required to measure group velocity making contamination from interfering phases more likely (Boschi et al., 2013).

Some of the assumptions I make are that nodes are spaced evenly from one another at known points and use a spherical geometry. Surface waves are treated as rays travelling along the great circle linking the source and receiver (in this case 2 seismic stations) and scattering is ignored. In addition, I assume the Earth is isotropic. I estimate the average phase velocity dispersion across the region with a spatial domain technique using the entire array. I accomplish this by fitting a zero order Bessel function of the first kind as a function of inter-station distance, frequency and phase velocity, to the real part of the fast Fourier transformed NCF by searching over phase velocities from 2.5 – 5 km/s in a 0.01 km/s step at each period of interest (Harmon et al., 2008, 2010). Then for each individual NCF the phase was measured at each period of interest by unwrapping the phase of the stacked NCF using the average phase velocity curve at the longest periods to resolve cycle ambiguity (Bensen et al., 2007; Harmon et al., 2008). I then used the phase delay from the phase estimates to calculate the phase velocity as the distance between the 2 stations divided by the phase delay time (Harmon et al., 2007).

The phase velocity maps are then generated by inverting the phase data using the Born approximation 2-D phase sensitivity kernels (Zhou et al., 2004). I justify the use of these kernels based on numerical estimates of ambient noise sensitivity kernels, which show for a uniform distribution of noise sources the kernel is essentially the same (Tromp et al., 2010; Harmon et al., 2013). The grid used for the nodes is a regular 0.25° x 0.25° grid (Figure 2.7) using a nodal parameterisation of the sensitivity kernel between each station pair (Harmon et al., 2013; Yang and Forsyth, 2006). At every period and for each station pair, I calculate the sensitivity kernel on a densely sampled grid (0.1° x 0.1° spacing). I then determine the value at each node by the Gaussian weighted average value of the sensitivity kernel on the densely sampled grid. The forward problem for the travel-time perturbation relative to an isotropic reference model is:

$$\mathbf{d} = \mathbf{G}\mathbf{m} \tag{2.6}$$

where **d** represents the data of all NCF for all station pairs at a given frequency, **G** is the kernel model of matrix derivatives and **m** is the model vector. The forward problem for surface wave tomography is given by:

$$\delta\phi = \int\int K_{\phi}^{c}(\mathbf{r},\omega)\frac{\delta c}{c}dxdy \tag{2.7}$$

where $\delta\phi$ is the phase difference between the predicted phase and the observed phase (equivalent to travel time misfit), K is the 2-D phase sensitivity kernel, $\frac{\delta c}{c}$ is the fractional change in phase velocity and x and y are the coordinates (Harmon et al., 2013). I solve the inverse problem for Equation (2.7) for $\frac{\delta c}{c}$ as our model parameters, indicated by vector **m**, using an iterative damped least squares inversion.

The estimated solution to the inverse problem (Aki and Richards, 1980) is the model:

$$\mathbf{m} = \mathbf{G^{-1}}\mathbf{d} \tag{2.8}$$

To solve as a least squares approach the solution is:

$$\mathbf{m} = (\mathbf{G}^{T}\mathbf{G})^{-1}\mathbf{G}^{T}\mathbf{d}$$

and I use an iterative damped least squares inversion, in two stage using:

$$\mathbf{\Delta m_i} = (\mathbf{G}^{T}\mathbf{C_{nn}}^{-1}\mathbf{G} + \mathbf{C_{mm}})^{-1}(\mathbf{G}^{T}\mathbf{C}_{nn}^{-1}\Delta\mathbf{d} + \mathbf{C}_{mm}^{-1}[m_i - m_0]) \tag{2.9}$$

where m_i is the current model at iteration i, Δm_i is the change to the model after the next iteration, G is the matrix of partial derivatives from the kernel at each node (Saito, 1988), C_{nn} is data covariance matrix, C_{mm} is the model covariance matrix, Δd is the difference between the observed and predicted phase, and m_0 is the starting model (Tarantola and Valette, 1982; Harmon et al., 2007). A damping factor with a priori errors of 0.2 km/s is applied to the model parameters for the shear velocities in the first stage and in the second stage the noise data are scaled to their misfit standard deviation in the data covariance matrix.

2.2.6 Shear Velocity Inversion

In the second stage of the tomography, I invert the phase velocity maps across all periods at each point in the map for shear velocity to generate a 3-D velocity structure, using the best fit shear velocity model from the 1-D dispersion curve as our starting model (Figure 2.8B). For the

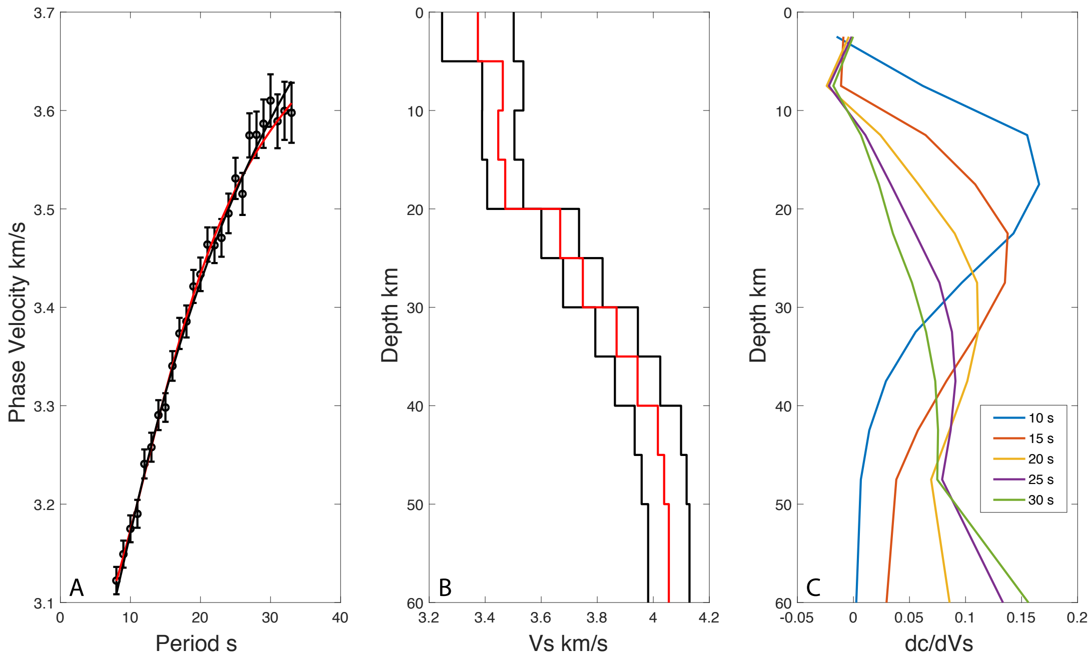

FIGURE 2.8: A) Average 1-D phase velocity for the study region with 3σ error bars (circles) with predicted dispersion from Gallacher et al. (2016) (black line) and our best fit shear velocity model dispersion overlain (red line). B) Best fit shear velocity model for the study region (Red line) and formal 2σ error bounds (black lines). C) Sensitivity kernels for Rayleigh waves at selected periods.

shear velocity inversion, I use a damped least squares approach (Tarantola and Valette, 1982) and parameterise the shear velocity at every 5 km vertically with 0.1° x 0.1° pixel size. I calculate the partial derivatives that relate variations in shear velocity to changes in phase velocity using DISPER80 (Saito, 1988). The shear velocity models are discretised at 5 km intervals in depth however, I interpolate the velocity structure in depth to 1 km intervals for presentation purposes using a linear interpolation. Plotting the sensitivity kernels for the shear velocity inversion at each period of interest (Figure 2.8) indicates the peak sensitivity depth and I therefore interpret to 60 km depth the limit of the sensitivity.

2.2.7 Additional Tests

Across the study region there are variations in sediment thickness and large bodies of water which may bias shear velocity structure to slower velocities at depth if not properly accounted for. I tested the effects of large slow layers on our shear velocity model by imposing a water layer to a thickness of 3 and 5 km in the Red Sea and Gulf of Aden with velocity and density values a priori from CRUST1.0 (Laske et al., 2013). I also performed the same tests with a sediment layer in the rifts using sediment thickness from CRUST1.0 (Laske et al., 2013). After 9 iterations (the same as for a standard inversion), these tests produced shear velocity models that were within error of our preferred model, leading to confidence in the results.

Depth (km)	Formal Resolution
2.5	0.01
7.5	0.15
12.5	0.33
17.5	0.37
22.5	0.38
27.5	0.37
32.5	0.34
37.5	0.30
42.5	0.26
47.5	0.20
62.5	0.32
87.5	0.14

Table 2.2: Resolution matrix from the diagonal of R.

2.2.8 Resolution and Errors

I assess the minimum interpretable length scales of our velocity anomalies by presenting checkerboard tests for 0.5° × 0.5° anomalies between 8 – 33 s period (Figure 2.10). The input for the checkerboard tests has a ± 15 % velocity anomaly for the average phase velocity and generate the synthetic data for the ambient noise station-to-station pairs by inverting only the phase, assuming the forward model used in Harmon and Rychert (2016). The tests indicate I can resolve anomalies at the scale of 0.5° across most of the region, particularly in regions with good ray path coverage within the MER and northwestern Afar (Figure 2.7). In areas of sparser ray coverage such as eastern Afar, the Red Sea and Gulf of Aden I have poorer resolution and northeast-southwest smearing of checkerboard tests. Consequently, I do not interpret these regions. I mask results outside the standard error contour of 0.07 km/s, the approximate contour of the 2σ error, from the linearised phase velocity inversion. I assess the vertical resolution of the shear velocity via the formal resolution matrix of the shear velocity inversion. Our model is not well resolved above 5 km and below 60 km depth with formal resolution values <0.10.

I also obtain the resolution matrix R using Equation (2.10) below:

$$\mathbf{R} = (\mathbf{G}^T\mathbf{C_{nn}}^{-1}\mathbf{G} + \mathbf{C_{mm}})^{-1}(\mathbf{G}^T\mathbf{C}_{nn}^{-1}\mathbf{G}) \tag{2.10}$$

Each row of R is a resolution map defining the resolution at one spatial node (Barmin et al., 2001). By taking the diagonals of R, I obtain the formal resolution (Table 2.2). Formal resolution values are typically around 0.37 for each 5 km thick layer in the 10 – 55 km depth range indicating I have independent constraints approximately every 10 – 15 km in depth (Figure 2.9). In other words, I can resolve average velocity variations over 10 - 15 km depth ranges.

2.3 Teleseismic and Ambient Noise Tomography

The ambient noise tomography (ANT) was restricted to crustal and uppermost mantle depths with structure in the uppermost mantle starting to be revealed from the ANT tomography. Using Rayleigh waves from teleseismic sources allows resolvability of the upper mantle by using longer

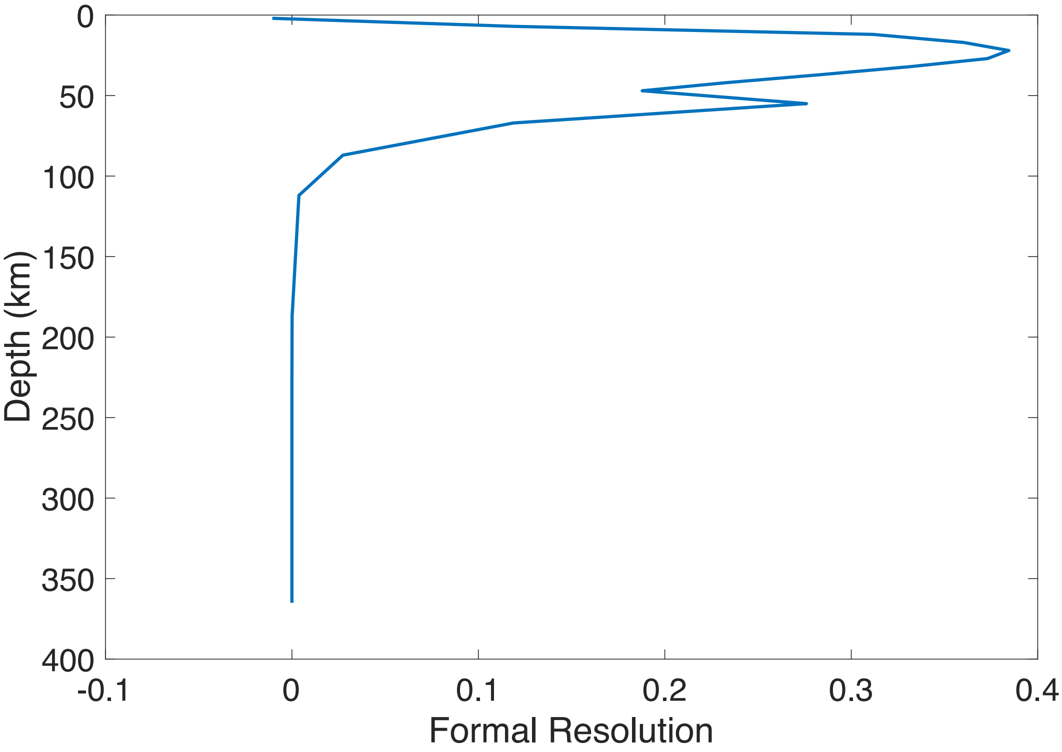

FIGURE 2.9: Backus resolution plot at 22.5 km depth.

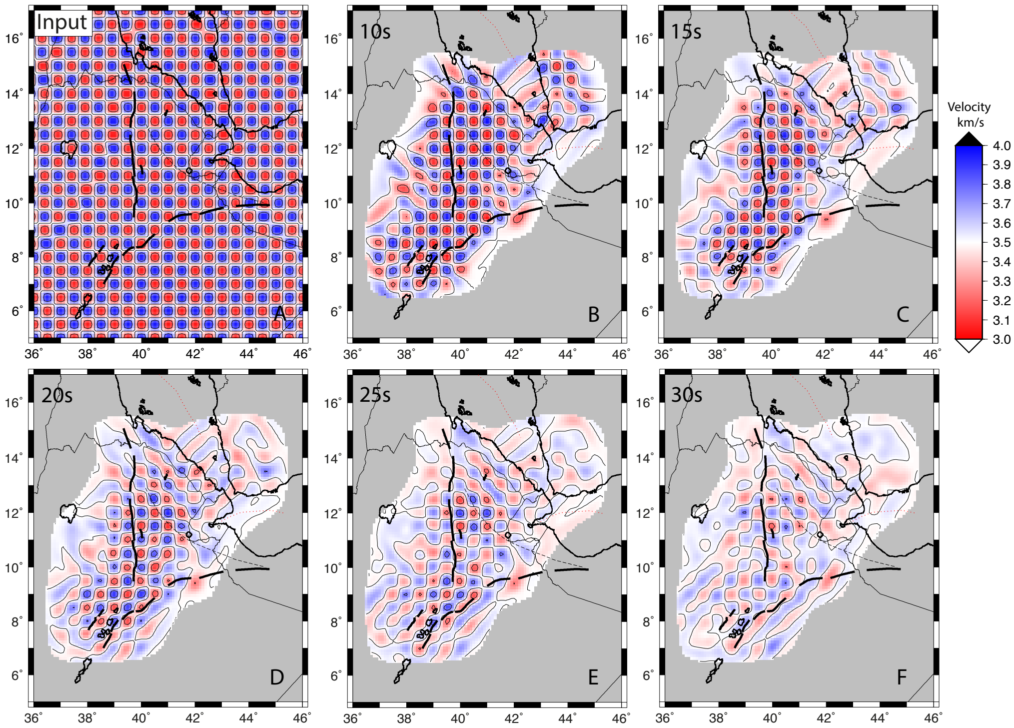

FIGURE 2.10: Checkerboard tests for 0.5° × 0.5°. Initial model shown in A) with B -F the resulting output model at 10, 15, 20, 25 and 30s respectively. Results are cropped outside the 0.7 standard error contour. Figure is from the supplementary material in Chambers et al. (2019), Appendix A.

periods than the ambient noise. To better resolve lower crustal and uppermost mantle depths I decided to perform a joint inversion between Rayleigh waves from the ANT and from teleseisms. The teleseismic tomography was initially undertaken by Gallacher et al. (2016), however I add in additional teleseisms and repick and run all events to ensure consistency in the results.

2.3.1 Initial Pre-Processing

I build on the work of Gallacher et al. (2016) and add surface waves from 2012 - 2017 that were not present in the original work. The additional data and previous teleseisms were all freely available from the IRIS Data Management Center (IRIS DMC) (http://service.iris.edu/fdsnws/dataselect/1/). As with the ambient noise each additional seismic network was downloaded separately using Standing Order for Data (SOD). Additional networks included the Plateau (YY), ARGOS (XM), and an extension of the Danakil Depression (2H) networks. The procedure is similar to the ambient noise but in this instance the SOD code asks the server for all recorded Teleseisms from 2011 - 2017 (from a global catalogue). The dataset is then cut to the corresponding time of the earthquake (-150 s to +3600 s) from each seismometer present within the location box with latitude 5° - 16° and longitude 34° - 46°. Only earthquakes with magnitudes >5.5 and epicentral distances of 25 - 150° were used. The epicentral distance range ensures that the energy of the Rayleigh wave is clearly distinguishable from that of the body waves and excludes the possibility of interference with the major arc Rayleigh wave. The range is widened from the traditional 30 - 150° distance due to the large region covered by the array. A station at the edge of the region may be up to 10° away from a station at the other end of the study area ignoring teleseisms outside this range, so a 5° buffer was incorporated to account for this. The choice of magnitude enhances the likelihood of an observable event. The data was also bandpass filtered from 0.005 - 5 Hz applied during download. The data from RiftVolc (Y6) was extracted using SEIS-UK in-house scripts and JWEED (Brisbourne, 2012). The dataset was pre-processed in the same way as those downloaded from the IRIS DMC.

The seismic signal was separated into 28 periods ranging from 10 to 200 s as performed by (Gallacher et al., 2016). This was done by filtering the amplitude values at ± 0.002 Hz around frequencies from 0.005 Hz to 0.015 Hz, at 0.001 Hz increments, and ± 0.005 Hz around frequencies from 0.02 Hz to 0.1 Hz, at 0.005 Hz increments. Rayleigh waves are dispersive so non incremental periods were chosen. The negative spectral information for each was removed using a Hilbert transform leaving the time analytic signal, which represents the envelope of the wave. The envelope of the wave is the information about the group velocity for each period of interest. The signal power at each station for each period is found by interpolating the signal amplitude with the predicted group velocity, based on the station event distance and the travel time (Figure 2.12 end panel). Quality control was performed manually by inspecting the Signal-to-Noise ratio (SNR), group velocity dispersion curve and wave energy for every station at each event (Figure 2.12). For each event the signal power for each good station was summed and from the resulting plot of group velocity against period the group velocity dispersion curve was picked manually along the path of peak power (Figure 2.11). For an event to be picked the seismogram required a signal to noise ratio (SNR) > 3 and peak energy between the approximate frequencies of interest, 0.01 Hz to 0.07 Hz. An event would only be picked if there were 8 or more good seismograms as this is the minimum station coverage needed for a stable answer.

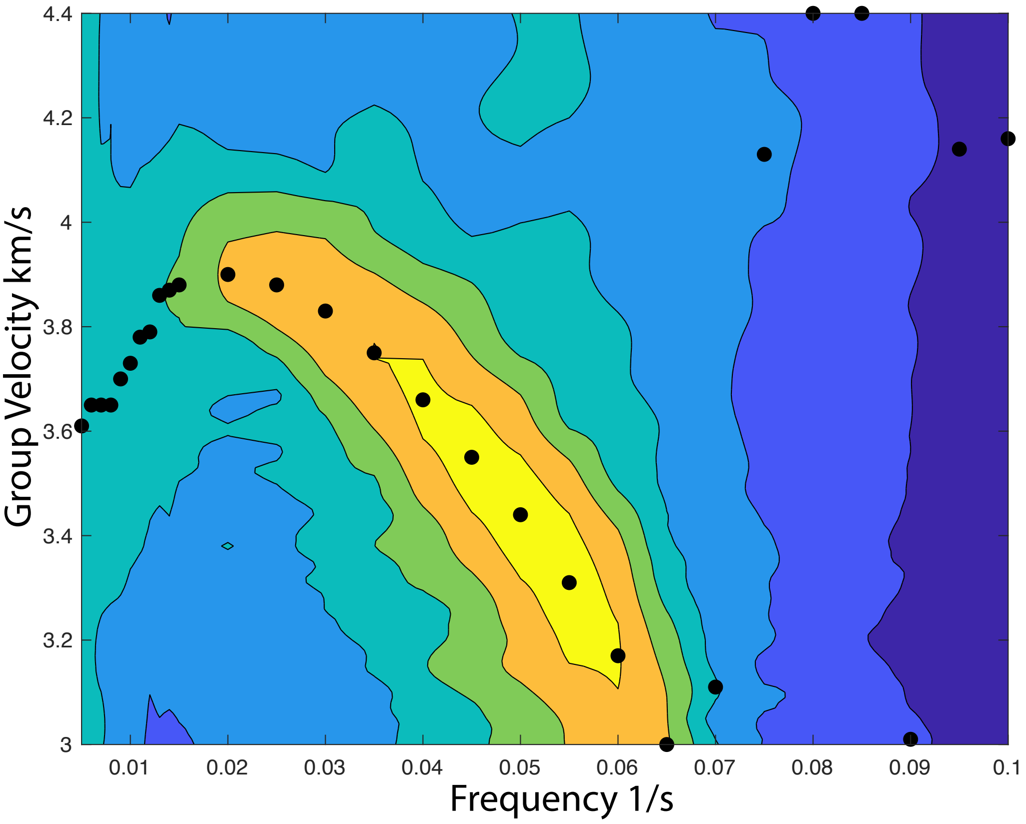

Figure 2.11: Example of a “good” dispersion curve in a frequency time analysis plot with clear dispersion from 0.01 - 0.065 s^{-1}.

The period and velocity information from the dispersion curve was then interpolated thus obtaining velocity information at each of the 18 periods of interest, from 20 to 167 s. This information was used to extract an idealised time variable filtered signal for each event, station and period (Landisman et al., 1969). The amplitude and phase information from each signal was obtained using a Fast Fourier transform and saved for use in the 1-D inversion. Events with amplitudes greater than 3x the median amplitude were removed and events with residual phase errors greater than 0.23 (∼4% out of phase) were also removed. This was done to prevent stations dominating the overall signal. Permanent stations ATD and FURI required removal prior to 2011 and 2012 respectively, potentially suggesting an amplitude problem. One notable problem, when using these stations without the amplitude correction, was that slow phase velocities focussed to the stations and moved anomalies away from the rift in contrast to all other station results. This was done for 1933 events (Teleseismic earthquakes) between 1st October 2012 and 5th October 2017 resulting in 483 good events. These were then combined with the previous 570 events of Gallacher et al. (2016), and all data were then manually repicked to ensure one consistent dataset with 1053 events. The locations of all teleseisms are shown in Figure 2.2 and the ray paths for all events are shown in Figure 2.13 which shows good ray path coverage everywhere in the study.

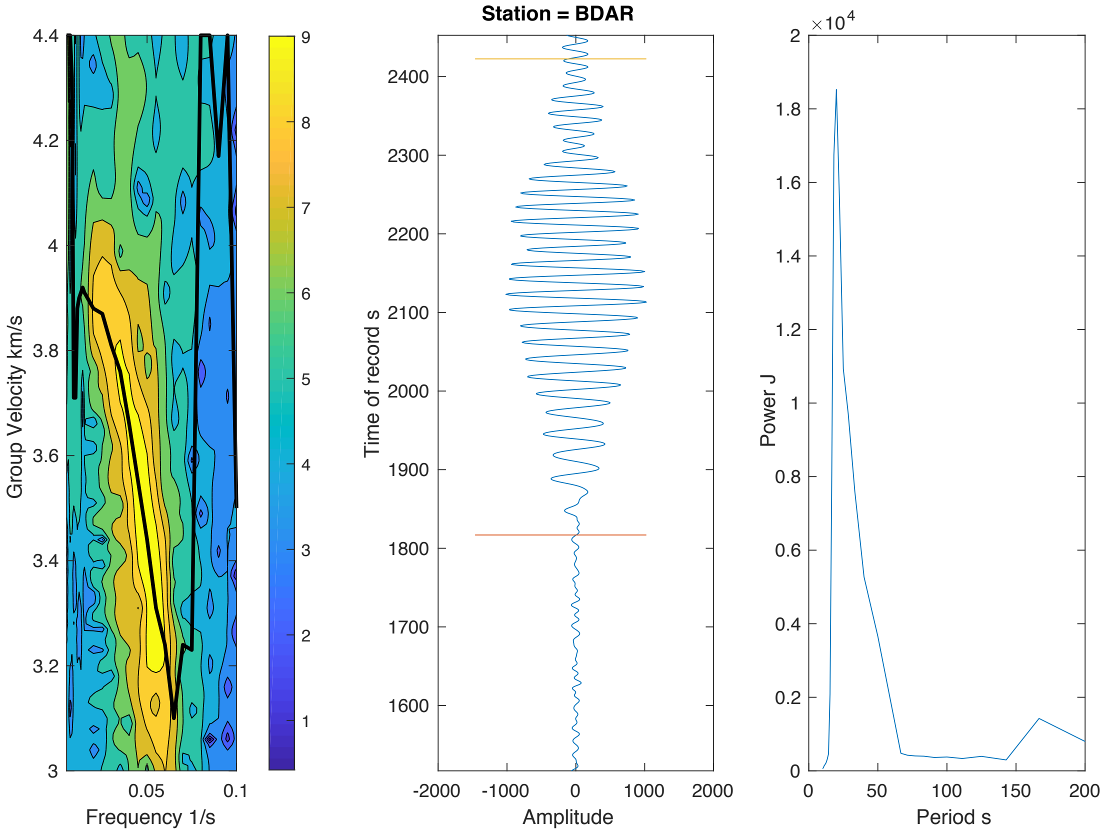

FIGURE 2.12: Example of a picked "good" dispersion curve from manual picking between 0.01 - 0.065 s^{-1} and automatically interpolated beyond these points (and not used). First panel shows the same as Figure 2.11 but with picked dispersion curve. Middle panel shows the surface waveform recorded on the seismometer after filtering. End panel shows the power spectrum. Note periods after 125s are not included due to low power and the inaccuracy of picking the dispersion curve at the shorter frequencies.

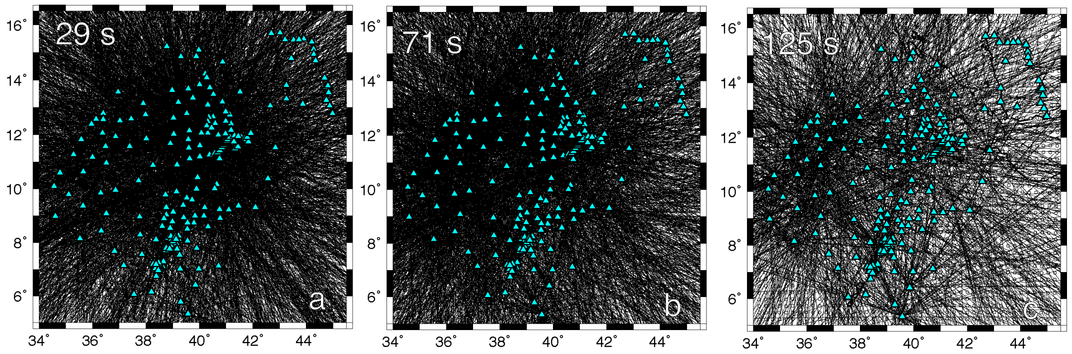

FIGURE 2.13: Nodal grid at 0.25 ° spacing with ray paths for teleseisms at 29, 71 and 125s overlain as black lines. Blue triangles indicate station locations.

2.3.2 Phase Velocity Inversion

To solve for phase velocity, I first invert amplitude and phase information from each seismogram by minimising the misfit in both the real and the imaginary components of the bandpass-filtered seismograms. I determine the average dispersion curve for the area using a 1D version of the two-plane wave approximation method (Forsyth and Li, 2005) which accounts for distortions in the incoming wave field. I also account for first order scattering using 2D Born approximation sensitivity kernels for amplitude and phase (Yang and Forsyth, 2006; Zhou et al., 2004). The inversion is completed in two stages, with the first stage utilising a simulated annealing method while trying a range of starting phase velocities for the model ranging from 3.00 – 4.40 km/s (Press et al., 1992). The inversion simultaneously solves for the phase velocity, azimuthal anisotropy and wave parameters for each event. The first stage is necessary due to the periodic non-linearity of the problem, in addition to the solution being ambiguous where the two-plane waves have similar azimuths. Using simulated annealing ensures a global minimum is found for input into the second stage which utilises a standard linearised inversion (Tarantola and Valette, 1982). After an initial set of inversions for the period range of interest, I quality control the data and assess the quality of fit, before a final set of inversions for the final 1D dispersion curve. The quality control consists of identifying events that cannot be fit with a plane wave model, either due to incoherent propagation across the array or complications in the sources.

For the 2D phase velocity maps we use prior knowledge of the average velocity structure using a combination of the average phase velocity derived from ambient noise from Chambers et al. (2019) from 8 - 26 s and the average model of Rayleigh wave tomography from Gallacher et al. (2016) for periods 29 – 125s as our starting model at each point across the map (Figure 2.14b). Similarly to the ambient noise, we first invert the average phase velocity using the method of Harmon et al. (2013) at each period and each node on a 0.25° x 0.25° nodal grid with the outermost row and column spaced at 1° to absorb velocity heterogeneities outside the region of interest (Figure 2.7). The phase velocity inversion uses 2-D finite frequency kernels (Forsyth and Li, 2005; Nishida, 2011; Tromp et al., 2010) and an iterative damped least squares approach (Tarantola and Valette, 1982). Any event >0.05 out of phase is removed and the inversion is repeated using the output phase velocity maps as input for the following iteration. The removal of this data is necessary as it removes waveforms with complicated source radiation patterns and other effects not accounted for in the inversion.

2.4 Joint Inversion

2.4.1 Combining with Ambient Noise Data

Before being able to combine the two surface wave datasets I needed to check that the methods were producing similar results at periods that overlapped. The phase velocities overlapped at periods of 20 - 33 seconds. As shown in Figure 2.15 there is good agreement in the velocities at these periods with the most similar being at the shorter periods. As the results were similar I chose to perform a hard cut on the data based on the best resolved periods. This resulted in the periods for ambient noise ranging from 8 - 26 seconds while the teleseismic periods ranged

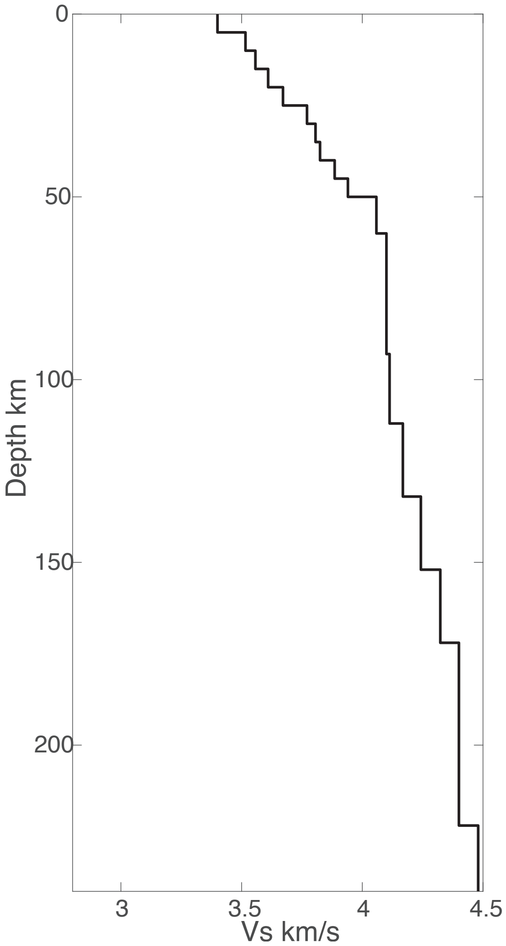

FIGURE 2.14: Initial starting model for the phase velocity inversion used in Chapter 4 using the average shear velocity from Chambers et al. (2019) and Gallacher et al. (2016).

from 29 - 125 seconds. I then concatenated the files to make a continuous dataset from 8 - 125 seconds.

2.4.2 Shear Velocity Inversion

The shear velocity inversion was again a linear least squares inversion and is the same method as used for ambient noise shear velocity as discussed in 2.2.6. I chose this method in order to preserve the variable velocity structure in the crust and observe step changes at the Moho. Using a linear least squares method has the caveat that mantle shear velocities are less smooth than many mantle tomography maps (e.g. Gallacher et al. (2016) who use an Occham inversion). For the starting model, I use the best fit shear velocity model from the 1-D dispersion curve as the starting model. I invert each pixel of the combined phase velocity maps across all periods (8 - 125 s) for the initial 1-D shear velocity structure as a function of depth. I assign a nominal a priori standard error for each node of 0.2 km/s and again fix the Vp/Vs ratio to 1.8, from the average of all Vp/Vs results in the region generated by receiver function analyses (Hammond et al., 2011; Stuart et al., 2006). Variations in the choice in Vp/Vs (1.5 - 2.1 the observed Vp/Vs ratios in this area), produce results that are within error of each other. For the shear velocity inversion, I again use a damped least squares approach (Tarantola and Valette, 1982) and parameterise the

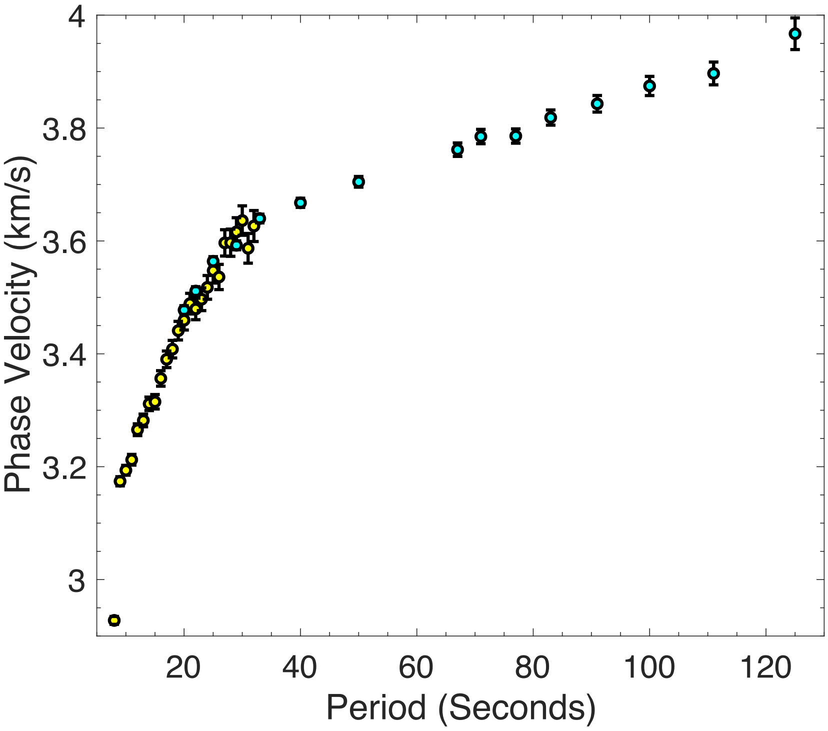

FIGURE 2.15: Average velocities for ambient noise (Yellow) and teleseisms (Blue) from Chambers et al. (2019) and Gallacher et al. (2016) respectively. Error bars are 3 x standard error.

shear velocity at every 5 km vertically with 0.1 x 0.1 pixel size. I calculate the partial derivatives that relate variations in shear velocity to changes in phase velocity using DISPER80 (Saito, 1988). Plotting the sensitivity kernels for the shear velocity inversion at each period of interest (Figure 2.16) indicates the depth of peak sensitivity. From this plot I interpret to 210 km which is the limit of the sensitivity. Again, I interpolate the shear velocity models from 5 km intervals to 1 km intervals in depth for presentation purposes.

2.4.3 Resolution and Errors

In the phase velocity maps the diagonals of the formal resolution matrix have maximum values of 0.31 at our best resolved period of 10 s and a formal resolution of ∼0.24 (Figure 2.19). We derive the resolution from the sensitivity kernels of the ray paths in Equation (2.10) and Figure 2.13 for 10, 20, 26, 29, 71 and 125 s period. Our formal resolution indicates we require at least 4 node spacings to produce an independent piece of information about velocity structure, in other words we can resolve 50 – 100 km laterally. We therefore limit our discussion to features >100 km laterally and resolve 10 - 15 km spacings in depth. In addition, we produce checkerboard tests at 1° spacings at 8 - 125 s period and at 1.5° and 2° for periods >29 s (Figure 2.18 and Figure 2.17). The checkerboard tests indicate we can resolve anomalies at 1° for 8 – 71 s period and 1.5° at all periods. In areas of sparser ray coverage such as the eastern part of Afar, the Red Sea, and Gulf of Aden we have poorer resolution and northeast-southwest smearing of checkerboard tests. Consequently, we do not interpret these areas. In addition, Yemen is not interpreted due to northwest-southeast smearing. We mask results outside the standard error contour of 0.07 km/s, the approximate contour of the 2σ error, from the linearised phase velocity inversion.

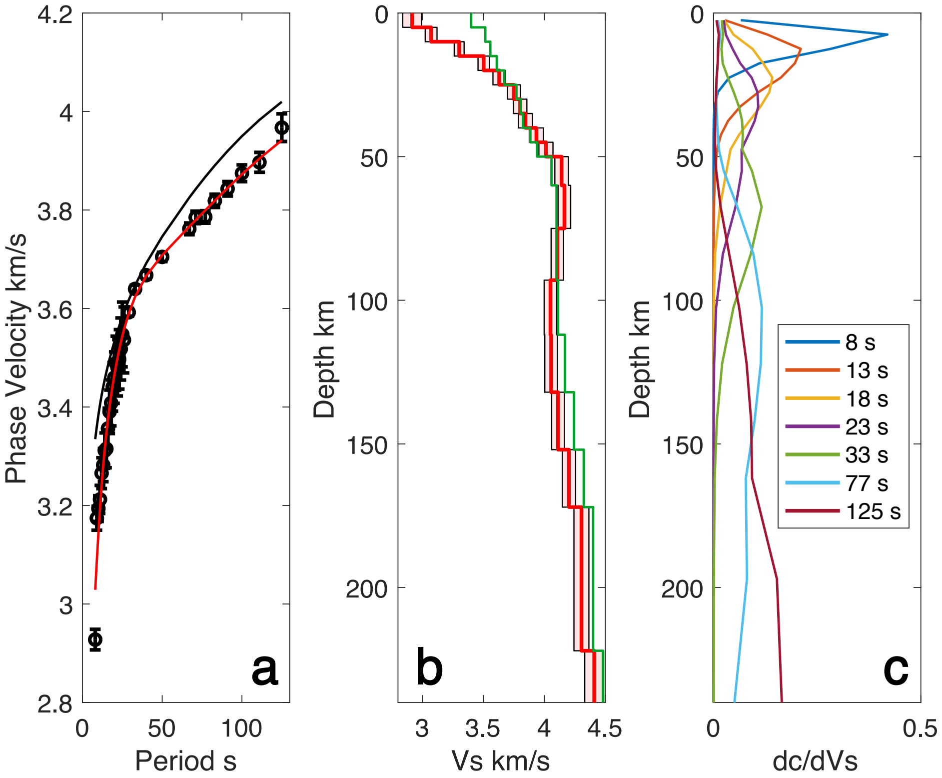

Figure 2.16: (a) Average 1-D phase velocity for the study area with 3σ error bars (circles) with our best fit shear velocity model dispersion overlain (red line). (b) Best fit shear velocity model for the study area (red line) and formal 2σ error bounds (thin black lines and shaded area). Green line is initial starting model using the average shear velocity from Chambers et al. (2019) and Gallacher et al. (2016). (c) Sensitivity kernels for Rayleigh waves at selected periods.

2.5 Cooling of the Flood Basalt

The flood basalt province on the Ethiopian Plateau displayed anomalously slow velocities which are discussed in Chapter 3 and Chapter 4. To test whether the velocities were impacted by the residual heat after emplacement, and were consequently slower than expected I solved the thermal heat equation in order to determine how long it would take for the flood basalts to cool. This was a rough back of the envelope calculation to give an upper limit on the time taken for the flood basalt to cool.

The assumptions I make are:

- The flood basalt has a constant thickness
- The crust beneath the flood basalt is constant thickness
- The flood basalt area is large enough that I can model it as an infinite plane
- Thermal diffusivity of the flood basalt layer is the same as the crust, and both are independent of temperature.
- The flood basalt layer appears instantaneously at the surface at mantle temperatures (clearly this is not true - layer builds up over millions of years, and each new layer will

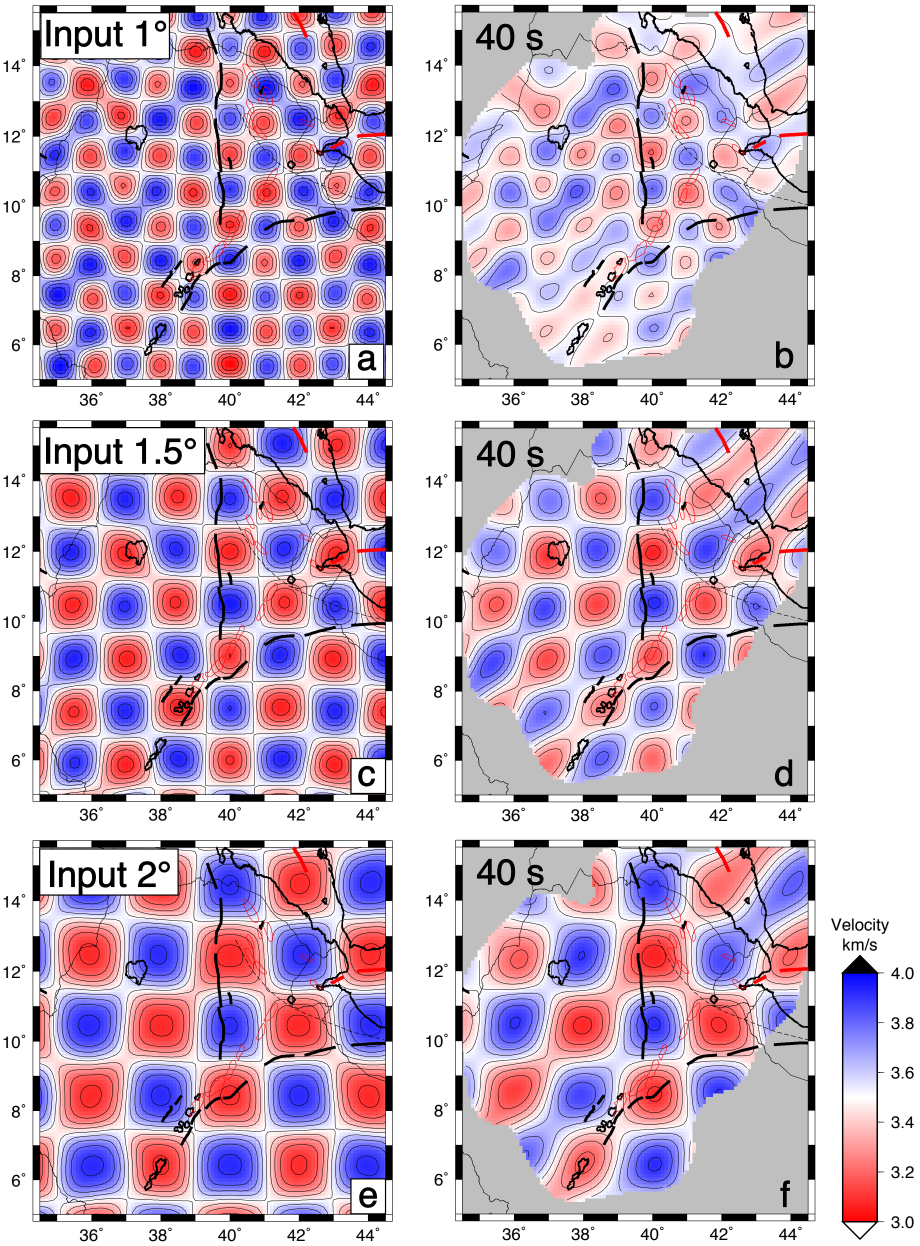

FIGURE 2.17: Checkerboard tests at 1° × 1°, 1.5° × 1.5° and 2° × 2° for teleseismic phase velocities at 40 s, the best resolved period. Initial model shown in (a), (c) and (e) with (b), (d) and (f) the resultant output model. Results are cropped to the 2σ standard error contour of the ambient noise. Thick black lines show border faults, red polygons magmatic segments, and dashed lines the Tendaho-Goba'ad discontinuity (TGD).

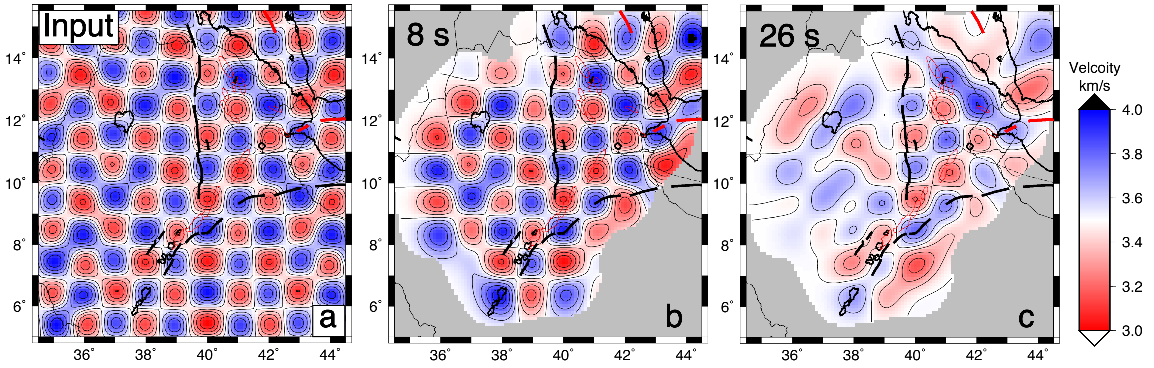

FIGURE 2.18: Checkerboard tests at 1° × 1° for ambient noise at the limits of our resolvable periods. Initial model shown in (a) with (b) and (c) showing the resultant output model at 8 and 26 s, the limits of our study. Results are cropped to the 2σ standard error contour. Thick black lines show border faults, red polygons magmatic segments, and dashed lines the Tendaho-Goba'ad discontinuity (TGD).

have time to cool before the next layer is added, so our calculation will be an overestimate of cooling time).

- Heat transfer at the basalt air boundary and at the crust mantle boundary happens much faster than within the basalt and crust layers, because air and mantle are fluids and convection will transfer heat faster than conduction, so I can assume temperatures at these boundaries remain constant on the timescales of interest to us
- There is no ongoing heating (from intrusions etc.) after the flood basalt begins to cool

Parameters (Visually shown in Figure 2.20)

- τ_{air} : air temperature (assume 300K)
- τ_{mantle}: mantle temperature (assume 1300K)
- $\Delta basalt$: thickness of basalt layer (assume 3km)
- $\Delta crust$: thickness of crust (assume 30km)
- κ: thermal diffusivity of crust and basalt (assume $0.5mm^2/s$ for mid crustal temperatures and conditions (Whittington et al., 2009))

I want to solve for $u(z,t)$, the temperature at depth z after time t from the start of cooling.

I assume that temperature varies only along the z dimension, and extent of the layers is infinite in the x, y plane, so the system is described by the 1-dimensional heat equation

$$\frac{\partial u(z,t)}{\partial t} = \kappa \frac{\partial^2 u(z,t)}{\partial z^2} \tag{2.11}$$

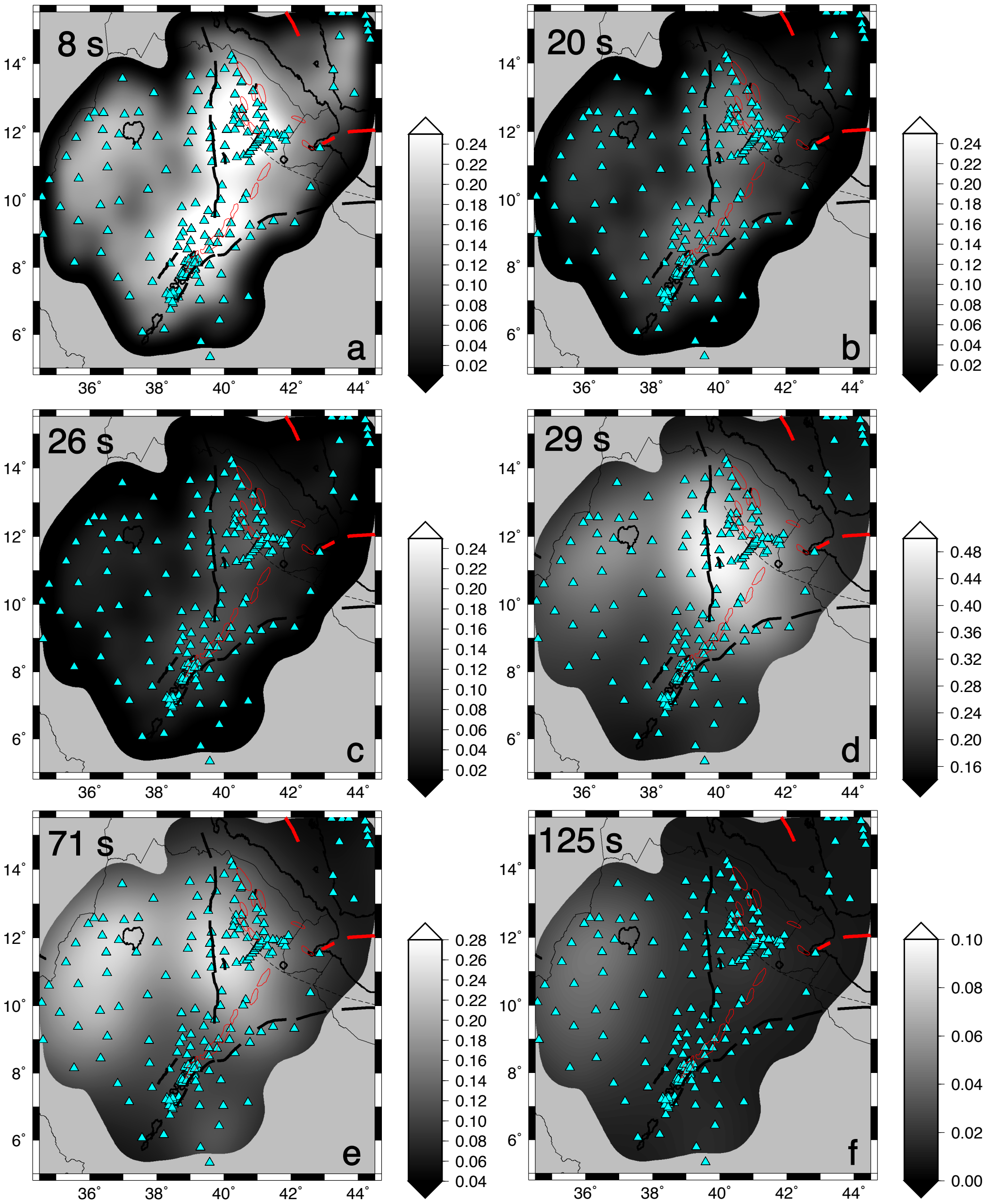

Figure 2.19: Formal resolution maps for 8, 20, 26, 29, 71 and 125s (a-f respectively). Blue triangles indicate station locations, thick black lines show border faults, red polygons magmatic segments, and dashed lines the Tendaho-Goba'ad discontinuity (TGD). Results are cropped to the 2σ error contour.

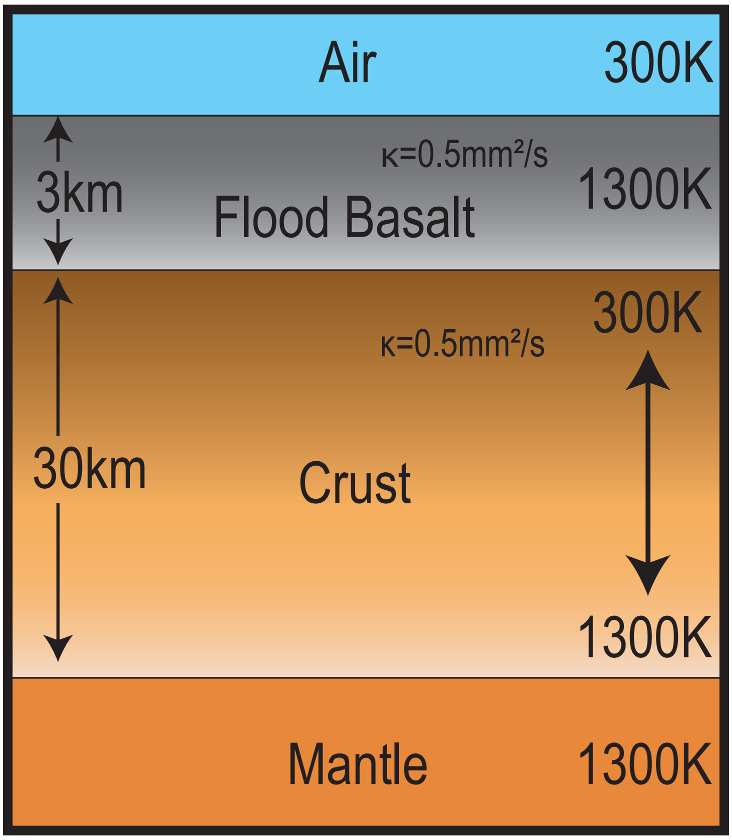

FIGURE 2.20: Diagram of the initial conditions for calculating the rate of cooling for a flood basalt.

Our initial condition is

$$u(z,0) = f(z) = \begin{cases} \tau_{\text{air}} & \text{if } z = 0 \\ \tau_{\text{mantle}} & \text{if } 0 < z \leq \Delta_{\text{basalt}} \\ \frac{\tau_{\text{mantle}} - \tau_{\text{air}}}{\Delta_{\text{crust}}}(z - \Delta_{\text{basalt}}) + \tau_{\text{air}} & \text{if } \Delta_{\text{basalt}} < z \leq \Delta_{\text{basalt}} + \Delta_{\text{crust}} \end{cases} \tag{2.12}$$

and boundary conditions are

$$u(0,t) = \tau_{\text{air}} \tag{2.13}$$

$$u(\Delta_{\text{basalt}} + \Delta_{\text{crust}}, t) = \tau_{\text{mantle}} \tag{2.14}$$

The solution to this differential equation is

$$u(z,t) = u_{\infty}(z) + \tilde{u}(z,t) \tag{2.15}$$

$$u_{\infty}(z) = \frac{\tau_{\text{mantle}} - \tau_{\text{air}}}{\Delta_{\text{basalt}} + \Delta_{\text{crust}}} z + \tau_{\text{air}} \tag{2.16}$$

$$\tilde{u}(z,t) = \sum_{n=1}^{\infty} A_n \sin\left(\frac{n\pi z}{\Delta_{\text{basalt}} + \Delta_{\text{crust}}}\right) e^{-\alpha\left(\frac{n\pi}{\Delta_{\text{basalt}}+\Delta_{\text{crust}}}\right)^2 t} \tag{2.17}$$

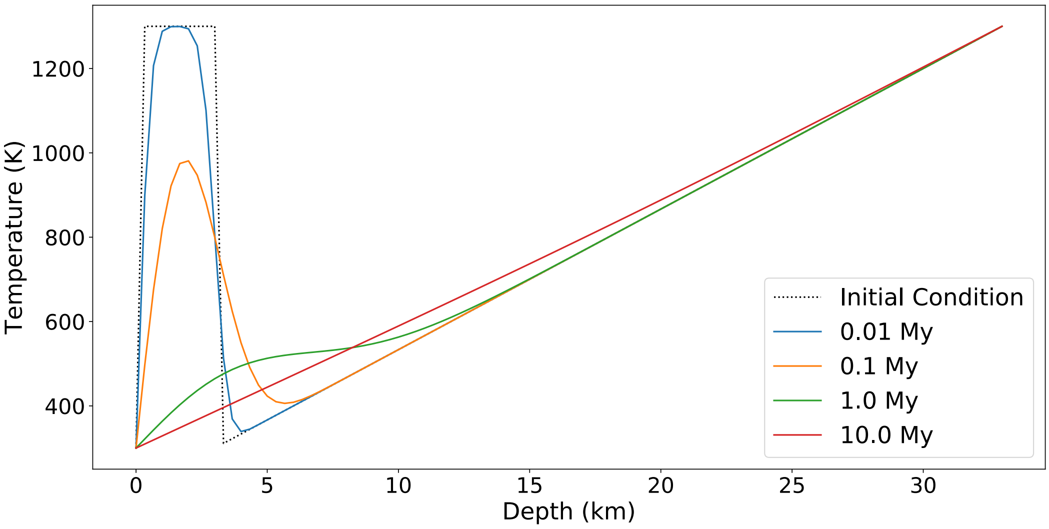

FIGURE 2.21: Cooling rate for a 3 km thick flood basalt emplaced at the surface. Black dotted line is initial temperate gradient assuming the flood basalt is 1300 K and the crust (30 km thick) linearly increases from 300 – 1300 K. The blue, orange, green and red lines are the temperature profile after 10,000, 100,000, 1,000,000 and 10,000,000 years respectively. By 1 Million years the temperature is nearly at equilibrium and by 10 Million years is at background temperatures.

where $u_\infty(z)$ is the stable (time-independent) solution which the system approaches in the large-time limit and $\tilde{u}(z,t)$ is the time-dependent component of the solution. A_n are the Fourier series coefficients of $f(z) - u_\infty(z)$:

$$A_n = \frac{2}{\Delta_{\text{basalt}} + \Delta_{\text{crust}}} \int_0^{\Delta_{\text{basalt}}+\Delta_{\text{crust}}} (f(z) - u_\infty(z)) \sin\left(\frac{n\pi z}{\Delta_{\text{basalt}} + \Delta_{\text{crust}}}\right) dz \tag{2.18}$$

which has the solution

$$A_n = \frac{2}{n\pi}\left(\tau_{\text{mantle}} - \tau_{\text{air}}\right)\left[1 - \cos\left(\frac{n\pi\Delta_{\text{basalt}}}{\Delta_{\text{basalt}} + \Delta_{\text{crust}}}\right) - \frac{\Delta_{\text{basalt}} + \Delta_{\text{crust}}}{n\pi\Delta_{\text{crust}}} \sin\left(\frac{n\pi\Delta_{\text{basalt}}}{\Delta_{\text{basalt}} + \Delta_{\text{crust}}}\right)\right]. \tag{2.19}$$

I calculated the solution using the first 100000 Fourier coefficients. I checked that this number of Fourier coefficients was sufficient for convergence to the solution. I then plot the temperature after $t$years, as shown in Figure 2.21

I find that the flood basalt would take ∼1 Ma to cool and no more than 10 Ma given the assumptions stated above which are an upper limit. The Ethiopian Flood Basalt was emplaced 30 Ma suggesting temperature from the flood basalts is not influencing the observed velocities and it is more likely caused by a component of partial melt from more recent magmatism, as discussed in Chapter 4. Furthermore, if the same flood basalt layer was placed in the centre of the crust, it would take a maximum of 20 Ma to reach equilibrium. However, it is more likely that smaller intrusions were occurring in the crust rather than the upper limit of a sea of melt induced in this scenario.

2.6 Anisotropy

The results of the joint inversion suggest there is potentially lateral flow of melt along the rift and off-rift beneath the Ethiopian Plateau. To pursue this further I calculate the radial anisotropy and determine whether anisotropy can account for changes in velocity and constrain flow and melt orientation. I determine the radial anisotropy for the ambient noise dataset and discuss the method in the following sections. For more information on the background and potential causes of anisotropy, please see Section §1.6.

2.6.1 Radial Anisotropy

Radial anisotropy looks at the ratio between the vertically polarised shear velocity (V_{SV}) and the horizontally polarised shear velocity (V_{SH}) in order to determine the proportion of vertically aligned shear waves versus horizontally aligned shear waves, often estimated from Rayleigh and Love waves. I calculate the radial anisotropy from the transverse component of the cross correlated ambient noise data (C_{tt}) to estimate Love wave dispersion using the same dataset as used for the ambient noise in the joint inversion (12 temporary networks and 5 permanent stations) (Figure 2.1). The Noise Correlation Function (NCF) for the symmetric vertical-to-vertical and transverse-to-transverse components are windowed to give the Rayleigh and Love wave components respectively.

It can be shown that the phase velocity c of surface waves have a dependence on the azimuthal direction ϕ of propagation by:

$$c(\omega, \phi) = A(\omega) + B(\omega)cos2\phi + C(\omega)sin2\phi + E(\omega)cos4\phi + F(\omega)sin4\phi \tag{2.20}$$

(Smith and Dahlen, 1973) where $A(\omega)$ is the isotropic phase velocity and $B(\omega)$ and $C(\omega)$ are the anisotropic contributions to the phase velocity. Cross correlations are therefore calculated similarly to the C_{zz} component, using the north and east components rather than vertical (z) and multiplying by the rotation matrix of cos and sin to obtain the transverse (C_{tt}) and radial components (C_{rr}) for each station pair (Lin et al., 2008; Sánchez-Sesma et al., 2006)(Figure 2.22). The cross correlations were then stacked for each station pair for every day. Station pairs spaced $<$2 x wavelength apart were removed. For practical applications the 4ϕ effects are often ignored as the amplitude for these terms is very small compared to the 2ϕ terms (Smith and Dahlen, 1973; Kendall et al., 2006). The resulting stacked cross correlations produced well resolved phase velocities between 13 - 26 s for the Love waves and 9 – 26 s for the Rayleigh waves and use a range of 13 - 26 s for both the Love and Rayleigh waves. Each stacked NCF was required to have a signal-to-noise ratio $>$3.

Phase velocities for each station pair were determined after Harmon et al. (2007) as in 2.2.5 where the average phase velocity is inverted at each period on the nodal grid (Harmon et al., 2013). The same nodal parameterisation is used as in the joint inversion (Figure 2.23). In the phase velocity maps for the Love wave inversions, the diagonals of the formal resolution matrix have maximum values of 0.40 at our best resolved period 15 s (Figure 2.23). This resolution is derived from the sensitivity kernels centred nominally on the ray paths. The formal resolution indicates at least 4 node spacings are required to produce an independent piece of information

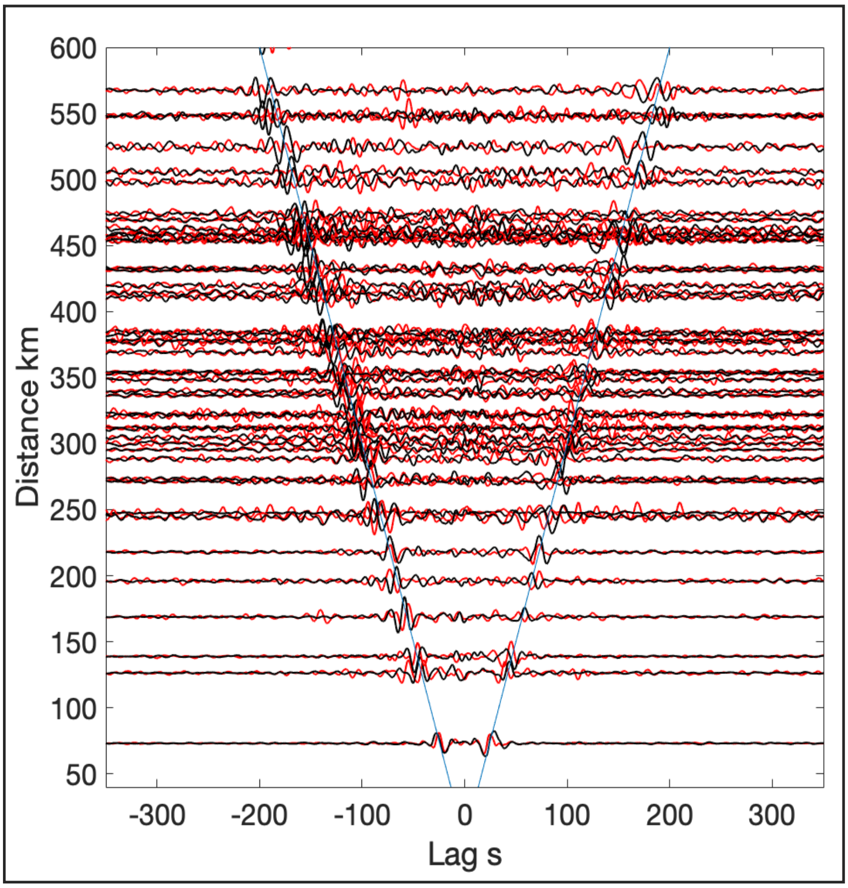

FIGURE 2.22: NCFs for transverse–transverse components (red) and vertical–vertical components (black).

about velocity structure, in other words 50 – 100 km lateral distances are resolvable. The errors for both the Rayleigh and Love waves are comparable (Figure 2.23).

The average dispersion curves for both the Rayleigh and Love waves were inverted for the best fitting shear velocity model from the joint inversion (Figure 2.16b) to obtain the radially anisotropic shear velocity for each location of the phase velocity maps (Figure 2.24). The radially anisotropic shear velocity is modelled from the phase velocity maps and 1-D dispersion curve. Five elastic parameters are used, $A = \rho V_{PH}^2$, $C = \rho V_{PV}^2$, $L = \rho V_{SV}^2$, $N = \rho V_{SH}^2$, and F (Montagner and Anderson, 1989), where V_P is compressional velocity and V_S is shear velocity. Subscript H and V refer to horizontal and vertical respectively. I use an alternative parameterisation, $\xi = N/L$, $\varphi = C/A$, $\eta = F/(A - 2L)$, V_{SV}, and V_{PH} for the elastic parameters (Saito, 1988). Usually only V_{SV} can be well resolved, so to reduce the number of parameters we scale $\delta\ln\varphi = -1.5\delta\ln\xi$ and $\delta\ln\eta = -2.5\ln\xi$ (Montagner and Anderson, 1989; Panning and Romanowicz, 2006). Again the Vp/Vs ratio is fixed to 1.80 from the average of all Vp/Vs results in the region generated by receiver function analyses (Hammond et al., 2011; Stuart et al., 2006). Variations in the choice in Vp/Vs again produce results that are within error of each other.

Each pixel of the phase velocity maps is inverted across all periods for the best fitting 1-D shear velocity structure as a function of depth. A nominal a priori standard error is assigned for each node of 0.2 km/s. The starting model is the best fit shear velocity model from the 1-D dispersion

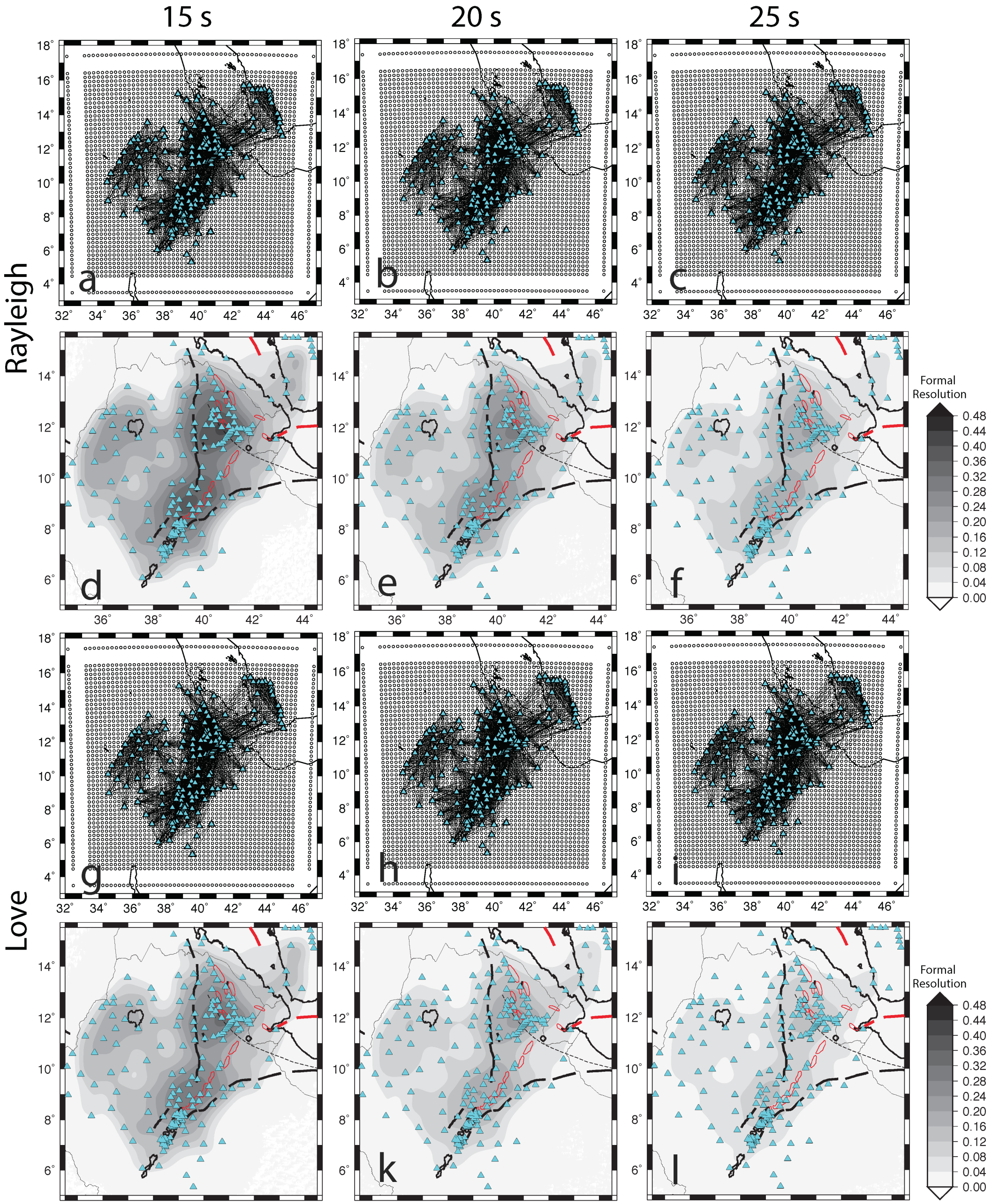

FIGURE 2.23: (a) Nodal grid with Rayleigh and Love ray paths (upper two and lower two panels respectively) and (b) formal resolution maps at 15, 20 and 25 s period. Stations are overlain as blue triangles.

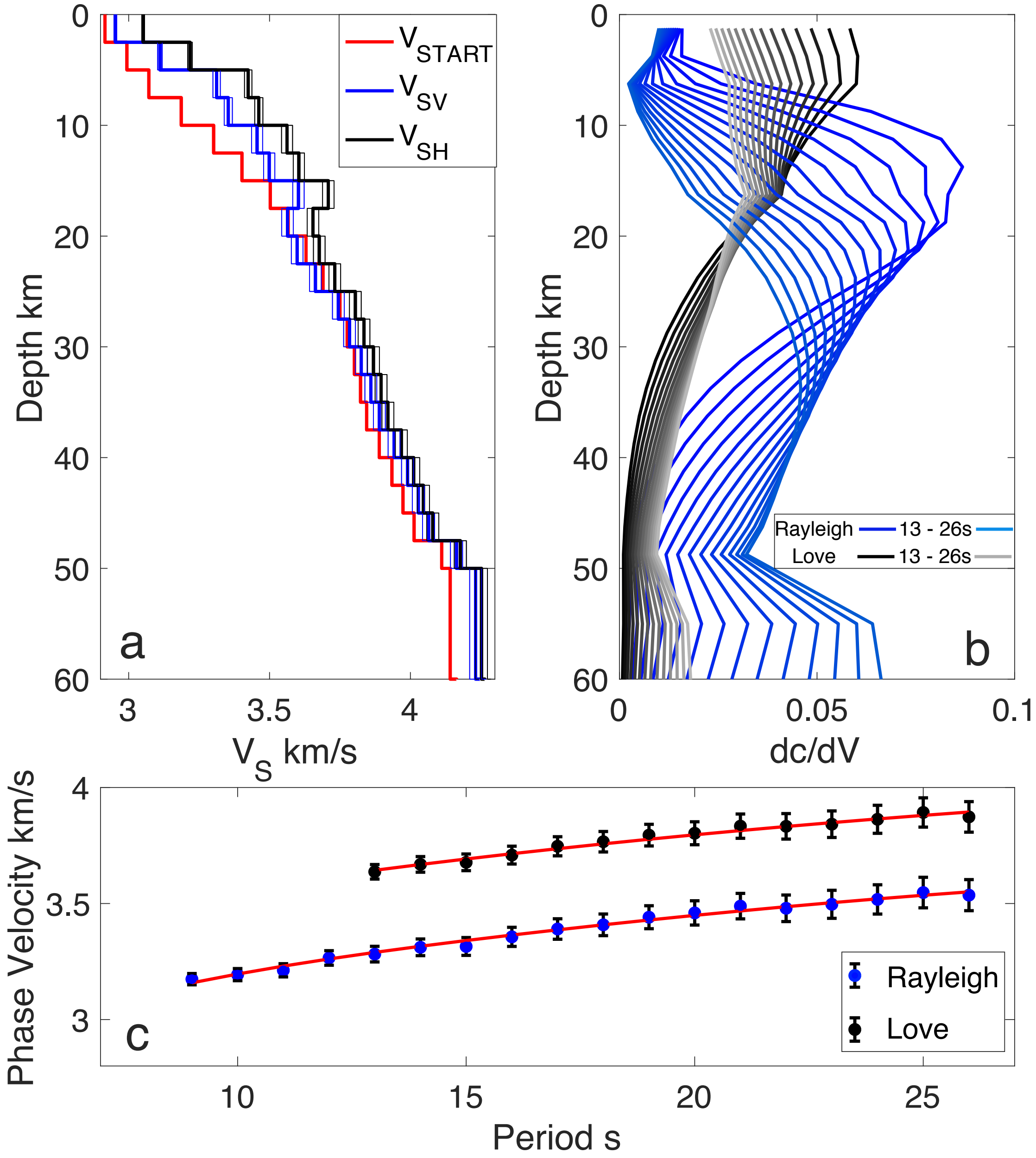

FIGURE 2.24: Left panel: Shear velocity structure for βV (light grey) and βH (dark grey) with 95% confidence regions, and the starting model (black). Right Panel: Sensitivity kernels for Love (dark grey) and Rayleigh (light grey) waves at select periods. Bottom Panel: One dimensional phase velocities for Love (dark grey circles) and Rayleigh (light grey circles) waves, with corresponding predicted phase velocity from the best fit shear velocity model in grey lines.

curve as the starting model (Figure 2.24). For the shear velocity inversion, a damped least squares approach is used (Tarantola and Valette, 1982), and the shear velocity is parameterised every 2.5 km vertically with 0.1° x 0.1° pixel size. The partial derivatives that relate variations in shear velocity to changes in phase velocity are calculated using DISPER80 (Saito, 1988). Although the shear velocity models are discretised at 2.5 km intervals in depth, I interpolate the velocity structure to 1 km depth for presentation purposes using a linear interpolation.

Anisotropy is presented as a percentage in terms of $\delta V = \left(\sqrt{\frac{V_{SH}^2}{V_{SV}^2}} - 1\right) * 100$. Values >0 ($V_{SH} > V_{SV}$) indicate radial anisotropy is horizontally aligned, whereas values <0 ($V_{SH} < V_{SV}$) indicate regions of vertically aligned anisotropy. The depth sensitivity for both Rayleigh and Love waves at this frequency range are broad, making precise determination of the depth difficult, so I present depth averages of radial anisotropy, acknowledging that there may be some trade-off in the absolute depth of the anisotropy (Rychert and Harmon, 2017). Anisotropy is significant from 5 – 30 km depth and we therefore only interpret anisotropy in this depth range, although sensitivity tests indicate we can image from 5 – 40 km depth.

2.6.2 Effective Medium Calculations – Thin Compositional Layers

To understand the potential cause of the dominant radial anisotropy ($V_{SH} < V_{SV}$) I model the simplest example of horizontal anisotropic structure as transversely isotropic layers with a vertical axis of symmetry(Babuska and Cara, 1991). I explore whether alternating thin compositional layers can account for the observed anisotropy and maximum apparent velocity discontinuity. This is done by modelling alternating thin layers of rock compositions with fast and slow seismic velocities that are parallel to the Earth's surface, with vertical symmetry axis. To get effective radial anisotropy, the layers must be much thinner than the seismic wavelength. Then the resulting radially anisotropic Christoffel Matrix can be calculated using effective medium theory (Backus, 1962).

For transversely isotropic mediums with a vertical symmetry axis and hexagonal symmetry (the case for multiple Earth environments) the elastic coefficients for the stiffness matrix C_{ij} are:

$$(C_{ij}) = \begin{pmatrix} A & A-2N & F & . & . & . \\ A-2N & A & F & . & . & . \\ F & F & C & . & . & . \\ . & . & . & L & . & . \\ . & . & . & . & L & . \\ . & . & . & . & . & N \end{pmatrix} \tag{2.21}$$

For anisotropy we are interested in L and N. In an isotropic case $N = L = \mu$ where μ is the shear modulus. The distinct eigenvalues for shear waves of the Christoffel matrix are:

$$V_{SH} = \sqrt{\frac{N}{\rho}} \tag{2.22}$$

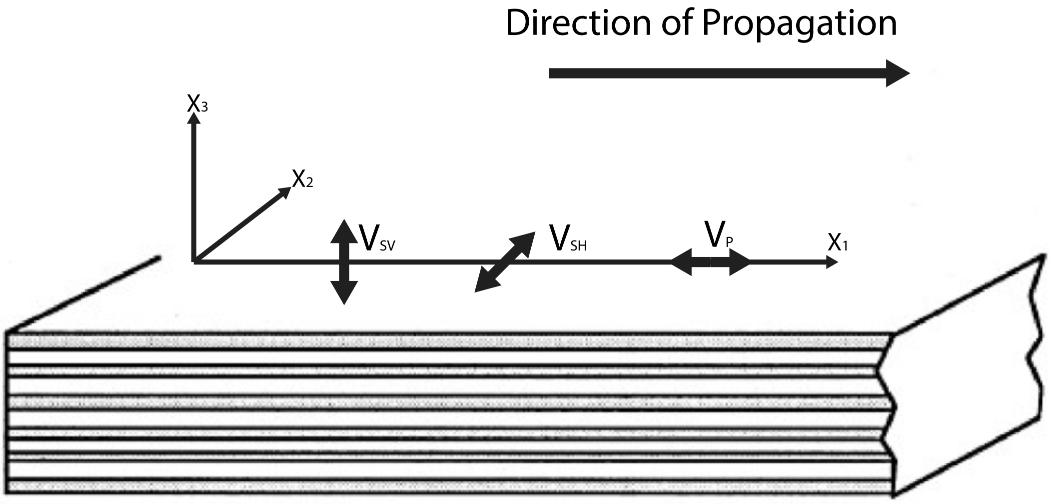

Figure 2.25: Setup for Backus anisotropy for compositionally thin layering with seismic plane waves propagating in the plane perpendicular to the symmetry axis. Adapted from Babuska and Cara (1991).

and

$$V_{SV} = \sqrt{\frac{L}{\rho}} \tag{2.23}$$

Where

$$L = \frac{1}{\frac{d_1}{\mu_1} + \frac{d_2}{\mu_2}} \tag{2.24}$$

and

$$N = \mu_1 d_1 + \mu_2 d_2 \tag{2.25}$$

Where d_1 and d_2 are the proportions of each layer (e.g. $d_1 = d_2 = 0.5$ for layering with 50% granite and 50% rhyolite), and μ_1 and μ_2 are the shear moduli for the 2 alternating layers.

The percentage anisotropy can then be calculated by δV given above.

Chapter 3

Using Ambient Noise to Image the Northern East African rift

This chapter focusses on using ambient noise to image the Northern East African Rift. The main aims were to generate a single absolute shear velocity model allowing direct comparison of regions at different stages of rifting. We also wanted to understand the role of fluids and in particular melt within the crust. Below is the paper published in Geochemistry, Geophysics and Geosystems (Chambers et al., 2019).

Chambers, E. L., Harmon, N., Keir, D., & Rychert, C. A. (2019). Using Ambient Noise to Image the Northern East African Rift. Geochemistry, Geophysics, Geosystems, 20, 2091–2109. https://doi.org/10.1029/2018GC0081291

Key Points:

- Uppermost mantle velocities are 9% slower than the ak135 model requiring elevated temperatures and fluids. Melt % estimates are 1.1 – 2%.
- The Main Ethiopian Rift has the slowest velocities at all depths in this study due to longer melt residence times within the crust.
- Shear velocity is heterogeneous beneath the northwestern plateau suggesting crustal structure and formation is more complex than thought.

3.1 Abstract

The northern East African Rift (EAR) is a unique location where we observe continental rifting in the Main Ethiopian Rift (MER) transitioning to incipient seafloor spreading in Afar. Here we present a 3-D absolute shear wave velocity model of the crust and uppermost mantle of the northern EAR generated from ambient noise tomography. We generate 4820 station pair correlation functions, from 170 stations (present over 12 years), which were inverted for phase velocity from 8–33s period and finally for 3-D absolute shear velocity structure to 60 km depth. Everywhere in the uppermost mantle, shear velocity is slower than expected for a mantle peridotite composition (<4.1 km/s). This suggests the presence of pervasive partial melt, with focused upwelling and melt storage beneath the MER, where the slowest velocities (3.20 ±0.03 km/s) are observed. Average crustal shear velocity is faster beneath Afar (3.83 ±0.04 km/s) than the MER (3.60 ±0.04 km/s), albeit Afar has localized slow velocities beneath active volcanic centers. We interpret these slow velocity regions (including the MER) as magmatic intrusions and heating of the crust. Beneath the northwestern plateau, crustal velocities are laterally heterogeneous (3.3 – 3.65 ±0.05 km/s at 10 km), suggesting a complex geological history and inhomogeneous magma distribution during rift development. Comparison between the MER and Afar allows us to draw conclusions between different stages of rifting. In particular, the MER has the slowest crustal velocities, consistent with longer magma residence times in the crust, early during the breakup process.

3.1.1 Plain Language Summary

In Ethiopia, the African Continent is rifting apart to slowly form a new ocean basin, which will expand the Red Sea and the Gulf of Aden. How and why this rifting is occurring remains an important unanswered question in earth science. We know tectonic forces are partly responsible, but magmatism also seems a key ingredient for breaking up Africa. Here we use seismic images obtained from signals pulled out of noise, to understand the crustal structure of the region; In particular, how and where magma is stored in the crust, and its relationship to the different stages of continental breakup visible in the region. We find evidence for long term melt storage in places where rifting is just beginning in southern Ethiopia; whereas in regions where the crust is thinner due to extensive rifting, magma erupts more regularly. The long term storage of magma in unrifted crust may help to heat and weaken it, allowing rifting to accelerate and propagate further south. We're also able to image regions with hydrothermal fluids in the shallow parts of the crust in inactive fault zones. These results provide insight into the breakup process and the role magma plays at different stages of rifting.

3.2 Introduction

Continents are thought to rift from a combination of tectonic and magmatic processes (Buck, 2004). Tectonic processes do not provide enough force to rift thick continental lithosphere, instead requiring emplacement of magma to rift with lower forces (Buck, 2006; Mackenzie et al., 2005). In areas of magma assisted rifting there is debate as to the distribution of melt storage and migration pathways, and how these change through time during the rifting to breakup process (Hutchison et al., 2015; Magee et al., 2016; White et al., 2008). To better understand the processes responsible for rifting the upper lithosphere, knowledge of the crustal structure both on and off the rift is required. The rift flanks give an insight into the original crustal structure while variations within the rift give clues to the importance of melt at different stages of rifting.

The Northern East African Rift (EAR) is the archetypal example of magma assisted rifting where the transition from continental rifting to seafloor spreading is observed within Ethiopia. The early stages of rifting are observed in the Main Ethiopian Rift (MER), with rifting becoming more evolved from south to north (Ebinger and Casey, 2001; WoldeGabriel et al., 1990). Afar is the end member of the EAR, transitioning from continental rifting to oceanic spreading (Makris and Ginzburg, 1987). The EAR forms one arm of the Afar triple junction while the other two arms, the Red Sea and Gulf of Aden rifts, have progressed to full seafloor spreading (Bonatti, 1985; McKenzie et al., 1970).

In this paper we use ambient noise tomography (ANT) from Rayleigh waves (Bensen et al., 2007; Shapiro and Campillo, 2004; Shapiro et al., 2005) to image the uppermost mantle and crustal structure in the northern EAR. Previous studies have used a variety of methods to analyze the crustal structure within rift segments including applying ANT to the MER and Afar, two sections of our study region. One study in Afar produced phase velocity maps and not inverting for shear velocity (Korostelev et al., 2015), while a second study focused on the northern and central sections of the MER using group velocities before inverting for absolute shear velocity (Kim et al., 2012). These studies found slow velocities at all depths beneath the rift flanks suggesting protracted magmatic modification of the crust coupled with 2 magmatic zones beneath the MER, indicative of a complex magmatic plumbing system (Kim et al., 2012; Korostelev et al., 2015). However, to facilitate direct comparisons between regions and thereby interpret evolution of rifting processes in space and time, we require a complete and self-consistent model for the northern EAR. Here we utilize 5 additional seismic networks (Figure 3.1A) and produce a crustal model for areas of Ethiopia, Eritrea, Djibouti and the southwest of Yemen, allowing direct comparison of regions at different stages of rifting. The absolute shear wave velocity model is used to interpret crustal structure and how rifting modifies the lithosphere by tectonic and magmatic processes. Shear wave velocities also allow us to infer areas containing fluids which will aid us in constraining where fluids, and potentially melt, reside within the crust and mantle.

3.3 Geological Background

Ethiopia is underlain by Precambrian basement formed during the Neoproterozoic Pan-African orogeny (Mège and Korme, 2004) (Figure 3.1B). The basement is composed of magmatic, metamorphic and sedimentary rocks (Berhe, 1990; Braathen et al., 2001; Kazmin et al., 1978; Merla et al., 1973), which have been crosscut by northwest-southeast trending Precambrian fractures (Mège and Korme, 2004). During the late Paleozoic to Mesozoic these fractures were reactivated to form several failed rift basins (Corti, 2009; Ebinger et al., 2000; Mège and Korme, 2004).

Volcanism initiated 45 Ma beneath our study area and continues to Recent times (e.g. Rooney et al. 2014; Barnie et al. 2016; Siegburg et al. 2018). The largest event was the emplacement of the ∼2 km thick flood basalt sequence 31 –29Ma (Hofmann et al., 1997; Ukstins et al., 2002), covering an area ∼600,000 km^2 (Rooney, 2017; White and Mckenzie, 1989). The flood basalts were later interspersed with shield volcanoes 22-11 Ma (e.g. Mt. Choke, Guna, & Guguftu)(Beccaluva et al., 2009; Kieffer et al., 2004). Present day volcanic activity is largely focused in the ∼70 km long and 20 km wide en-echelon magmatic segments within the rift axis (Barnie et al., 2016;

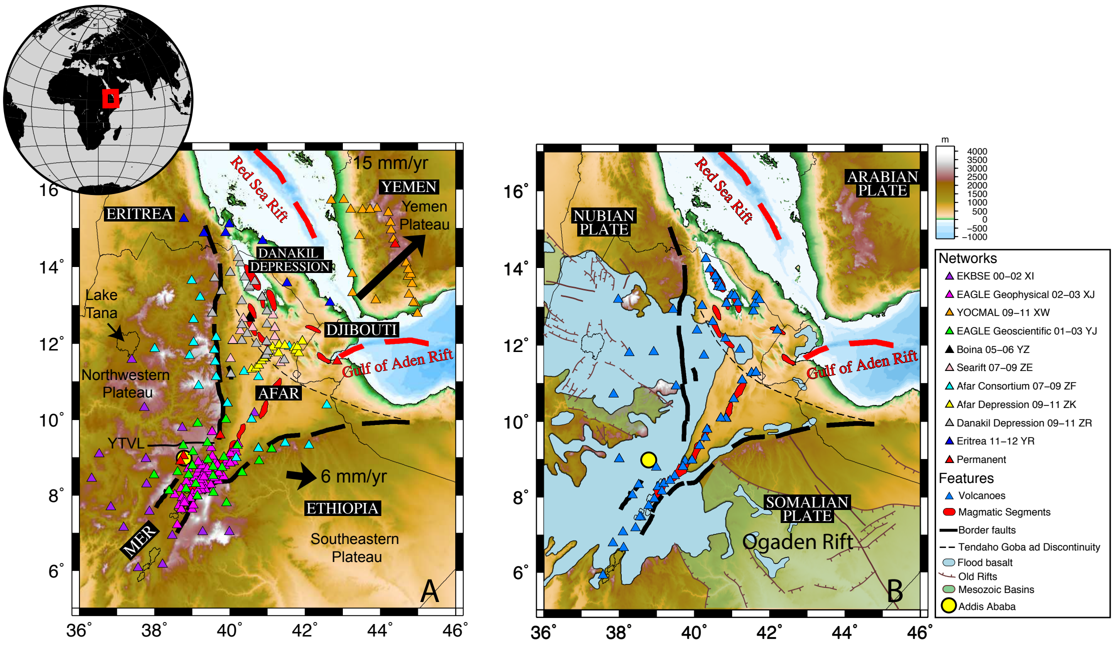

Figure 3.1: A) Seismic Station map of the northern EAR. Thick black lines show border faults, red polygons magmatic segments and dashed lines the Tendaho-Goba'ad discontinuity (TGD). Stations are triangles colored to their project deployment with pink (EAGLE 02-03), light pink (Searift), yellow (Afar Depression), grey (Danakil Depression) and black (Boina) networks not used for ambient noise prior to this study. Addis Ababa is marked by a yellow circle. B) Geological map. Volcanoes are represented by blue triangles and magmatic segments red polygons. Flood basalt provinces are shown in blue and rifts are bordered by brown faults and filled in green.

Ebinger and Casey, 2001; Hayward and Ebinger, 1996; Rooney et al., 2014; Siegburg et al., 2018; Wolfenden et al., 2004). Recent volcanism also occurs off-axis such as in the Yerer-Tullu Wellel Volcanotectonic Lineament (YTVL) and around Lake Tana (Keranen and Klemperer, 2008; Kieffer et al., 2004) (Figure 3.1).

Approximately coeval with the main flood basalt emplacement 31 − 29 Ma was the onset of rifting (Bosworth et al., 2005; Wolfenden et al., 2004), subsequently forming the Red Sea and Gulf of Aden Rifts (Hofmann et al., 1997; Pik et al., 1998). Rifting initiated later at 20Ma in the Southern MER, and 18-11 Ma for the central and northern sections (Kazmin et al., 1978; Wolfenden et al., 2004). The three rifts form the Afar triple junction separating the Nubian Somalian and Arabian plates (Figure 3.1B) (Ebinger et al., 1993; McKenzie et al., 1970; Wolfenden et al., 2004) On a smaller scale, Oligocene − Miocene border faults separate the plateaus (northwestern and southeastern) from the rift in the MER and Afar (Figure 3.1A) (Corti et al., 2013). Within Afar, the locus of extension shifted from the border faults to smaller faults and volcanic segments at around 10Ma (Wolfenden et al., 2005). In southernmost Afar and the MER, extension localized to the rift axis later at 6.6 − 3Ma (Wolfenden et al., 2004). Geodetic constraints in the MER and Afar suggest that >80% of the present-day extension is focused within the magmatic segments (Bilham et al., 1999; Ebinger and Casey, 2001). The rifting rates vary between regions with full spreading rates of 18, 16 and 6 mm/yr. for the Red Sea Rift (McClusky et al., 2010; Vigny et al., 2006), Gulf of Aden Rift (Jestin et al., 1994; Vigny et al., 2006), and MER respectively (Casey et al., 2006; Jestin et al., 1994; Saria et al., 2014) (Figure 3.1B).

Rifting processes have modified the crust resulting in variations in crustal thicknesses throughout the region. The thickest crust is found beneath the plateaus with the southeastern plateau 35-40 km thick and the northwestern plateau 40-45 km thick (Hautot et al., 2006; Mackenzie et al., 2005; Stuart et al., 2006). The crust thins into the MER where the crust is 38 km thick in the south and 30 km beneath the northern MER (Hammond et al., 2011; Maguire et al., 2006; Stuart et al., 2006). In Afar, the crust is ∼26 km thick, thinning to ∼16 km beneath the Danakil depression, the thinnest crust in the region (Dugda et al., 2005; Dugda and Nyblade, 2006; Hammond et al., 2011; Lavayssière et al., 2018).

The mantle beneath the region is thought to have elevated temperatures and pervasive melt based on seismic, geochemical and geodynamic studies (Armitage et al., 2015; Bastow et al., 2005; Ferguson et al., 2013; Gallacher et al., 2016; Lavayssière et al., 2018; Rooney et al., 2012a; Rychert et al., 2012). Mantle seismic velocities are slower than the global average (Bastow et al., 2005, 2008; Fishwick, 2010; Gallacher et al., 2016; Stork et al., 2013), which complements geochemical and geodynamic studies of inferred elevated mantle temperatures of 100-170°C above normal mantle temperatures (Armitage et al., 2015; Rooney et al., 2012a). Beneath the rift, velocities are typically slow with an absence or low amplitude lithosphere-asthenosphere boundary (Lavayssière et al., 2018; Rychert et al., 2012), interpreted by some previous studies as evidence of decompression melting or dyke induced lithospheric thinning (Havlin et al., 2013; Rychert et al., 2012; Stork et al., 2013). The MER axis also displays slow mantle velocities, which have previously been interpreted as evidence for partial melt generated by ongoing rifting processes (Bastow et al., 2005; Gallacher et al., 2016; Hammond et al., 2013).

3.4 Methods

We use data from continuous vertical component seismometers recorded by 10 temporary and 4 permanent networks (Figure 3.1A) between 1999 and 2012. The vertical component data from each of the 170 stations was split into 24-hour sections and resampled to 1 Hz. Instrument responses were removed and the waveforms were then normalized and whitened with a bandpass filter of 0.005–0.14 Hz (Bensen et al., 2007). Cross correlations and linear stacking were performed between all pairs of concurrently running stations with >10 days of continuous recording, using the methods of Bensen et al. (2007); Harmon et al. (2007, 2008) and (Harmon and Rychert, 2016), resulting in 4820 noise correlation functions (NCF) (Figure 3.2A).

We estimate the phase velocities from the NCF in the following way. We first estimate the average phase velocity dispersion across the region using a spatial domain technique using the entire array. We accomplish this by fitting a zero order Bessel function of the first kind as a function of interstation distance, frequency and phase velocity, to the real part of the fast Fourier transformed NCF by searching over phase velocities from $2.5 - 5$ km/s in a 0.01 km/s step at each period of interest (Harmon et al., 2008, 2010). Then for each individual NCF the phase was measured at each period of interest by unwrapping the phase of the stacked NCF using the average phase velocity curve at the longest periods to resolve cycle ambiguity(Bensen et al., 2007; Harmon et al., 2008). We then used the phase delay from the phase estimates to calculate the phase velocity as the distance between the 2 stations divided by the phase delay time (Harmon et al., 2007).

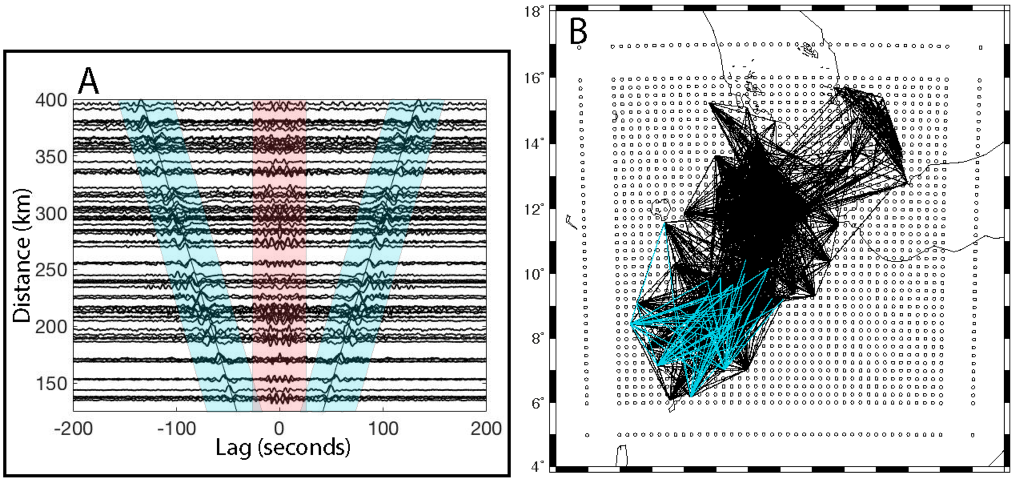

FIGURE 3.2: A) Example Noise correlation functions plotted as a function of distance and lag. Rayleigh waves highlighted in light blue with P-wave arrivals (unused) in red. B) nodal grid at 0.25° spacing overlain with ray paths at 18 seconds in black. Blue lines are ray paths used in 2A.

We use a two-stage inversion to generate our 3-D shear velocity model. We first invert the measured phase for phase velocity maps using the method of Harmon et al. (2013) from 8 – 33s period. We parameterize our model space for phase velocity using a 0.25° x 0.25° nodal grid (Figure 3.2B) and use the average phase velocity at each period as the starting model. The phase velocity inversion uses 2-D finite frequency kernels (Nishida, 2011; Tromp et al., 2010) and an iterative damped least squares approach (Tarantola and Valette, 1982). The sensitivity kernels for each NCF are averaged onto each node. We assign a nominal a priori standard error for each node of 0.2 km/s and fix the Vp/Vs ratio to 1.8, based on averaged receiver function results (Hammond et al., 2011; Stuart et al., 2006). For a given period, we only invert phase data for NCFs with interstation distances greater than twice the wavelength and apply a smoothing factor of 40 km. In the second stage, we invert the phase velocity maps across all periods at each point in the map to generate a 3-D velocity structure, using the best fit shear velocity model from the 1-D dispersion curve as our starting model. For the shear velocity inversion, we use a damped least squares approach (Tarantola and Valette, 1982) and parameterize the shear velocity at every 5 km vertically with 0.1x0.1 pixel size. We calculate the partial derivatives that relate variations in shear velocity to changes in phase velocity using DISPER80 (Saito, 1988). Although our shear velocity models are discretized at 5 km intervals in depth, we interpolate the velocity structure in depth to 1 km depth for presentation purposes using a linear interpolation.

Across the study region there are variations in sediment thickness and large bodies of water which may bias shear velocity structure to slower velocities at depth if not properly accounted for. We tested the effects of large slow layers on our shear velocity model by imposing a water layer to a thickness of 3 and 5 km in the Red Sea and Gulf of Aden with velocity and density values a priori from CRUST1.0 (Laske et al., 2013). We also performed the same tests with a sediment layer in the rifts using sediment thickness from CRUST1.0 (Laske et al., 2013). After 9 iterations, these tests produced shear velocity models that were within error of our preferred model, leading to confidence in our results.

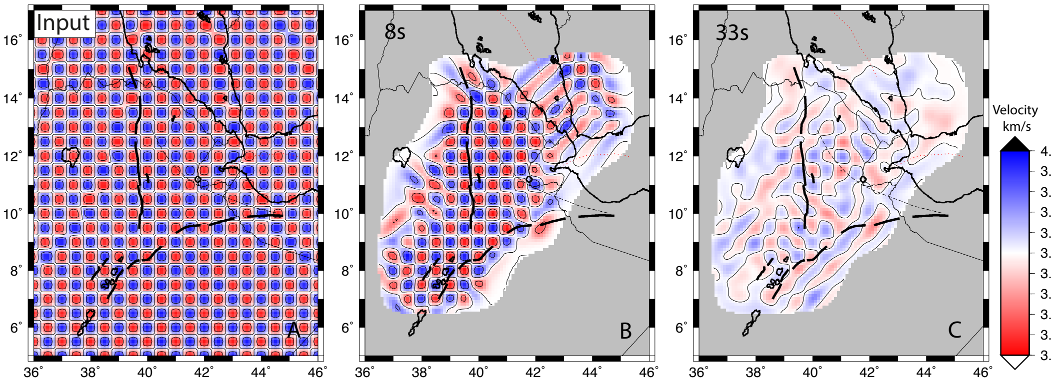

FIGURE 3.3: Checkerboard tests for 0.5° × 0.5°. Initial model shown in A) with B) and C) showing the resultant output model at 8 and 33s, the limits of our study. Results are cropped outside the 0.7 standard error contour. See text for details.

3.5 Resolution and Errors

We assess the minimum interpretable length scales of our velocity anomalies by presenting checkerboard tests for 0.5°×0.5° anomalies between 8 – 33s period. The tests indicate we can resolve anomalies at the scale of 0.5° across most of the region (Figure 3.3), particularly in regions with good ray path coverage within the MER and northwestern Afar (Figure 3.2B). In areas of sparser ray coverage such as eastern Afar, the Red Sea and Gulf of Aden we have poorer resolution and northeast-southwest smearing of checkerboard tests. Consequently, we do not interpret these regions. We mask results outside the standard error contour of 0.07 km/s, the approximate contour of the 2σ error, from the linearized phase velocity inversion.

We assess the vertical resolution of the shear velocity via the formal resolution matrix of the shear velocity inversion. Our model is not well resolved above 5 km and below 60 km depth with formal resolution values <0.10. Formal resolution values are typically around 0.37 for each 5 km thick layer in the 10 – 55 km depth range indicating we have independent constraints approximately every 10 – 15 km in depth. In other words, we can resolve average velocity variations over 10 - 15 km depth ranges.

3.6 Results

3.6.1 Phase Velocities

Our average 1-D phase velocity dispersion curve for the full study region ranges from 3.13 ±0.03 km/s at 8s period to 3.61 ±0.05 km/s at 33s period (Figure 3.4A). From our final velocity maps (Figure 3.5 and Figure 3.6), we take 1-D phase velocity curves from individual pixels in the maps and their corresponding 1-D shear velocity profiles (Figure 3.7), allowing us to directly compare regions of interest labelled from “a – h.” The slowest phase velocities for all depths are located within the MER (Figure 3.7 A and B, “a,” “g” and “h”) ranging from 3.18 ±0.03 km/s at 8s period to 3.56 ±0.05 km/s at 33s period. The Danakil depression, “c,” has the fastest velocities from 3.21 ±0.04 km/s at 8s period to 3.60 ±0.06 km/s at 33s period. At short periods of 8 to

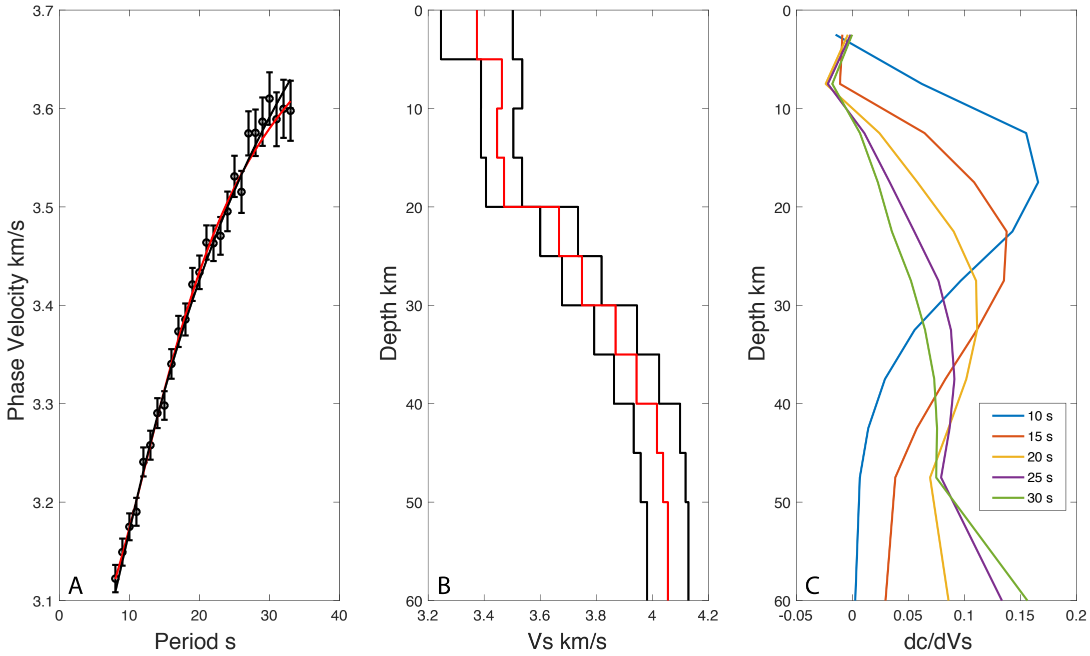

FIGURE 3.4: A) Average 1-D phase velocity for the study region with 3σ error bars (circles) with predicted dispersion from Gallacher et al. (2016) (black line) and our best fit shear velocity model dispersion overlain (red line). B) Best fit shear velocity model for the study region (Red line) and formal 2σ error bounds (black lines). C) Sensitivity kernels for Rayleigh waves at selected periods.

13 seconds we observe slow velocities at “e” beneath the northwestern plateau. In general, the plateau regions, “d – f,” have faster phase velocities at shorter periods than the MER and Afar averages, “a-c”.

Within our phase velocity maps (Figure 3.5), we observe variations across the region that correlate with surface geologic and tectonic features. For example, we observe slow velocities beneath the MER at all periods, with minimum velocities ranging from 2.95 ±0.03 km/s at 8s period, to 3.45 ±0.05 km/s at 33s period (Figure 3.5A-D “a”). Beneath Afar we observe moderate velocities with maximum velocities ranging from 3.30 ±0.04 km/s at 8s period to 3.65 ±0.06 km/s at 33s period (Figure 3.5 A-D “b – c”). The northwestern plateau has the greatest lateral velocity variations, with minimum velocities ranging from 3.00 ±0.05 km/s at 8s period, to 3.55 ±0.07 km/s at 33s period (Figure 3.5 A-D “d”) and maximum velocities ranging from 3.35 ±0.05 km/s at 8s period, to 3.70 ±0.07 km/s at 33s period at “f”. In contrast, phase velocities for the southeastern plateau are more laterally homogenous, with phase velocities of 3.30 ±0.05 km/s at 8s period increasing to 3.60 ±0.07 km/s at 33s period (Figure 3.5 A-D “e”). Although at 8s period, the phase velocity map exhibits the greatest lateral heterogeneity.

3.6.2 Shear Velocities

Our average 1-D shear velocity model across all nodes ranges from 3.36 ±0.04 km/s at 5 km depth to 4.04 ±0.05 km/s at 60 km depth (Figure 3.4 B). Our best fit model does not have a fast lid or slow velocity zone visible at mantle depths, rather shear velocity monotonically increases with depth. 1-D profiles through our shear velocity volumes (Figure 3.7 C and D) show similarities

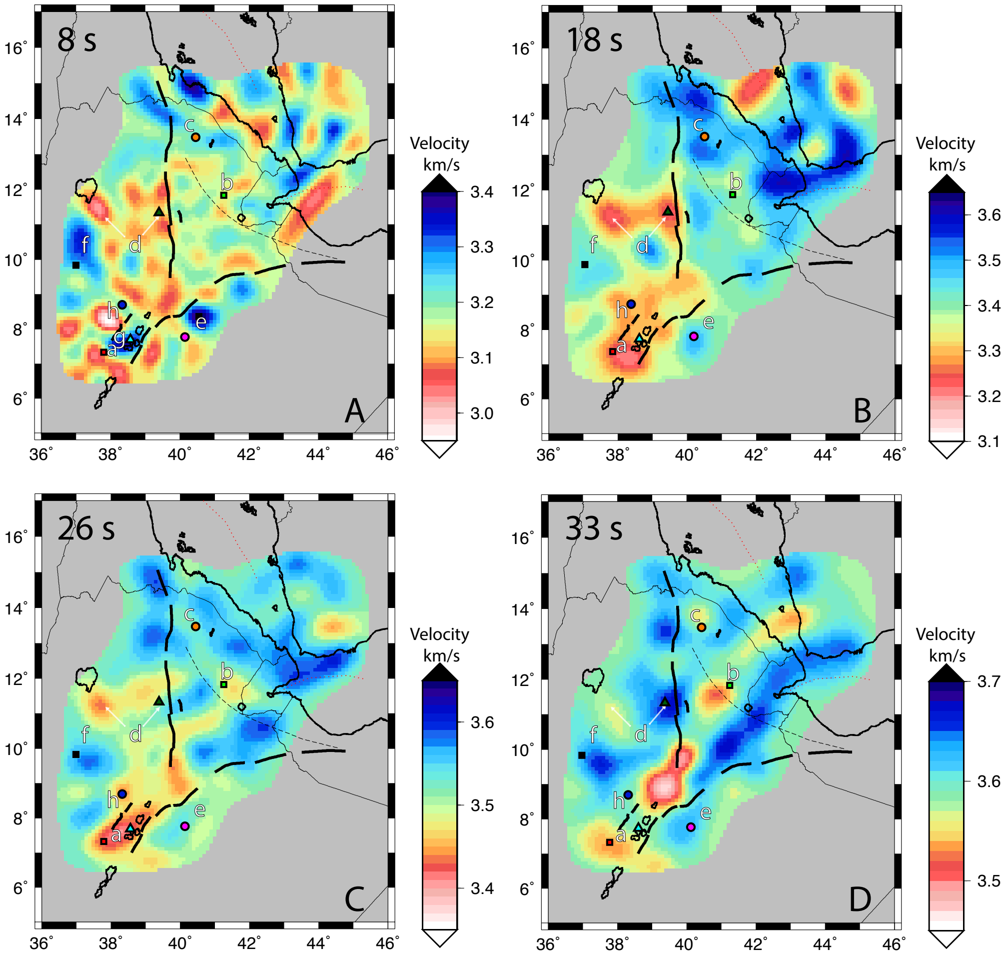

FIGURE 3.5: A-D: Phase velocity maps resulting from tomographic inversion of ambient noise dispersion data at 8, 18, 26 and 33s respectively. Models has been cropped to the standard error contour. Red indicates slower velocities and blue faster velocities. Sections get, on average, progressively faster with depth. Colored symbols indicate the locations of profiles shown in Figure 3.7. Thick black lines indicate border faults. Letters a – h are regions referred to in the text.

to the phase velocity maps. The slowest velocities for all depths are again located within the MER, "a," ranging from 3.28 ±0.03 km/s at 10 km depth to 3.83 ±0.04 km/s at 40 km depth, with a broad velocity increase from 20-50 km depth. Within Afar, "b," velocities increase from 3.45 ±0.04 km/s at 10 km and increase to 3.86 ±0.05 km/s at 40 km depth, with the sharpest gradient between 5-20 km depth. The Danakil depression, "c," has the fastest velocities from 3.64 ±0.04 km/s at 10 km depth to 3.98 ±0.06 km/s at 40 km depth, again with the sharpest gradient between 5-20 km depth. The Danakil depression, in contrast to the starting model and most of our study region, requires a fast lid, with a slow velocity zone minimum at 45 km depth. Beneath the northwestern and southeastern plateaus, "e-f," we observe fast shear velocities of 3.5 ±0.05 km/s to 3.85 ±0.07 km/s at 40 km depth. The exception to this is the slow velocity zone beneath "d," where velocities are slower at 3.3 km/s ±0.05 km/s at 10 km depth. Velocities become progressively faster until 40 km depth where they are similar to the overall plateau velocity structure.

Absolute shear wave velocity maps (Figure 3.6) show similarities to phase velocities, ranging from 3.20 – 4.10 ±0.06 km/s. At 40-60 km, mantle depths, we observe velocities ranging from 3.60 – 4.10 ±0.06 km/s beneath the region. These are all slower than the global model ak135 which has a velocity of 4.48 km/s for mantle beneath the continents (Kennett et al., 1995). We observe slow velocities beneath the MER at all depths, with minimum velocities ranging from 3.20 ±0.03 km/s at 10 km depth to 3.75 ±0.04 km/s at 40 km depth (Figure 3.6 "a"). The slow velocity anomaly is roughly 200 km long by 100 km wide trending along the rift valley. It is broad and distributed at depth, becoming focused to the rift valley in the crust. A smaller slow velocity region follows the surface trend of the YTVL (Figure 3.6 A-C "h"). The anomaly is approximately 50 km wide trending east-west with velocities of 3.20 ±0.03 km/s at 10 km depth increase to 3.60 ±0.04 km/s at 30 km depth. While most of the MER displays slow velocities, at "g" we observe a zone of faster velocity, relative to the surroundings, between the Aluto and Corbetti volcanoes with velocities of 3.65 ±0.03 km/s above 20 km depth, approximately 40 km in diameter (Figure 3.6 A-B, and Figure 3.8 A).

Beneath Afar, velocities are fast everywhere relative to the MER, with maximum velocities ranging from 3.75 ±0.04 km/s at 10 km depth to 4.05 ±0.06 km/s at 40 km depth (Figure 6 A-D "b and c"). Beneath most of the active magmatic segments (Figure 3.6 open red polygons and "b") in Afar, we observe slower velocities down to 3.45 ±0.04 km/s at 10 km depth and 3.85 ±0.06 km/s at 40 km depth. The transition from the MER into Afar is also marked by a distinct 5% increase in velocity where the rift widens into Afar.

While the MER and Afar are broadly consistent within their regions, the plateaus display greater heterogeneity, with lateral variability of 0.5 km/s as compared to 0.3 km/s outside the plateaus. The velocities beneath the majority of the plateaus are fast, typically around 3.65 ±0.05 km/s at 10 km depth and ∼3.95 ±0.07 km/s at 40 km depth (Figure 3.6 and Figure 3.7 "e – f"). However, in localized regions, velocities are in some cases as slow as the MER. For example, near "d" on the northwestern plateau (Figure 3.6 A-C and Figure 3.8 B), velocities are as slow as 3.25 ±0.05 km/s at 10 km increasing to 3.65 ±0.07 km/s at 30 km depth. In addition, on the Yemen Plateau the velocity is 3.30 ±0.05 km/s at 10 km, and this slow velocity continues down to 20 km depth (Figure 3.6 A-B and Figure 3.8 A).

3.6.3 The lower crust and Moho

Based on the studies of Keranen et al. (2009) the Moho beneath the MER can be approximated with an absolute shear velocity of 3.75 km/s. We produce 2 transects through our model, along the rift and across the MER, approximately coinciding with the EAGLE active source line (Figure 3.8) and use this 3.75 km/s contour as a proxy for Moho depth. We then compare to previous direct measures of crustal thickness from receiver function studies (Dugda et al., 2005; Hammond et al., 2011; Stuart et al., 2006). To do this we interpolate the model to every 1 km and take a velocity slice at 3.75 km/s and overlay crustal thickness from receiver function studies in Afar (Hammond et al., 2011), and the MER (Figure 3.9) (Dugda et al., 2005; Stuart et al., 2006). Along the rift we see the 3.75 km/s contour shallowing from 40 km beneath the MER to 20 km in Afar. The crust is relatively thin beneath the Red Sea (17 km) and thickens to 29 km beneath Yemen (Figure 3.8 A). There is some agreement between the 3.75 km/s contour and crustal thickness studies in the MER and Afar rifts, however many points do not appear to correlate. Across the rift axis (Figure 3.8B and Figure 3.9) and beneath the northwestern and southeastern

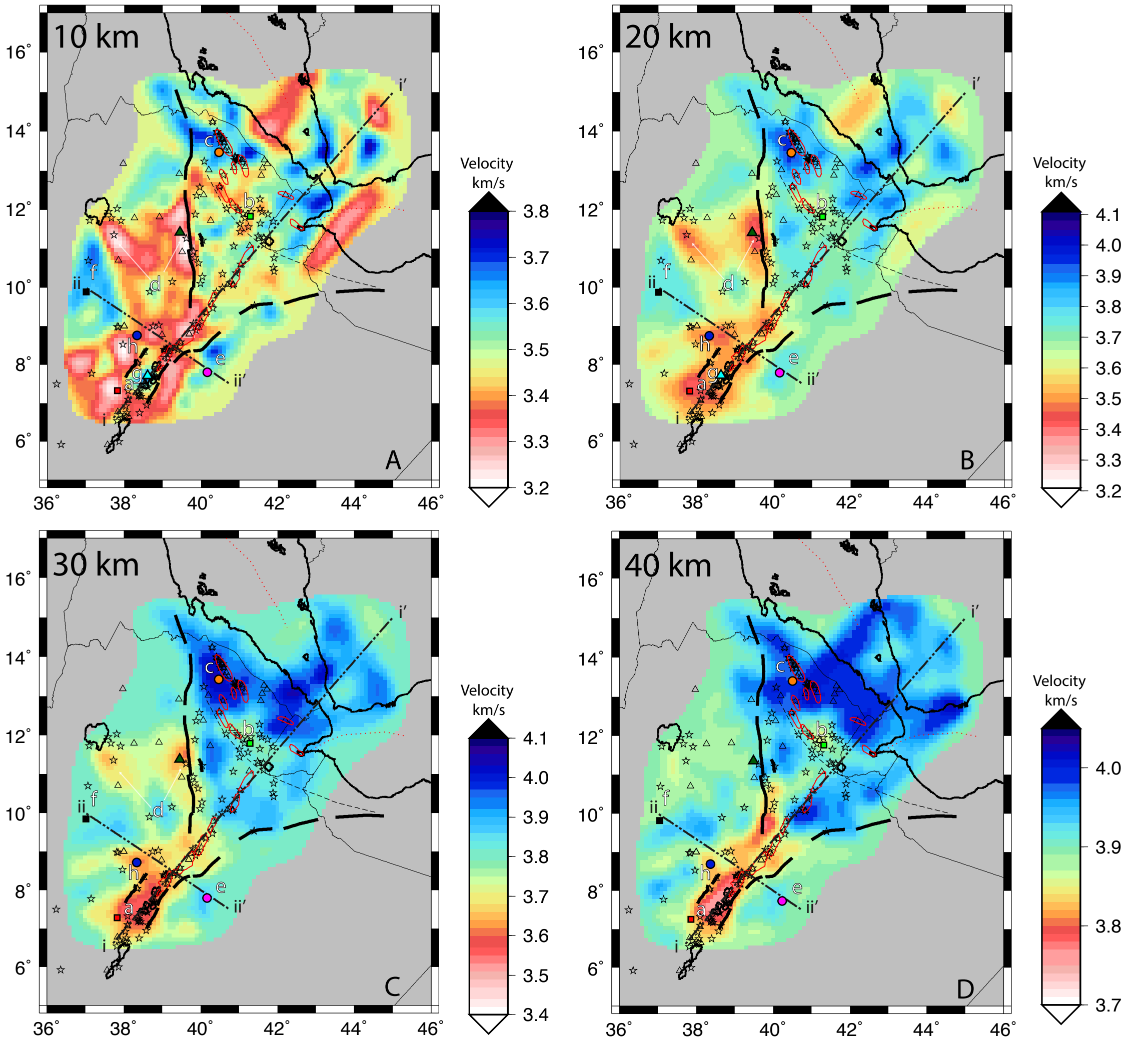

FIGURE 3.6: A-D: Interpolated depth slices at 10, 20, 30 and 40 km. Sections get progressively faster with depth with the vertical resolution smoothed across 10 km. Dashed black lines show cross sections in Figure 3.8A and B with thick black lines indicating the border faults. Letters a – h are regions referred to in the text. 1-D profile locations (colored symbols) are described in Figure 3.7. Red polygons indicate magmatic segments, black triangles volcanoes and black stars geothermal activity.

plateaus, we no longer match the estimates of crustal thickness. Here we observe depths of ∼20-37 km compared to 32-45 ±3 km on the northwestern plateau and 20–38 km compared to 32-43 ±3 km for the southeastern plateau (Figure 3.9B). There are also some differences between the Moho and 3.75 km/s contour in regions where crustal thickness changes over short distances (e.g. from the plateau into Afar, and near the TGD in Afar). Our model laterally smooths across these short length scales and therefore does not fully recover sharp gradients in crustal thickness and the sharp increase in velocity at the Moho (Figure 3.9).

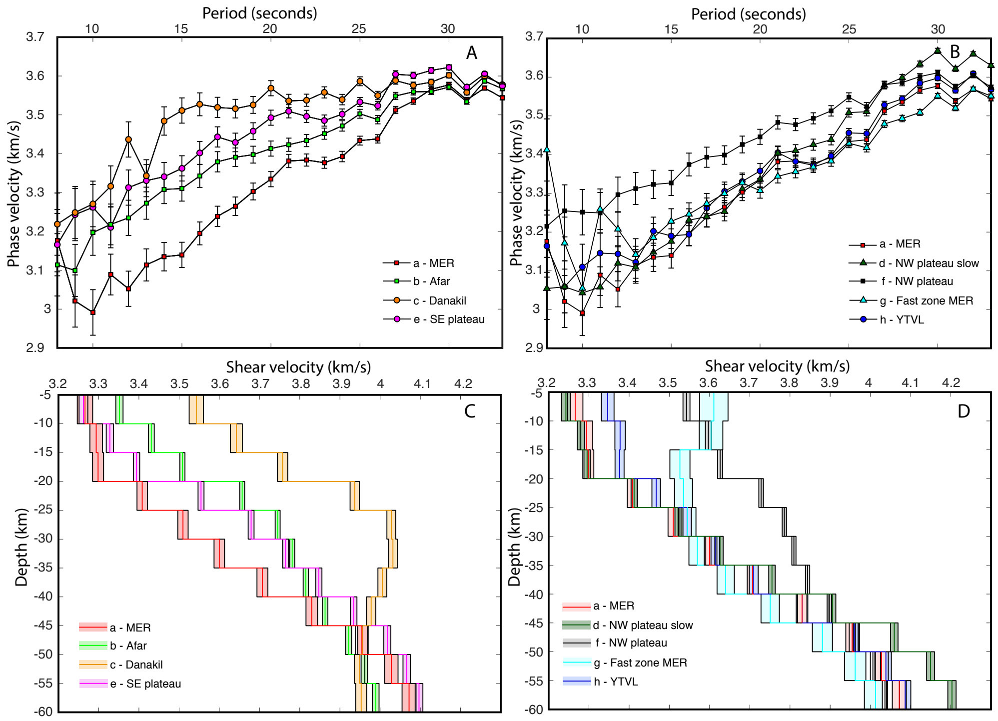

Figure 3.7: 1-D phase and shear velocity profiles for key areas discussed in the text. A) Phase velocities comparing the MER, Danakil, Afar and southeastern plateau. Error bars are 3 error. B) 1-D profiles for the plateau and MER regions. C) and D) are same as A) and B) but for shear velocities. See Figure 3.5 and Figure 3.6 for 1-D profile locations.

3.7 Discussion

Our velocity model constrains shear wave velocities of the crust and uppermost mantle. The key observations of our shear wave velocity model are: (1) Velocities in the uppermost mantle are everywhere slower than the global average for continents using ak135, in particular beneath the MER (3.75 ±0.04 km/s), (2) The MER is significantly slower than Afar with a clear increase in velocity at all depths as the rift widens into Afar, and (3) The Ethiopian plateau displays heterogeneity in crustal velocity. In the following section, we use our velocity maps to interpret velocity variations and use these to answer key questions about the nature of the crust and mantle structure when rifting modifies the lithosphere during the rifting to breakup process. This will allow us to identify where fluids, and potentially melt, reside within the crust and mantle.

3.7.1 Mantle Velocities

Mantle velocities in our region are anomalously slow, when compared to global averages appropriate for continental regions such as iasp91, by up to 9-16% over the uppermost mantle. Previous studies in the region have found similarly slow velocities in the mantle, for example Gallacher et al. (2016) and Keranen et al. (2009) found values of 3.8 – 4.0 km/s and 3.9 – 4.2 km/s respectively. The low values are also similar to slow shear velocities observed in mid ocean ridge systems such as the southern East Pacific Rise (∼3.9 km/s) (Harmon et al., 2009), the Eastern

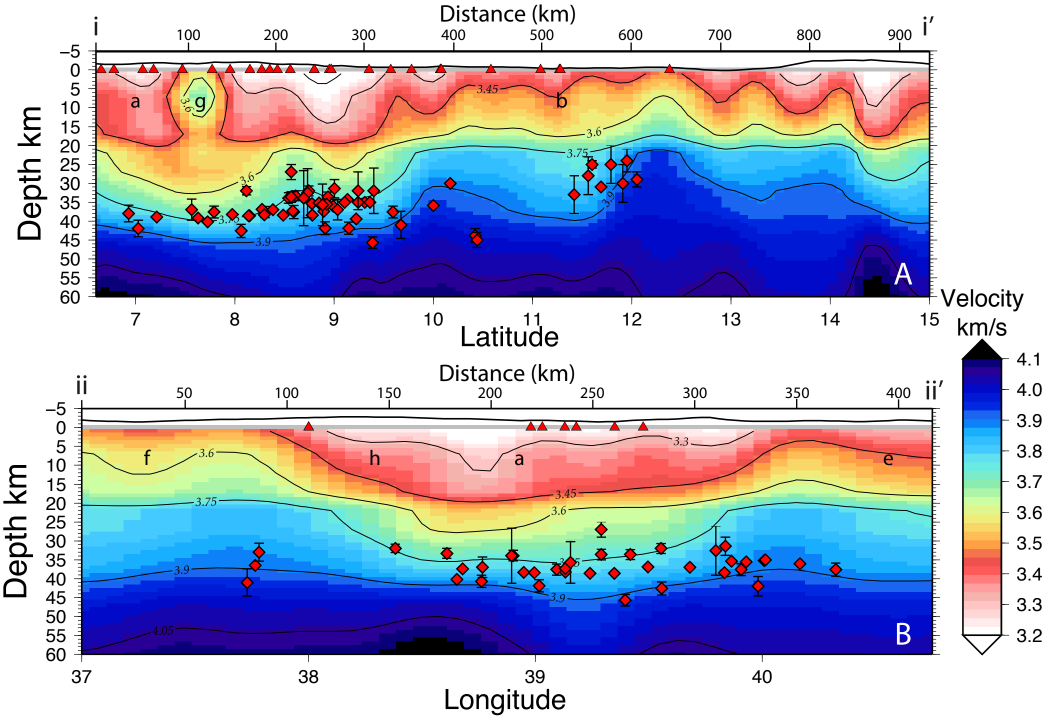

FIGURE 3.8: Cross-sections of the shear velocity maps, interpolated to 1 km depth resolution. See Figure 3.6 for locations of cross sections. A) Profile along the rift axis. B) Profile across the MER and plateau. Receiver function Moho depths plotted as diamonds within 1 degree of the profile (Ayele et al., 2004; Dugda et al., 2005; Hammond et al., 2011; Stuart et al., 2006).

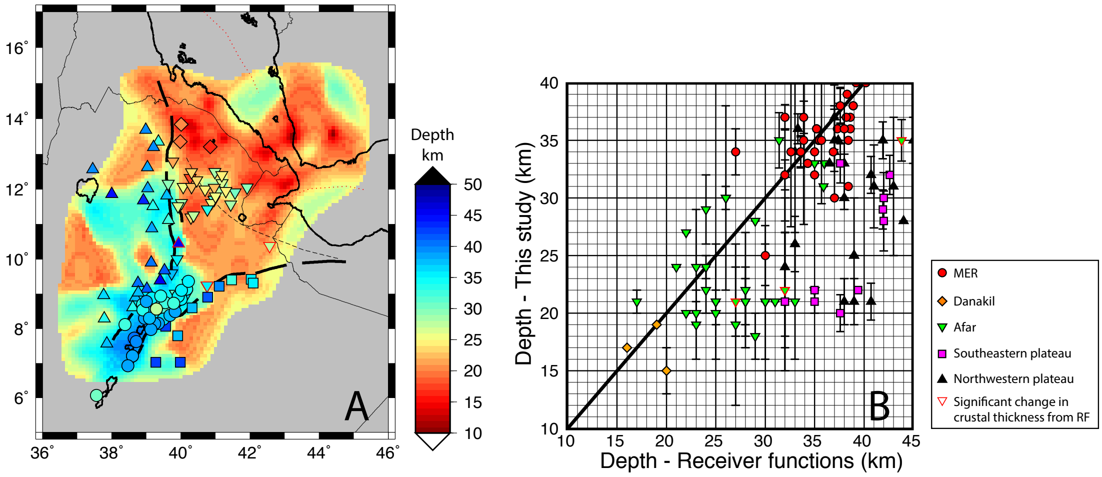

FIGURE 3.9: A) Interpolated velocity slice at 3.75 km/s used as an indicator for crustal thickness. Symbols are depths from receiver function studies (RF) for regions within Ethiopia (Ayele et al., 2004; Dugda et al., 2005; Hammond et al., 2011; Stuart et al., 2006). B) Depth to the Moho from receiver function studies vs. this study. Colors and symbols represent different regions. Please see the legend for details.

Lau Back Arc Spreading Center (∼3.6 km/s, (Wei et al., 2015)) and The Juan De Fuca/Gorda Ridges (∼3.8 km/s (Gao, 2016)). Although there are significant differences in the tectonic environments the possible causes for these anomalously slow velocities are likely similar, mantle upwelling and associated volcanism at the surface.

3.7.1.1 Possible Causes for Anomalously Slow Mantle Velocities

In this region shear velocities are everywhere slower than expected for a mantle peridotite composition (<4.1 ±0.06 km/s including beneath the plateau) in the uppermost mantle down to 60 km depth (Hacker and Abers, 2004). Compositional variation in peridotites yields little shear velocity reduction (<1.5%) for the range of expected densities and compositions (Lee, 2003; Schutt and Lesher, 2006). Mantle composition in the northern EAR has heterogeneity but is predominantly peridotite (Rooney, 2017). We therefore do not think that variation in composition across the region is the cause of the slow velocities we observe.

In the upper mantle, shear velocities are sensitive to variations in temperature and grain size (Faul and Jackson, 2005; Jackson and Faul, 2010). Mantle velocities of 3.60 km/s – 4.10 km/, a 9-16% reduction from the global average, are likely accommodated at least in part by an increase in mantle temperature and/or grain size changes. Petrological estimates and models suggest a mantle potential temperature for this region of between 1350°C (Armitage et al., 2015; Pinzuti et al., 2013; Rychert et al., 2012) and 1490°C (Armitage et al., 2015; Ferguson et al., 2013; Rooney et al., 2012a) and therefore ranging from normal ambient mantle to ∼140°C hotter than average (Rooney et al., 2012a). We use a Burgers model relating shear velocity and temperature (Jackson and Faul, 2010), for a peridotite mantle at grain sizes between 1-20 mm, (based on xenoliths in the MER (Rooney et al., 2005) with an estimate for the geotherm for the MER, to determine the mantle temperature required to match our observations. We require a temperature between 1650°C and 1900°C for grain sizes of 1 – 20 mm respectively. This temperature is 160 – 550°C hotter than predicted estimates, requiring additional explanations for the slow mantle velocities. At a given temperature grain size changes can also reduce velocity by up to 3% (Faul and Jackson, 2005; Jackson and Faul, 2010) when grain size is increased from 1-20 mm. However, grain size cannot in and of itself explain our observations again requiring an additional explanation.

We therefore require a fluid component, most likely partial melt, at greater depths and potentially hydrothermal fluids shallower. Assuming slower velocities in the upper mantle are from melt we can use the relationship of 1% melt slows shear velocities by 7.9% (Hammond and Humphreys, 2000a). We find 1.1% melt beneath both plateaus and 2.0% melt beneath the slowest region of the MER. These values are similar to previous teleseismic tomography studies where partial melt of 0.6 – 4% are calculated (Bastow et al., 2011; Civiero et al., 2015, 2016; Ferguson et al., 2013; Gallacher et al., 2016). Forward modelling of the crust and mantle found similar values of <5% melt (Armitage et al., 2018). Variations in melt percentage within the mantle to previous tomography studies may arise from greater ray path density and broader frequency content, particularly the inclusion of high frequencies, compared to teleseismic techniques (Shapiro and Campillo, 2004; Shapiro et al., 2005). Vs studies will have more significant velocity reductions, relative to Vp, in the presence of melt (Karato, 2004).

We also observe slow mantle velocities, compared to global average velocities, at Moho depths (defined by receiver functions) (Dugda et al., 2005; Hammond et al., 2011; Stuart et al., 2006). The Moho is an interface which previous modelling studies using magnetotelluric and seismic data propose to be an area of 2-7% melt accumulation (Armitage et al., 2015, 2018; Desissa et al., 2013). We therefore suggest partial melt is more localized near the Moho than at depth.

3.7.1.2 The Moho and lower crustal intrusions

Inferred crustal thickness beneath our study region using a 3.75 km/s contour, are broadly consistent with previous direct measures of crustal thickness particularly beneath the MER and Afar from receiver functions and active source studies (Dugda et al., 2005; Hammond et al., 2011; Stuart et al., 2006; Ayele et al., 2004; Maguire et al., 2006) (Figure 3.9). Within the rift, the 3.75 km/s contour shallows from the MER to Afar which is likely an effect of crustal thinning with progressive rifting (Hammond, 2014; Tiberi et al., 2005). The shallowest inferred Moho depths are beneath the Red Sea and the Danakil depression, in good agreement with receiver function studies (Hammond et al., 2011). Beneath the plateaus the 3.75 km/s contour is shallower than the receiver function-derived Moho depth, implying faster velocities within the lower crust. Faster velocities in the lower crust suggest the crustal composition has been modified and we propose the most likely change is from solidified lower crustal mafic intrusions. Solidified mafic intrusions in the lower crust increase velocity, thereby shallowing the depth of the 3.75 km/s contour and reducing the contrast between lower crustal and mantle seismic velocities (Hammond et al., 2011; Lavayssière et al., 2018; Stuart et al., 2006; Thybo and Nielsen, 2009). The EAGLE active source experiment also observed a fast velocity Vp layer in the lower crust coupled with a dense lower crust beneath the northwestern plateau (Cornwell et al., 2006; Mackenzie et al., 2005; Maguire et al., 2006), while receiver functions observe a reverberation from the top and base of the underplate (Lavayssière et al., 2018; Stuart et al., 2006). Our crustal thickness estimate based on the 3.75 km/s depth contour would probably select the top of the underplate, yielding apparent thinner crust, thus supporting widespread solidified lower crustal intrusions beneath the plateau.

In contrast to the fast velocities on most of the plateau, we observe a smaller slow velocity region that trends east-west following the surface trend of the YTVL (Figure 3.6 A-C “h”) a line of Quaternary-Recent volcanoes. This suggests we are imaging a thermal or fluid anomaly associated with ongoing magmatic processes. Beneath the eastern end of the YTVL, highly localized high conductivities are seen in MT surveys (Whaler and Hautot, 2006) coupled with collocated clusters of lower crustal seismicity (Keir et al., 2009a) suggest ongoing, but localized lower crustal melt emplacement within the solidified crust.

3.7.2 Crustal Velocities

3.7.2.1 MER axis

We define crustal velocities for our discussion here using the crustal thicknesses estimated by receiver functions across the region (Ayele et al., 2004; Dugda et al., 2005; Hammond et al., 2011; Stuart et al., 2006). The shear wave velocities range from 3.20 ±0.03 km/s at 10 km depth, to 3.55

±0.04 km/s at 30 km with a slow velocity anomaly roughly 200 km by 100 km wide positioned beneath the MER axis (Figure 3.6 "a"). The observation is in apparent contradiction to the elevated Vp for the MER crust at 10 − 30 km depth, as determined by first arrival travel time tomography and the EAGLE controlled-source survey (Keranen et al., 2004; Mackenzie et al., 2005; Maguire et al., 2006). These studies interpreted fast Vp values as continental crust intruded by now solidified mafic rock. The presence of solidified mafic rock predicts Vs that is faster than we observe. The slow Vs is also not explained by widespread silicic or intermediate rock type. These typically have Vs of 3.64 km/s, and 3.78 km/s (Birch, 1960; Simmons, 1964), faster than we observe, but also contrary to the elevated Vp from previous studies. We therefore conclude that rock composition does not broadly explain the slow Vs in the MER.

Elevated temperatures would also produce slow velocities within the crust. If we assume the crust within the rift axis is predominantly gabbroic intrusions (Mazzarini et al., 2013; Rooney et al., 2014), crustal temperatures of 600°C generate velocities >3.81 km/s (Hacker and Abers, 2004) significantly faster than what we observe. Assuming a diorite composition, velocities reach 3.67 km/s under the same conditions. Therefore, temperature cannot solely account for the velocity reductions beneath the MER and we therefore appeal to a fluid component.

The MER is volcanically active, with geodetic evidence for melt input into crustal magma bodies and interaction with hydrothermal reservoirs (Biggs et al., 2011; Hutchison et al., 2016). Fluids may be present in the form of small volumes of partial melt or from the release of volatiles within cooling magmatic systems (Holtzman and Kendall, 2010; Korostelev et al., 2015). If we assume the velocity reduction in the crust is solely from melt, we can estimate the amount of melt using the experimental relationship of 0.1 km/s decrease in shear velocity requires 1% melt (Caricchi et al., 2008). We compare to the Vs structure of the southeastern plateau, least modified by rifting. We estimate ∼3% melt for the MER, within the range of ∼0.5-5% from previous seismic studies (Gallacher et al., 2016; Guidarelli et al., 2011; Hammond et al., 2014). However, models from magnetotelluric and gravity studies yield higher melt fractions of 3 –20 % (Cornwell et al., 2010; Keranen et al., 2009; Whaler and Hautot, 2006).

Placing constraints on percent melt is complicated by anisotropy and the alignment and shape of melt (Hammond et al., 2014; Hammond and Kendall, 2016). Rayleigh waves show a velocity reduction for both horizontally and vertically aligned melt with greater sensitivity to horizontal melt in contrast to Love waves which are more sensitive to vertically aligned melt (Hammond and Kendall, 2016). Furthermore, melt stored as horizontal disks requires up to 10% less melt to generate a reduction in Rayleigh wave shear velocity than spherical melt bodies (Hammond and Kendall, 2016). Geochemical, seismic and magnetotelluric studies provide evidence for a series of stacked sills at the base of the crust (Ferguson et al., 2013; Hammond et al., 2014; Johnson et al., 2015), and may suggest that our velocity estimates are biased towards higher quantities of melt due to anisotropy. Further work is required to assess the radial and azimuthal anisotropy across the region to understand the degree of bias.

Generally, our slow velocity anomalies within the crust are spatially correlated along-rift with the active volcanic segments (Red polygons Figure 3.6 A-D), though our velocities are commonly broader, in part due to the wide lateral sensitivity of Rayleigh waves. While we cannot rule out sediment infill to explain slow shear velocities near the surface (Christensen, 1996; Hacker and Abers, 2004; Mazzarini et al., 2013), it is more likely the velocities are associated with the active magmatism in the rift axis. The slow velocities end at the southern extent of the visible magmatic segments where we observe a fast velocity of 3.65 ±0.03 km/s above 20 km depth (Figure 3.6 A-B and Figure 3.8 A “g”). Slower velocities are more wide spread at depth near the Moho with the slowest velocities being beneath the rift. The slow velocities are present at all depths within the crust beneath the rift axis.

3.7.2.2 Afar

The Afar crust has relatively fast Vs in our study (3.75 ±0.04 km/s at 10 km depth to 4.05 ±0.06 km/s at 40 km depth) excluding “b” at 10 km depth where velocities are as slow as 3.45 km/s (Figure 3.6 A). This observation is consistent with fast Vp imaged previously (Makris and Ginzburg, 1987; Prodehl et al., 1997) and supports the hypothesis that most of the Afar crust includes a significant component of solidified mafic rock (Furman et al., 2006). Afar also appears fast in depth sections that cut through the Afar mantle, consistent with faster velocities for mantle peridotite than crustal rocks. This is especially noticeable beneath the Danakil Depression, where particularly thin crust (∼16 km thick) (Berckhemer et al., 1975; Hammond et al., 2011), significantly reduces the depth of the mantle compared to other regions (Figure 3.6 A “c”).

An exception to the fast Afar crust is a region of slower velocities broadly beneath the magmatic segments (Figure 3.6 A-D “b”), down to 3.45 ±0.04 km/s at a depth of 10 km and 3.85 ±0.06 km/s at a depth of 40 km. This is most clearly evident at the Dabbahu and Hararo magmatic segments, the location of the 2005-2010 Dabbahu dyking event (Ebinger et al., 2010; Grandin et al., 2012; Illsley-Kemp et al., 2018b). Previous studies also find slow velocities (Korostelev et al., 2015; Stork et al., 2013) and high conductivities (Desissa et al., 2013; Johnson et al., 2015), which have been used to estimate a 500 km^3 melt body with 13% melt beneath this region associated with the dyking event (Desissa et al., 2013). Slow velocities coupled with the recent dyking event suggest we image melt associated with the event. We see a similar slow velocity zone beneath the Nabro volcanic chain which erupted in 2011 (Goitom et al., 2015) suggesting we are again imaging hotter crust and partial melt in the crust.

3.7.2.3 Comparison of the MER to Afar

The transition from the MER into Afar is marked by a distinct 5% increase in velocity where the rift widens into Afar. Both areas have had recent volcanic eruptions (Hutchison et al., 2015; Macgregor, 2015; Wadge et al., 2016) but Afar has more rapid melt extraction to the near surface (e.g. the Erta Ale lava lake, 2008 Alu-Dalafilla eruption and the 2005 Dabbahu dyking event). Afar is extending 3-4 times faster than the MER (Keir et al., 2013), and we would therefore expect higher rates of melt production beneath Afar (Rooney et al., 2005; Rooney, 2010). We do not observe a correlation between slow Vs and predicted total rates of melt production and volcanism. Instead we observe slow Vs in parts of the rift valley with the lowest surface expression of recent basaltic type volcanism, suggesting that time scales of melt storage plays an important role in controlling Vs. Petrological studies of the two regions find the most chemically evolved compositions are associated with volcanoes of the MER (Hutchison et al., 2018; Rooney et al., 2013). In Afar, the on-axis segments produce less evolved melts while at Erta Ale, the most advanced stage of rifting, there is little evidence for melt evolution and assimilation (Hutchison et al., 2018). Our observations of slow velocities in the MER is consistent with petrological constraints that the residence time of melts is longer during the earlier stages of rifting. Longer melt residence times would allow greater melt accumulation as more melt is added but not erupted and would heat the surrounding crust. Both effects would reduce seismic velocities.

Melt accumulation beneath the MER may also be aided by thicker crust and a narrow rift (Bastow et al., 2008; Debayle et al., 2001; Faccenna et al., 2008; Gallacher et al., 2016), coupled with significant changes in lithospheric structure which could act to focus melt beneath the rift (Dugda et al., 2005; Hammond et al., 2011; Stuart et al., 2006). We therefore propose 3-D melt focusing coupled with longer residence times of melt within the crust of the MER to explain the slowest velocities of our study.

3.7.2.4 The northwestern and southeastern plateaus

The plateaus display greater heterogeneity than the MER and Afar. The velocities are predominantly fast beneath the plateaus, typically around 3.65 ±0.05 km/s at 10 km depth and ∼3.95 ±0.07 km/s at 40 km depth (Figure 3.6 A-D and Figure 3.8 B “e” and “f”). The southeastern plateau has limited recent volcanism suggesting it has not been modified by melt. Therefore, the southeastern plateau may represent the background velocity of the region. Further evidence for limited melt is corroborated by Vp/Vs ratios of ∼1.78 and highly resistive crust (Hammond et al., 2011; Whaler and Hautot, 2006).

In contrast to the southeastern plateau, we observe localized regions with slow velocities of 3.25 ±0.05 km/s at 10 km going down to 3.65 ±0.07 km/s at 30 km depth beneath the northwestern plateau (Figure 3.6 A-C and Figure 3.8 B “d”). At the surface, “d” underlies the Choke and Guguftu shield volcanoes which last erupted 22 Ma (Kieffer et al., 2004; Pik et al., 1998, 1999), timescales over which melt would no longer be present due to cooling. One anomaly follows the trend of the border faults and known geothermal activity (Figure 3.6 A-D), suggesting fluids and geothermal circulation in the fault system may be responsible for the slow Vs anomalies. This was also observed by (Korostelev et al., 2015), who drew a link with geothermal activity and slow velocities.

The slow anomaly west of the border faults at “d” may have a similar origin. On either side of the flood basalts are northwest – southeast trending faults. On the southeastern plateau we have the Ogaden rift (Figure 3.1 B) and on the northwestern plateau are the Blue Nile and Atbara Rifts (Mège and Korme, 2004). It is likely that these failed rifts underlie the Ethiopian flood basalts and could produce similar geothermal systems to those of the border faults. Surface evidence of fumaroles and geothermal activity is present in this region (Keir et al., 2009a) particularly at the southeastern edge of lake Tana (Figure 3.6 A-D). These geothermal systems indicate that there are continuous intrusions beneath this region or ongoing conductive cooling leading to the release of volatiles. We therefore propose that slow velocities beneath the plateau at “d” are generated by geothermal systems with fluids migrating through large scale fault structures (Keir et al., 2009a). The slow velocity zones also correlate well with high conductivities from MT studies (Hautot et al., 2006; Whaler and Hautot, 2006) and perhaps link to geothermal activity at the border faults (Korostelev et al., 2015). In contrast, the slow velocities of 3.30 ±0.05 km/s beneath the Yemen plateau (Figure 3.6A-B and Figure 3.8 A) correlate well with the active Harras of Dhamar volcanic field (Korostelev et al., 2015).

3.7.2.5 Implications for magma plumbing systems during continental rifting

Our absolute shear velocity models provide evidence for more protracted melt storage in the crust during the earlier stages of rifting (e.g. the MER). Melt accumulation is particularly localized near the Moho but distributed spatially across a relatively broad region beneath the rift valley and surrounding plateaus. This contributes to the growing body of evidence that deep crustal magma complexes play an important role in the evolution of magma in continental rifts (Annen et al., 2006). Controlled source imaging of continental rifts (e.g. The Baikal rift (Thybo and Nielsen, 2009)) and magmatic passive margins (e.g. The North Atlantic (White et al., 2008)) suggest melt is primarily arranged as complexes of stacked sills. The accumulation of melt is aided by strong density contrasts of the higher rigidity continental crust overlying weaker mantle (Bradley, 1965; Kavanagh et al., 2006).

In Afar, we observe faster crustal seismic velocities mostly consistent with a crust rich in frozen mafic rock, denser than continental crust. The ascent of melt through the crust primarily relies on its high buoyancy relative to the mantle and crust (Harmon and Rychert, 2015; Sawyer, 1994). The time-accumulation of dense mafic intrusion during progressive rifting, coupled with ongoing crustal thinning likely aids melt ascent through the crust during continued continental breakup in contrast to the thicker crust of the Ethiopian plateau and MER. Such an interpretation satisfies our seismic images, as well as petrological constraints on magma residence times (Hutchison et al., 2018).

Our seismic images beneath the northwestern plateau suggest localized melt emplacement and related hydrothermal processes continuing outside of the rift valley to the present day. This interpretation is somewhat contrary to the widely held belief that all magmatism becomes localized to a rift valley during progressive rifting. New GPS constraints from Ethiopia showing the presence of ongoing extension of the plateau (Birhanu et al., 2016) provides a mechanism to explain recent magmatic processes here, and supports the view that extension coupled with magmatism may remain distributed later into the breakup process than previously believed.

3.8 Conclusions

We have generated a 3-D absolute shear wave velocity map for the crust and uppermost mantle of the northern EAR. This unified model allows direct comparisons of shear velocity between the MER, Afar and adjacent plateaus. We have used 170 seismic stations to produce 4820 cross correlations which have been stacked and inverted for phase and shear velocity on a 0.25° x 0.25° nodal grid. Shear velocities range from 3.20 – 4.10 km/s with the slowest average velocities within the MER (3.60 ±0.03 km/s) and fastest beneath the Danakil depression (3.83 ±0.04 km/s). The key findings of our study are:

1. Mantle velocities (3.60 – 4.10 km/s) are everywhere slower than the global average for a mantle peridotite composition and require moderate elevated temperatures combined with a fluid component and/or partial melt

2. Average shear velocities for the MER (3.60 ±0.03 km/s) are slower than Afar (3.83 ±0.04 km/s). Slow velocities in the MER vs Afar are interpreted as melt focusing from dramatic changes in lithospheric topography coupled with longer residence times and complex magmatic pathways within the crust. Faster velocities within Afar are attributed to solidified crustal intrusions and isolated areas of melt too small to be imaged in this study.

3. The Ethiopian plateau displays heterogeneity in crustal velocity structure (3.25 ±0.05 km/s at 10 km depth, to 3.87 ±0.07 km/s at 40 km depth at "d" and 3.65 ±0.05 km/s at 10 km depth, to 3.95 ±0.065 km/s at 40 km depth at "e"), suggesting a complex geological history and an inhomogeneous magma distribution during evolution. Slower crustal velocities near the border fault regions and pre-existing failed rifts are interpreted as geothermal systems within the faults beneath the Ethiopian flood basalts.

Acknowledgments, Samples, and Data

E.L.C is funded through NERC studentship NE/L002531/1. D.K. is supported by NERC Grant Number NE/L013932. C.A.R. and N.H. acknowledge funding from the Natural Environment Research Council (NE/M003507/1 and NE/K010654/1) and the European Research Council (GA 638665). All data needed to generate these models are freely available from The IRIS Data Management Center (IRISDMC): http://service.iris.edu/fdsnws/dataselect/1/. IRIS Data Services are funded through the Seismological Facilities for the Advancement of Geoscience and EarthScope (SAGE) Proposal of the National Science Foundation under Cooperative Agreement EAR-126168. We thank SEIS-UK for use of the instruments and their computing facilities. The facilities of SEIS-UK are supported by the Natural Environment Research Council (NERC) under Agreement R8/H10/64.F. Some figures were made using the Generic Mapping Tools (Wessel and Smith, 2013).

For supplementary material see Appendix A.

Chapter 4

A joint inversion of Rayleigh waves from ambient noise tomography and teleseisms to image melt and seismic structure in the northern East African Rift

This chapter focusses on a joint inversion between the ambient noise discussed in the previous chapter and teleseismic Rayleigh waves updated from the work of Gallacher et al. (2016). The main reasons for performing a joint inversion were to provide better resolution at lower crustal and uppermost mantle depths (~35 - 60 km depth) and increased depth resolution at mantle depths by incorporating the ambient noise. In addition, this work produced a single absolute shear wave velocity model for the full northern East African Rift (EAR) allowing comparisons between regions at varying stages of rifting at depths from 10 - 210 km. Below is the paper submitted to Journal of Geophysical Research: Solid Earth, which is currently under review.

Chambers, E. L., Harmon, N., Keir, D., Rychert, C. A., Gallacher, R. A joint inversion of Rayleigh waves, from teleseisms and ambient noise tomography, to image the northern East African Rift

Key Points:

- A fast lid is imaged beneath the rift flanks, while in the rift we find slow velocities likely associated with shallow partial melt.
- Slow asthenospheric velocity anomalies are segmented and exist in the rift and beneath normal lithosphere unaffected by rifting.
- Asthenospheric melt anomalies are not located beneath the slowest crustal anomalies, suggesting melt is ephemeral or travels laterally.

4.1 Abstract

Within the northern East African Rift, multiple models have been proposed to understand the evolution of lithospheric stretching and magmatism. Comprehensive seismic imaging of the region can aid a better understanding of the process. Although seismic imaging has been performed in different areas of the rift, variations in method, resolution, and scale among the methods make direct comparisons on and off rift challenging. Here we jointly invert surface waves from ambient noise and teleseismic Rayleigh waves to obtain absolute shear velocity maps from 10–210 km depth, enabling us to analyse variations in crustal and upper mantle velocity structure with progressive rift evolution. At crustal depths, velocities are slowest beneath the melt-rich Main Ethiopian Rift, and the off rift Ethiopian Plateau ($<3.00 - 3.75 \pm 0.04$ km/s, 10–40 km depth) suggesting ongoing magmatic emplacement within these locations. The transition from a fast lid to a low velocity zone, interpreted as the lithosphere-asthenosphere-boundary, is observed at 60–80 km depth off rift (>0.1 km/s faster than surroundings). The fast lid is obscured beneath the rift, suggesting melt is infiltrating the lithosphere. At asthenospheric depths slow velocity anomalies ($<4.15 \pm 0.04$ km/s at 80–130 km depth) are not directly beneath melt-rich crustal regions, suggesting mantle melt is ephemeral and/or melt migrates laterally during ascent. Furthermore, the anomalies are segmented along the rift, existing in areas that have not undergone significant crustal thinning (segments ~110x80 km wide, ~60–130 km deep), suggesting segmented melt supply starts prior to significant plate deformation.

4.2 Introduction

Plate extension is commonly associated with decompression melting of the asthenosphere (Foucher et al., 1982; Rychert et al., 2012; Wang et al., 2009), and typically focused beneath the extending rift (e.g. Buck, 2006). Most studies attempt to address processes governing production and the role of melt in localising extension to the rift (e.g. Ebinger and Casey, 2001; Kendall et al., 2005; Rychert et al., 2012). Within the northern East African Rift (EAR), magma assisted rifting is considered the dominant rifting mechanism (Ebinger and Casey, 2001; Ebinger and Sleep, 1998) and is also where we can observe the initial stages of rifting through to incipient seafloor spreading (Ebinger and Casey, 2001; Furman et al., 2006). Importantly, this is all occurring subaerially providing a unique opportunity to study how rifting develops through progressive rift sector development (Barberi et al., 1972). However, a full understanding of the dynamics on and off rift, including melt generation and migration across the region, has yet to be established. While the northern EAR has been extensively studied, the magmatic and tectonic processes occurring beneath the rift flanks, such as the Ethiopian Plateau, have yet to be comprehensively imaged seismically (Chambers et al., 2019; Keranen et al., 2009). The flanks of the rift provide key information about the structure prior to rifting, which allows us to understand how deformation has proceeded to the present day. By better imaging magmatically rifting areas, the location of melt generation and migration across the region can be better understood, including off rift.

Seismic tomography provides constraints on the average properties of the Earth over large swaths of the world. Studies of the northern EAR have imaged velocity variations within the rift and attributed changes to the presence of melt within the crust and mantle by using methods including Ambient Noise Tomography (ANT) (Chambers et al., 2019; Kim et al., 2012; Korostelev et al., 2015), teleseismic Rayleigh wave tomography (Gallacher et al., 2016), Pn tomography (Stork et al., 2013) and body wave tomography (Bastow et al., 2005, 2008). There are now multiple velocity models for various sections of the region, which are not necessarily directly comparable, for instance on and off rift, due to variations in methodology, resolution, and scale. These comparisons are important for interpreting melt generation and migration processes, and the spatial variations in plate structure. To address this, we create a comprehensive absolute velocity model of the region, to determine whether melt is confined to the rift and distinguish variations in plate structure. The model is generated by performing a joint inversion between Rayleigh waves from ambient noise and teleseisms to generate absolute shear wave velocity maps from 10 - 210 km depth. Laterally we use data from seismometers present from 1999 – 2017 in Ethiopia, Yemen, Djibouti and Eritrea allowing coverage of regions unaffected by rifting (e.g. west of the Ethiopian Plateau) to areas at incipient seafloor spreading (e.g. Afar).

4.3 Geological Background and Previous Tomographic Studies

Precambrian basement underlies much of Ethiopia and the surrounding area, and formed during the Neoproterozoic Pan-African orogeny (Mège and Korme, 2004). Volcanism initiated 45 Ma and continues to the present day (Barnie et al., 2016; Rooney et al., 2014; Siegburg et al., 2018), with the largest event, the emplacement of the Ethiopian flood basalt province, occurring 31 – 29 Ma (Hofmann et al., 1997; Rooney et al., 2012b; Ukstins et al., 2002). The Ethiopian Plateau continued to have sporadic volcanism with alkali shield volcanoes emplaced above the flood basalts (e.g. Choke and Guguftu 22 Ma (Kieffer et al., 2004)). Volcanic activity today is largely focused within magmatic segments at the rift axis (Ebinger and Casey, 2001; Wolfenden et al., 2004), but does occur off rift south of Lake Tana (Keranen and Klemperer, 2008; Kieffer et al., 2004), at Nabro in Afar (Goitom et al., 2015) and in the Yerer-Tullu Wellel Volcanotectonic Lineament (YTVL), a 700 km long, 80 km wide corridor of faults and volcanoes (Rooney et al., 2014) (Figure 4.1). The volcanic segments in Afar and the MER are the main focus of present day extension, while prior to the Pleistocene, extension was focussed at the border faults (Ebinger and Casey, 2001; Wolfenden et al., 2004, 2005).

Rifting of the Red Sea and Gulf of Aden rifts initiated approximately coeval with the main flood basalt emplacement (Bosworth et al., 2005; Hofmann et al., 1997; Pik et al., 1998; Wolfenden et al., 2004) while the MER started rifting later at 20 Ma in the south, and 11 Ma in the north (Kazmin et al., 1978; Wolfenden et al., 2004). Extension rates are variable with full spreading rates of 18 mm/yr. for the Red Sea Rift (McClusky et al., 2010; Vigny et al., 2006), 16 mm/yr. for the Gulf of Aden Rift (Jestin et al., 1994; Vigny et al., 2006), and ∼6 mm/yr. for the MER (Birhanu et al., 2016; Jestin et al., 1994; Saria et al., 2014) (Figure 4.1b). The Tendaho Goba'ad discontinuity (TGD) separates the east-west directed extension in the northern-most MER from the northeast-southwest directed extension in Afar (Tesfaye et al., 2003).

Crustal thickness has been modified by rifting and volcanism, with the western edge of the Ethiopian Plateau and Somalian Plateau considered to be representative of pre-rifted unmodified crust which are 30 – 40 km thick (Mackenzie et al., 2005; Ogden et al., 2019; Stuart et al., 2006). The western edge of the Ethiopian Plateau is 30 – 35 km thick and considered the area least modified by the flood basalt emplacement (Ogden et al., 2019). The Somalian Plateau had minor modification during the flood basalt emplacement on the western margin, but is otherwise unmodified crust that is 35 - 40 km thick (Mackenzie et al., 2005; Stuart et al., 2006). In contrast, the eastern part of the Ethiopian Plateau has been significantly affected by lower crustal intrusions and has thicker crust ranging from 40 - 45 km thick (Mackenzie et al., 2005; Stuart et al., 2006; Ogden et al., 2019). The crust beneath the rift is predominantly thinner than the plateaus, with the exception of the southern MER, where crustal thickness ranges from 30 – 38 km with evidence for lower crustal intrusions beneath the thickest crust (Hammond et al., 2011; Maguire et al., 2006; Stuart et al., 2006). In Afar, crustal thickness ranges from <16 - 26 km, with the Danakil depression having the thinnest crust of the subaerial rift system (Dugda et al., 2005; Hammond et al., 2011; Lavayssière et al., 2018).

Lithosphere-asthenosphere-boundary (LAB) depths have been interpreted from S-to-P receiver functions, surface wave tomography and a joint inversion between Rayleigh wave velocities and receiver functions. The LAB is thought to lie at 60 - 80 km depth beneath the Ethiopian Plateau; whereas within the rift the LAB is much shallower, with seismic imaging suggesting that the mantle lithosphere is either very thin or non-existent (Dugda et al., 2007; Lavayssière et al., 2018; Rychert et al., 2012).

Previous tomographic studies suggest the upper mantle beneath Ethiopia is slower than expected for a mantle peridotite (Vs = 3.80 – 4.25 km/s from the uppermost mantle to 400 km depth) (Bastow et al., 2005, 2008; Chambers et al., 2019; Fishwick, 2010; Gallacher et al., 2016). This is significantly slower than those observed at similar depths beneath continental interiors, where shear velocities are typically >4.45 km (Kennett et al., 1995). Elevated mantle temperatures of 100 - 170°C supported by petrological modelling (Armitage et al., 2015; Ferguson et al., 2013; Rooney et al., 2012a) are also present beneath Ethiopia and can account for the velocity variations between tomographic models and ak135 in areas off rift (e.g. Gallacher et al., 2016). Regional studies find significantly slow velocities beneath the rift valley, which require a component of partial melt after accounting for variations in temperature and composition (Bastow et al., 2005; Chambers et al., 2019; Gallacher et al., 2016; Hammond et al., 2013).

At crustal depths within the rift, P-wave studies find fast velocities, interpreted as solidified magmatic intrusions (Mackenzie et al., 2005; Maguire et al., 2006). S-wave velocity studies, which are more sensitive to fluids, observe slow velocities in the rift valley (Chambers et al., 2019; Kim et al., 2012; Korostelev et al., 2015) and consequently Vp/Vs ratios for the crust are high, and in places >2.0 (Hammond et al., 2011). This indicates fluids, most likely melt, are present beneath the rift (Dugda et al., 2005; Hammond et al., 2011; Ogden et al., 2019; Stuart et al., 2006). Magnetotelluric surveys have imaged high conductivity bodies within the crust beneath the MER and Afar which provide further evidence for ongoing magmatic emplacement beneath the rift (Samrock et al., 2018; Whaler and Hautot, 2006). Off rift, there is similar evidence for ongoing lower crustal intrusions and magmatic activity. S-wave studies beneath parts of the Ethiopian Plateau, YTVL and Nabro find slow velocities (Chambers et al., 2019; Kim et al., 2012) coupled with high conductivity bodies beneath the YTVL (Didana et al., 2014; Samrock et al., 2015, 2018; Whaler and Hautot, 2006). In addition, Nabro volcano in Eritrea erupted in 2011 (Goitom et al., 2015).

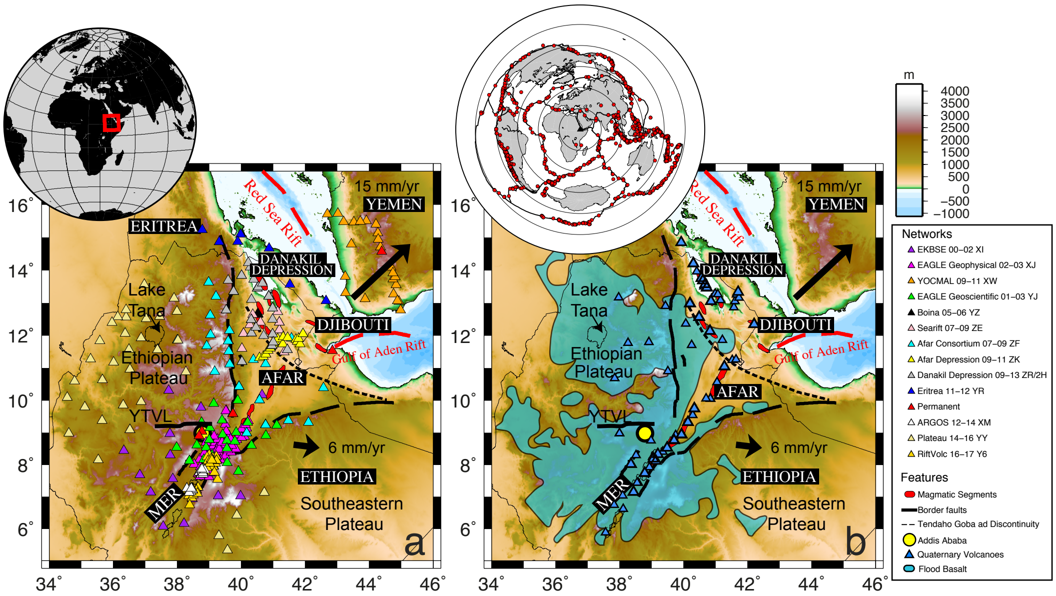

FIGURE 4.1: (a) Seismic Station map of the northern East African Rift. Thick black lines show border faults, red polygons magmatic segments, and dashed lines the Tendaho-Goba'ad discontinuity (TGD). Stations are triangles coloured to their project deployment with white (ARGOS 12-14), light yellow (Plateau 14-16) and Gold (RiftVolc 16-17) are networks not used for ambient noise prior to this study with grey (Danakil depression 09-13) newly used from 11-13. Addis Ababa is marked by yellow circle. (b) Geological map. Volcanoes are represented by blue triangles and magmatic segments red polygons. Flood basalt provinces are shown in blue. Inset figure red dots show locations of the 1053 earthquakes used in this study.

4.4 Methods

4.4.1 Ambient Noise Phase Velocity

We used data from continuous vertical component seismometers recorded by 13 temporary networks and 5 permanent stations (Figure 4.1b) between 1999 and 2017. We included 58 stations from 3 networks (ARGOS XM 2012 - 2014, Plateau YY 2014 - 2016 and Afar0911 2H 2012 – 2013), in addition to those used in the Chambers et al. (2019) and Gallacher et al. (2016) studies (Figure 4.1a). We did not include the RiftVolc Y6 2016 – 2017 network for the ambient noise due to short deployment duration and close proximity of stations but did include the network for the teleseismic data adding a further 41 stations. A bandpass filter of 0.005 – 0.4 Hz was applied to the data and was pre-processed following the methods of Bensen et al. (2007). We then followed the method for ambient noise cross correlations and phase velocity inversion as described in Chambers et al. (2019), and references therein, and Harmon et al. (2007). This resulted in 6716 cross correlations and well resolved phase velocities between 8 - 26 s. We inverted for the phase velocity map at each period on a 0.25° x 0.25° nodal grid (Figure 4.2) using the method of Harmon et al. (2013) and use our average phase velocity at each period as the starting model. The phase velocity inversion used 2-D finite frequency kernels (Nishida, 2011; Tromp et al., 2010) and an iterative damped least squares approach (Tarantola and Valette, 1982). We only inverted phase data for noise correlation functions with interstation distances greater than twice the wavelength and with a smoothing length of 40 km.

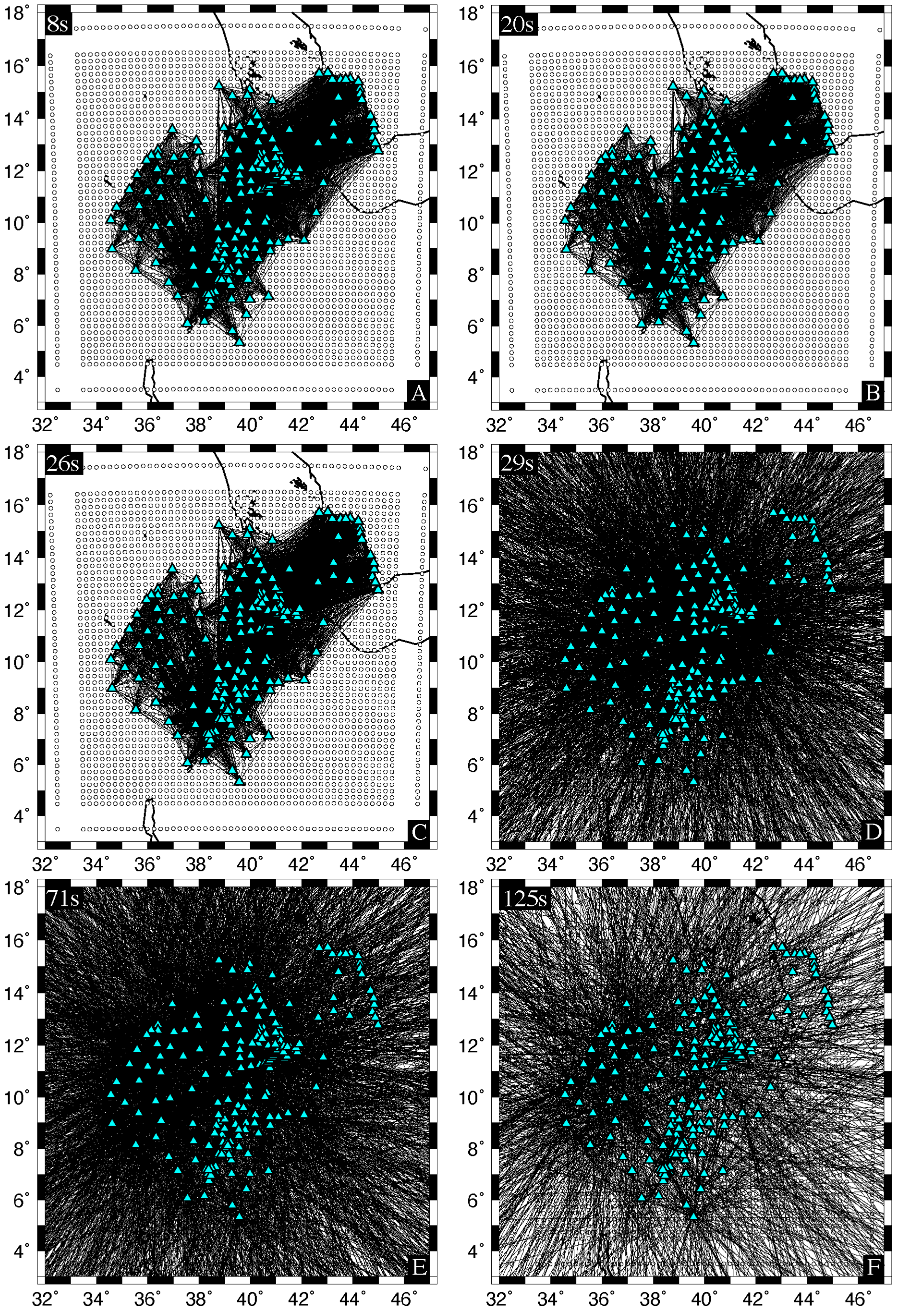

FIGURE 4.2: Nodal grid at 0.25 ° spacing with ray paths for ambient noise (a – c, 8, 20 and 26s) and teleseisms (d – f, 29, 71 and 125s) overlain as black lines. Blue triangles indicate stations.

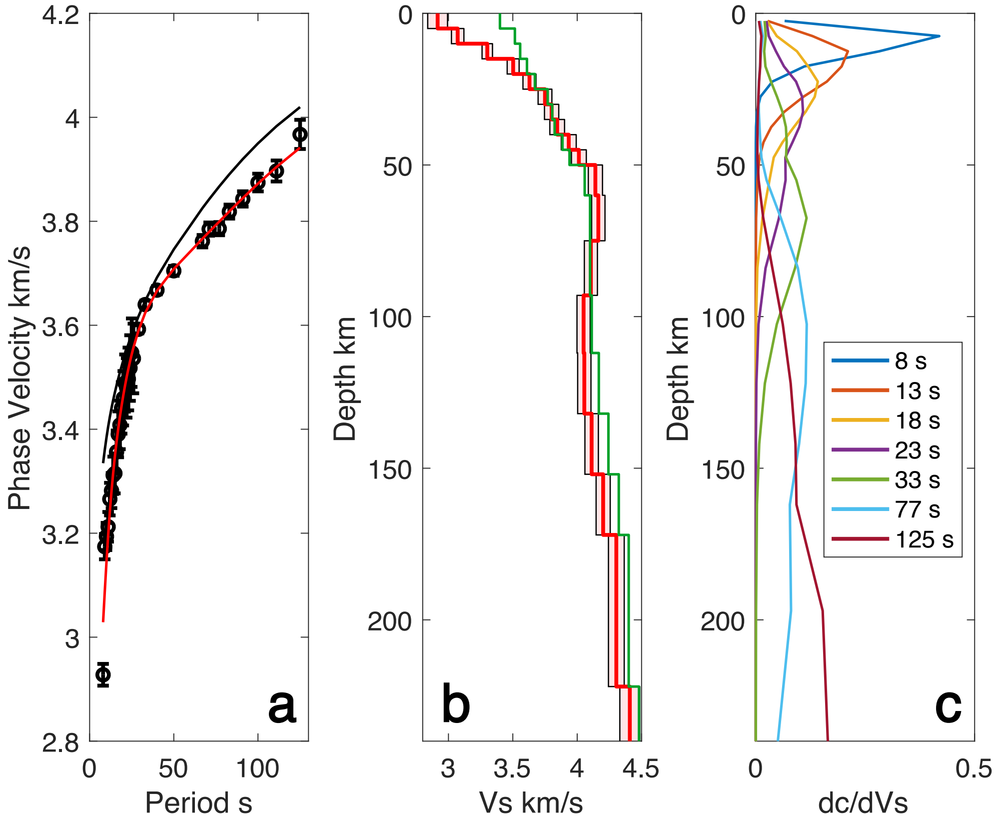

Figure 4.3: (a) Average 1-D phase velocity for the study area with 3σ error bars (circles), starting model (black line) with our best fit shear velocity model dispersion overlain (red line). (b) Best fit shear velocity model for the study area (red line) and formal 2σ error bounds (thin black lines and shaded area). Green line is initial starting model using the average shear velocity from Chambers et al. (2019) and Gallacher et al. (2016). (c) Sensitivity kernels for Rayleigh waves at selected periods.

4.4.2 Teleseismic Rayleigh wave phase velocity

4.4.2.1 1-D phase velocity inversion.

To solve for phase velocity, we first inverted amplitude and phase information from earthquakes >5.5 magnitude and epicentral distances of 25 - 150° (1053 events, Figure 4.1 inset). We determined the average dispersion curve for the area using a 1-D version of the two-plane wave inversion method (Forsyth and Li, 2005). The inversion was completed in two stages, with the first stage utilising a simulated annealing method to fit the two plane wave parameters, while trying a range of starting phase velocities for the model ranging from 3.00 – 4.40 km/s (Press et al., 1992). This ensured a global minimum was found for input into the second stage which utilised a standard linearised inversion (Tarantola and Valette, 1982) (Figure 4.3).

4.4.2.2 2-D phase velocity inversion.

For the 2-D phase velocity maps we used prior knowledge of the average velocity structure using a combination of the average phase velocity derived from ambient noise from Chambers et al.

(2019) from 8 - 26 s and the average model of Rayleigh wave tomography from Gallacher et al. (2016) for periods 29 – 125 s as our starting model at each point across the map. Similar to the procedure described for ambient noise, we first inverted for the phase velocity map using the method of Harmon et al. (2013) at each period and each node on a 0.25° x 0.25° nodal grid with the outermost row and column spaced at 1° to absorb velocity heterogeneities outside the region of interest (Figure 4.2). The phase velocity inversion used 2-D finite frequency kernels (Forsyth and Li, 2005; Nishida, 2011; Tromp et al., 2010) and an iterative damped least squares approach (Tarantola and Valette, 1982). The starting model was the average phase velocity at each period. Any event >0.05 out of phase was removed and the inversion was repeated using the output phase velocity maps as input for the following iteration. For more details on the teleseismic Rayleigh wave phase velocity methods we refer the reader to Gallacher et al. (2016).

4.4.3 Joint inversion for shear velocities

The phase velocity maps from the ambient noise and teleseismic results were combined for 8 - 26s and 29 - 125s respectively (Figure 4.4). We inverted each pixel of the phase velocity maps across all periods for a 1-D shear velocity structure as a function of depth. We assigned a nominal a priori standard error for each node of 0.2 km/s and fix the Vp/Vs ratio to 1.8, which is the crustal average from receiver function analyses (Hammond et al., 2011; Stuart et al., 2006) and also a typical mantle value (Dziewonski and Anderson, 1981). Variations in the choice in Vp/Vs produced results that are within error of each other. As our starting model, we used the best fit shear velocity model from the 1-D dispersion curve as the starting model (Figure 4.3). For the shear velocity inversion, we used a damped least squares approach (Tarantola and Valette, 1982) and parameterise the shear velocity at every 5 km vertically with 0.1° x 0.1° pixel size. We calculated the partial derivatives that relate variations in shear velocity to changes in phase velocity using DISPER80 (Saito, 1988). Although our shear velocity models are discretised at 5 km intervals in depth, we interpolated the velocity structure to 1 km depth for presentation purposes using a linear interpolation.

4.4.4 Errors and resolution

In the phase velocity maps the diagonals of the formal resolution matrix have maximum values of 0.36 at our best resolved period of 10 s and a formal resolution of 0.48 (Figure 4.5). We derive the resolution from the sensitivity kernels of the ray paths in Figure 4.2 for 8, 20, 26, 29, 71 and 125 s period. Our formal resolution indicates we require at least 3 node spacings to produce an independent piece of information about velocity structure, in other words we can resolve 50 – 100 km laterally. Therefore, we limit our discussion to features >100 km. In addition, we produce checkerboard tests at 1 spacings at 8 - 125 s period and at 1.5 and 2 for periods >29 s (Figure 4.6 and Figure 4.7). The checkerboard tests indicate we can resolve anomalies at 1 for 8 – 71 s period and 1.5 at all periods. In areas of sparser ray coverage such as the eastern part of Afar, the Red Sea, and Gulf of Aden we have poorer resolution and there is northeast-southwest smearing of the checkerboards and there is northwest-southeast smearing in Yemen. Consequently, we do not interpret these areas. In addition, we mask results outside the standard error contour of 0.07 km/s, the approximate contour of the 2σ error, from the linearised phase velocity inversion.

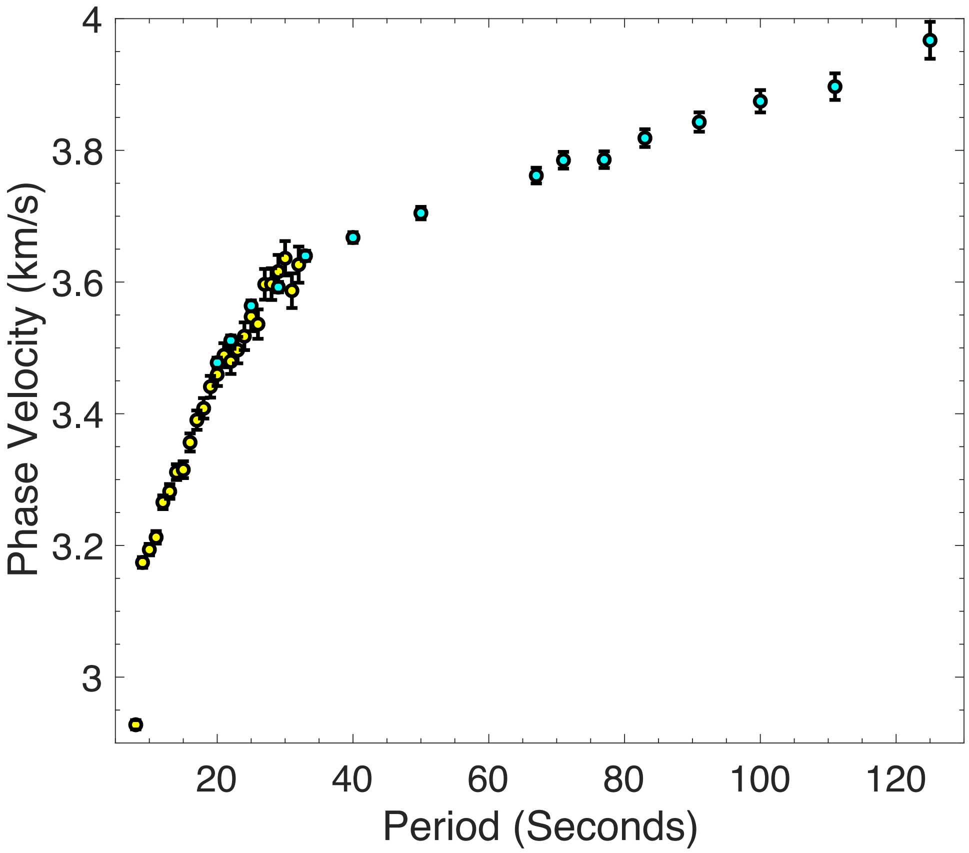

Figure 4.4: Average velocities for ambient noise (Yellow) and teleseisms (Blue) from Chambers et al. 2019 and Gallacher et al. 2016 respectively. Error bars are 3 x standard error.

To examine the vertical resolution, we plot the Backus–Gilbert resolving kernels (Backus and Gilbert, 1970) for a range of model depths (Figure B.1). These kernels show the recovery of a spike function at the target depth and are based on the formal resolution matrix described above. This shows that shear velocities we be averages over ± 10 km at 22 km depth to ± 45 km at 122 km depth. These values are obtained for the best-resolved part of the kernel, which is defined as 0.15 for 20 km, and 0.1 for 122 km.

4.5 Results

4.5.1 1-D dispersion curves and shear velocity model

Average 1-D dispersion curves measured from the ambient noise and teleseismic data are shown in Figure 4.3. The phase velocities range from 2.93 ± 0.02 km/s at 8s to 3.97 ± 0.03 km/s at 125s (Figure 4.3 and Figure 4.8). Where the phase velocities from the ambient noise and teleseisms overlap (20 – 33 s) (Figure 4.4), the velocities are similar to one another and within the standard error. The shear velocity structure is displayed in Figure 4.3b with shear velocities ranging from 3.10 ± 0.02 km/s at 5 km depth to 4.42 ± 0.03 km/s at 150 km depth. The average 1-D shear velocities are slower than the input model (green line) at most depths except from 40 - 80 km depth. In Figure 4.3c we present the depth sensitivity kernels for the shear velocity inversion

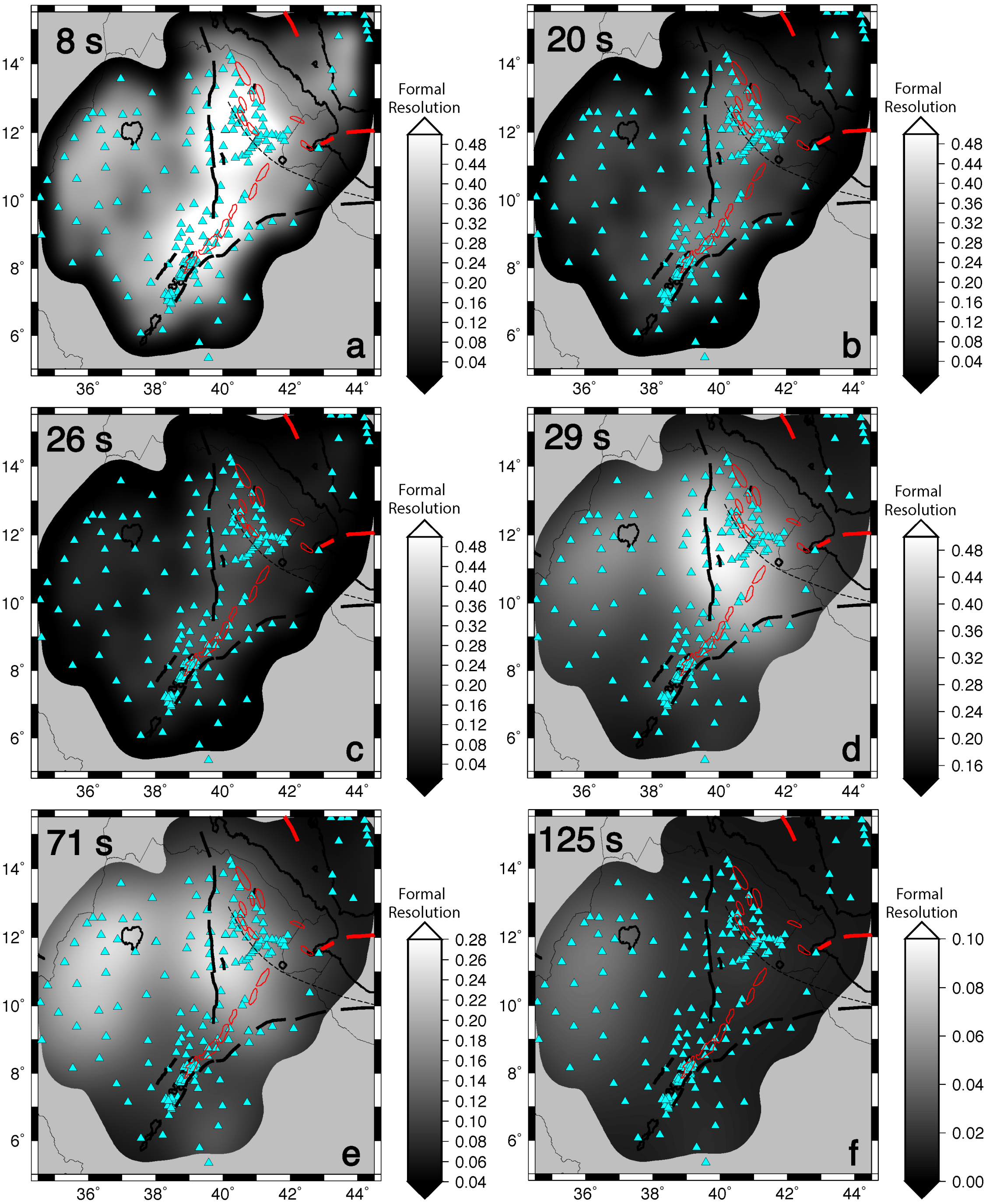

FIGURE 4.5: Formal resolution maps for 8, 20, 26, 29, 71 and 125s (a-f respectively). Blue triangles indicate station locations, thick black lines show border faults, red polygons magmatic segments, and dashed lines the Tendaho-Goba'ad discontinuity (TGD). Results are cropped to the 2σ error contour.

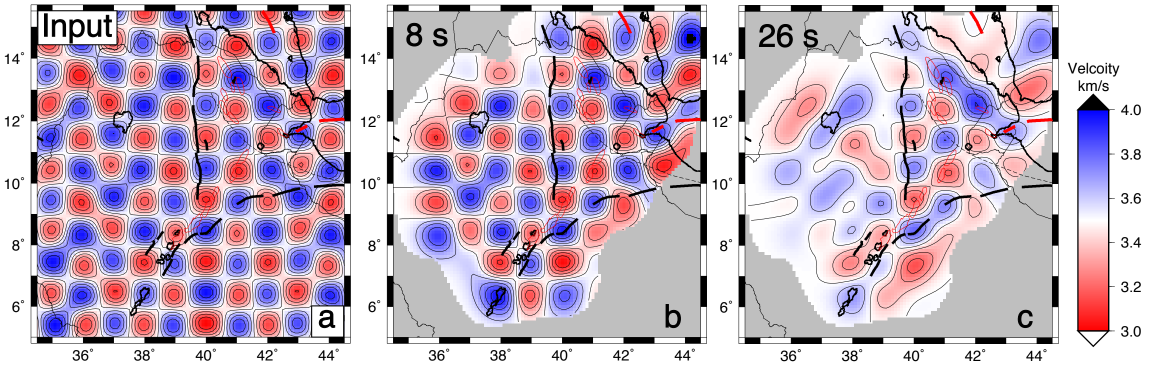

Figure 4.6: Checkerboard tests at 1° × 1° for ambient noise at the limits of our resolvable periods. Initial model shown in (a) with (b) and (c) showing the resultant output model at 8 and 26 s, the limits of our study. Results are cropped to the 2σ standard error contour. Thick black lines show border faults, red polygons magmatic segments, and dashed lines the Tendaho-Goba'ad discontinuity (TGD).

for 8, 13, 18, 23, 33, 77 and 125 s period, which indicate the depths of peak sensitivity at each period. We interpret to 210 km depth, the limit of our sensitivity but show average plots from 100 – 200 km depth due to the broadly similar velocity structure of our results at these depths.

4.5.2 2-D Phase Velocities

We generate phase velocity maps from 8 – 125 s (Figure 4.8) and observe velocity variations that correlate with geologic and tectonic features. Phase velocities are more variable at shorter periods ranging from 2.85 – 3.45 ±0.04 km/s at 8 s becoming less laterally variable at 125 s period (3.85 – 3.95 ±0.06 km/s).

Within the rift system, the MER is the slowest region of our study for all periods. We observe minimum velocities ranging from 2.90 ±0.03 km/s at 8 s to 3.85 ±0.04 km/s at 125 s period. Beneath Afar, velocities are ~0.20 km/s faster than the MER at all periods. Phase velocity ranges from 3.15 ±0.03 km/s at 8 s to 3.90 ±0.04 km/s at 125 s period. Within the rifts, slow velocities are not laterally continuous and at periods <71 s display segmentation. The anomalies are ~100 km in length and show good correlation with quaternary volcanism.

The velocity structure on the Ethiopian Plateau is variable exhibiting, both high and low velocity regions across the period range of interest. The eastern part of the Ethiopian Plateau is slow at short periods (from 8 to 26 s) with velocities of 3.00 ±0.04 km/s at 8 s to 3.50 ±0.05 km/s at 26 s period. The two areas of slow velocity connect at 20 to 26 s period along the western border fault in addition to the northwest – southeast direction from the rift into the Ethiopian Plateau. At longer periods (>29 s period), phase velocities beneath the eastern part of the Ethiopian Plateau are similar to background phase velocity values (~3.80 – 3.90 ±0.05 km/s). In contrast, the western part of the Ethiopian Plateau is the fastest area of our study at all periods with phase velocities of 3.35 ±0.04 km/s at 8 s period increasing to 3.92 ±0.05 km/s at 125 s depth.

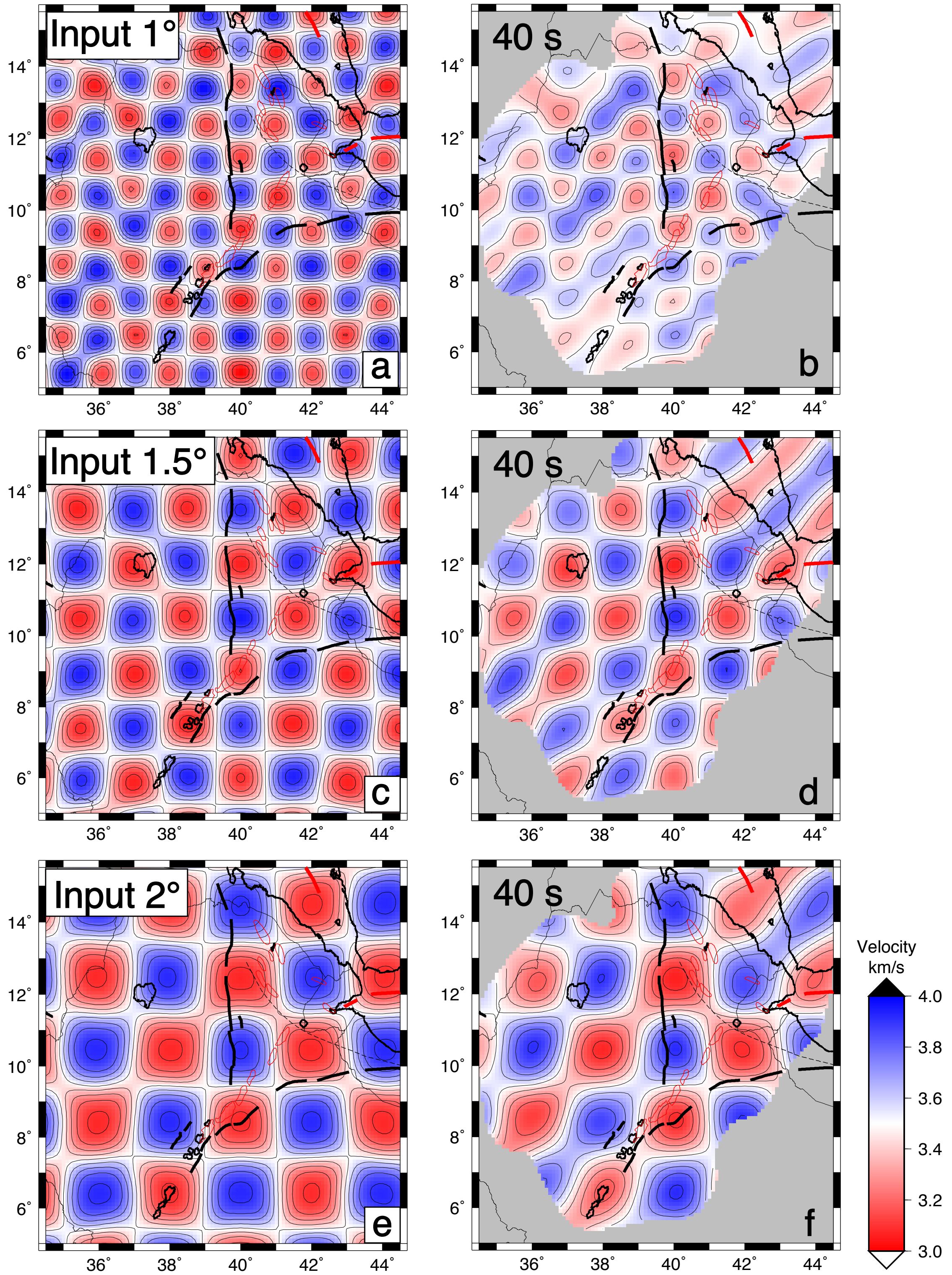

Figure 4.7: Checkerboard tests at 1° × 1°, 1.5° × 1.5° and 2° × 2° for teleseismic phase velocities at 40 s, our best resolved period. Initial model shown in (a), (c) and (e) with (b), (d) and (f) the resultant output model. Results are cropped to the 2σ standard error contour of the ambient noise. Thick black lines show border faults, red polygons magmatic segments, and dashed lines the Tendaho-Goba'ad discontinuity (TGD).

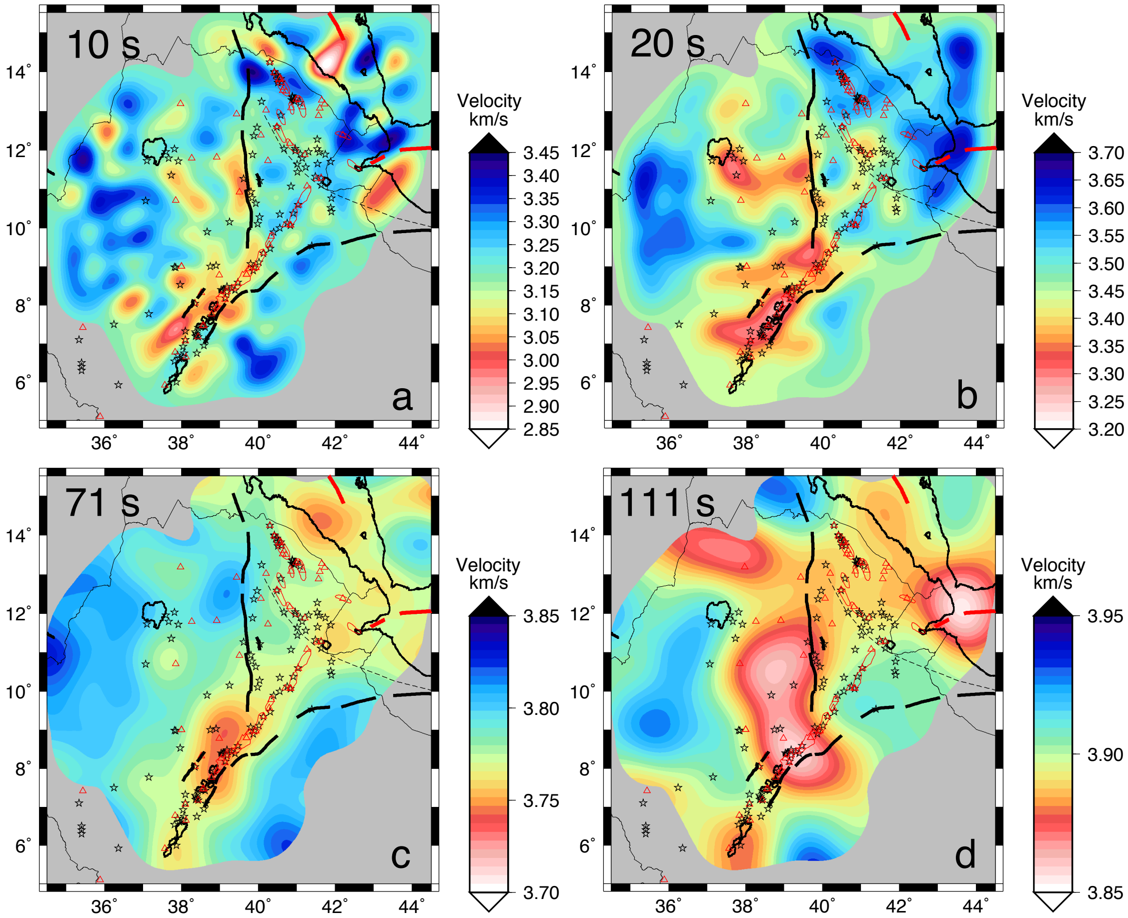

FIGURE 4.8: Phase velocity maps resulting from tomographic inversion of ambient noise dispersion data at 10 and 20s (a-b) and teleseisms 71 and 111s (c-d respectively). Models have been cropped to the 2σ standard error contour. Red indicates slower velocities and blue faster velocities. thick black lines indicate border faults, red polygons magmatic segments, dashed lines the Tendaho-Goba'ad discontinuity (TGD), red triangles volcanoes, and black stars geothermal activity.

4.5.3 2-D and 3-D Shear Velocities

At lithospheric depths (10 - 80 km), we observe strong lateral variations in shear velocity, by up to 0.85 km/s across our study region, which likely reflect a combination of significant changes in crustal thickness and variability in mantle structure. Figure 4.9 and Figure 4.10 show depth slices and cross-sections through the shear velocity model, respectively. The slowest velocities in the region are beneath the MER. For instance, at crustal depths (10 km) we find Vs = 3.00 ± 0.03 km/s and at mantle depths (~60 km) we find Vs = 4.05 ± 0.03 km/s at 60 km depth (Figure 4.9a - c). In profile A – A' (Figure 4.10a) south of the MER, there is a fast lid visible between 37 – 39° E Longitude at 60 – 80 km depth. This fast lid is intermittently visible within the rift before becoming more prevalent near the Arabian Peninsula.

At 20 – 40 km depth there is a slow velocity region centred ~100 km southeast of Lake Tana beneath the eastern part of the Ethiopian Plateau (3.10 – 3.85 ± 0.04 km/s at depths of 10 to 40 km respectively) and another anomaly ~100 km east of this anomaly centred beneath the border fault region. These anomalies diminish by 60 km depth (Figure 4.9c).

The western Ethiopian Plateau is one of the fastest regions at 20 – 40 km depth with velocities >3.8 km/s at 20 km and >4.15 km/s at 40 km (± 0.04 km/s), but is close to the average velocity across the region at 60 km. Profile B-B' (Figure 4.10b Profile B-B') shows there is a high velocity lid (velocity >4.15 km/s), from 60 - 80 km depth east of the rift (<39° E Longitude), and to the west of the rift (>40° E Longitude). We note that this study is the first to obtain shear wave velocities this far west on the Ethiopian Plateau due to the addition of recent seismic networks (Figure 4.1).

Afar has the some of the fastest velocities in the region at 20 km depth at ∼3.80 km/s, which likely reflects the thinner crust in this region compared to the Plateau. At 40 - 60 km depth the Afar region is characterised by several punctuated low velocity regions with velocities <3.9 km/s, some of which are coincident with regions of active hydrothermal sites (stars in Figure 4.9) or recent volcanism (red polygons in Figure 4.9). Specifically, beneath the magmatic segments and along the TGD (shown in Figure 4.1 as red polygons and dashed line respectively) the velocities are ∼0.2 km/s slower than the rest of Afar at all lithospheric depths.

At asthenospheric depths, >80 km, we also observe several punctuated slow velocity regions. Specifically, in the 100 - 200 km depth range, the region beneath the MER is the slowest in the region with velocities <4.15 km/s (Figure 4.9d). The slow velocity anomaly is not centred beneath the rift, but is offset towards the west, extending off rift towards Lake Tana. There are two other slow velocity regions with velocities <4.15 km/s located near the Red Sea and the Gulf of Aden. Within Afar, in this depth range, the slow velocities are more muted.

The slow velocity anomalies within the rift appear to systematically extend to shallower depths going from the MER northwards. Profile A-A' along the MER rift axis (Figure 4.10a), extending into Afar shows the relationship between the slow velocity anomalies at depth. Near the MER, the slow velocities are visible beneath the fast lid, extending from 85 - 130 km depth using the 4.05 km/s contour. Going northwards, the slow velocity anomalies occur at shallower depths going to 75 and then to 65 km depth beneath Afar using the depth to the 4.05 km/s velocity contour. The base of the anomalies appears fairly constant at ∼130 km depth. There does not appear to be much variation in structure at greater depths in our models.

The strongest anomalies at crustal depths in the MER and southeast of Lake Tana are displaced from the strongest anomalies in the asthenosphere, while in Afar the anomalies in the asthenosphere are close to regions of geologically recent volcanism. In the MER the slow velocities at 20 km depth are located ∼100 km southwest of the lowest velocities in the asthenosphere. Similarly, the 20 - 40 km depth anomalies near Lake Tana are located ∼200 km away from the slowest velocities in the asthenosphere, nearer the MER. Beneath Afar, the slow velocity regions are generally located beneath the locations of active hydrothermal sites (stars Figure 4.9) and recent volcanoes (red triangles Figure 4.9).

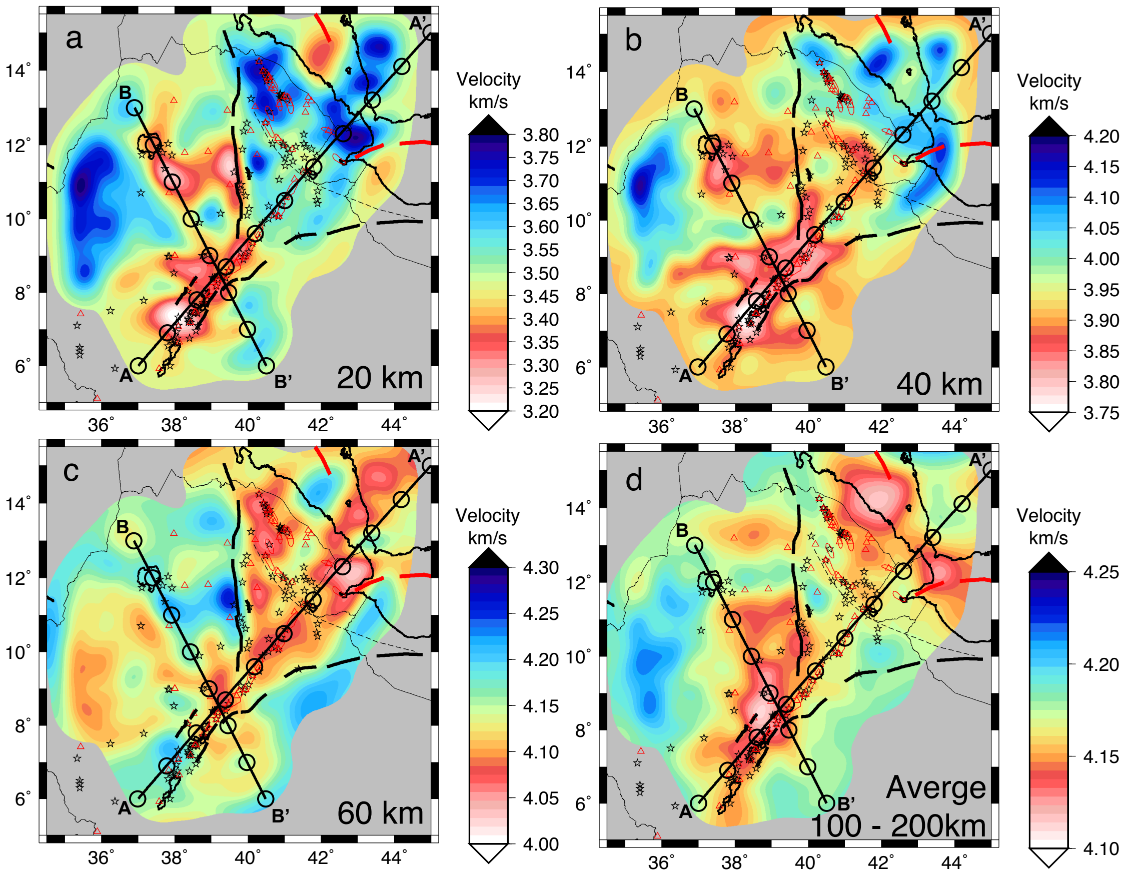

FIGURE 4.9: Interpolated absolute Shear wave velocity at 20, 40, 60 and averaged slice from 100 – 200 km depth labelled a – d respectively. Models have been cropped to the standard error contour. Red indicates slower velocities and blue faster velocities. Thick black lines indicate border faults. 2 profiles with rings are the cross-section locations for Figure 4.10. Red polygons indicate magmatic segments, red triangles volcanoes, and black stars geothermal activity.

4.6 Interpretation

4.6.1 Crustal Structure

At shallow depths (10 - 40 km) we observe the largest range in shear velocity which can be attributed to changes in crustal thickness. We compare our shear velocity structure to previous estimates of crustal thickness from receiver function analysis and find general good agreement between the depth of the Moho with the depth to the 3.60 – 3.75 km/s velocity contour (Dugda et al., 2005; Hammond et al., 2011; Lavayssière et al., 2018; Ogden et al., 2019; Stuart et al., 2006) (Figure 4.10). Specifically, we observe crustal thinning in Afar to thicknesses of <20 km (based on the 3.60 km/s contour). Crustal thickness beneath the MER and Ethiopian Plateau are 30 - 40 km, indicating limited crustal thinning beneath the MER particularly at the southern end. The faster velocities in Afar at 20 – 40 km depth are consistent with slower than average mantle velocities (3.80 – 4.05 ±0.02 km/s) constrained in previous studies (e.g. Bastow et al., 2008; Gallacher et al., 2016).

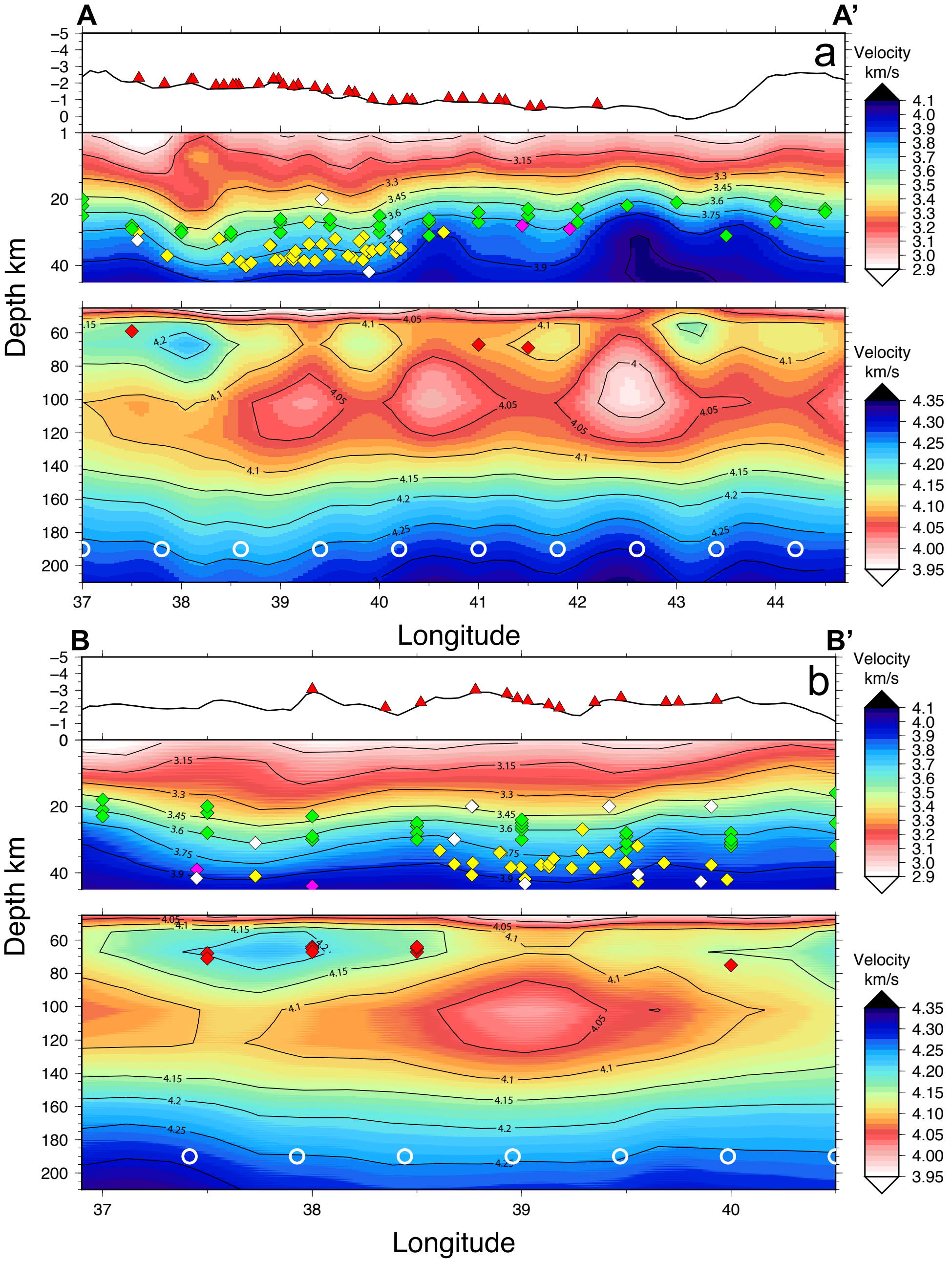

FIGURE 4.10: Cross-sections through the interpolated absolute shear velocity depth slices a) along the rift and b) across the rift (see Figure 4.9 for locations). The cross-sections have been split into crustal section (0-45 km depth, top panel) and mantle (45 – 210 km depth, bottom panel) for display purposes. Red indicates slower velocities and blue faster velocities. Red triangles above section indicate quaternary volcanoes with topography as black line. Thin lines are velocity contours and diamonds represent previous receiver function results for the Moho in top sections (green (Lavayssière et al., 2018), magenta (Hammond et al., 2011), yellow (Stuart et al., 2006), white (Ogden et al., 2019)) and LAB in bottom sections (red(Lavayssière et al., 2018)). White circles are same as in Figure 4.9 for location reference.

Within the MER, the observed velocities are slow with some lateral variation generating focussed areas of slowest velocity, which could be partially explained by variations in composition. Laboratory experiments suggest felsic compositions are seismically slower than mafic compositions (Christensen and Mooney, 1995; Hammond and Humphreys, 2000a). In geochemical studies, both the crust and volcanic rocks of the MER have been interpreted as more felsic than Afar (Hutchison et al., 2018; Maguire et al., 2006; Rooney, 2020; Siegburg et al., 2018)(Hutchison et al., 2018; Maguire et al., 2006; Rooney, 2020; Siegburg et al., 2018), and could result in shear velocities as low as 3.64 km/s (Birch, 1960; Simmons, 1964). However, such a compositional variation is not enough to explain the slowest seismic velocities we observe (3.00 – 3.55 ± 0.03 km/s) (for further details on velocity variations due to crustal composition we refer the reader to Chambers et al. (2019)).

Higher temperatures combined with magmatic activity in the crust are required to explain the observed slow crustal velocities. The thicker crust of the MER, relative to Afar, could play an important role since thicker crust can increase melt residence times. This scenario will also result in more felsic magma compositions, consistent with geochemical and modelling studies (Karakas and Dufek, 2015; Siegburg et al., 2018) and potentially create a deep crustal hot zone, further decreasing seismic velocity (Annen et al., 2006; Karakas and Dufek, 2015). In contrast, mafic intrusions within the thinner crust of Afar, contain geochemical signatures consistent with melt sourced directly from the mantle with little residence time in the crust (Hutchison et al., 2018).

Beneath the rift axis in Afar, slow velocities are observed beneath most of the Quaternary-Recent magmatic segments in our model ($>$0.2 km/s slower than surroundings, Vs = 3.50 ± 0.02 km/s) (Figure 4.9). The velocities we observe beneath the magmatic segments of Afar are again too slow to be explained by standard continental crust (3.60 km/s at 20 km depth (Rudnick and Fountain, 1995)) or rifted crust (3.70 km/s at 20 km depth (Rudnick and Fountain, 1995)) and require partial melt. This agrees with geodetic and magnetotelluric studies which have also been interpreted in terms of the presence of melt within the crust with a focus at the magmatic segments (e.g. Desissa et al., 2013; Keir et al., 2009b).

Off rift, we observe slow anomalies southeast of Lake Tana on the eastern part of the Ethiopian Plateau (3.10 – 3.85 ± 0.04 km/s at depths of 10 to 40 km). The slow velocity anomalies are a similar magnitude to those within the MER (which we interpret as containing partial melt), and correlate in map view to known volcanoes and geothermal activity (Figure 4.9). There has not been recent volcanism beneath the Ethiopian Plateau for $>$21 Myrs (Rooney, 2017). It is therefore unlikely that a remnant thermal anomaly could explain our observations (Figure B.2), as simple conductive cooling calculations indicate that a 1300°C thermal anomaly would dissipate in $<$ 10 Myr. It is therefore likely that there has been further recent magmatic emplacement. We explore the likely source of this new magmatism below and when we discuss the source of the asthenospheric anomalies.

A ubiquitous feature of our velocity images are slow velocity anomalies (slow enough to contain melt) that connect in the lower crust between the MER and the Ethiopian Plateau (3.80 – 3.85 km/s connecting at 39.5° E Longitude 9.5° N Latitude). The MER is a narrow rift with sharp variations in plate thickness that could focus melt to the axis (Kendall et al., 2005). In more developed mid ocean ridge systems melt is focussed to the axis forcing melt to migrate laterally due to rheological and density contrasts at the Moho (Garmany, 1989) (e.g. the East

Pacific Rise (Varga et al., 2008), Gulf of California (Wang et al., 2009) and the Mid Atlantic Ridge (Braun and Sohn, 2003; Ghods and Arkani-Hamed, 2000)). Melt migration can occur off rift due to tectonic processes such as plate flexure, extension or pre-existing zones of weakness (Pilet et al., 2016) and by melt focussing from a wide melt zone (Ghods and Arkani-Hamed, 2000). In Afar, geodetic observations and models of coupled but spatially distant zones of subsidence and uplift provides strong evidence for lateral melt migration near the base of the crust over length scales of ∼80 km along rift (Grandin et al., 2012; Illsley-Kemp et al., 2018a). We suggest lateral melt migration could be ongoing with melt flowing into areas weakened by tectonic processes.

In contrast to the east, the western part of the Ethiopian Plateau is one of the fastest areas of this study and is located 250 – 500 km from the rift. This area has not been comprehensively imaged up until this point. The distance from the rift coupled with geological studies (e.g. Jones, 1976; Rooney, 2019) suggests the western part of the Ethiopian Plateau has been minimally impacted by rifting processes. In addition there is little evidence for significant flood basalt magmatism (Mège and Korme, 2004). We interpret the velocity observations as being most similar to original plate structure before rifting. Ogden et al. (2019) performed receiver function analysis in the same area, finding crustal thicknesses of ∼30 km at the western edge of the Ethiopian Plateau and interpreted the area as being unaffected by lower crustal intrusion from the Oligocene flood basalts or younger rifting, consistent with our observations.

4.6.2 Lithospheric Structure

At 60 – 80 km depth we observe a fast lid in 1-D profiles (Figure 4.3) and cross-sections (Figure 4.10) that are >0.1 km/s faster than the surroundings, although the velocities are much slower than lithospheric mantle observed in other continental settings (maximum of 4.30 ± 0.05 km/s for our model in comparison to 4.45 km/s for ak135) (Kennett et al., 1995). The base of the fast lid is commonly associated with the lithosphere-asthenosphere-boundary (LAB) (Fishwick, 2010; Lavayssière et al., 2018). We plot the S-to-P results of Lavayssière et al. (2018) on our cross-sections (Figure 4.10 red diamonds in lower panels) and find good agreement between the locations of our fastest velocities (Vs >4.15 km/s) and the existence of a strong LAB phase from the S-to-P results. The fast lid is most prominent off rift beneath the rift flanks and plateau in Profile B-B' (Figure 4.10b), in regions less affected by rifting. In the rift Profile A-A' (Figure 4.10a), from the MER to Afar, the fast velocity zone is intermittently visible and is underlain by the slowest asthenospheric velocities (discussed in the next section). The fast lid becomes prevalent again near the Arabian Peninsula. Our result, with no discernible fast lid in Afar, is consistent with S-to-P results that did not find a strong, significant LAB phase beneath the majority of the rift (Lavayssière et al., 2018; Rychert et al., 2012). The presence of the slowest asthenospheric velocities (3.98 – 4.06 ± 0.03 km/s) beneath areas where receiver functions do not detect an LAB (Lavayssière et al., 2018; Rychert et al., 2012) is consistent with a lack of a fast lid in these regions, possibly caused by partial melt at shallow depths (10 - 60 km depth) in these regions.

4.6.3 Asthenospheric Anomalies

At greater depths ($>$ 60 km depth in our models), we observe velocities of 4.30 $\pm$0.05 km/s beneath the Ethiopian Plateau which are similar to the global average using ak135 (4.45 km/s) which could be explained by moderately elevated temperatures (Gallacher et al., 2016; Kennett et al., 1995) (Figure 4.3b and Figure 4.9). We consequently do not interpret these areas further. In contrast, velocities beneath the active continental and oceanic rifts in our study are slower than the plateaus with velocities ranging from 3.95 – 4.10 $\pm$0.03 km/s at asthenospheric depths, significantly slower than the global average (4.45 km/s (Kennett et al., 1995)) and we explore the cause in the paragraphs below.

The slow velocity anomalies within the rifts are punctuated in segments ~110 x 80 km wide and spaced ~70 km apart, getting progressively shallower and broader in lateral extent northwards, towards areas at more advanced stages of rifting. The slowest velocity anomalies (Vs $<$ 4.05 km/s) start at 60 – 80 km depth and extend down to 130 km. The slowest, largest anomaly with the shallowest depth extent exists beneath Afar, the region in the latest stage of rifting. We note that while the anomalies themselves are well-resolved, absolute depths could vary by 20-30 km given our sensitivity at these depths. Given mantle potential temperatures are only moderately elevated (~1450 °C (Armitage et al., 2015; Ferguson et al., 2013; Rooney et al., 2012a; Rychert et al., 2012)) we would expect velocities to be reduced by 3%, instead of the observed 9% when comparing the segments to the rift flanks, using a Burgers model (Jackson and Faul, 2010) and the same parameterisation as Chambers et al. (2019). We therefore require partial melt to explain the slow velocity segments, in agreement with previous tomographic studies (Bastow et al., 2008; Chambers et al., 2019; Gallacher et al., 2016). The anomalies occur at depths consistent with previous geochemical estimates of melt generation (53 – 120 km depth) (Ferguson et al., 2013; Rooney et al., 2005).

The slow velocity segments are present at the earliest stages of rifting beneath areas where the crust has not significantly thinned (40 km thick crust and 70 km to the top of the slow velocity segment furthest south (Lavayssière et al., 2018; Stuart et al., 2006)) and maintain crustal velocities to deeper depths ($<$3.75 km/s (Chambers et al., 2019)). Furthermore the segments persist into areas of later stage rifting (crustal thicknesses of 22 km with depth to top of segment of 60 km (Hammond et al., 2011)). These observations suggest segmented melt supply starts prior to significant crustal and plate thinning. Segmentation beneath rifts is not isolated to this study and has been observed beneath more mature oceanic rifts (e.g. Gulf of California, Red Sea Rift, the Mid Atlantic Ridge (Lekic et al., 2011; Ligi et al., 2012; Wang et al., 2009)) and beneath the EAR (Civiero et al., 2015, 2019; Gallacher et al., 2016).

The processes generating segmentation beneath the EAR are debated with hypotheses ranging from multiple plumelets off the African superplume (Civiero et al., 2015, 2019), to decompression melting due to plate spreading (Bastow et al., 2008; Rychert et al., 2012), possibly enhanced via melt buoyancy (Gallacher et al., 2016; Ligi et al., 2012). We do not image any structures that resemble a single narrow plume conduit rising continuously from great depth, and our resolution suggests that we would be able to image one that was $>$ 100 km in diameter. Therefore, we rule out the influence of one plume, unless the plume is very thin or much larger than the aperture of our array. We cannot rule out the influence of smaller plumelets from a deeper plume (Civiero et al., 2015), but again, the anomalies need to be smaller than our resolution of ~100 km.

This leaves decompression melting, and buoyancy driven upwelling as more likely hypotheses for controlling the locus of asthenospheric melting. Similarly beneath more mature rifts active upwelling is considered to increase melt production (Buck and Su, 1989; Eilon and Abers, 2017) and generate segmentation (Nielsen and Hopper, 2004; Wang et al., 2009). Our observations suggest the processes controlling segmentation develop early during the rifting process and are active for much of a rift's lifetime. However, we cannot rule out that our depth sensitivity may not be sufficient to image deeper plume structures and reiterate that the veloities are slow everywhere in the mantle beneath this study.

Off rift beneath the Ethiopian Plateau the slowest velocity anomalies at asthenospheric depths are not located directly beneath the slowest crustal velocity anomalies (Figure 4.10). A potential explanation is that melt production in the asthenosphere is ephemeral across the region (Sim et al., 2020). Asthenospheric melt that produced the crustal anomalies we observe today, may have been drained (Civiero et al., 2015). Closer to the rift where we observe a break in the border faults (38.5° E Longitude, 9° N Latitude), skewed mantle upwelling could result in asymmetric rifting and segmentation (Sparks et al., 1993; Toomey et al., 2007), explaining the disconnect between melt production offset from the axis of the MER and melt storage within the crust. Alternately, lateral migration of melt along the base of the lithosphere might be responsible for the apparent disconnect between our inferred regions of melt generation in the asthenosphere and melt residing in the crust. In this case, melt may laterally migrate along a permeability boundary (Sparks and Parmentier, 1991) before reaching its final intrusion/eruption point (Toomey et al., 2007; Rychert et al., 2018). Lateral melt migration has been observed at fully developed mid ocean ridges such as the fast spreading East Pacific Rise (Varga et al., 2008), the Gulf of California (Wang et al., 2009) and the slower spreading Mid Atlantic Ridge (Braun and Sohn, 2003; Ghods and Arkani-Hamed, 2000). Within our study area lateral melt migration has been observed during the Dabbahu rifting episode (2005 – 2010) where melt migrated >80 km along rift near the base of the crust (Grandin et al., 2012; Illsley-Kemp et al., 2018a). The dynamics of melt and mantle upwelling may be important for our understanding of the evolution of the rifts through time and the locations of active volcanic/hydrothermal regions through melt migration.

4.7 Conclusions

We present the results from a joint inversion of ambient noise and teleseismic Rayleigh waves to produce a 3-D absolute shear velocity map from 10 - 210 km depth, for the northern East African Rift. At crustal depths we observe significant lateral velocity variations which can be partly explained by variations in crustal thickness. At crustal depths velocities are slowest beneath the Main Ethiopian Rift and the eastern part of the Ethiopian Plateau and are slow enough to require a component of partial melt coupled with elevated temperatures. A fast lid, inferred to be the Lithosphere-Asthenosphere-Boundary, is observed at 60 – 80 km depth off rift (>0.1 km/s faster than surroundings). Within the rift the fast lid is obscured which we interpret as melt infiltration to shallow depths. At asthenospheric depths beneath the plateaus we observe velocities only slightly slower (4.30 ± 0.05 km/s) than global models that can be explained by elevated temperatures. The rift is significantly slower than off rift at asthenospheric depths, and we observe segmented slow velocity anomalies at 60 - 130 km depth, including in areas that have not undergone significant crustal thinning. The segments are interpreted as areas of partial melt and suggest segmented melt supply starts prior to significant crustal and plate thinning. Furthermore, asthenospheric anomalies are not directly beneath the melt-rich crustal regions, including those off rift, suggesting melt laterally migrates within the mantle, or melt production is ephemeral with the source for the anomalies observed at crustal depths drained.

4.8 Acknowledgments

E.L.C acknowledges funding from NERC studentship NE/L002531/1. C.A.R. and N.H. acknowledge funding from NERC grants NE/M003507/1 and NE/K010654/1 and ERC grant GA 638665. D.K. is supported by NERC grant NE/L013932 and by MiUR through PRIN grant 2017P9AT72. All data used in these models are freely available from the IRIS Data Management Center (IRISDMC; https://service.iris.edu/fdsnws/dataselect/1/) and the final shear velocity model can be found at https://doi.org/10.5258/SOTON/D1408. IRIS Data Services are funded through SAGE Proposal of the NSF under Cooperative Agreement EAR-126168. We thank SEIS-UK for use of instruments and computing facilities. The facilities of SEIS-UK are supported by NERC under agreement R8/H10/64.F. Some figures were made using GMT (Wessel and Smith, 2013).

For supplementary material see Appendix B.

Chapter 5

Variations in melt emplacement beneath the northern East African Rift from radial anisotropy

This chapter focusses on determining radial anisotropy from the ambient noise dataset used in Chapter 4. I decided to determine anisotropy to investigate the controls on velocity within the crust and uppermost mantle. Radial anisotropy gives an indication of the orientation of layering, either horizontally or vertically aligned. This information can then be used to determine if there is melt and if it is stored as dykes, sills or without a preferential fast direction. Below is the paper which is in preparation with the aim of being submitted to Earth and Planetary Science Letters.

Chambers, E. L., Harmon, N., Keir, D., Rychert, C. A. Variations in melt emplacement beneath the northern East African Rift from radial anisotropy

Key Points:

- For most of the region $V_{SH} > V_{SV}$ (up to 6.5%) suggesting the crust is inherently layered beneath Ethiopia.
- In the upper-mid crust beneath the Main Ethiopian Rift and Ethiopian Plateau $\delta V>3\%$, requiring alternating thin layers of continental crust and sills.
- $V_{SV} > V_{SH}$ in the Erta Ale Magmatic Segment is interpreted as dykes and vertically aligned cracks used as conduits for melt.

5.1 Abstract

Large lateral variations in shear velocity have been observed beneath the northern East African Rift. Previous studies have interpreted low velocities beneath the rift as indicative of melt, however velocities of similar magnitude are present off rift which are less easy to reconcile.

In order to understand the primary controls on the velocity structure both off and on rift we determine the radial anisotropy using surface waves from Love and Rayleigh waves from 13 – 26 s period. The Rayleigh - Love wave phase speed difference cannot be accounted for by an isotropic model, with Love waves 0.40 ±0.03 km/s faster than Rayleigh waves. We require radial anisotropy in the crust, with our 1-D average V_{SV} 0.15 ±0.03 km/s slower than V_{SH} from 5 – 30 km depth. Below 30 km radial anisotropy is not required. For most of the region $V_{SH} > V_{SV}$ and is strongest in the upper 5 – 15 km, suggesting the crust is inherently layered. Effective medium theory suggests thin compositional layering of felsic and mafic intrusions can account for anisotropy up to 4%. However to reconcile the highest observed anisotropy (7%), and lowest velocities we require 2 - 4% partial melt oriented in sills. Along rift horizontally aligned radial anisotropy gets weaker towards areas at more advanced rifting, suggesting sills become less dominant with progressive rifting. Similarly, anisotropy is weaker at 16 - 30 km depth but velocities are slow enough to require melt which we interpret as melt stored as sills and isotropic bodies. The Erta Ale magmatic segment is the only location where $V_{SV} > V_{SH}$, suggesting the crust is dominated by vertically aligned micro-cracks and dykes providing conduits for vertical flow of melt.

5.2 Introduction

During rifting, the crust is thinned and faulted to accommodate extension, however, in magmatic rift systems there may be significant crustal addition due to intrusive and extrusive magmatism (Buck, 2006; McKenzie et al., 1970). Where and how magma is stored in the crust has important implications for the strength of the crust as the presence of partial melt and heat weakens the surrounding crust. The depth of magma storage is a key factor for magmatic evolution, transforming mafic melts from the mantle to more felsic compositions. In addition, the depth of storage, location and geometry of partial melt presents another control on mineralization, important for economic resources. Yet, in many rifts globally the depths and geometry of magmatic emplacement both past and present remains difficult to constrain.

The subaerial northern East African Rift (nEAR) provides a unique opportunity to investigate the modification of the crust during rifting processes via magmatic emplacement and eruption (Ebinger and Casey, 2001). Previous geophysical studies have revealed insights into the location of melt and fluids in the crust (e.g. Bastow et al., 2010; Chambers et al., 2019; Hammond et al., 2014; Hammond, 2014; Whaler and Hautot, 2006) and volcanoes provide information at the surface. Evidence from surface geology, recent geophysical and geodetic studies have interpreted melt beneath the Main Ethiopian Rift (MER) at mid-lower crustal depths and as shallow magma chambers at ∼5 km depth beneath the magmatic segments (Biggs et al., 2011; Chambers et al., 2019; Hübert et al., 2018; Lloyd et al., 2018; Whaler and Hautot, 2006), while beneath the Ethiopian Plateau melt has been imaged within the mid-lower crust (Chambers et al., 2019; Cornwell et al., 2006; Mackenzie et al., 2005; Whaler and Hautot, 2006), as far north as Lake Tana (Hautot et al., 2006). Seismic anisotropy can provide further insight into the structure of magmatic systems, as it can be caused by Shape Preferred Orientation (SPO) of planar features such as faults, sills and dykes, that cause a significant velocity contrast with the country rock (Crampin and Kirkwood, 1981) Previous studies of anisotropy within the EAR, have found evidence for melt beneath the rifts and Ethiopian Plateau at mantle and crustal depths (Bastow et al., 2010; Hammond et al., 2014; Keir et al., 2011; Kendall et al., 2005). Previous studies of anisotropy suggest at asthenospheric depths anisotropy is dominated from lattice preferred orientation (LPO) of olivine. However, within and near the base of the mantle lithosphere, oriented melt pockets likely become increasingly important in controlling the anisotropy (Bastow et al., 2010; Gao et al., 2010; Hammond et al., 2014; Kendall et al., 2006). At lower crustal depths anisotropic H-k stacking (Hammond, 2014) and surface waves (Bastow et al., 2010) found evidence for melt stored in stacked sills beneath the MER and the off-rift Ethiopian Plateau, with local earthquake splitting and H-k stacking suggesting the sills in the rift connect to the upper crust through a series of dykes and aligned fracture networks (Hammond, 2014; Keir et al., 2005, 2011). In contrast the surface wave study found evidence for $V_{SH} > V_{SV}$ consistent with strong layering in the upper 10 km of crust (Bastow et al., 2010). While we have some insight into the storage of melt in the crust, the models focus on smaller regions and are not directly comparable further complicating our knowledge on how melt is stored and whether magma reservoir geometry changes through rift evolution.

The rift comprises 3 arms, the Red Sea rift, Gulf of Aden rift and the MER. Rifting of the Red Sea and Gulf of Aden started first at 25-35 Ma (Bosworth et al., 2005; Leroy et al., 2010), roughly coeval with the emplacement of the Ethiopian flood basalt province (Courtillot et al., 1999). Rifting started later in the MER, initially at 20 Ma in the south, and later at 18 and 11 Ma in the central and northern sections respectively (Figure 5.1a) (Wolfenden et al., 2004). Within the Afar depression the 16 − 25 km thick crust is highly intruded compared to the 35 − 45 km thick crust of the Ethiopian Plateau and MER (Hammond et al., 2011; Maguire et al., 2006; Ogden et al., 2019; Stuart et al., 2006). Quaternary-Recent volcanism has focussed to the ∼70 km long, ∼20 km wide magmatic segments within the rift, while the Ethiopian Plateau has little evidence for Recent eruptions (Hayward and Ebinger, 1996). Geothermal activity in contrast is present both on and off rift with significant activity on the western border fault (Keir et al., 2009b) which separates the Plateau from the rift (Wolfenden et al., 2005).

Here we present a new high resolution radially anisotropic shear velocity model for the crust of the nEAR, from ambient noise cross correlation functions. We use this model to interpret variations in crustal structure due to compositional laying, alignment of micro-cracks and the presence of fluids and use this to infer the past and present emplacement of melt within the crust in an active rift system.

5.3 Methods

We used data from continuous broadband seismometers recorded by 12 temporary networks and 5 permanent stations (Figure 5.1a) between 1999 and 2017. A bandpass filter of 0.005 − 0.4 Hz was applied to the data and was pre-processed following the methods of Bensen et al. (2007). The method for cross correlations is similar to that described in Chambers et al. (2019) and Harmon et al. (2007) but uses the north and east components in conjunction with the vertical component, to calculate the radial and transverse components for each station pair (Lin et al., 2008; Sánchez-Sesma et al., 2006). The cross correlations were then stacked for each station pair for every day. Station pairs spaced less than twice the wavelength of the Rayleigh wave at a given period were removed.

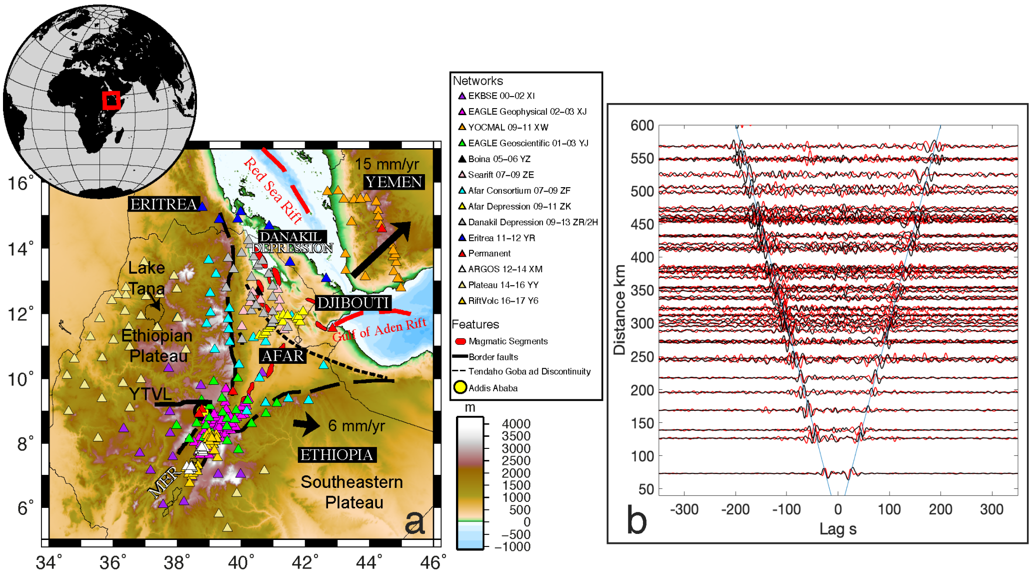

Figure 5.1: (a) Seismic Station map of the northern East African Rift. Thick black lines show border faults, red polygons magmatic segments, and dashed lines the Tendaho-Goba'ad discontinuity (TGD). Stations are triangles coloured to their project deployment. Addis Ababa is marked by yellow circle. (b) NCF for transverse–transverse components (red) and vertical–vertical components (black).

Phase velocities for each station pair were determined after Harmon et al. (2007). The Noise Correlation Function (NCF) for the symmetric vertical-to-vertical and transverse-to-transverse components were windowed to give the Rayleigh and Love wave components respectively. The resulting cross correlations produced well resolved phase velocities between 13 - 26 s for the Love waves and 9 – 26 s for the Rayleigh waves (Figure 5.1b). We therefore focused on a range of 13 – 26 s for both the Love and Rayleigh waves. Each stacked NCF was required to have a signal-to-noise ratio >3. For further results on the Rayleigh waves we refer the reader to Chambers et al. (2019) and Chambers et al., (in review).

We used a nodal parameterisation with a 0.25° spacing in latitude and longitude (Figure 5.2). We inverted the average phase velocity at each period on the nodal grid using the method of Harmon et al. (2013). The phase velocity inversion uses 2-D finite frequency kernels (Nishida, 2011; Tromp et al., 2010) and an iterative damped least squares approach (Tarantola and Valette, 1982). We used a smoothing length of 40 km to average the kernel values onto the nodes.

In the phase velocity maps for the Rayleigh and Love wave inversions, the diagonals of the formal resolution matrix have maximum values of 0.32 at our best resolved period 15 s (Figure 5.2). The resolution is derived from the sensitivity kernels centred nominally on the ray paths shown in Figure 5.2, for 15, 20, 25 s period. Our formal resolution indicates we require at least 3 node spacings to produce an independent piece of information about velocity structure, in other words we can resolve 50 – 100 km laterally. We therefore limit our discussion to features >100 km laterally (Figure 5.2).

We use the following parameterisation and assumptions to invert Rayleigh and Love wave dispersion for the radially anisotropic shear velocity structure (Figure 5.3 and Figure 5.5). We use density and five elastic parameters, $A = \rho V_{PH}^2$, $C = \rho V_{PV}^2$, $L = \rho V_{SV}^2$, $N = \rho V_{SH}^2$, and F (Montagner and Anderson, 1989), where V_P is compressional velocity and V_S is shear velocity.

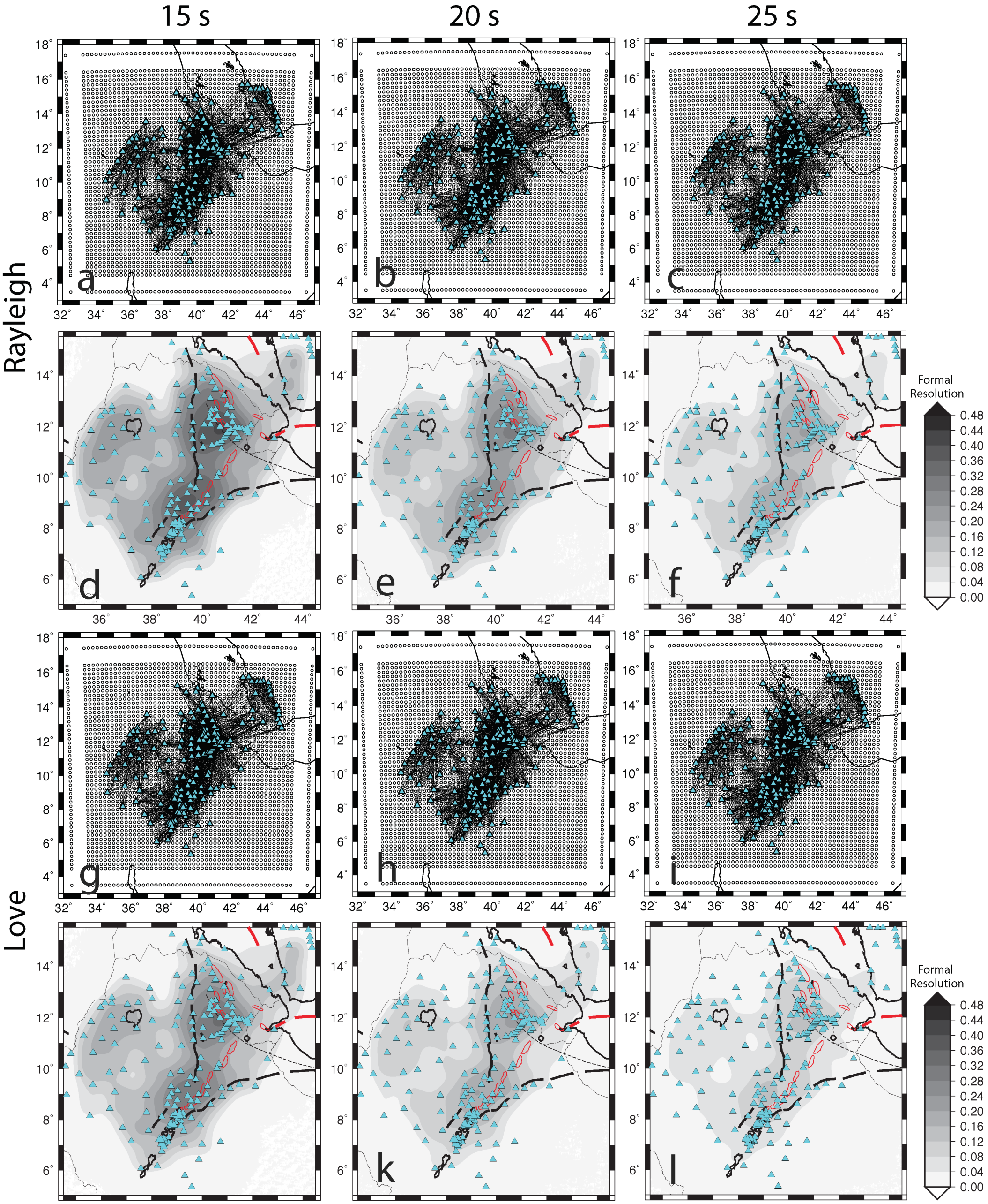

FIGURE 5.2: Nodal grid with Rayleigh (a-c) and Love (d-f) ray paths and formal resolution maps (g-i Rayleigh and j-l Love) at 15, 20 and 25 s period. Stations are overlain as blue triangles.

Subscript H and V refer to horizontal and vertical respectively. We use an alternative parameterisation, $\xi = \mathrm{N/L}$, $\varphi = \mathrm{C/A}$, $\eta = \mathrm{F/(A - 2L)}$, V_{SV}, and V_{PH} for the elastic parameters (Saito, 1988). Usually only V_{SV} and ξ can be well resolved, so to reduce the number of parameters we scale $\delta\ln\varphi = -1.5\delta\ln\xi$ and $\delta\ln\eta = -2.5\ln\xi$ (Montagner and Anderson, 1989; Panning and Romanowicz, 2006). We fix the V_{PH}/V_{SV} ratio to 1.80 from the average of all Vp/Vs results in the region generated by receiver function analyses (Hammond et al., 2011; Stuart et al., 2006). Variations in the choice in Vp/Vs again produce results that are within error of each other.

For the shear velocity inversion, we use a damped least squares approach (Tarantola and Valette, 1982). We calculated the partial derivatives that relate variations in shear velocity to changes in phase velocity using DISPER80 (Saito, 1988). We assign a nominal a priori standard error for each model parameter of 0.2 km/s for shear velocity and 0.1 for ξ. We first invert the average dispersion for Love and Rayleigh waves for an average 1-D shear velocity structure as a function of depth (Figure 5.3). We then use this as our starting model for the 3-D inversion, where we inverted each pixel of the phase velocity maps across all periods and the collected 1-D inversions create the 3-D volume. The resulting 3-D velocity structure is shown from 5 – 40 km depth (Figure 5.5). Although our shear velocity models are discretised at 2.5 km intervals in depth, we interpolated the velocity structure to 1 km depth for presentation purposes using a linear interpolation (Figure 5.3).

We present our results for anisotropy in terms of $\delta V = \left(\sqrt{\frac{V_{SH}^2}{V_{SV}^2}} - 1\right) * 100$. Values >0 ($V_{SH} > V_{SV}$) indicate radial anisotropy is horizontally aligned, whereas values <0 ($V_{SH} < V_{SV}$) indicate regions of vertically aligned anisotropy. The depth sensitivity for both Rayleigh and Love waves at this frequency range are broad, making precise determination of the depth difficult, so we present depth averages of radial anisotropy, where the formal resolution matrix indicates we have a well resolved average, acknowledging that there may be some trade-off in the absolute depth of the anisotropy (Rychert and Harmon, 2017). Anisotropy is significant from 5 – 30 km depth (Figure 5.3a) and we therefore only interpret anisotropy in this depth range, although sensitivity tests indicate we can image from 5 – 40 km depth (Figure 5.3b).

5.3.1 Effective Medium Calculations – Thin Compositional Layers

To understand the potential cause of the dominant radial anisotropy ($V_{SH} > V_{SV}$) we model the simplest example of horizontal anisotropic structure as transversely isotropic layers with a vertical axis of symmetry (Babuska and Cara, 1991). We explore whether alternating thin compositional layers can account for the observed anisotropy and maximum apparent velocity discontinuity. This is done by modelling alternating thin layers of rock compositions with fast and slow seismic velocities that are parallel to the Earth's surface, with vertical symmetry axis. To get effective radial anisotropy, the layers must be much thinner than the seismic wavelength. Then the resulting radially anisotropic Christoffel Matrix can be calculated using effective medium theory (Backus, 1962).

For transversely isotropic mediums with a vertical symmetry axis and hexagonal symmetry (the case for multiple Earth environments) the elastic coefficients for the stiffness matrix C_{ij} are:

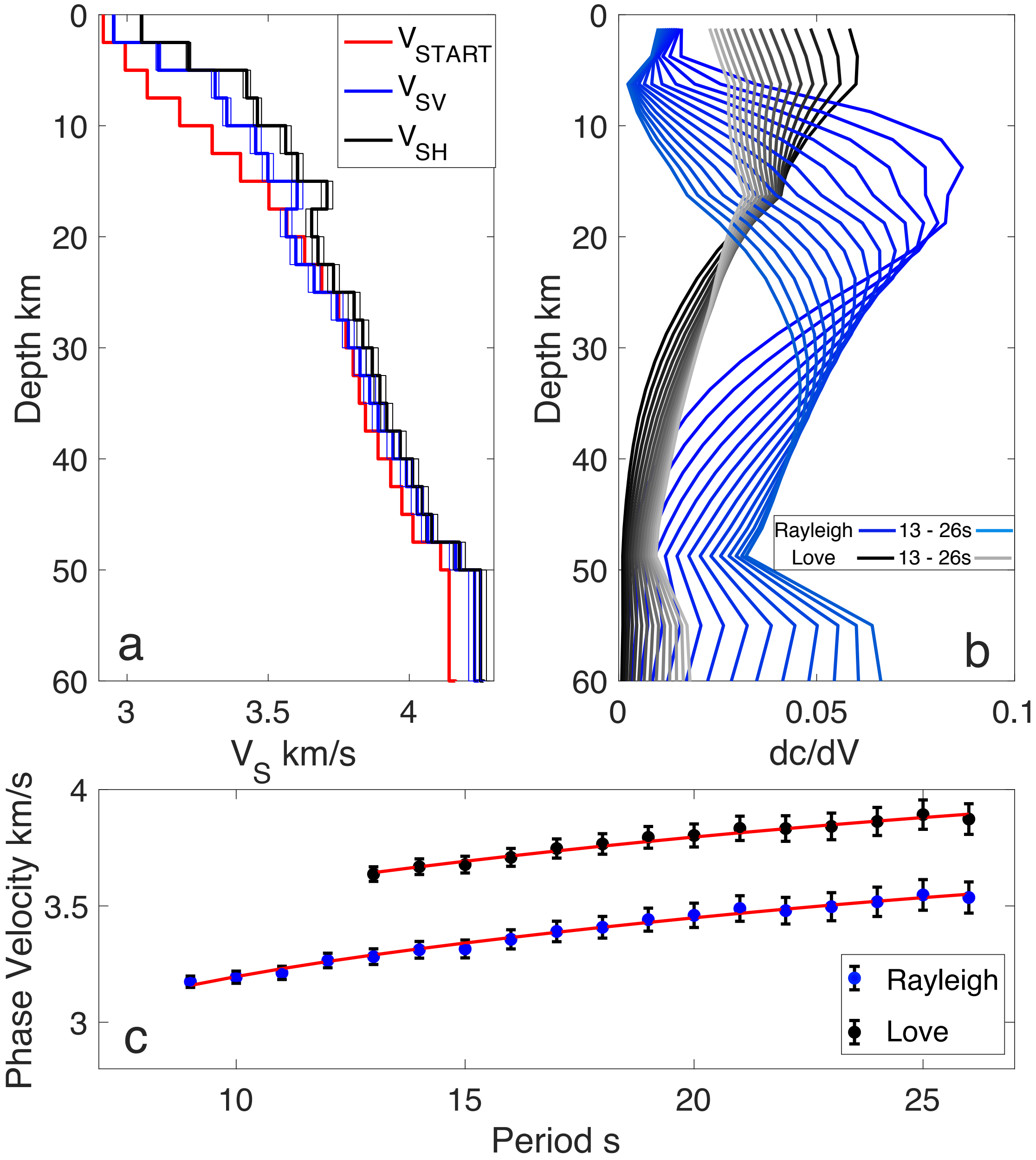

Figure 5.3: a) Shear velocity structure for βV (blue) and βH (black) with 95% confidence regions, and the starting model (red). b) Sensitivity kernels for Love (black) and Rayleigh (blue) waves at select periods. c) One dimensional phase velocities for Love (black circles) and Rayleigh (blue circles) waves, with corresponding predicted phase velocity from the best fit shear velocity model in red lines.

$$(C_{ij}) = \begin{pmatrix} A & A-2N & F & . & . & . \\ A-2N & A & F & . & . & . \\ F & F & C & . & . & . \\ . & . & . & L & . & . \\ . & . & . & . & L & . \\ . & . & . & . & . & N \end{pmatrix} \tag{5.1}$$

For anisotropy we are interested in L and N as described above. In an isotropic case $N = L = \mu$ where μ is the shear modulus whereas in the anisotropic case $N \neq L$. The distinct eigenvalues for shear waves of the Christoffel matrix are:

$$V_{SH} = \sqrt{\frac{N}{\rho}} \tag{5.2}$$

and

$$V_{SV} = \sqrt{\frac{L}{\rho}} \tag{5.3}$$

Where

$$L = \frac{1}{(\frac{1}{\mu_1})d_1 + (\frac{1}{\mu_2})d_2} \tag{5.4}$$

and

$$N = \mu_1 d_1 + \mu_2 d_2 \tag{5.5}$$

Where d_1 and d_2 are the proportions of each layer (e.g. $d_1 = d_2 = 0.5$ for layering with 50% granite and 50% rhyolite), and μ_1 and μ_2 are the shear moduli for the 2 alternating layers.

The percentage anisotropy was then calculated by δV given above.

5.4 Results

5.4.1 1-D Dispersion Curves and Shear Velocity Model

Average 1-D dispersion curves measured from the ambient noise data show Love wave phase velocities range from 3.66 – 3.87 ±0.03 km/s at 13 – 26 s period, while Rayleigh waves range from 3.21 – 3.56 km/s for 9 – 26 s period (Figure 5.3c). The average phase velocity dispersion curves show that phase velocity of Love waves is greater than Rayleigh waves. The shear velocity structure is displayed in Figure 5.3a with the starting model for our inversions the best fitting model from Chambers et al., (in review) which increases from 2.95 km/s at 2.5 km depth to 4.14 ±0.05 km/s at 60 km depth. V_{SV} and V_{SH} have a broadly similar fit to the starting model with V_{SV} ranging from 2.97 – 4.21 ±0.02 km/s from 5 – 60 km depth and V_{SH} moderately faster, ranging from 3.05 – 4.22 ±0.02 km/s for the same depth range. Our 1-D shear velocity inversion of the Love and Rayleigh waves shows that from >30 km depth, V_{SV} is not significantly different

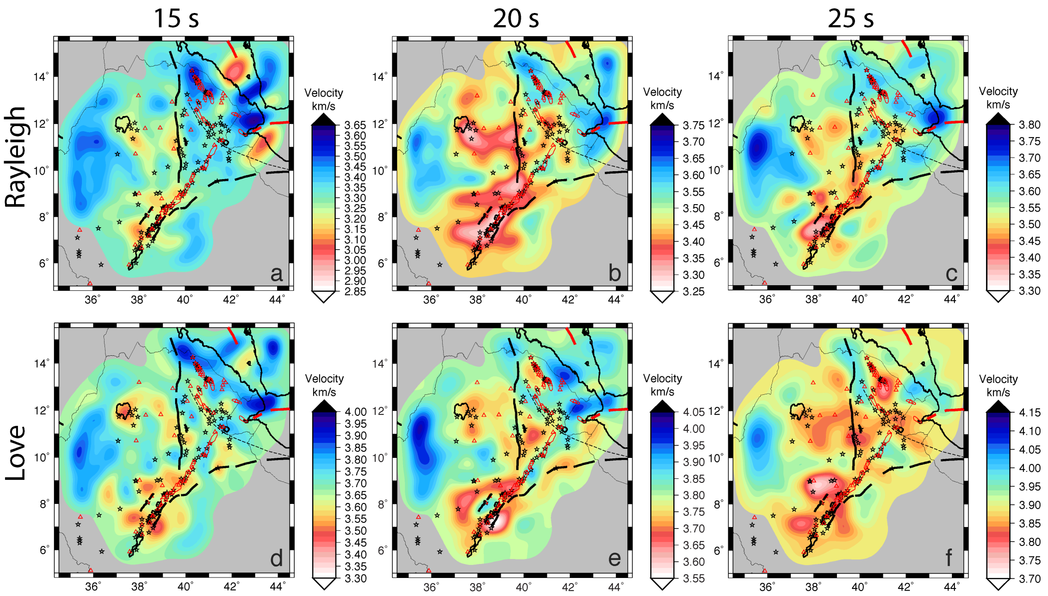

FIGURE 5.4: Phase velocity maps for Rayleigh (top) and Love (bottom) for 15, 20 and 25 s period. Red indicates slower velocities and blue faster velocities. Thick black lines indicate border faults, red polygons magmatic segments, dashed lines the Tendaho-Goba'ad discontinuity, red triangles volcanoes, and black stars geothermal activity.

from V_{SH} and therefore radial anisotropy is not required to explain the data (Figure 5.3a). Between 5 and 30 km depth $V_{SH} > V_{SV}$ and outside the 95% confidence limits for the model parameters, requiring a maximum δV of 5.5% anisotropy. Furthermore, anisotropy is strongest in the upper 20 km and is weaker from 20 – 30 km depth.

5.4.2 2-D Phase Velocities

The phase velocity maps for Love and Rayleigh waves show broadly consistent structures (Figure 5.4). Average Love wave phase velocities range from 3.40 – 4.05 ±0.03 km/s at 15 – 25 s period, while Rayleigh waves range from 2.95 – 3.78 ±0.03 km/s for the same period range. A low velocity anomaly is observed within the MER and beneath the eastern part of the Ethiopian Plateau. The low velocity beneath the rift is centred west of the rift axis straddling the rift flank at periods longer than 20 s for both Love and Rayleigh phase velocities (3.10 – 3.45 ±0.03 km/s for Rayleigh and 3.45 – 3.80 ±0.03 km/s for Love phase velocities). Furthermore, there is a low velocity anomaly visible in the Rayleigh phase velocities that extends along the MER from 6 - 8 °N, whereas Love waves have relatively fast velocities at 15 - 20 s period at 38°E 8°N (Love phase velocity 3.70 - 3.85 ±0.04 km/s vs. Rayleigh phase velocity 3.45 – 3.70 ±0.03 km/s) (Figure 5.4). The Love waves show low velocities beneath Lake Tana (3.45 ±0.05 km/s) which moves progressively southeast with increasing period in contrast to Rayleigh waves which stay focussed southeast of Lake Tana. Beneath the Erta Ale magmatic segment (EAMS), velocities are high for Rayleigh waves (3.60 ±0.03 km/s for all periods) but are low for Love waves where velocities are 3.75 – 3.85 ±0.03 km/s at periods longer than 20 s.

5.4.3 Shear Velocity

The vertically polarised shear velocity maps of Ethiopia and the surrounding areas are laterally heterogeneous with velocities varying from 3.20 – 4.10 ± 0.03 km/s from 5 – 40 km depth. The lowest velocities are beneath the MER and the eastern part of the Ethiopian Plateau (southeast of Lake Tana and west of the border fault) with minimum velocities of 3.20 – 3.75 ± 0.04 km/s (Figure 5.5a-b). From 5 – 20 km depth the MER and Ethiopian Plateau are disparate with isolated low velocities (Figure 5.5a), whereas from 21 – 40 km depth the low velocities are continuous and broadly connected (Figure 5.5b). The highest velocities are beneath northern Afar at the EAMS from 5 – 40 km depth (minimum velocities of 3.65 – 4.10 ± 0.03 km/s) (Figure 5.5a-b). We also observe high velocities beneath the western part of the Ethiopian Plateau (west of 37° E) at 5 - 40 km (velocities of 3.60 – 4.10 ± 0.05 km/s)(Figure 5.5a-b). Velocities get faster along the rift going northwards from the MER to Afar with velocities at the Tendaho Goba-ad Discontinuity (dashed line Figure 5.5, location where the MER transitions to Afar) ranging from 3.50 ± 0.03 km/s at 5 – 20 km depth, increasing to 3.85 ± 0.03 km/s at 21 – 40 km depth.

5.4.4 Anisotropy

Radial anisotropy varies from -1% to 6.5% (Figure 5.5c-d) averaged from 5 – 15 and 16 – 30 km depth. The average is not zero in our region, and is ∼2% at 5 - 15 km depth and ∼1% at 16 - 30 km depth suggesting $V_{SH} > V_{SV}$ for most of the region. The horizontally aligned anisotropy is strongest in the upper crust becoming weaker at lower crustal depths (Figure 5.5c-d). The main areas of horizontally aligned anisotropy are located where we observe the lowest shear velocity within the MER (2.5 – 6%) and off rift beneath the Ethiopian Plateau southeast of Lake Tana, and along the western border fault (39.5° E Longitude, 10.5 – 12.5° N Latitude) (2.5 – 6.5%). The strength of radial anisotropy decreases towards areas at more advanced rifting, dropping from >4% in the MER to 2 - 3% in Afar at 5 - 15 km depth. Within Afar there are areas where $V_{SV} > V_{SH}$, with the most significant (and above our threshold of ± 0.5%) near the EAMS with anisotropy broadly consistent for crustal depths (-1%) from 5-15 km depth. At 16 - 30 km depth anisotropy is weaker (-0.5%) within the EAMS.

5.4.5 Effective Medium Calculations - Thin Compositional Layers

We tested a variety of setups for felsic and mafic rocks with varying proportions of layers (Figure 5.6). Layers in equal proportion to one another result in the maximum apparent isotropic velocity contrast. V_{SV} and δV were taken from the shear velocity and anisotropic models. For the felsic layer we assigned a density of 2790 kgm^{-3} and 3000 kgm^{-3} for the mafic intrusions (Cornwell et al., 2006; Lewi et al., 2016). We specified μ_1 to be the shear modulus of the felsic continental rock and μ_2 to be the shear modulus of a solidified mafic intrusion, allowing both to be free parameters. We then calculated the required value of μ_1 and μ_2 at different fractions of μ_2 from 0 – 1, where 1 represents a crust of 100% mafic intrusions. We did this for central Afar using $V_{SV} = 3.43$ km/s and δV = 1.98%, the MER $V_{SV} = 3.21$ km/s and δV = 4.94% and the Ethiopian Plateau $V_{SV} = 3.29$ km/s and δV = 5.94% which are averages from 5 – 15 km depth taken from the anisotropy and shear velocity models. We also plot the expected ranges of μ_1

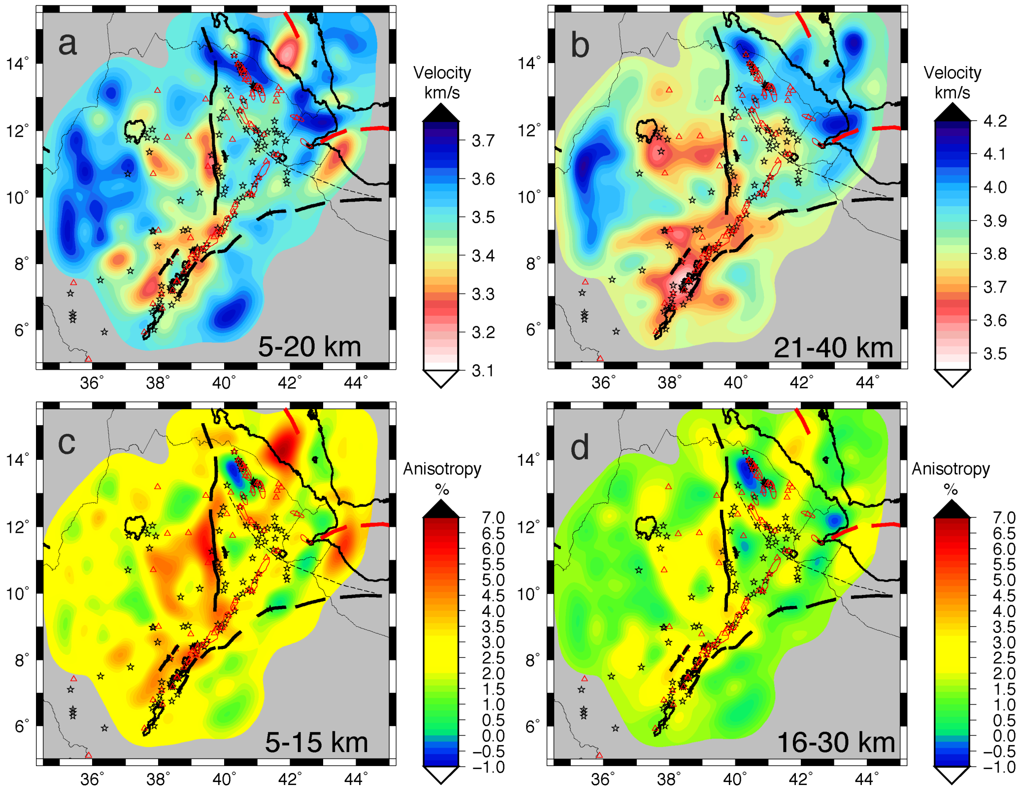

FIGURE 5.5: Depth averaged vertical shear velocity (0–20 km, 21–40 km) and δV (5-15 km, 16–30 km) depth. Thick black lines indicate border faults, red polygons magmatic segments, dashed lines the Tendaho-Goba'ad discontinuity, red triangles volcanoes, and black stars geothermal activity.

and μ_2 for a granitic crust (27.4 – 40 GPa) and a basaltic intrusion (40 – 60 GPa) (Hacker and Abers, 2004; Ji et al., 2010) and geologically inferred proportions of mafic intrusions in the crust on Figure 6 as dashed lines for Afar, the MER and Ethiopian Plateau. The proportions have been calculated from the discrepancy between the observed crustal thickness and the crustal thickness predicted from the stretching factor of the rifts. For Afar the proportion of intrusions is 50% ((Eagles et al., 2002; Hammond et al., 2011; Maguire et al., 2006; Mohr, 1989; Redfield et al., 2003), 25% in the MER (Daniels et al., 2014), and 20% for the Ethiopian Plateau (Daniels et al., 2014). We find μ_1 is satisfied for Afar suggesting solidified intrusions can account for the observed anisotropy. In the MER and Ethiopian Plateau where anisotropy is stronger than the background of 2% we require a component of partial melt with more required in the MER (Figure 5.6).

We explore further the amount of partial melt needed to produce the observed anisotropy. Using the Voigt average for μ_1=34 GPa and μ_2=60 GPa for a basaltic intrusion we compare the observed anisotropy and velocity to those calculated with fixed μ_1 and μ_2. Other parameters are same as above. To match the observed and calculated velocities we require a velocity reduction of up to 28% in the MER and up to 24% in the Ethiopian Plateau. Using the approximation that a 7.9% velocity decrease results in 1% melt we require up to 4% partial melt in the MER and 3.4% in the Ethiopian Plateau, though these are upper approximations. This percentage of partial melt is in agreement with previous studies interpreting 0.5 – 4% partial melt (e.g. Chambers et al., 2019; Gallacher et al., 2016; Hammond et al., 2011). We also observe areas where velocity is slow

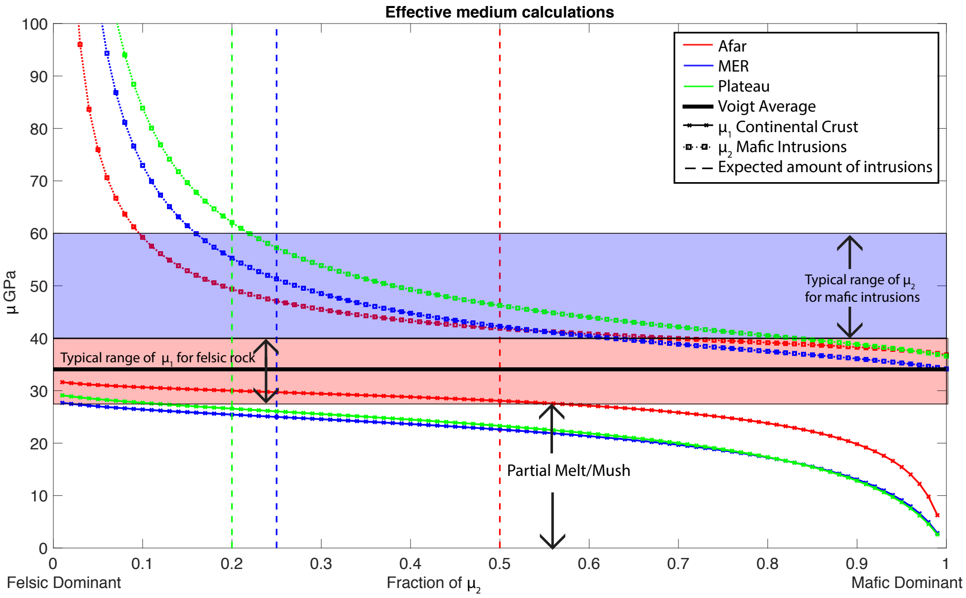

FIGURE 5.6: Modelling of Backus anisotropy for thin compositional layering of felsic country rock and mafic intrusions. V_{SV} and δV were taken from the shear velocity and anisotropic models. For the felsic layer we assigned a density of 2790 kgm^{-3} and 3000 kgm^{-3} for the mafic intrusions (Cornwell et al., 2006; Lewi et al., 2016). We specified μ_1 to be the shear modulus of the felsic continental rock and μ_2 to be the shear modulus of a solidified mafic intrusion, allowing both to be free parameters. We then calculated the required value of μ_1 and μ_2 at different fractions of μ_2 from 0 – 1, where 1 represents a crust of 100% mafic intrusions. We did this for central Afar, the MER and Ethiopian Plateau and compared the results to expected values of μ_1 and μ_2 given a granitic crust (27.4 – 40 GPa) and a basaltic intrusion (40 – 60 GPa) (Hacker and Abers, 2004; Ji et al., 2010). We also plot the expected proportion of mafic intrusions in the crust as dashed lines for Afar, the MER and Ethiopian Plateau.

but radial anisotropy is weak. While melt will reduce shear velocity, anisotropy could increase if melt is stored as stacked sills but would decrease if unaligned, suggesting the low velocity areas contain unaligned melt.

5.5 Interpretation

Some of the velocity variations in the V_{SV} maps of Ethiopia and surrounding areas, from 5 – 40 km depth (Figure 5.5a-b), can be attributed to variations in crustal thickness (Hammond et al., 2011; Lavayssière et al., 2018; Ogden et al., 2019; Stuart et al., 2006), with velocities in Afar and the northernmost MER faster due to the mantle contributing to the image (Chambers et al., in review). The V_{SV} maps show there are several low velocity regions associated with the Ethiopian Plateau, MER and Afar. As has been discussed in greater detail in previous work (e.g. Chambers et al. 2019; Chambers et al., in review), these velocities are slower than expected for crystalline crust and likely require some amount of partial melt. For example, the low velocity anomalies beneath the Ethiopian Plateau and MER have been interpreted as ongoing melt emplacement both on and off rift. Low velocities are observed to get progressively faster along the rift northwards and focussed to the magmatic segments and interpreted as melt focussing to the rift axis with progressive rifting. Beneath the Danakil depression shear velocities are fast which has previously been interpreted as more mafic rock compositions coupled with thinner crust (e.g. Chambers et al. 2019; Chambers et al., in review).

The dominant $V_{SH} > V_{SV}$ anisotropy suggests an inherently layered crustal structure within the nEAR. SPO of planar structures with contrasting elastic moduli can effectively create radial anisotropy, as demonstrated by Backus (1962) and is well described by effective medium theory. In extensional environments, fault systems, sedimentary deposition, and magmatic intrusion/extrusion can give rise to this type of anisotropy. In addition, although not relevant to our case, azimuthal anisotropy can be generated by crustal stretching causing LPO, oriented parallel to the extension direction (Moschetti et al., 2007; Shapiro and Campillo, 2004). In our region, sediment thickness is relatively small (<2 km), so is unlikely the cause of anisotropy since we image depths >5 km. Furthermore, sedimentary layers in continental crust would not produce the largest observed variations in anisotropy. Magmatic intrusion is an effective way to generate SPO anisotropy from compositional layering of continental crust and mostly mafic intrusions within the magmatically active rift (Gao et al., 1997; Kendall et al., 2006; Obrebski et al., 2010). Therefore, we interpret the background average $V_{SH} > V_{SV}$ of 2% across the region (5 - 15 km depth) as indicating a layered felsic/mafic crustal structure reflecting widespread flood basalt volcanism in the past 30 My and possibly older fabric. In other words, the entire region does not comprise of a simple 2 layer felsic upper crust overlying a mafic lower crust (Rudnick and Fountain, 1995), but likely has widespread intrusions in the upper crust.

There are several strong $V_{SH} > V_{SV}$ anomalies across the region, and we observe the strongest horizontally polarised anisotropy beneath the eastern part of the Ethiopian Plateau (2.5 to 6.5%). This area is close to the western border fault where there are steeply dipping faults at the surface. We would expect $V_{SV} > V_{SH}$ in the vicinity of the steeply dipping faults, but it is not observed. We therefore suggest surface wave radial anisotropy may not resolve fine scale vertical features or that the vertical extent of these faults is limited to $<$ 5 km (above our depth average of 5-15 km) (Holtzman and Kendall, 2010). Strong radial anisotropy beneath the Ethiopian Plateau is likely due to crust with a higher concentration of layered horizontal sills. The high values of radial anisotropy (up to 6% Figure 5.5c-d) are difficult to produce from solidified mafic/felsic rocks (Figure 5.6) especially at the likely proportions of felsic/mafic materials in the crust. However, for a small amount of partial melt (up to 3.4%) and a reasonable μ for country rock, we can match our V_{SV} and V_{SH}. Anisotropy is stronger in the 5 - 15 km depth slice than the deeper 16 - 30 km slice suggesting melt is stored as sills in the upper to mid crust. Our interpretation is supported by recent geophysical studies finding strong layered lower crustal reflectors (Maguire et al., 2006), and at mid crustal depths highly conductive (Hautot et al., 2006; Whaler and Hautot, 2006) and low velocity anomalies (Chambers et al., 2019) as far north as Lake Tana. Geochemistry studies also find evidence for melt in sills beneath the Ethiopian plateau (Rooney et al., 2007) which combined with significant geothermal activity (Keir et al., 2009b) and high Vp/Vs ratios (>1.8) (Hammond et al., 2011; Stuart et al., 2006) support an interpretation of melt.

The MER also has significant radial anisotropy (>5%) present beneath the full width of the rift, and effective medium calculations suggest this area also requires partial melt. The anisotropy is stronger in the upper 5 − 15 km which we interpret as horizontal layering of sills. At 16 − 30 km depth anisotropy is weaker but shear velocity is slow enough to require melt (3.55 – 3.75 ± 0.03 km/s). We therefore suggest melt is present but is less layered and is more randomly distributed than the mid-upper crust. Previous geophysical studies find evidence for mid to upper crustal melt zones beneath volcanoes in the rift (Biggs et al., 2011; Lloyd et al., 2018; Tepp et al., 2018; Whaler and Hautot, 2006) further supporting this interpretation. Anisotropy becomes weaker along rift from 6% in the southern MER to 2% in the northern MER and -1% in the EAMS. We also observe anisotropy beneath the full rift width in the south which localises to the magmatic segments in the north. These observations can be interpreted either as a change from sill emplacement in the narrow MER to dyke emplacement in Afar or a reduction in the melt present in the crust towards later stage rifting.

Beneath the EAMS, we observe $V_{SV} > V_{SH}$ (up to -1%), indicating vertically oriented planar features. Geodetic observations of northern Afar show this region has experienced recent upper crustal dyking events (Temtime et al., 2020). Our observations suggest these aligned dykes and associated fractures extend to 15 km depth, or more, as the anisotropic signature is visible in our 16 - 30 km depth average. Our interpretation is supported by models of the influence of gravitational loading on dyke propagation which show shallow and wide rift depressions favour in-rift dyke arrivals whereas narrow and deep depressions favour off-rift arrivals (Maccaferri et al., 2014).

The strongest $V_{SH} > V_{SV}$ radial anisotropy in our study region is consistently in the upper crust at 5 - 15 km depth, suggesting either the density structure of the crust or the state of stress is amenable to sill formation. Furthermore, velocities at lower crustal depths remain slow despite weakening anisotropy suggesting melt is required but is stored as a combination of stacked sills and uniform melt bodies.

Variations arise between the different anisotropy methods which can lead to differing interpretations. The surface waves and shear-wave splitting studies find differences within the MER, with fast direction in shear wave splitting studies consistent with vertically aligned fluid filled cracks observed at mid and upper crustal depths (Keir et al., 2005, 2011; Kendall et al., 2005), which are not imaged by surface waves (e.g. Bastow et al., 2010; Kendall et al., 2006). This is likely due to the varying sensitivities of the two methods. Vertically propagating shear-waves will not be sensitive to $V_{SH} > V_{SV}$ anisotropy caused by layering, whereas surface-waves are most sensitive to layering, though given their relatively broad lateral sensitivity (∼100 km) will struggle to resolve localised anisotropy over <50 km lateral scales (Kendall et al., 2006). Furthermore, shear wave splitting results may be most sensitive to structure <5 km deep, where our work is poorly resolved. We therefore suggest melt is stored both as stacked sills and oriented melt pockets with a higher concentration of dykes in Afar and more sills in the MER.

Our observations are in good agreement with geochemical studies that suggest melt has a primary mantle origin and propagate as dykes in Afar, whereas more crustal assimilation and evolved magmas are observed in the MER where melt is thought to be stored as sills (Hutchison et al., 2018). In northern Afar anisotropy studies find similar results that suggest dykes are the most efficient transport mechanism of melt (Hammond et al., 2014; Hammond, 2014; Keir et al., 2011). At mantle depths beneath the EAMS, we observe little anisotropy suggesting melt retains no preferential alignment, in agreement with Hammond et al. (2014). Active source profiles beneath the Ethiopian Plateau and the MER find evidence for horizontal layering and lower crustal intrusions which decrease towards Afar (Mackenzie et al., 2005; Maguire et al., 2006). Our results suggest layering resulting in anisotropy extends to 30 km, but no deeper, requiring lower crustal intrusions observed at >30 km depth to have no dominant orientation.

Melt ascends due to variations in the buoyancy between melt and the crust. Melt will stop when it reaches neutral buoyancy in the crust or where the elastic and tectonic stresses prevent the melt from rising further (Bradley, 1965; Roberts, 1970). In the East African Rift system, we expect the density structure and stress regime to change as the relatively thick continental crust and narrow rift in the MER transitions to the thin crust and broader rift zone of the Afar region based on numerical models of rift evolution (Maccaferri et al., 2011, 2014). Specifically, in a narrow rift, with a strong asthenospheric upwelling component, the crust may be in a compressional regime within the rift (Huismans et al., 2001; Mondy et al., 2018) which would typically favour sill formation (Roberts, 1970). As the rift widens, the centre of the rift is in an extensional regime, while on the flanks near the border faults the rift is in a compressional regime, which would favour dyke formation in the centre of the rift and sill formation near the flanks (Mondy et al., 2018). Stacked sill complexes are consistent with more recent conceptual models of incremental magma reservoirs (Cashman and Giordano, 2014) and variations in the geochemistry of erupted rocks (Hutchison et al., 2018; Siegburg et al., 2018).

The presence of stacked sills in the crust of a narrow rift and dykes at a wider rift are observed in other rifting/mid-ocean ridge regions and volcanic regions around the globe. In rifting environments evidence for horizontal layering consistent with low to mid crustal sill emplacement is observed in the NoMelt experiment (Russell et al., 2019) and significant lower crustal intrusions as stacked sills in the Baikal rift (Thybo and Nielsen, 2009). In some mid ocean ridge environments, purely laminar structures are proposed (e.g. Kennett et al., 2014; Shito et al., 2015), however, these results require strong radial but weak azimuthal anisotropy, in contrast to the observations in the nEAR. In regions of upwelling such as the East Pacific Rise vertical anisotropy ($V_{SV} > V_{SH}$) is observed (Toomey et al., 2007) and interpreted as vertical flow of melt. This is similar to what we observe within the EAMS. Beneath volcanic regions strong radial anisotropy in the crust has been observed beneath large calderas in arc settings, continental hotspots such as Yellowstone and the basin and range rift system, interpreted as the locus of voluminous silicic magmatism forming as large sill complexes supporting the concept of long-term incremental evolution of magma bodies (Jaxybulatov et al., 2014; Jiang et al., 2018; Koulakov et al., 2016). Similarly in magmatic regions with thickened continental crust, strong lower crustal radial anisotropy has been interpreted as deep sills that occur in thickened regions which may accelerate the processing of primary basalts to continental compositions (Harmon and Rychert, 2015). Away from the caldera and along hot spot trends anisotropy weakens suggesting seismic contrasts fade with crystallisation (Jiang et al., 2018).

We summarise our interpretation of the anisotropy and how melt is stored in the crust in Figure 5.7. Our results suggest magmatic storage varies from horizontally aligned stacked sills in the lower and mid crust within the MER where the rift is narrow, rotating to unaligned homogenous melt bodies and dykes as the rift widens into Afar. The new knowledge of the structure and depth of melt storage and the ascent mechanism of melt is important for our understanding of the evolution of rifting.

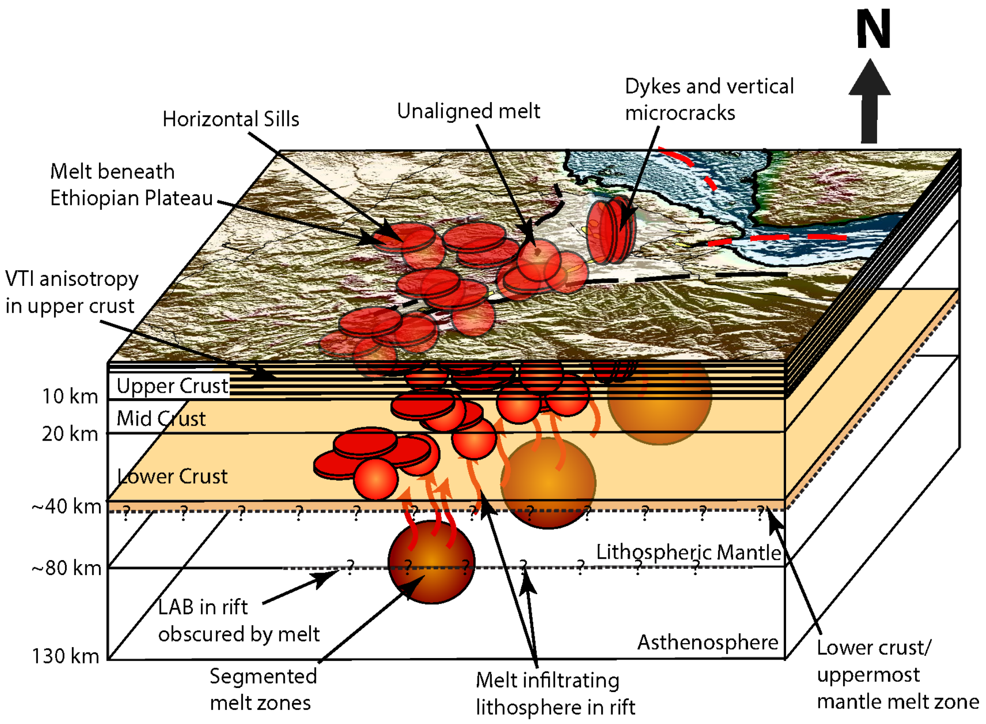

Figure 5.7: Schematic of the magmatic plumbing system beneath the northern East African Rift. Within the upper crust horizontal layering is pervasive and interpreted as alternating continental crust and mafic intrusions. Sills (red horizontal discs) are then located in the mid and upper crustal layers both on rift and off rift. At lower crustal depths melt is stored in sills and as heterogeneous structures (red circles) reflective of the reduced anisotropy with slow velocity. As rifting progresses melt storage rotates from horizontal sills to vertical dykes (vertical red discs) beneath the Erta Ale magmatic segment, which are likely interspersed with vertical cracks that extend from the base of the crust to the surface. At uppermost mantle depths a slow velocity melt zone is likely present beneath the full system though its thickness is unknown (orange layer). Features visible at the surface are more transparent at deeper depths. We also show the structure in the Lithospheric mantle and upper asthenosphere based on Chambers et al., (in review) where segmented melt zones (Large orange/brown spheres) at asthenospheric depths are located beneath the rift axis with melt infiltrating the lithosphere (red arrows) and obscuring the Lithosphere Asthenosphere Boundary at 60 – 80 km depth (dashed line with ? at ~80 km depth).

5.6 Conclusions

We determine the radial anisotropy using surface waves from Love and Rayleigh waves from 13 – 26 s period finding Love waves 0.40 ± 0.03 km/s faster than Rayleigh waves for a 1-D model. In the crust we require an anisotropic model from 5 – 30 km and deeper than 30 km radial anisotropy is not required. We observe $V_{SH} > V_{SV}$ across most of our study suggesting the crust is inherently layered. Effective medium calculations indicate thin compositional layering of felsic crust and mafic intrusions can account for up to 4% of the anisotropy including horizontally polarised anisotropy in Afar. However, to reconcile larger anisotropy in the MER and Ethiopian Plateau where we observe the lowest velocities and largest anisotropy (up to 7%), partial melt is required, stored as stacked sills. Our model suggests the largest anisotropy and lowest velocities beneath both the MER and Ethiopian Plateau can be interpreted as stacked sills in the upper-mid crust both on and off rift. In the southern MER radial anisotropy is horizontally aligned and gets progressively weaker towards areas at more advanced rifting suggesting stacked sills in the upper-mid crust become less dominant with progressive rifting. Similarly, anisotropy is weaker at lower crustal depths (16 - 30 km) but velocities are slow enough to require melt which we interpret as melt stored as sills and isotropic bodies. As the rift widens and crust thins anisotropy reduces suggesting melt storage changes from dominantly horizontally aligned (sills) to vertical (dykes) or unaligned melt. Beneath the EAMS we observe $V_{SV} > V_{SH}$, which we interpret as vertically aligned micro-cracks and dykes providing conduits for vertical flow of melt to feed recent eruptions. Our results suggest rift width and crustal thickness provide controls on how melt is stored in the crust and stacked sills may be pervasive both on and off rift in narrow rift zones.

5.7 Acknowledgments

E.L.C acknowledges funding from NERC studentship NE/L002531/1. C.A.R. and N.H. acknowledge funding from NERC grants NE/M003507/1 and NE/K010654/1 and ERC grant GA 638665. D.K. is supported by NERC grant NE/L013932 and by MiUR through PRIN grant 2017P9AT72. All data used in these models are freely available from the IRIS Data Management Center (IRISDMC; https://service.iris.edu/fdsnws/dataselect/1/). IRIS Data Services are funded through SAGE Proposal of the NSF under Cooperative Agreement EAR-126168. We thank SEIS-UK for use of instruments and computing facilities. The facilities of SEIS-UK are supported by NERC under agreement R8/H10/64.F. Some figures were made using GMT (Wessel and Smith, 2013).

Chapter 6

Conclusions

This final chapter aims to summarise the findings of my analyses and then to discuss these results in a wider context, highlighting how the research questions have been addressed.

6.1 Summary of findings and addressing Questions

Below are the questions that I set out to address. After each question I state the findings from the thesis that best answer these initial questions.

6.1.1 What is the seismic structure of the crust within the northern East African Rift System and how does it inform our understanding of continental rifting in melt rich environments?

The first chapter of my thesis generated an absolute shear velocity model from Rayleigh waves of ambient noise data which captured the seismic structure of the crust and uppermost mantle from 5 - 40 km depth, at 50 - 100 km lateral resolution (Chapter 3) (Figure 6.1).

At crustal depths, large lateral variations in velocity can partly be attributed to changes in crustal thickness. The seismic structure in areas away from the rift, such as the Somalian and western part of the Ethiopian Plateau, is fast which I interpret as areas that have not undergone significant rifting or been affected by the flood basalt event 30 Ma. These areas probably best reflect the crustal structure pre-rifting. I observe the slowest velocities beneath the MER and Ethiopian Plateau which require a component of partial melt. Shear velocities beneath the MER are the slowest in the region interpreted as melt focusing from dramatic changes in lithospheric topography coupled with longer residence times and complex magmatic pathways within the crust.

Beneath the eastern part of the Ethiopian Plateau, which was significantly intruded during the emplacement of the Oligocene flood basalts, velocities are laterally heterogeneous with two areas of slow velocity that are as slow as the MER. One is located southeast of Lake Tana and the other east of Lake Tana near the western border fault. The variations in velocity suggest a complex geological history and an inhomogeneous magma distribution during evolution. Furthermore, the velocities are slow enough to require melt suggesting there is ongoing magmatic activity off rift beneath the Ethiopian Plateau. The slow velocities of the MER connect to those of the Plateau in the lower crust and upper most mantle suggesting a similar origin. The velocities are slow enough to be best explained with partial melt though composition and elevated temperatures may also contribute.

The velocity structure within Afar is faster than the MER with slow velocities focussed to the magmatic segments again suggesting an interpretation of melt that feeds the volcanism. Velocities within the Erta Ale segment at crustal depths are the fastest in our study which likely reflects the thinner crust and more mafic composition of the crust. Geochemical analysis find more mafic compositions interpreted as shorter melt residence times in Afar than within the MER (Hutchison et al., 2018) and explains the absence of slow velocities beneath Afar. Further interpretations of the geochemistry suggest melt is more likely to be stored as dykes in Afar and as sills in the MER. We test this hypothesis in Chapter 5.

Our absolute shear velocity model provides evidence for more protracted melt storage in the crust during the earlier stages of rifting (e.g. the MER). Melt accumulation is particularly localised near the Moho but distributed spatially across a relatively broad region beneath the rift valley and surrounding plateaus. This contributes to the growing body of evidence that deep crustal magma complexes play an important role in the evolution of magma in continental rifts (Annen et al., 2006). In Afar, faster crustal seismic velocities are mostly consistent with a crust rich in frozen mafic rock, denser than continental crust. The time-accumulation of dense mafic intrusion during progressive rifting, coupled with ongoing crustal thinning likely aids melt ascent through the crust during continued continental breakup in contrast to the thicker crust of the Ethiopian plateau and MER. Beneath the northwestern plateau localised melt emplacement and related hydrothermal processes continue outside of the rift valley to the present day. This interpretation is somewhat contrary to the widely held belief that all magmatism becomes localised to a rift valley during progressive rifting though new GPS constraints from Ethiopia show the presence of ongoing extension of the plateau (Birhanu et al., 2016) providing a mechanism to explain recent magmatic processes here, and supports the view that extension coupled with magmatism may remain distributed later into the breakup process than previously believed.

6.1.2 At what stage does segmentation of the melt zone occur in the breakup process and how does melt migrate into the lithosphere?

The second chapter performed a joint inversion between Rayleigh waves from ambient noise and teleseisms from 10 - 210 km depth which broadly shows the same seismic structure in the crust and upper most mantle but expands further in depth and laterally beneath the Ethiopian Plateau. The Ethiopian Plateau was a region not previously tomographically imaged. Broadly, the shear velocity structure is laterally heterogeneous particularly in the crust as discussed above (Chapter 4) (Figure 6.1).

At mantle depths, velocities are slow everywhere compared to the global average of 4.45 km/s using ak135 (Kennett et al., 1995). Off rift, shear velocities of 4.30 km/s can be explained by elevated mantle temperatures. Velocities beneath the rift are slower than off rift (<4.10 km/s)

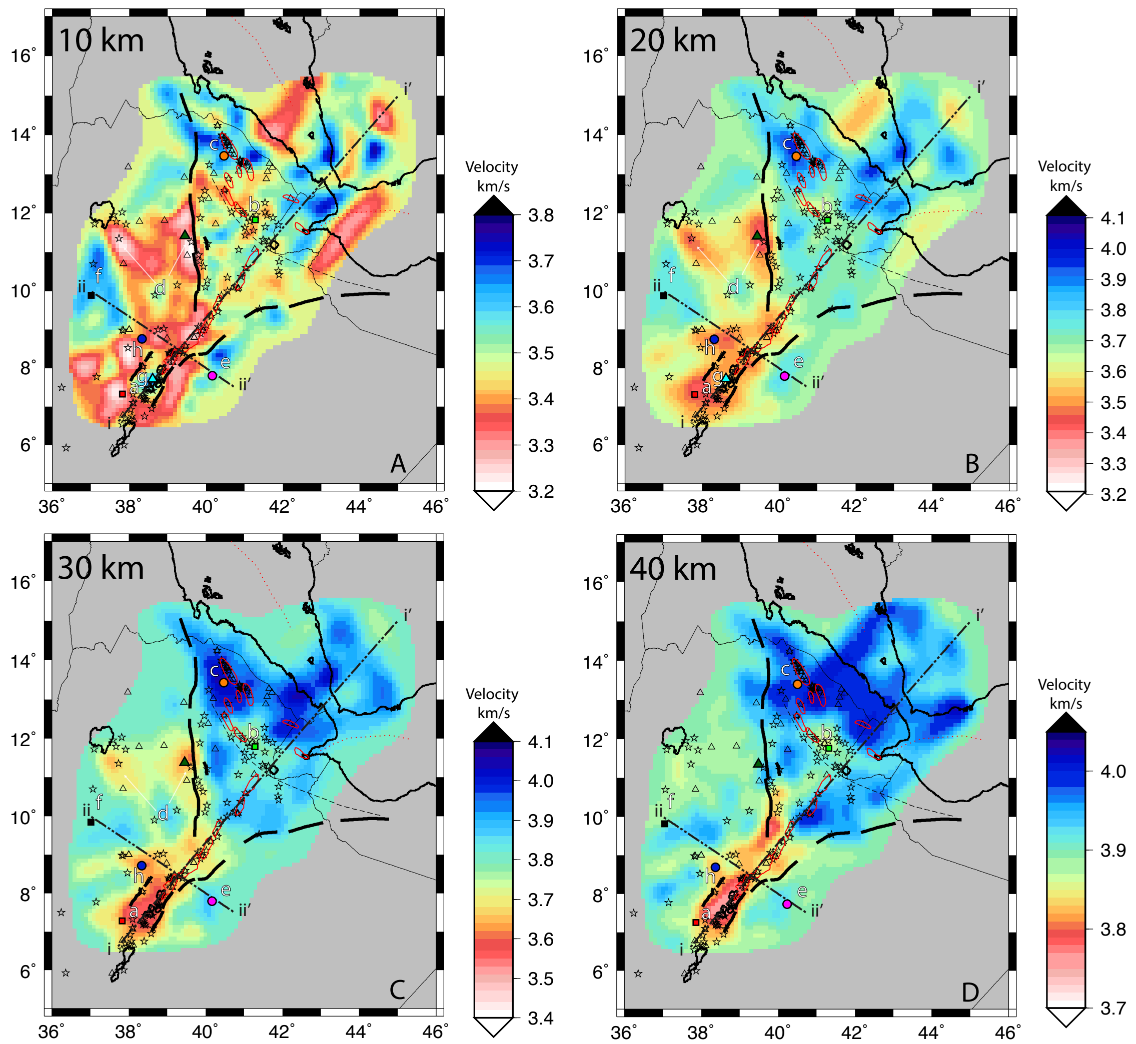

Figure 6.1: Interpolated absolute shear wave velocity at 10, 20, 30 and 40 km depth labelled A-D respectively showing seismic structure beneath the region from ambient noise tomography. Models have been cropped to the standard error contour. Red indicates slower velocities and blue faster velocities. Thick black lines indicate border faults. Red polygons indicate magmatic segments, red triangles volcanoes, and black stars geothermal activity. From Chapter 3.

and are best explained with a component of partial melt. Along the rift, slow velocities are segmented at asthenospheric depths getting progressively shallower and broader in lateral extent northwards, towards areas at a more advanced stage of rifting (Figure 6.2). The slow velocity segments are present at the earliest stages of rifting beneath areas where the crust has not significantly thinned. These observations suggest segmented melt supply starts prior to significant crustal and plate thinning, implying the magma assisted rifting model of Buck (2006) is most similar to the processes occurring in the northern EAR, with melt crucial to initially weakening the plate and allowing rifting to develop.

Segmentation beneath rifts is not isolated to this study and has been observed beneath more mature oceanic rifts (e.g. Gulf of California, Red Sea Rift, the Mid Atlantic Ridge (Lekic et al., 2011; Ligi et al., 2012; Wang et al., 2009) and beneath the East African Rift (Civiero et al., 2015, 2019; Gallacher et al., 2016; Hammond et al., 2013). Beneath more mature rifts active upwelling is considered to be a mechanism to increase melt production (Buck and Su, 1989; Eilon and Abers, 2017) and generate segmentation (Nielsen and Hopper, 2004; Wang et al., 2009). Our observations suggest the processes controlling segmentation develop early during the rifting process and are active through continental breakup and into seafloor spreading.

At lithosphere-asthenosphere-boundary depths there is evidence for a fast lid at 60 - 80 km depth. This boundary is visible off rift, however within the rift the fast boundary is obscured which is interpreted as melt infiltrating to shallower depths. The absence of a fast lid at lithosphere asthenosphere boundary depths within the rift can be explained as due to melt, likely sourced from a segmented melt zone, infiltrating the lithosphere directly beneath the rift. The fast lid is present off rift. By near-Moho depths, the mantle is slow everywhere suggesting there is an uppermost mantle melt zone restricted by the viscosity difference between the crust and underlying mantle.

At crustal depths within the northern East African Rift, geophysical techniques suggest there is pervasive melt in the mantle and crust with hydrothermal activity in the upper crust (e.g. Whaler and Hautot, 2006; Keir et al., 2009a; Hautot et al., 2006; Hammond et al., 2011; Ferguson et al., 2013; Maguire et al., 2006; Cornwell et al., 2010). While the slowest velocities in the asthenosphere are focussed to the rift, those within the crust and uppermost mantle are offset suggesting melt laterally migrates within the mantle or that melt is ephemeral with the source for the crustal slow velocities off rift effectively drained. Lateral melt migration has been observed at fully developed mid ocean ridges such as the fast spreading East Pacific Rise (Varga et al., 2008), the Gulf of California (Wang et al., 2009) and the slower spreading Mid Atlantic Ridge (Braun and Sohn, 2003; Ghods and Arkani-Hamed, 2000). Within our study area lateral melt migration has been observed during the Dabbahu rifting episode (2005 – 2010) where melt migrated >80 km along rift near the base of the crust (Grandin et al., 2012; Illsley-Kemp et al., 2018a).

6.1.3 What is the shape of melt within the crust and how does this change with progressive rifting?

The final chapter produced a model for radial anisotropy using Love and Rayleigh waves (Chapter 5) in order to understand variations in how melt is stored within the crust. I find that anisotropy is present for depths of 5 - 30 km but is not required at greater depths.

Within the crust $V_{SH} > V_{SV}$ across most of the region suggesting the crust has an inherently layered structure. Effective medium calculations suggest some of the anisotropy (up to 4%) can be attributed to thin layering of solidified mafic intrusions and continental crust. The strongest horizontally polarised anisotropy is beneath the eastern part of the Ethiopian Plateau (2.5 to 6.5%) suggesting the Ethiopian Plateau is significantly layered with melt present as horizontal sills in the upper to mid crust. I observe similarly strong anisotropy in the upper and mid crust of the MER (2.5 - 6%) which I again interpret as horizontal layering with melt present as sills. The strongest $V_{SH} > V_{SV}$ radial anisotropy in this area is consistently in the upper crust at 5 - 15 km depth, suggesting either the density structure of the crust or the state of stress is amenable to sill formation. Furthermore, velocities at lower crustal depths remain slow despite weakening anisotropy suggesting melt is required but is stored as a combination of stacked sills and uniform melt bodies.

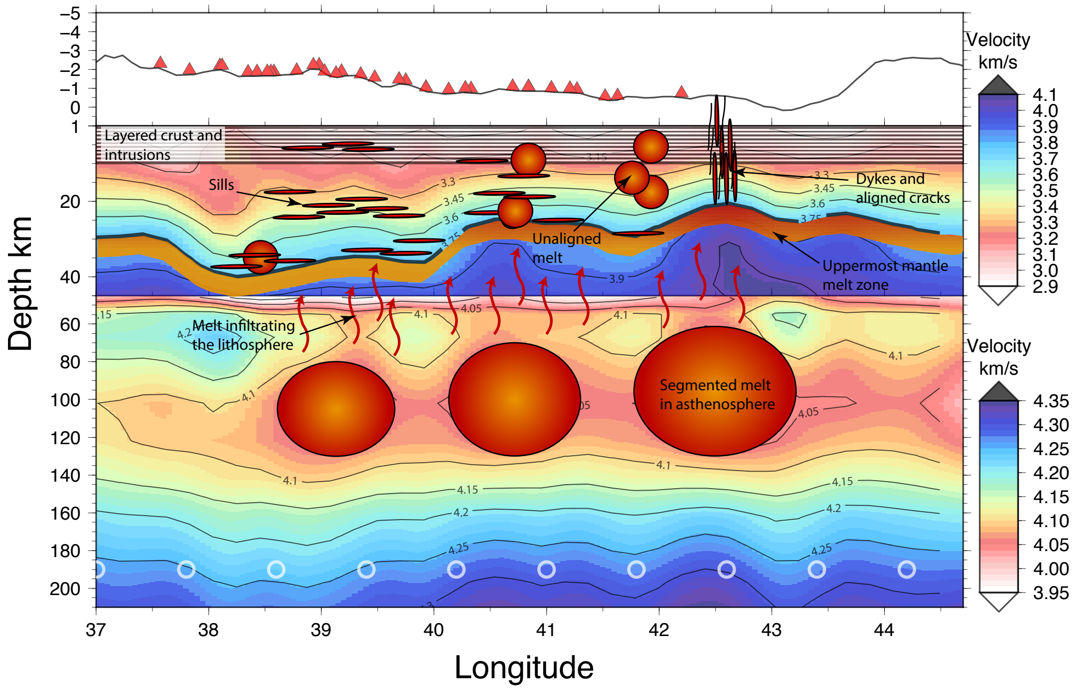

FIGURE 6.2: Modified cross section along rift of the asthenospheric segmentation and how it connects to the plumbing system above. The rift contains discrete segmented slow velocity zones containing melt (circles 65 - 130 km depth) which get progressively larger and shallower towards more advanced rifting. The most southerly segment, reflecting the youngest rifting, is beneath crust that has not undergone significant thinning. Melt from the segments propagates upwards infiltrating the lithosphere (red arrows) and the fast lid at lithosphere asthenosphere boundary depths imaged off rift is not present within the rift. At uppermost mantle depths a slow velocity melt zone is likely present beneath the full system though the extent is unknown. As rifting progresses melt storage rotates from horizontal sills (horizontal red discs) to vertical dykes (linear red discs) beneath the Erta Ale segment which are likely interspersed with vertical cracks that extend from the base of the crust to the surface.

Radial anisotropy becomes weaker along rift from 6% in the southern MER to 2% in the northern MER and -1% ($V_{SV} > V_{SH}$) in the Erta Ale magmatic segment. I also observe anisotropy beneath the full rift width in the south which localises to the magmatic segments in the north. These observations can be interpreted either as a change from sill emplacement in the narrow MER (horizontal red discs Figure 6.3) to dyke emplacement (vertical red discs Figure 6.3) in Afar or a reduction in the melt present in the crust towards later stage rifting. These observations are in good agreement with geochemical studies that suggest melt has a primary mantle origin and propagate as dykes in Afar, whereas more crustal assimilation and evolved magmas are observed in the MER where melt is thought to be stored as sills (Hutchison et al., 2018). Furthermore, in the East African Rift system, we expect the density structure and stress regime to change as the relatively thick continental crust and narrow rift in the MER transitions to the thin crust and broader rift zone of the Afar region based on numerical models of rift evolution (Maccaferri et al., 2011, 2014).

The presence of stacked sills in the crust of a narrow rift and dykes at a wider rift are observed in other rifting/mid-ocean ridge regions and volcanic regions around the globe. Analysis of other rift systems also find evidence for melt storage changing from stacked sills in the crust within a narrow rift, to dykes in wider rifting areas (Thybo and Nielsen, 2009; Russell et al., 2019). In regions of upwelling such as the East Pacific Rise vertical anisotropy ($V_{SV} > V_{SH}$) is observed

(Toomey et al., 2007) and interpreted as vertical flow of melt, similarly to what I observe within the Erta Ale magmatic segment. The new knowledge of the structure and depth of melt storage and the ascent mechanism of melt is important for our understanding of the evolution of rifting.

6.2 The Overall Picture and What is New

This thesis provides new insight into the velocity structure and distribution of melt beneath the northern East African Rift. Of particular note is the generation of an integrated seismic model from 5 - 210 km depth for all areas of the northern part of the East African Rift allowing comparisons between all areas of the rift. In addition, this is the first study to tomographically image the Ethiopian Plateau providing additional information on how rifting affects areas off rift.

I display the overall findings of this thesis in Figure 6.3.

6.3 Further Research

Following the results of this thesis there are still several unknowns. Radial anisotropy, while useful to characterise the shape of melt and structures within the crust, is not sufficient to determine the orientation of the anisotropy. Determining azimuthal anisotropy would provide knowledge on the orientation of structures in the lithosphere and potential flow patterns. This is of particular importance between the Main Ethiopian Rift and Ethiopian Plateau where there is potential for off axis lateral melt migration and the source of melt beneath the Ethiopian Plateau is debated.

Another area of research is to focus on variations through time in the ambient noise tomography, particularly in areas of recent intrusions such as the Dabbahu dyking event and the Erta Ale eruptions. The velocity models I have created are a snapshot of 20 years of seismometer deployments. While I have gained insight into how the crust is modified at different stages of rifting by comparing the Ethiopian Plateau, MER and Afar, variations in the seismic velocity structure over time have not been highlighted. Looking at how the tomography changes before, during and after an eruption may provide clues into the active processes of rifting. Furthermore, to provide better resolution and more results, time variant ambient noise could be deployed. Many of the seismic networks are present for a short time period providing only a few years' worth of data in each location. By performing cross correlations between pairs of stations present at different time periods and linking to a permanent station would increase ray coverage in sparsely populated areas and provide a better resolved velocity model.

Finally, this thesis has focused on the northern East African Rift but has not linked into the rest of the East African Rift where processes and seismic structure of the crust are likely to have significant differences. In the future we will require one absolute velocity model of the full rift at a resolution of 10s of kms (or better) to truly compare variations in crustal structure as rifting progresses.

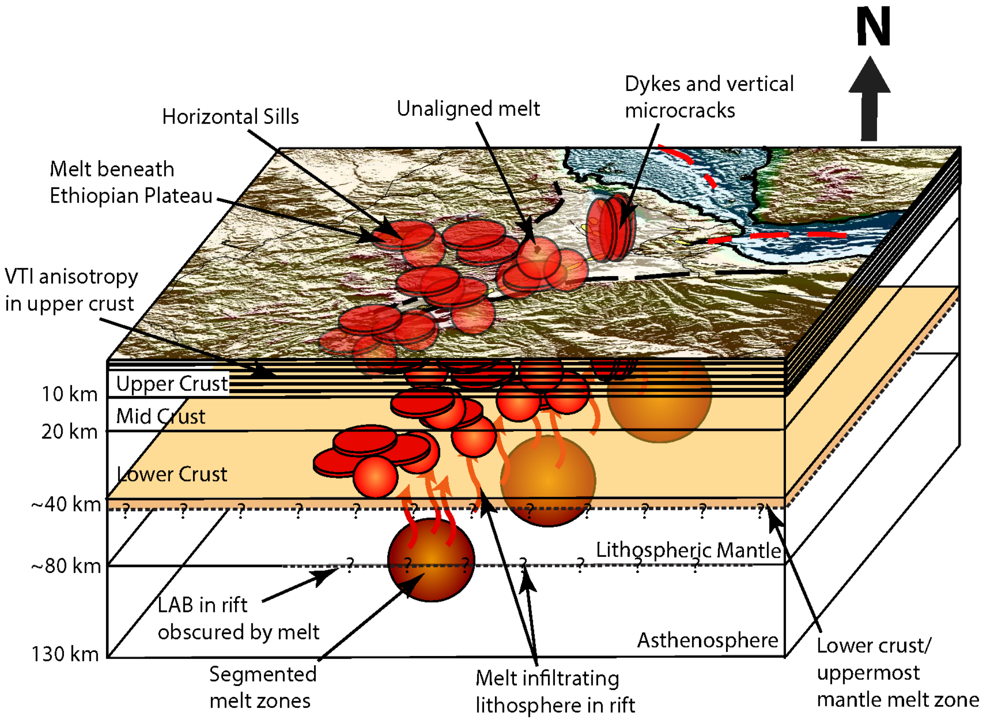

Figure 6.3: Schematic of the magmatic plumbing system beneath the northern East African Rift based on the conclusions of this thesis. Within the upper crust horizontal layering is pervasive and interpreted as alternating continental crust and mafic intrusions. Sills (red horizontal discs) are then located in the mid and upper crustal layers both on rift and off rift. At lower crustal depths melt is stored in sills and as heterogeneous structures (red circles) reflective of the reduced anisotropy with slow velocity. As rifting progresses melt storage rotates from horizontal sills to vertical dykes (vertical red discs) beneath the Erta Ale magmatic segment, which are likely interspersed with vertical cracks that extend from the base of the crust to the surface. At uppermost mantle depths a slow velocity melt zone is likely present beneath the full system though its thickness is unknown (orange layer). Features visible at the surface are more transparent at deeper depths. At lithosphere-asthenosphere-boundary depths a fast lid is present off rift but is obscured by melt within the rift (black curved arrows). Within the asthenosphere, the rift contains discrete segmented slow velocity zones containing melt (circles 65 - 130 km depth) which get progressively larger and shallower towards more advanced rifting. The most southerly segment reflecting the youngest rifting is beneath crust that has not undergone significant thinning suggesting melt supply starts prior to significant crustal thinning.

Appendix A

Supplementary Material for Chapter 3: Using Ambient Noise to Image the Northern East African rift

Supplementary material for **Chambers, E. L.**, Harmon, N., Keir, D., and Rychert, C. A. (2019). Using Ambient Noise to Image the Northern East African Rift. *Geochemistry, Geophysics, Geosystems,* 20, 2091-2109. (Chambers et al., 2019).

In this supplementary part, we show a figure displaying additional resolution tests at a larger number of periods. These supplement Figure 3 in the main text in which we show the 8s and 33s period tests. Here in Figure S1 we display additional checkerboard tests at 10, 15, 20, 25 and 30 seconds period.

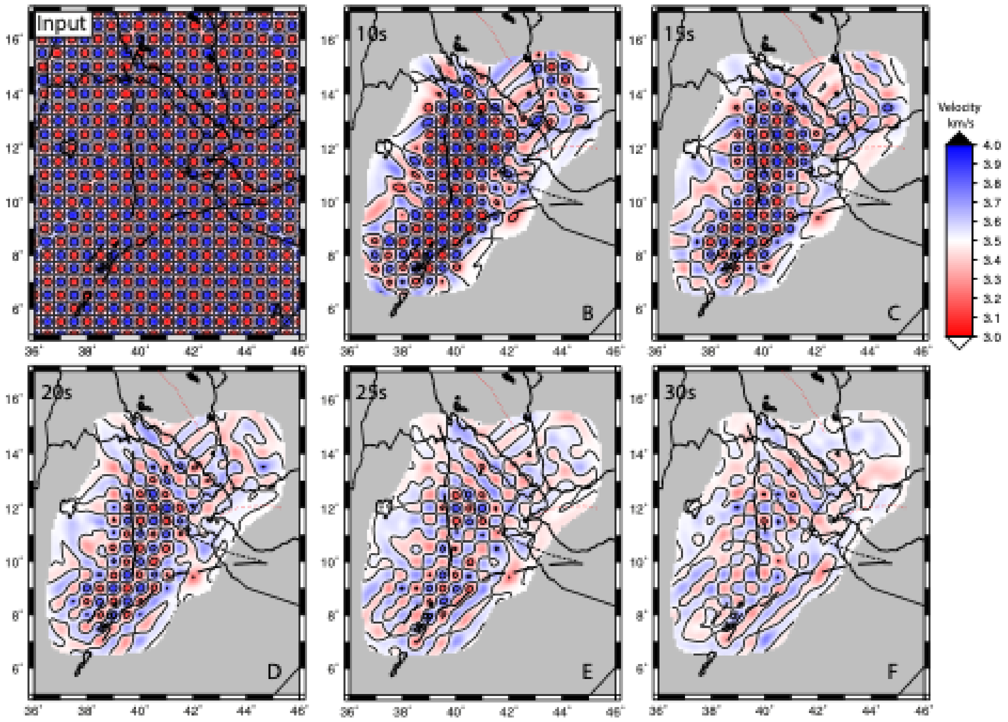

FIGURE A.1: Checkerboard tests for 0.5° × 0.5°. Initial model shown in A) with B) -F) the output model at 10, 15, 20, 25 and 30s respectively. Figure 3 in the main text shows 8 and 33s, the limits of our study. Results are cropped outside the 0.7 standard error contour.

Appendix B

Supplementary Material for Chapter 4: A joint inversion of Rayleigh waves from ambient noise tomography and teleseisms to image melt and seismic structure in the northern East African Rift

Supplementary material for **Chambers, E. L.**, Harmon, N., Keir, D., Rychert, C. A. and Gallacher, R. (in review). A joint inversion of Rayleigh waves from ambient noise tomography and teleseisms to image melt and seismic structure in the northern East African Rift. *Journal of Geophysical Research: Solid Earth.*

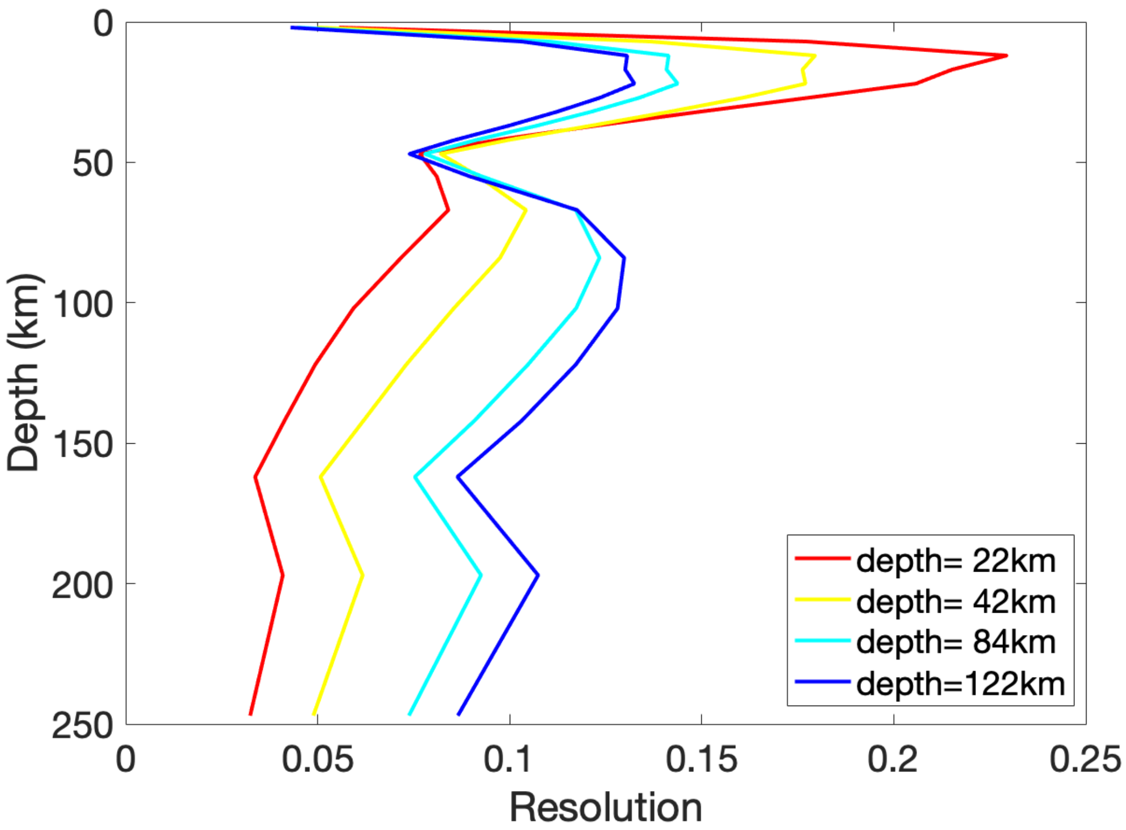

FIGURE B.1: Backus-Gilbert resolution kernels for depths of 22, 42, 84 and 122 km depth. Smearing ranges from ± 10 km at 22 km depth to ± 45 km at 122 km depth.

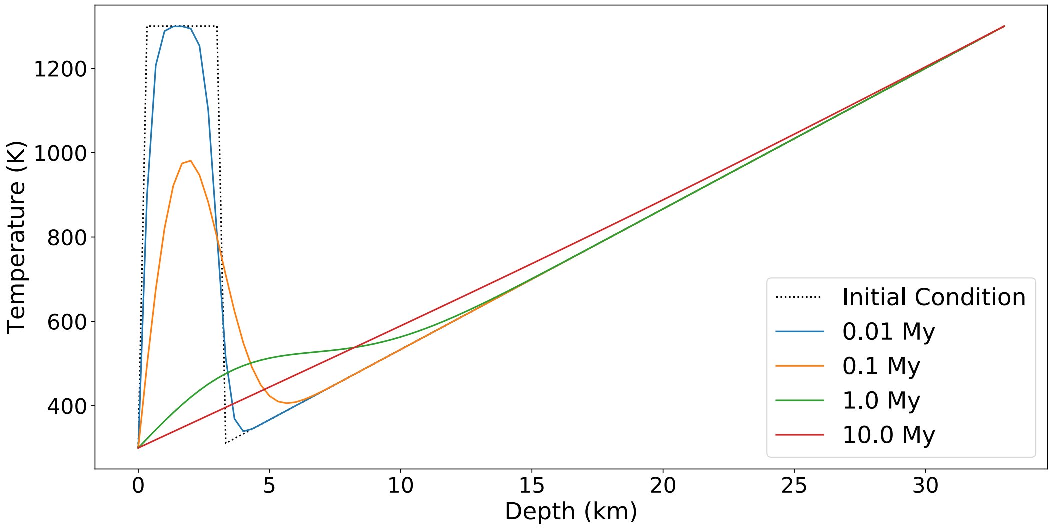

FIGURE B.2: Cooling rate for a 3 km thick flood basalt emplaced at the surface. Black dotted line is initial temperate gradient assuming the flood basalt is 1300K and the crust (30 km thick) linearly increases from 300 – 1300 K. The blue, orange, green and red lines are the temperature profile after 10,000, 100,000, 1,000,000 and 10,000,000 years respectively. By 1 My, the temperature is nearly at equilibrium and by 10 My is at background temperatures. The Ethiopian Flood Basalt was emplaced 30 Million years ago.

Bibliography

Ahmed, A., Tiberi, C., Leroy, S., Stuart, G. W., Keir, D., Sholan, J., Khanbari, K., Al-Ganad, I., and Basuyau, C. (2013). Crustal structure of the rifted volcanic margins and uplifted plateau ofwestern yemen from receiver function analysis. *Geophysical Journal International*, 193(3):1673–1690.

Aki, K. and Richards, P. G. (1980). *Quantitative Seismology.* 2nd edition.

Albaric, J., Déverchère, J., Perrot, J., Jakovlev, A., and Deschamps, A. (2014). Deep crustal earthquakes in North Tanzania, East Africa: Interplay between tectonic and magmatic processes in an incipient rift. *Geochemistry, Geophysics, Geosystems*, 15(2):374–394.

Annen, C., Blundy, J. D., and Sparks, R. S. J. (2006). The genesis of intermediate and silicic magmas in deep crustal hot zones. *Journal of Petrology*, 47(3):505–539.

Armitage, J. J., Ferguson, D. J., Goes, S., Hammond, J. O. S., Calais, E., Rychert, C. A., and Harmon, N. (2015). Upper mantle temperature and the onset of extension and break-up in Afar, Africa. *Earth and Planetary Science Letters*, 418:78–90.

Armitage, J. J., Petersen, K. D., and Pérez-Gussinyé, M. (2018). The Role of Crustal Strength in Controlling Magmatism and Melt Chemistry During Rifting and Break-Up. *Geochemistry, Geophysics, Geosystems.*

Ayele, A., Stuart, G. W., and Kendall, J.-M. (2004). Insights into rifting from shear wave splitting and receiver functions: An example from Ethiopia. *Geophysical Journal International*, 157(1):354–362.

Babuska, V. and Cara, M. (1991). *Seismic Anisotropy in the Earth.* Kluwer Academic Publishers, London, volume 10 edition.

Backus, G. E. (1962). Long-wave elastic anisotropy produced by horizontal layering. *Journal of Geophysical Research*, 67(11):4427–4440.

Backus, G. E. and Gilbert, F. (1970). Uniqueness in the inversion of inaccurate gross Earth data. *Philosophical Transactions of the Royal Society of London. Series A, Mathematical and Physical Sciences*, 266:123–192.

Bagley, B. and Nyblade, A. A. (2013). Seismic anisotropy in eastern Africa, mantle flow, and the African superplume. *Geophysical Research Letters*, 40(8):1500–1505.

Barberi, F., Tazieff, H., and Varet, J. (1972). Volcanism in the Afar Depression: Its Tectonic and Magmatic Significance. *Developments in Geotectonics*, 7(C):19–29.

Barmin, M. P., Ritzwoller, M. H., and Levshin, A. L. (2001). A Fast and Reliable Method for Surface Wave Tomography. *Pure and Applied Geophysics*, 158:1351–1375.

Barnie, T. D., Keir, D., Hamling, I. J., Hofmann, B., Belachew, M., Carn, S. A., Eastwell, D., Hammond, J. O. S., Ayele, A., Oppenheimer, C., and Wright, T. J. (2016). A multidisciplinary study of the final episode of the Manda Hararo dyke sequence, Ethiopia, and implications for trends in volcanism during the rifting cycle. *Geological Society, London, Special Publications*, 420(1):149–163.

Bastow, I. D. and Keir, D. (2011). The protracted development of the continent-ocean transition in Afar. *Nature Geoscience*, 4(4):248–250.

Bastow, I. D., Keir, D., and Daly, E. (2011). The Ethiopia Afar Geoscientific Lithospheric Experiment (EAGLE): Probing the transition from continental rifting to incipient seafloor spreading. *The Geological Society of America Special Papers*, 478:51–76.

Bastow, I. D., Nyblade, A. A., Stuart, G. W., Rooney, T. O., and Benoit, M. H. (2008). Upper mantle seismic structure beneath the Ethiopian hot spot: Rifting at the edge of the African low-velocity anomaly. *Geochemistry, Geophysics, Geosystems*, 9(12).

Bastow, I. D., Owens, T. J., Helffrich, G., and Knapp, J. H. (2007). Spatial and temporal constraints on sources of seismic anisotropy: Evidence from the Scottish highlands. *Geophysical Research Letters*, 34(5).

Bastow, I. D., Pilidou, S., Kendall, J.-M., and Stuart, G. W. (2010). Melt-induced seismic anisotropy and magma assisted rifting in Ethiopia: Evidence from surface waves. *Geochemistry, Geophysics, Geosystems*, 11(6):1–19.

Bastow, I. D., Stuart, G. W., Kendall, J.-M., and Ebinger, C. J. (2005). Upper-mantle seismic structure in a region of incipient continental breakup: Northern Ethiopian rift. *Geophysical Journal International*, 162(2):479–493.

Beccaluva, L., Bianchini, G., Natali, C., and Siena, F. (2009). Continental flood basalts and mantle plumes: A case study of the Northern Ethiopian Plateau. *Journal of Petrology*, 50(7):1377–1403.

Belachew, M., Ebinger, C. J., Coté, D., Keir, D., Rowland, J. V., Hammond, J. O. S., and Ayele, A. (2011). Comparison of dike intrusions in an incipient seafloor-spreading segment in Afar, Ethiopia: Seismicity perspectives. *Journal of Geophysical Research: Solid Earth*, 116(6):1–23.

Benoit, M. H., Nyblade, A. A., and VanDecar, J. C. (2006). Upper mantle P-wave speed variations beneath Ethiopia and the origin of the Afar hotspot. *Geology*, 34(5):329–332.

Bensen, G. D., Ritzwoller, M. H., Barmin, M. P., Levshin, A. L., Lin, F.-C., Moschetti, M. P., Shapiro, N. M., and Yang, Y. (2007). Processing seismic ambient noise data to obtain reliable broad-band surface wave dispersion measurements. *Geophysical Journal International*, 169(3):1239–1260.

Berckhemer, H., Baier, B., Bartelsen, H., Behle, A., Burkhardt, H., Gebrande, H., Makris, J., Menzel, H., Miller, H., and Vees, R. (1975). Deep seismic soundings in the Afar region and on the highland of Ethiopia. In Pilger, A. and Rosler, A., editors, *Afar Depression of Ethiopia*, chapter Afar Geoph, pages 89–107. E. Schweizerbart'sche Verlagsbuchhandlung, Stuttgart.

Berhe, S. (1990). Ophiolites in Northeast and East Africa: implications Proterozoic crustal growth for. *Journal of the Geological Society London*, 147:41–57.

Biggs, J., Bastow, I. D., Keir, D., and Lewi, E. (2011). Pulses of deformation reveal frequently recurring shallow magmatic activity beneath the Main Ethiopian Rift. *Geochemistry, Geophysics, Geosystems*, 12(9):1–11.

Bilham, R., Bendick, R., Larson, K., Mohr, P., Braunmiller, J., Tesfaye, S., and Asfaw, L. (1999). Secular and tidal strain across the Main Ethiopian Rift. *Geophysical Research Letters*, 26(18):2789–2792.

Birch, F. (1960). The velocity of compressional waves in rocks to 10 kilobars, Part 1. *Journal of Geophysical Research*, 65(4):1083–1102.

Birhanu, Y., Bendick, R., Fisseha, S., Lewi, E., Floyd, M., King, R., and Reilinger, R. (2016). GPS constraints on broad scale extension in the Ethiopian Highlands and Main Ethiopian Rift. *Geophysical Research Letters*, 43(13):6844–6851.

Bonatti, E. (1985). Punctiform initiation of seafloor spreading in the Red Sea during transition from a continental to an oceanic rift. *Nature*, 316:33–37.

Boschi, L. and Weemstra, C. (2015). Stationary-phase integrals in the cross correlation. *Reviews of Geophysics*, 53:411–451.

Boschi, L., Weemstra, C., Verbeke, J., Ekström, G., Zunino, A., and Giardini, D. (2013). On measuring surface wave phase velocity from station-station cross-correlation of ambient signal. *Geophysical Journal International*, 192(1):346–358.

Bosworth, W. (1987). Off-axis volcanism in the Gregory rift, east Africa: Implications for models of continental rifting'. *Geology*, 15:397–400.

Bosworth, W., Huchon, P., and McClay, K. (2005). The Red Sea and Gulf of Aden Basins. *Journal of African Earth Sciences*, 43(1-3):334–378.

Braathen, A., Grenne, T., Selassie, M. G., and Worku, T. (2001). Juxtaposition of Neoproterozoic units along the Baruda-Tulu Dimtu shear-belt in the East African Orogen of western Ethiopia. *Precambrian Research*, 107:215–234.

Bradley, J. (1965). Intrusions of major dolerite sills. *Transactions of the Royal Society of New Zealand*, 3(4):27–55.

Braun, M. G. and Sohn, R. A. (2003). Melt migration in plume-ridge systems. *Earth and Planetary Science Letters*, 213(3-4):417–430.

Brisbourne, A. M. (2012). How to store and share geophysical data. *Astronomy and Geophysics*, 53(4).

Buck, W. R. (2004). Consequences of asthenospheric variability on continental rifting. In Karner G.D., Taylor B., D. N. &. K. D., editor, *Rheology and Deformation of the Lithosphere at Continental Margins*, pages 1–30. Columbia University Press, New York.

Buck, W. R. (2006). The role of magma in the development of the Afro-Arabian Rift System. *Geological Society, London, Special Publications*, 259(1):43–54.

Buck, W. R. and Su, W. (1989). Focussed mantle upwelling below mid-ocean ridges due to feedback between viscosity and melting. *Geophysical Research Letters*, 16(7):641–644.

Calais, E., D'Oreye, N., Albaric, J., Deschamps, A., Delvaux, D., Déverchère, J., Ebinger, C., Ferdinand, R. W., Kervyn, F., Macheyeki, A. S., Oyen, A., Perrot, J., Saria, E., Smets, B., Stamps, D. S., and Wauthier, C. (2008). Strain accommodation by slow slip and dyking in a youthful continental rift, East Africa. *Nature*, 456(7223):783–788.

Calais, E., Ebinger, C. J., Hartnady, C., and Nocquet, J. M. (2006). Kinematics of the East African Rift from GPS and earthquake slip vector data. *Geological Society, London, Special Publications*, 259:9–22.

Caricchi, L., Burlini, L., and Ulmer, P. (2008). Propagation of P and S-waves in magmas with different crystal contents : Insights into the crystallinity of magmatic reservoirs. *Journal of Volcanology and Geothermal Research*, 178(4):740–750.

Casey, M., Ebinger, C. J., Keir, D., Gloaguen, R., and Mohamed, F. (2006). Strain accommodation in transitional rifts: extension by magma intrusion and faulting in Ethiopian rift magmatic segments. *Geological Society, London, Special Publications*, 259(2003):143–163.

Cashman, K. V. and Giordano, G. (2014). Calderas and magma reservoirs. *Journal of Volcanology and Geothermal Research*, 288:28–45.

Chambers, E. L., Harmon, N., Keir, D., and Rychert, C. A. (2019). Using Ambient Noise to Image the Northern East African Rift. *Geochemistry, Geophysics, Geosystems*, 20:2091–2109.

Chambers, E. L., Harmon, N., Keir, D., Rychert, C. A., and Gallacher, R. J. (in review). A joint inversion of Rayleigh waves from ambient noise tomography and teleseisms to image melt and seismic structure in the northern East African Rift. *Journal of Geophysical Research: Solid Earth*.

Chen, W.-P. and Molnar, P. (1983). Focal depths of intracontinental and intraplate earthquakes and their implications for the thermal and mechanical properties of the lithosphere. *Journal of Geophysical Research*, 88:4183–4214.

Chorowicz, J. (2005). The East African rift system. *Journal of African Earth Sciences*, 43:379–410.

Christensen, N. I. (1996). Poisson's ratio and crustal seismology. *Journal of Geophysical Research*, 101(B2):3139–3156.

Christensen, N. I. and Mooney, W. D. (1995). Seismic velocity structure and composition of the continental crust: A global view. *Journal of Geophysical Research: Solid Earth (1978-2012)*, 100(B6):9761–9788.

Civiero, C., Armitage, J. J., Goes, S., and Hammond, J. O. S. (2019). The Seismic Signature of Upper-Mantle Plumes: Application to the Northern East African Rift. *Geochemistry, Geophysics, Geosystems*, pages 1–17.

Civiero, C., Goes, S., Hammond, J. O. S., Fishwick, S., Ahmed, A., Ayele, A., Doubre, C., Goitom, B., Keir, D., Kendall, J.-M., Leroy, S., Ogubazghi, G., Rümpker, G., and Stuart, G. W. (2016). Small-scale thermal upwellings under the northern East African Rift from S travel time tomography. *Journal of Geophysical Research : Solid Earth*, 2010:1–14.

Civiero, C., Hammond, J. O. S., Goes, S., Fishwick, S., Ahmed, A., Ayele, A., Doubre, C., Goitom, B., Keir, D., Kendall, J.-M., Leroy, S., Ogubazghi, G., Rümpker, G., and Stuart, G. W. (2015). Multiple mantle upwellings in the transition zone beneath the northern East-African Rift system from relative P-wave travel-time tomography. *Geochemistry, Geophysics, Geosystems*, 16(9):2949–2968.

Clarisse, L., Coheur, P. F., Theys, N., Hurtmans, D., and Clerbaux, C. (2014). The 2011 Nabro eruption, a SO2 plume height analysis using IASI measurements. *Atmospheric Chemistry and Physics*, 14(6):3095–3111.

Conticelli, S., Sintoni, M., Abebe, T., Mazzarini, F., and Manetti, P. (1999). Petrology and Geochemistry of Ultramafic Xenoliths and Host Lavas from the Ethiopian Volcanic Province: an insight into the Upper Mantle under Eastern Africa. *Acta Vulcanologica*, 11(January 1999).

Corbeau, J., Rolandone, F., Leroy, S., Al-Lazki, A., Stork, A. L., Keir, D., Stuart, G. W., Hammond, J. O., Doubre, C., Vergne, J., Ahmed, A., and Khanbari, K. (2014). Uppermost mantle velocity from Pn tomography in the Gulf of Aden. *Geosphere*, 10(5):958–968.

Cornwell, D. G., Mackenzie, G. D., England, R. W., Maguire, P. K. H., Asfaw, L., and Oluma, B. (2006). Northern Main Ethiopian Rift crustal structure from new high-precision gravity data. *Geological Society, London, Special Publications*, 259(1):307–321.

Cornwell, D. G., Maguire, P. K. H., England, R. W., and Stuart, G. W. (2010). Imaging detailed crustal structure and magmatic intrusion across the Ethiopian Rift using a dense linear broadband array. *Geochemistry, Geophysics, Geosystems*, 11(1).

Corti, G. (2009). Continental rift evolution: From rift initiation to incipient break-up in the Main Ethiopian Rift, East Africa. *Earth-Science Reviews*, 96(1-2):1–53.

Corti, G. (2012). Tectonophysics Evolution and characteristics of continental rifting : Analog modeling-inspired view and comparison with examples from the East African Rift System. *Tectonophysics*, 522-523:1–33.

Corti, G., Philippon, M., Sani, F., Keir, D., and Kidane, T. (2013). Re-orientation of the extension direction and pure extensional faulting at oblique rift margins: Comparison between the Main Ethiopian Rift and laboratory experiments. *Terra Nova*, 25(5):396–404.

Courtillot, V., Jaupart, C., Manighetti, I., Tapponnier, P., and Besse, J. (1999). On causal links between flood basalts and continental breakup. *Earth and Planetary Science Letters*, 166(3-4):177–195.

Craig, T. J., Jackson, J. A., Priestley, K., and Mckenzie, D. (2011). Earthquake distribution patterns in Africa: Their relationship to variations in lithospheric and geological structure, and their rheological implications. *Geophysical Journal International*, 185(1):403–434.

Crampin, S. (1994). The fracture criticality of crustal rocks. *Geophysical Journal International*, 118(2):428–438.

Crampin, S. and Kirkwood, S. C. (1981). Velocity Variations In Systems Of Anisotropic Symmetry. *Journal Of Geophysics-Zeitschrift Fur Geophysik*, 49(1):35–42.

Dalton, C. A., Gaherty, J. B., and Courtier, A. M. (2011). Crustal VS structure in northwestern Canada: Imaging the Cordillera-craton transition with ambient noise tomography. *Journal of Geophysical Research: Solid Earth*, 116(12):1–30.

Daly, E., Keir, D., Ebinger, C. J., Stuart, G. W., Bastow, I. D., and Ayele, A. (2008). Crustal tomographic imaging of a transitional continental rift : the Ethiopian rift. *Geophysical Journal International*, 172:1033–1048.

Daniels, K. A., Bastow, I. D., Keir, D., Sparks, R. S. J., and Menand, T. (2014). Thermal models of dyke intrusion during development of continent-ocean transition. *Earth and Planetary Science Letters*, 385:145–153.

Daradich, A., Mitrovica, J. X., Pysklywec, R. N., Willett, S. D., and Forte, A. M. (2003). Mantle flow, dynamic topography, and rift-flank uplift of Arabia. *Geology*, 31(10):901–904.

Debayle, E., Lévêque, J. J., and Cara, M. (2001). Seismic evidence for a deeply rooted low-velocity anomaly in the upper mantle beneath the northeastern Afro/Arabian continent. *Earth and Planetary Science Letters*, 193(3-4):423–436.

Desissa, M., Johnson, N. E., Whaler, K. A., Hautot, S., Fisseha, S., and Dawes, G. J. (2013). A mantle magma reservoir beneath an incipient mid-ocean ridge in Afar, Ethiopia. *Nature Geoscience*, 6(10):861–865.

Dick, H. J. (1989). Abyssal peridotites, very slow spreading ridges and ocean ridge magmatism. *Geological Society Special Publication*, 42(42):71–105.

Didana, Y. L., Thiel, S., and Heinson, G. (2014). Magnetotelluric imaging of upper crustal partial melt at Tendaho graben in Afar, Ethiopia. *Geophysical Research Letters*, 41(9):3089–3095.

Dugda, M. T. and Nyblade, A. A. (2006). New constraints on crustal structure in eastern Afar from the analysis of receiver functions and surface wave dispersion in Djibouti. *Afar Volcanic Province within the East African Rift System*, 259:239–251.

Dugda, M. T., Nyblade, A. A., and Julia, J. (2007). Thin lithosphere beneath the Ethiopian Plateau revealed by a joint inversion of Rayleigh wave group velocities and receiver functions. *Journal of Geophysical Research: Solid Earth*, 112(8):1–14.

Dugda, M. T., Nyblade, A. A., Julia, J., Langston, C. A., Ammon, C. J., and Simiyu, S. (2005). Crustal structure in Ethiopia and Kenya from receiver function analysis : Implications for rift development in eastern Africa. *Journal of Geophysical Research*, 110.

Dziewonski, A. M. and Anderson, D. L. (1981). Preliminary reference Earth model. *Physics of the Earth and Planetary Interiors*, 25(4):297–356.

Eagles, G., Gloaguen, R., and Ebinger, C. J. (2002). Kinematics of the Danakil microplate. *Earth and Planetary Science Letters*, 203:607–620.

Eaton, D. W., Darbyshire, F., Evans, R. L., Grütter, H., Jones, A. G., and Yuan, X. (2009). The elusive lithosphere-asthenosphere boundary (LAB) beneath cratons. *Lithos*, 109(1-2):1–22.

Ebinger, C., Djomani, Y. P., Mbede, E., Foster, A., and Dawson, J. B. (1997). Rifting Archaean lithosphere: The Eyasi-Manyara-Natron rifts, East Africa. *Journal of the Geological Society*, 154(6):947–960.

Ebinger, C. J. (2005). Continental break-up: The East African perspective. *Astronomy and Geophysics*, 46(2):2.16–2.21.

Ebinger, C. J., Ayele, A., Keir, D., Rowland, J. V., Yirgu, G., Wright, T. J., Belachew, M., and Hamling, I. J. (2010). Length and Timescales of Rift Faulting and Magma Intrusion: The Afar Rifting Cycle from 2005 to Present. *Annual Review of Earth and Planetary Sciences*, 38(1):439–466.

Ebinger, C. J. and Casey, M. (2001). Continental breakup in magmatic provinces: An Ethiopian example. *Geology*, 29(6):527–530.

Ebinger, C. J., Deco, A. L., Drake, R. E., and Tesha, A. L. (1989a). Chronology of Volcanism and Rift Basin Propagation: Rungwe Volcanic Province, East Africa. *Journal of Geophysical Research*, 94:15785 – 15803.

Ebinger, C. J., Forsyth, D. W., and Bowin, C. O. (1989b). Effective Elastic Plate Thickness Beneath the East African and Afar Plateaus and Dynamic Compensation of the Uplifts. *Journal of Geophysical Research*, 94:2883–2901.

Ebinger, C. J., Keir, D., Ayele, A., Calais, E., Wright, T. J., Belachew, M., Hammond, J. O. S., Campbell, E., and Buck, W. R. (2008). Capturing magma intrusion and faulting processes during continental rupture: Seismicity of the Dabbahu (Afar) rift. *Geophysical Journal International*, 174(3):1138–1152.

Ebinger, C. J. and Sleep, N. H. (1998). Cenozoic magmatism throughout east Africa resulting from impact of a single plume. *Nature*, 395(October):788–791.

Ebinger, C. J., Yemane, T., Harding, D. J., Tesfaye, S., Kelley, S. P., and Rex, D. C. (2000). Rift deflection, migration, and propagation: Linkage of the Ethiopian and Eastern rifts, Africa. *Bulletin of the Geological Society of America*, 112(2):163–176.

Ebinger, C. J., Yemane, T., WoldeGabriel, G., Aronson, J. L., and C., W. R. (1993). Late Eocene-Recent volcanism and faulting in the southern main Ethiopian rift. *Journal of the Geological Society London*, 150:99–108.

Eilon, Z. C. and Abers, G. A. (2017). High seismic attenuation at a mid-ocean ridge reveals the distribution of deep melt. *Science Advances*, 3(5).

Emry, E. L., Shen, Y., Nyblade, A. A., Flinders, A., and Bao, X. (2019). Upper Mantle Earth Structure in Africa From Full-Wave Ambient Noise Tomography. *Geochemistry, Geophysics, Geosystems*, 20(1):120–147.

Euler, G. G., Wiens, D. A., and Nyblade, A. A. (2014). Evidence for bathymetric control on the distribution of body wave microseism sources from temporary seismic arrays in Africa. *Geophysical Journal International*, 197(3):1869–1883.

Faccenna, C., Rossetti, F., Becker, T. W., Danesi, S., and Morelli, A. (2008). Recent extension driven by mantle upwelling beneath the Admiralty Mountains (East Antarctica). *Tectonics*, 27(4):1–13.

Faul, U. H. and Jackson, I. (2005). The seismological signature of temperature and grain size variations in the upper mantle. *Earth and Planetary Science Letters*, 234:119–134.

Ferguson, D. J., MacLennan, J., Bastow, I. D., Pyle, D. M., Jones, S. M., Keir, D., Blundy, J. D., Plank, T., and Yirgu, G. (2013). Melting during late-stage rifting in Afar is hot and deep. *Nature*, 499(7456):70–73.

Field, L., Barnie, T., Blundy, J., Brooker, R. A., Keir, D., Lewi, E., and Saunders, K. (2012). Integrated field, satellite and petrological observations of the November 2010 eruption of Erta Ale. *Bulletin of Volcanology*, 74(10):2251–2271.

Fischer, K. M., Ford, H. A., Abt, D. L., and Rychert, C. A. (2010). The Lithosphere-Asthenosphere Boundary. *Annual Review of Earth and Planetary Sciences*, 38(1):551–575.

Fishwick, S. (2010). Surface wave tomography: Imaging of the lithosphere-asthenosphere boundary beneath central and southern Africa? *Lithos*, 120(1-2):63–73.

Fishwick, S. and Bastow, I. D. (2011). Towards a better understanding of African topography: a review of passive-source seismic studies of the African crust and upper mantle. *Geological Society, London, Special Publications*, 357(1):343–371.

Forsyth, D. W. and Li, A. (2005). Array analysis of two-dimensional variations in surface wave phase velocity and azimuthal anisotropy in the presence of multipathing interference. *Seismic Earth: Array Analysis of Broadband Seismograms*, pages 81–97.

Foucher, J.-P., Pichon, X. L., and Sibuet, J.-C. (1982). The ocean-continent transition in the uniform lithospheric stretching model: role of partial melting in the mantle. *Philosophical Transactions of the Royal Society of London. Series A, Mathematical and Physical Sciences*, 305:27–43.

French, S. W. and Romanowicz, B. (2015). Broad plumes rooted at the base of the Earth's mantle beneath major hotspots.

Furman, T., Bryce, J., Rooney, T. O., Hanan, B. B., Yirgu, G., and Ayalew, D. (2006). Heads and tails: 30 million years of the Afar plume. *Geological Society, London, Special Publications*, 259:95–119.

Gaherty, J. B., Kato, M., and Jordan, T. H. (1999). Seismological structure of the upper mantle: a regional comparison of seismic layering. *Physics of the Earth and Planetary Interiors*, 110:21–41.

Gallacher, R. J., Keir, D., Harmon, N., Stuart, G. W., Leroy, S., Hammond, J. O. S., Kendall, J.-M., Ayele, A., Goitom, B., Ogubazghi, G., and Ahmed, A. (2016). The initiation of segmented buoyancy-driven melting during continental breakup. *Nature Communications*, 7:13110.

Gani, N. D., Gani, M. R., and Abdelsalam, M. G. (2007). Blue Nile incision on the Ethiopian Plateau: Pulsed plateau growth, Pliocene uplift, and hominin evolution. *GSA Today*, 17(9):4–11.

Gao, H. (2016). Seismic velocity structure of the Juan de Fuca and Gorda plates revealed by a joint inversion of ambient noise and regional earthquakes. *Geophysical Research Letters*, 43(10):5194–5201.

Gao, S. S., Davis, P. M., Liu, H., Slack, P. D., Rigor, A. W., Zorin, Y. A., Mordvinova, V. V., Kozhevnikov, V. M., and Logatchev, N. A. (1997). SKS splitting beneath continental rift zones. *Journal of Geophysical Research: Solid Earth*, 102(B10):22781–22797.

Gao, S. S., Liu, K. H., and Abdelsalam, M. G. (2010). Seismic anisotropy beneath the Afar Depression and adjacent areas: Implications for mantle flow. *Journal of Geophysical Research: Solid Earth*, 115(12):1–15.

Garmany, J. (1989). Accumulations of melt at the base of young Oceanic Crust. *Nature*, 340:628–632.

George, R., Rogers, N., and Kelley, S. P. (1998). Earliest magmatism in Ethiopia: Evidence for two mantle plumes in one flood basalt province. *Geology*, 26(10):923–926.

Gerstoft, P., Shearer, P. M., Harmon, N., and Zhang, J. (2008). Global P, PP, and PKP wave microseisms observed from distant storms. *Geophysical Research Letters*, 35(23):4–9.

Ghods, A. and Arkani-Hamed, J. (2000). Melt migration beneath mid-ocean ridges. *Geophysical Journal International*, 140(3):687–697.

Ghosh, A., Holt, W. E., and Flesch, L. M. (2009). Contribution of gravitational potential energy differences to the global stress field. *Geophysical Journal International*, 179(2):787–812.

Ghosh, A., Holt, W. E., Wen, L., Haines, A. J., and Flesch, L. M. (2008). Joint modeling of lithosphere and mantle dynamics elucidating lithosphere-mantle coupling. *Geophysical Research Letters*, 35(16):1–5.

Globig, J., Fernàndez, M., Vergés, J., Robert, A., and Faccenna, C. (2016). New insights into the crust and lithospheric mantle structure of Africa from elevation, geoid, and thermal analysis. *Journal of Geophysical Research : Solid Earth*, 121:5389–5424.

Goitom, B., Oppenheimer, C., Hammond, J. O. S., Grandin, R., Barnie, T. D., Donovan, A., Ogubazghi, G., Yohannes, E., Kibrom, G., Kendall, J.-M., Carn, S. A., Fee, D., Sealing, C., Keir, D., Ayele, A., Blundy, J. D., Hamlyn, J. E., Wright, T. J., and Berhe, S. (2015). First recorded eruption of Nabro volcano, Eritrea, 2011. *Bulletin of Volcanology*, 77(10).

Grandin, R., Jacques, E., Nercessian, A., Ayele, A., Doubre, C., Socquet, A., Keir, D., Kassim, M., Lemarchand, A., and King, G. C. (2012). Seismicity during lateral dike propagation: Insights from new data in the recent Manda Hararo-Dabbahu rifting episode (Afar, Ethiopia). *Geochemistry, Geophysics, Geosystems*, 12(4):1–24.

Green, R. G. (2016). *The structure and seismicity of Icelandic rifts.* PhD thesis.

Grijalva, A., Nyblade, A. A., Homman, K., Accardo, N. J., Gaherty, J. B., Ebinger, C. J., Shillington, D. J., Chindandali, P. R., Mbogoni, G., Ferdinand, R. W., Mulibo, G. D., O'Donnell, J. P., Kachingwe, M., and Tepp, G. (2018). Seismic Evidence for Plume- and Craton-Influenced Upper Mantle Structure Beneath the Northern Malawi Rift and the Rungwe Volcanic Province, East Africa. *Geochemistry, Geophysics, Geosystems*, 19(10):3980–3994.

Guidarelli, M., Stuart, G. W., Hammond, J. O. S., Kendall, J.-M., Ayele, A., and Belachew, M. (2011). Surface wave tomography across Afar, Ethiopia: Crustal structure at a rift triple-junction zone. *Geophysical Research Letters*, 38(24).

Hacker, B. R. and Abers, G. A. (2004). Subduction Factory 3: An Excel worksheet and macro for calculating the densities, seismic wave speeds, and H2O contents of minerals and rocks at pressure and temperature. pages 1–7.

Hamlyn, J. E., Keir, D., Wright, T. J., Neuberg, J. W., Goitom, B., Hammond, J. O. S., Pagli, C., Oppenheimer, C., Kendall, J.-M., and Grandin, R. (2014). Seismicity and subsidence following the 2011 Nabro eruption, Eritrea: Insights into the plumbing system of an off-rift volcano. *Journal of Geophysical Research: Solid Earth*, 119(11):8267–8282.

Hammond, J. O. S. (2014). Constraining melt geometries beneath the Afar Depression, Ethiopia from teleseismic receiver functions: The anisotropic H-k stacking technique. *Geochemistry, Geophysics, Geosystems*, 15(4):1316–1322.

Hammond, J. O. S. and Kendall, J.-M. (2016). Constraints on melt distribution from seismology : a case study in Ethiopia. *Geological Society, London, Special Publications*, 420:127–147.

Hammond, J. O. S., Kendall, J.-M., Angus, D., and Wookey, J. (2010). Interpreting spatial variations in anisotropy: Insights into the Main Ethiopian Rift from SKS waveform modelling. *Geophysical Journal International*, 181(3):1701–1712.

Hammond, J. O. S., Kendall, J.-M., Stuart, G. W., Ebinger, C. J., Bastow, I. D., Keir, D., Ayele, A., Belachew, M., Goitom, B., Ogubazghi, G., and Wright, T. J. (2013). Mantle upwelling and initiation of rift segmentation beneath the Afar Depression. *Geology*, 41(6):635–638.

Hammond, J. O. S., Kendall, J.-M., Stuart, G. W., Keir, D., Ebinger, C. J., Ayele, A., and Belachew, M. (2011). The nature of the crust beneath the Afar triple junction: Evidence from receiver functions. *Geochemistry, Geophysics, Geosystems*, 12(12):1–24.

Hammond, J. O. S., Kendall, J.-M., Wookey, J., Stuart, G. W., Keir, D., and Ayele, A. (2014). Differentiating flow, melt, or fossil seismic anisotropy beneath Ethiopia. *Geochemistry, Geophysics, Geosystems*, 15:1878–1894.

Hammond, W. C. and Humphreys, E. D. (2000a). Upper mantle seismic wave attenuation: Effects of realistic partial melt distribution. *Journal of Geophysical Research: Solid Earth*, 105:10987–10999.

Hammond, W. C. and Humphreys, E. D. (2000b). Upper mantle seismic wave velocity: Effects of realistic partial melt geometries. *Journal of Geophysical Research: Solid Earth*.

Hansen, S. E., Nyblade, A. A., and Benoit, M. H. (2012). Mantle structure beneath Africa and Arabia from adaptively parameterized P-wave tomography: Implications for the origin of Cenozoic Afro-Arabian tectonism. *Earth and Planetary Science Letters*, 319-320:23–34.

Harmon, N., De La Cruz, M. S., Rychert, C. A., Abers, G. A., and Fischer, K. M. (2013). Crustal and mantle shear velocity structure of Costa Rica and Nicaragua from ambient noise and teleseismic Rayleigh wave tomography. *Geophysical Journal International*, 195(2):1300–1313.

Harmon, N., Forsyth, D. W., and Webb, S. C. (2007). Using ambient seismic noise to determine short-period phase velocities and shallow shear velocities in young oceanic lithosphere. *Bulletin of the Seismological Society of America*, 97(6):2009–2023.

Harmon, N., Forsyth, D. W., and Weeraratne, D. S. (2009). Thickening of young Pacific lithosphere from high-resolution Rayleigh wave tomography: A test of the conductive cooling model. *Earth and Planetary Science Letters*, 278(1-2):96–106.

Harmon, N., Gerstoft, P., Rychert, C. A., Abers, G. A., De La Cruz, M. S., and Fischer, K. M. (2008). Phase velocities from seismic noise using beamforming and cross correlation in Costa Rica and Nicaragua. *Geophysical Research Letters*, 35:1–6.

Harmon, N. and Rychert, C. A. (2015). Seismic imaging of deep crustal melt sills beneath Costa Rica suggests a method for the formation of the Archean continental crust. *Earth and Planetary Science Letters*, 430:140–148.

Harmon, N. and Rychert, C. A. (2016). Joint inversion of teleseismic and ambient noise Rayleigh waves for phase velocity maps, an application to Iceland. *Journal of Geophysical Research : Solid Earth*, 121:5966–5987.

Harmon, N., Rychert, C. A., and Gerstoft, P. (2010). Distribution of noise sources for seismic interferometry. *Geophysical Journal International*, 183(3):1470–1484.

Hassan, R., Williams, S. E., Gurnis, M., and Müller, D. (2020). East African topography and volcanism explained by a single, migrating plume. *Geoscience Frontiers*, (January).

Hasselmann, K. (1963). A statistical analysis of the generation of microseisms. *Reviews of Geophysics*, 1(2):177–210.

Hautot, S., Whaler, K. A., Gebru, W., and Desissa, M. (2006). The structure of a Mesozoic basin beneath the Lake Tana area, Ethiopia, revealed by magnetotelluric imaging. *Journal of African Earth Sciences*, 44(3):331–338.

Havlin, C., Parmentier, E. M., and Hirth, G. (2013). Dike propagation driven by melt accumulation at the lithosphere - asthenosphere boundary. *Earth and Planetary Science Letters*, 376:20–28.

Hayward, N. J. and Ebinger, C. J. (1996). Variations in the along-axis segmentation of the Afar Rift system. *Tectonics*, 15(2):244–257.

Hillers, G., Graham, N., Campillo, M., Kedar, S., Landés, M., and Shapiro, N. (2012). Global oceanic microseism sources as seen by seismic arrays and predicted by wave action models. *Geochemistry, Geophysics, Geosystems*, 13(1).

Hirth, G. and Kohlstedt, D. L. (1996). Water in the oceanic upper mantle: Implications for rheology, melt extraction and the evolution of the lithosphere. *Earth and Planetary Science Letters*, 144(1-2):93–108.

Hofmann, C., Courtillot, V., Féraud, G., Rochette, P., Yirgu, G., Ketefo, E., and Pik, R. (1997). Timing of the ethiopian flood basalt event and implications for plume birth and global change. *Nature*, 389(6653):838–841.

Holtzman, B. K. (2016). Questions on the existence, persistence, and mechanical effects of a very small melt fraction in the asthenosphere. *Geochemistry, Geophysics, Geosystems*, 17:470–484.

Holtzman, B. K. and Kendall, J.-M. (2010). Organized melt, seismic anisotropy, and plate boundary lubrication. *Geochemistry, Geophysics, Geosystems*, 11(12):1–29.

Hübert, J., Whaler, K. A., and Fisseha, S. (2018). The Electrical Structure of the Central Main Ethiopian Rift as Imaged by Magnetotellurics : Implications for Magma Storage and Pathways. *Journal of Geophysical Research : Solid Earth*, 123:6019–6032.

Huismans, R. S., Podladchikov, Y. Y., and Cloetingh, S. (2001). Transition from passive to active rifting: Relative importance of asthenospheric doming and passive extension of the lithosphere. *Journal of Geophysical Research: Solid Earth*, 106(B6):11271–11291.

Hutchison, W., Mather, T. A., Pyle, D. M., Biggs, J., and Yirgu, G. (2015). Structural controls on fluid pathways in an active rift system: A case study of the Aluto volcanic complex. *Geosphere*, 11(3):542–562.

Hutchison, W., Mather, T. A., Pyle, D. M., Boyce, A. J., Gleeson, M. L. M., Yirgu, G., Blundy, J. D., Ferguson, D. J., Vye-Brown, C., Millar, I. L., Sims, K. W. W., and Finch, A. A. (2018). The evolution of magma during continental rifting: New constraints from the isotopic and trace element signatures of silicic magmas from Ethiopian volcanoes. *Earth and Planetary Science Letters*, 489:203–218.

Hutchison, W., Pyle, D. M., Mather, T. A., Yirgu, G., Biggs, J., Cohen, B. E., Barfod, D. N., and Lewi, E. (2016). The eruptive history and magmatic evolution of Aluto volcano : new insights into silicic peralkaline volcanism in the Ethiopian rift. *Journal of Volcanology and Geothermal Research*, 328:9–33.

Illsley-Kemp, F., Greenfield, T., and Keir, D. (2018a). Seismic Anisotropy Reveals a Dynamic Link Between Adjacent Magmatic Segments Prior to Dyke Intrusion. *Journal of Geophysical Research: Solid Earth*, 123(11):9800–9816.

Illsley-Kemp, F., Keir, D., Bull, J. M., Ayele, A., Hammond, J. O. S., Kendall, J.-M., Gallacher, R. J., Gernon, T. M., and Goitom, B. (2017). Local earthquake magnitude scale and b-value for the Danakil region of northern afar. *Bulletin of the Seismological Society of America*, 107(2):521–531.

Illsley-Kemp, F., Keir, D., Bull, J. M., Gernon, T. M., Ebinger, C. J., Ayele, A., Hammond, J. O. S., Kendall, J.-M., Goitom, B., and Belachew, M. (2018b). Seismicity During Continental Breakup in the Red Sea Rift of Northern Afar. *Journal of Geophysical Research: Solid Earth*, 123(3):2345–2362.

Jackson, I. and Faul, U. H. (2010). Grainsize-sensitive viscoelastic relaxation in olivine: Towards a robust laboratory-based model for seismological application. *Physics of the Earth and Planetary Interiors*, 183(1-2):151–163.

Jaxybulatov, K., Shapiro, N. M., Koulakov, I., Mordret, A., Landès, M., and Sens-Schönfelder, C. (2014). A large magmatic sill complex beneath the Toba caldera. *Science*, 346(6209):617–619.

Jestin, F., Huchon, P., and Gaulier, J. M. (1994). The Somalia Plate and the East-African Rift System - Present- Day Kinematics. *Geophysical Journal International*, 116(3):637–654.

Ji, S., Sun, S., Wang, Q., and Marcotte, D. (2010). Lamé parameters of common rocks in the Earth's crust and upper mantle. *Journal of Geophysical Research: Solid Earth*, 115(6).

Jiang, C., Schmandt, B., Farrell, J., Lin, F.-C., and Ward, K. M. (2018). Seismically anisotropic magma reservoirs underlying silicic calderas. *Geology*, 46(8):727–730.

Johnson, N. E., Whaler, K. A., Hautot, S., Fisseha, S., Desissa, M., and Dawes, G. J. (2015). Magma imaged magnetotellurically beneath an active and an inactive magmatic segment in Afar, Ethiopia. *Geological Society, London, Special Publications*, 14:150000.

Jones, P. W. (1976). Age of the lower flood basalts of the Ethiopian plateau. *Nature*, 261(5561):567–569.

Karakas, O. and Dufek, J. (2015). Melt evolution and residence in extending crust: Thermal modeling of the crust and crustal magmas. *Earth and Planetary Science Letters*, 425:131–144.

Karato, S. I. (2004). Mapping water content in the upper mantle. *Geophysical Monograph Series*, 138(April):135–152.

Kavanagh, J. L., Menand, T., and Sparks, R. S. J. (2006). An experimental investigation of sill formation and propagation in layered elastic media. *Earth and Planetary Science Letters*, 245(3-4):799–813.

Kazmin, V., Shifferaw, A., and Balcha, T. (1978). The Ethiopian basement: Stratigraphy and possible manner of evolution. *Geologische Rundschau*, 67(2):531–546.

Keir, D., Bastow, I. D., Pagli, C., and Chambers, E. L. (2013). The development of extension and magmatism in the Red Sea rift of Afar. *Tectonophysics*, 607:98–114.

Keir, D., Bastow, I. D., Whaler, K. A., Daly, E., Cornwell, D. G., and Hautot, S. (2009a). Lower crustal earthquakes near the Ethiopian rift induced by magmatic processes. *Geochemistry, Geophysics, Geosystems*, 10(6):1–10.

Keir, D., Belachew, M., Ebinger, C. J., Kendall, J.-M., Hammond, J. O. S., Stuart, G. W., Ayele, A., and Rowland, J. V. (2011). Mapping the evolving strain field during continental breakup from crustal anisotropy in the Afar Depression. *Nature Communications*, 2:285–287.

Keir, D., Ebinger, C. J., Stuart, G. W., Daly, E., and Ayele, A. (2006a). Strain accommodation by magmatism and faulting as rifting proceeds to breakup: Seismicity of the northern Ethiopian rift. *Journal of Geophysical Research: Solid Earth*, 111(5):1–17.

Keir, D., Hamling, I. J., Ayele, A., Calais, E., Ebinger, C. J., Wright, T. J., Jacques, E., Mohamed, K., Hammond, J. O. S., Belachew, M., Baker, E., Rowland, J. V., Lewi, E., and Bennati, L. (2009b). Evidence for focused magmatic accretion at segment centers from lateral dike injections captured beneath the Red Sea rift in Afar. *Geology*, 37(1):59–62.

Keir, D., Kendall, J.-M., Ebinger, C. J., and Stuart, G. W. (2005). Variations in late syn-rift melt alignment inferred from shear-wave splitting in crustal earthquakes beneath the Ethiopian rift. *Geophysical Research Letters*, 32(23):1–4.

Keir, D., Stuart, G. W., Jackson, A., and Ayele, A. (2006b). Local earthquake magnitude scale and seismicity rate for the Ethiopian rift. *Bulletin of the Seismological Society of America*, 96(6):2221–2230.

Kendall, J.-M. (1994). Teleseismic arrivals at a mid-ocean ridge: Effects of mantle melt and anisotropy. *Geophysical Research Letters*, 21(4):301–304.

Kendall, J.-M. (2000). Seismic Anisotropy in the Boundary Layers of the Mantle.

Kendall, J.-M., Pilidou, S., Keir, D., Bastow, I. D., Stuart, G. W., and Ayele, A. (2006). Mantle upwellings , melt migration and the rifting of Africa : insights from seismic anisotropy. *Geological Society, London, Special Publications*, 259:55–72.

Kendall, J.-M., Stuart, G. W., Ebinger, C. J., Bastow, I. D., and Keir, D. (2005). Magma-assisted rifting in Ethiopia. *Nature*, 433(7022):146–148.

Kennett, B. L., Engdahl, E. R., and Buland, R. (1995). Constraints on seismic velocities in the Earth from traveltimes. *Geophysical Journal International*, 122(1):108–124.

Kennett, B. L., Furumura, T., and Zhao, Y. (2014). High-frequency Po/So guided waves in the oceanic lithosphere: II-Heterogeneity and attenuation. *Geophysical Journal International*, 199(1):614–630.

Keranen, K. M. (2013). Exploring extensional tectonics beyond the Ethiopian Rift.

Keranen, K. M. and Klemperer, S. L. (2008). Discontinuous and diachronous evolution of the Main Ethiopian Rift: Implications for development of continental rifts. *Earth and Planetary Science Letters*, 265(1-2):96–111.

Keranen, K. M., Klemperer, S. L., Gloaguen, R., and EAGLE Working Group (2004). Three-dimensional seismic imaging of a protoridge axis in the Main Ethiopian rift. *Geology*, 32(11):949–952.

Keranen, K. M., Klemperer, S. L., Julia, J., Lawrence, J. F., and Nyblade, A. A. (2009). Low lower crustal velocity across Ethiopia: Is the Main Ethiopian Rift a narrow rift in a hot craton? *Geochemistry, Geophysics, Geosystems*, 10(5).

Kieffer, B., Arndt, N. T., Lapierre, H., Bastien, F., Bosch, D., Pecher, A., Yirgu, G., Ayalew, D., Weis, D., Jerram, D. A., Keller, F., and Meugniot, C. (2004). Flood and Shield Basalts from Ethiopia: Magmas from the African Superswell. *Journal of Petrology*, 45(4):793–834.

Kim, S., Nyblade, A. A., Rhie, J., Baag, C.-E., and Kang, T.-S. (2012). Crustal S -wave velocity structure of the Main Ethiopian Rift from ambient noise tomography. *Geophysical Journal International*, 191(2):865–878.

King, S. D. and Ritsema, J. (2000). African hot spot volcanism: Small-scale convection in the upper mantle beneath cratons. *Science*, 290(5494):1137–1140.

Kirkwood, S. C. and Crampin, S. (1981). Surface wave propagation in an ocean basin with an anisotropic upper mantle: observations of polarization anomalies. *Geophysical Journal of the Royal Astronomical Society*, 64(2):487–497.

Kohlstedt, D. L. and Holtzman, B. K. (2009). Shearing Melt Out of the Earth: An Experimentalist's Perspective on the Influence of Deformation on Melt Extraction. *Annual Review of Earth and Planetary Sciences*, 37(1):561–593.

Kolawole, F., Atekwana, E. A., Malloy, S., Stamps, D. S., Grandin, R., Abdelsalam, M. G., Leseane, K., and Shemang, E. M. (2017). Aeromagnetic, gravity, and Differential Interferometric Synthetic Aperture Radar analyses reveal the causative fault of the 3 April 2017 Mw 6.5 Moiyabana, Botswana, earthquake. *Geophysical Research Letters*, 44(17):8837–8846.

Koptev, A., Calais, E., Burov, E., Leroy, S., and Gerya, T. (2018). Along-Axis Variations of Rift Width in a Coupled Lithosphere-Mantle System, Application to East Africa. *Geophysical Research Letters*, 45(11):5362–5370.

Korostelev, F., Weemstra, C., Leroy, S., Boschi, L., Keir, D., Ren, Y., Molinari, I., Ahmed, A., Stuart, G. W., Rolandone, F., Khanbari, K., Hammond, J. O. S., Kendall, J.-M., Doubre, C., Ganad, I. A., Goitom, B., and Ayele, A. (2015). Magmatism on rift flanks: Insights from ambient noise phase velocity in Afar region. *Geophysical Research Letters*, 42(7):2179–2188.

Koulakov, I., Maksotova, G., Jaxybulatov, K., Kasatkina, E., Shapiro, N. M., Luehr, B., Khrepy, S., and Al-Arifi, N. (2016). Structure of magma reservoirs beneath Merapi and surrounding volcanic centers of Central Java modeled from ambient noise tomography. *Geochemistry, Geophysics, Geosystems*, 17:4195–4211.

Landisman, M., Dziewonski, A., and Satô, Y. (1969). Recent Improvements in the Analysis of Surface Wave Observations. *Geophysical Journal of the Royal Astronomical Society*, 17:369–403.

Laske, G., Masters, G., Ma, Z., and Pasyanos, M. E. (2013). Update on CRUST1.0 - A 1-degree global model of Earth's crust. *EGU General Assembly 2013*, 15:2658.

Lavayssière, A., Drooff, C., Ebinger, C. J., Gallacher, R. J., Illsley-Kemp, F., Oliva, S. J., and Keir, D. (2019). Depth Extent and Kinematics of Faulting in the Southern Tanganyika Rift, Africa. *Tectonics*, 38(3):842–862.

Lavayssière, A., Rychert, C. A., Harmon, N., Keir, D., Hammond, J. O. S., Kendall, J.-M., Doubre, C., and Leroy, S. (2018). Imaging lithospheric discontinuities beneath the northern East African Rift using S-to-P receiver functions. *Geochemistry, Geophysics, Geosystems*.

Lebedev, S. and Van Der Hilst, R. D. (2008). Global upper-mantle tomography with the automated multimode inversion of surface and S-wave forms. *Geophysical Journal International*, 173(2):505–518.

Lee, C.-T. A. (2003). Compositional variation of density and seismic velocities in natural peridotites at STP conditions: Implications for seismic imaging of compositional heterogeneities in the upper mantle. *Journal of Geophysical Research: Solid Earth*, 108(B9).

Lees, M. E., Rudge, J. F., and McKenzie, D. (2020). Gravity, Topography, and Melt Generation Rates From Simple 3-D Models of Mantle Convection. *Geochemistry, Geophysics, Geosystems*, 21(4).

Lekic, V., French, S. W., and Fischer, K. M. (2011). Lithospheric Thinning Beneath Rifted Regions of Southern California. *Science*, 334(November):783–788.

Leroy, S., Lucazeau, F., D'Acremont, E., Watremez, L., Autin, J., Rouzo, S., Bellahsen, N., Tiberi, C., Ebinger, C. J., Beslier, M. O., Perrot, J., Razin, P., Rolandone, F., Sloan, H., Stuart, G. W., Lazki, A. A., Al-Toubi, K., Bache, F., Bonneville, A., Goutorbe, B., Huchon, P., Unternehr, P., and Khanbari, K. (2010). Contrasted styles of rifting in the eastern Gulf of Aden: A combined wide-angle, multichannel seismic, and heat flow survey. *Geochemistry, Geophysics, Geosystems*, 11(7):1–14.

Levin, V. and Park, J. (2000). Shear zones in the Proterozoic lithosphere of the Arabian shield and the nature of the Hales discontinuity. *Tectonophysics*, 323(3-4):131–148.

Lewi, E., Keir, D., Birhanu, Y., Blundy, J. D., Stuart, G. W., Wright, T. J., and Calais, E. (2016). Use of a high-precision gravity survey to understand the formation of oceanic crust and the role of melt at the southern Red Sea rift in Afar, Ethiopia. *Geological Society, London, Special Publications*, 420(1):165–180.

Ligi, M., Bonatti, E., Bortoluzzi, G., Cipriani, A., Cocchi, L., Caratori Tontini, F., Carminati, E., Ottolini, L., and Schettino, A. (2012). Birth of an ocean in the Red Sea: Initial pangs. *Geochemistry, Geophysics, Geosystems*, 13(8):1–29.

Lin, F.-C., Moschetti, M. P., and Ritzwoller, M. H. (2008). Surface wave tomography of the western United States from ambient seismic noise: Rayleigh and Love wave phase velocity maps. *Geophysical Journal International*, 173(1):281–298.

Lithgow-Bertelloni, C. and Silver, P. G. (1998). Dynamic topography, plate driving forces and the African superswell. *Nature*, 395(6699):269–272.

Lloyd, R., Biggs, J., Birhanu, Y., Wilks, M., Gottsmann, J. H., Kendall, J.-M., Ayele, A., Lewi, E., and Eysteinsson, H. (2018). Sustained Uplift at a Continental Rift Caldera. *Journal of Geophysical Research : Solid Earth*, 123:5209–5226.

Longuet-Higgins, M. S. (1950). A Theory of the Origin of Microseisms. *Philosophical Transactions of the Royal Society of London. Series A, Mathematical and Physical Sciences*, 243(857):1 LP – 35.

Maccaferri, F., Bonafede, M., and Rivalta, E. (2011). A quantitative study of the mechanisms governing dike propagation, dike arrest and sill formation. *Journal of Volcanology and Geothermal Research*, 208(1-2):39–50.

Maccaferri, F., Rivalta, E., Keir, D., and Acocella, V. (2014). Off-rift volcanism in rift zones determined by crustal unloading. *Nature Geoscience*, 7(4):297–300.

Macgregor, D. (2015). History of the development of the East African Rift System: A series of interpreted maps through time. *Journal of African Earth Sciences*, 101:232–252.

Mackenzie, G. D., Thybo, H., and Maguire, P. K. H. (2005). Crustal velocity structure across the Main Ethiopian Rift: Results from two-dimensional wide-angle seismic modelling. *Geophysical Journal International*, 162(3):994–1006.

Magde, L. S. and Sparks, D. W. (1997). Three-dimensional mantle upwelling, melt generation, and melt migration beneath segment slow spreading ridges. *Journal of Geophysical Research: Solid Earth*, 102(B9):20571–20583.

Magee, C., Muirhead, J. D., Karvelas, A., Holford, S. P., Jackson, C. A., Bastow, I. D., Schofield, N., Stevenson, C. T., McLean, C., McCarthy, W., and Shtukert, O. (2016). Lateral magma flow in mafic sill complexes. *Geosphere*, 12(3):809–841.

Maguire, P. K. H., Keller, G. R., Klemperer, S. L., Mackenzie, G. D., Keranen, K. M., Harder, S., O'Reilly, B., Thybo, H., Asfaw, L., Khan, M. A., and Amha, M. (2006). Crustal structure of the northern Main Ethiopian Rift from the EAGLE controlled-source survey; a snapshot of incipient lithospheric break-up. *Geological Society, London, Special Publications*, 259(1):269–291.

Maguire, R., Ritsema, J., Bonnin, M., vanÂ Keken, P. E., and Goes, S. (2018). Evaluating the Resolution of Deep Mantle Plumes in Teleseismic Traveltime Tomography. *Journal of Geophysical Research: Solid Earth*, 123(1):384–400.

Makris, J. and Ginzburg, A. (1987). The Afar Depression: transition between continental rifting and sea-floor spreading. *Tectonophysics*, 141(1-3):199–214.

Mazzarini, F., Keir, D., and Isola, I. (2013). Spatial relationship between earthquakes and volcanic vents in the central-northern Main Ethiopian Rift. *Journal of Volcanology and Geothermal Research*, 262:123–133.

McClusky, S., Reilinger, R., Ogubazghi, G., Amleson, A., Healeb, B., Vernant, P., Sholan, J., Fisseha, S., Asfaw, L., Bendick, R., and Kogan, L. (2010). Kinematics of the southern Red Sea - Afar Triple Junction and implications for plate dynamics. *Geophysical Research Letters*, 37:1–5.

McKenzie, D. (1978). Some remarks on the development of sedimentary basins. *Earth and Planetary Science Letters*, 40(1):25–32.

McKenzie, D., Davies, D., and Molnar, P. (1970). Plate Tectonics of the Red Sea and East Africa. *Nature*, 226:243–248.

Mège, D. and Korme, T. (2004). Dyke swarm emplacement in the Ethiopian Large Igneous Province: Not only a matter of stress. *Journal of Volcanology and Geothermal Research*, 132(4):283–310.

Merla, G., Abbate, E., Canuti, P., Sagri, M., and Tacconi, P. (1973). Geological map of Ethiopia and Somalia.

Meshesha, D. and Shinjo, R. (2008). Rethinking geochemical feature of the Afar and Kenya mantle plumes and geodynamics implications. *Journal of Geophysical Research: Solid Earth*, 113.

Mohr, P. (1989). Nature of the crust under Afar: new igneous, not thinned continental. *Tectonophysics*, 167(1):1–11.

Mondy, L. S., Rey, P. F., Duclaux, G., and Moresi, L. (2018). The role of asthenospheric flow during rift propagation and breakup. *Geology*, 46(2):103–106.

Montagner, J. P. and Anderson, D. L. (1989). Constrained reference mantle model. *Physics of the Earth and Planetary Interiors*, 58(2-3):205–227.

Moore, C., Wright, T. J., Hooper, A., and Biggs, J. (2019). The 2017 Eruption of Erta ' Ale Volcano , Ethiopia : Insights Into the Shallow Axial Plumbing System of an Incipient Mid-Ocean Ridge. *Geochemistry, Geophysics, Geosystems*, 20:1–17.

Moorkamp, M., Fishwick, S., Walker, R. J., and Jones, A. G. (2019). Geophysical evidence for crustal and mantle weak zones controlling intra-plate seismicity - the 2017 Botswana earthquake sequence. *Earth and Planetary Science Letters*, 506:175–183.

Mordret, A., Mikesell, T. D., Harig, C., Lipovsky, B. P., and Prieto, G. A. (2016). Monitoring South-West Greenland's ice sheet melt with ambient seismic noise. *Science Advances*, 2(May):1–8.

Morgan, W. J. (1971). Convection plumes in the lower mantle. *Nature*, 230(5288):42–43.

Moschetti, M. P., Ritzwoller, M. H., and Shapiro, N. M. (2007). Surface wave tomography of the western United States from ambient seismic noise: Rayleigh wave group velocity maps. *Geochemistry, Geophysics, Geosystems*, 8(8):1–10.

Nelson, R. A., Patton, T. L., and Morley, C. K. (1992). Rift-Segment Interaction and Its Relation to Hydrocarbon Exploration in Continental Rift Systems. *AAPG Bulletin*, 76(8):1153–1169.

Nelson, W. R., Furman, T., van Keken, P. E., Shirey, S. B., and Hanan, B. B. (2012). OsHf isotopic insight into mantle plume dynamics beneath the East African Rift System. *Chemical Geology*, 320-321:66–79.

Nielsen, T. K. and Hopper, J. R. (2004). From rift to drift: Mantle melting during continental breakup. *Geochemistry, Geophysics, Geosystems*, 5(7).

Nishida, K. (2011). Two-dimensional sensitivity kernels for cross-correlation functions of background surface waves. *Comptes Rendus - Geoscience*, 343(8-9):584–590.

Niu, Y. (2018). Origin of the LLSVPs at the base of the mantle is a consequence of plate tectonics - A petrological and geochemical perspective. *Geoscience Frontiers*, 9(5):1265–1278.

Nyblade, A. A. (2011). The upper-mantle low-velocity anomaly beneath Ethiopia, Kenya, and Tanzania: Constraints on the origin of the African superswell in east- ern Africa and plate versus plume models of mantle dynamics. *Geological Society of America Special Papers*, 478:37–50.

Obrebski, M., Kiselev, S., Vinnik, L., and Montagner, J. P. (2010). Anisotropic stratification beneath Africa from joint inversion of SKS and P receiver functions. *Journal of Geophysical Research: Solid Earth*, 115(9):1–15.

Ogden, C. S., Bastow, I. D., Gilligan, A., and Rondenay, S. (2019). A Reappraisal of the H-κ Stacking Technique: Implications for Global Crustal Structure. *Geophysical Journal International*, 219:1491–1513.

Panning, M. and Romanowicz, B. (2006). A three-dimensional radially anisotropic model of shear velocity in the whole mantle. *Geophysical Journal International*, 167(1):361–379.

Pasyanos, M. E. and Nyblade, A. A. (2007). A top to bottom lithospheric study of Africa and Arabia. *Tectonophysics*, 444(1-4):27–44.

Pearson, N. J., O'Reilly, S. Y., and Griffin, W. L. (1995). The crust-mantle boundary beneath cratons and craton margins: a transect across the south-west margin of the Kaapvaal craton. *Lithos*, 36(3-4):257–287.

Petrunin, A. G., Kaban, M. K., El Khrepy, S., and Al-Arifi, N. (2020). Mantle Convection Patterns Reveal the Mechanism of the Red Sea Rifting. *Tectonics*, 39(2):1–11.

Pik, R., Deniel, C., Coulon, C., Yirgu, G., Hofmann, C., and Ayalew, D. (1998). The northwestern Ethiopian Plateau flood basalts: classification and spatial distribution of magma types. *Journal of Volcanology and Geothermal Research*, 81(1-2):91–111.

Pik, R., Deniel, C., Coulon, C., Yirgu, G., and Marty, B. (1999). Isotopic and trace element signatures of Ethiopian flood basalts: Evidence for plume-lithosphere interactions. *Geochimica et Cosmochimica Acta*, 63(15):2263–2279.

Pik, R., Marty, B., Carignan, J., and Lavé, J. (2003). Stability of the Upper Nile drainage network (Ethiopia) deduced from (U-Th)/He thermochronometry: Implications for uplift and erosion of the Afar plume dome. *Earth and Planetary Science Letters*, 215(1-2):73–88.

Pik, R., Marty, B., and Hilton, D. R. (2006). How many mantle plumes in Africa? The geochemical point of view. *Chemical Geology*, 226(3-4):100–114.

Pilet, S., Abe, N., Rochat, L., Kaczmarek, M. A., Hirano, N., Machida, S., Buchs, D. M., Baumgartner, P. O., and Müntener, O. (2016). Pre-subduction metasomatic enrichment of the oceanic lithosphere induced by plate flexure. *Nature Geoscience*, 9(12):898–903.

Pinzuti, P., Humler, E., Manighetti, I., and Gaudemer, Y. (2013). Petrological constraints on melt generation beneath the Asal Rift (Djibouti) using quaternary basalts. *Geochemistry, Geophysics, Geosystems*, 14(8):2932–2953.

Press, W. H., Teukolsky, S. A., Vetterling, W. T., and Flannery, B. P. (1992). Press. In *Numerical recipes in C: The art of scientific computing*, pages 444–455. Cambridge University Press, second edn edition.

Priestley, K. and McKenzie, D. (2006). The thermal structure of the lithosphere from shear wave velocities. *Earth and Planetary Science Letters*, 244(1-2):285–301.

Priestley, K., Mckenzie, D., Debayle, E., and Pilidou, S. (2008). The African upper mantle and its relationship to tectonics and surface geology. *Geophysical Journal International*, 175(3):1108–1126.

Prodehl, C., Fuchs, K., and Mechie, J. (1997). Seismic-refraction studies of the Afro-Arabian rift system - A brief review. *Tectonophysics*, 278(1-4):1–13.

Redfield, T. F., Wheeler, W. H., and Often, M. (2003). A kinematic model for the development of the Afar Depression and its paleogeographic implications. *Earth and Planetary Science Letters*, 216(3):383–398.

Ritsema, J., van Heijst, H. J., and Woodhouse, J. H. (1999). Complex shear wave velocity structure beneath Africa and Iceland. *Science*, 286(DECEMBER):1925–1928.

Roberts, J. L. (1970). The Intrusion of Magma into Brittle Rocks. *Journal of Geology*, 2:380.

Rogers, N., Macdonald, R., Fitton, J. G., George, R., Smith, M. L., and Barreiro, B. (2000). Two mantle plumes beneath the east African rift system: Sr, Nd and Pb isotope evidence from Kenya Rift basalts. *Earth and Planetary Science Letters*, 176(3-4):387–400.

Rooney, T. O. (2010). Geochemical evidence of lithospheric thinning in the southern Main Ethiopian Rift. *Lithos*, 117(1-4):33–48.

Rooney, T. O. (2017). The Cenozoic magmatism of East-Africa: Part I - Flood basalts and pulsed magmatism. *Lithos*, 286-287:264–301.

Rooney, T. O. (2019). The Cenozoic Magmatism of East Africa: Part V - Magma sources and Processes in the East African Rift. *Lithos*.

Rooney, T. O. (2020). The Cenozoic magmatism of East Africa: Part II - Rifting of the mobile belt. *Lithos*, 360-361:105291.

Rooney, T. O., Bastow, I. D., Keir, D., Mazzarini, F., Movsesian, E., Grosfils, E. B., Zimbelman, J. R., Ramsey, M. S., Ayalew, D., and Yirgu, G. (2014). The protracted development of focused magmatic intrusion during continental rifting. *Tectonics*, 33:875–897.

Rooney, T. O., Furman, T., Bastow, I. D., Ayalew, D., and Yirgu, G. (2007). Lithospheric modification during crustal extension in the Main Ethiopian Rift. *Journal of Geophysical Research: Solid Earth*, 112(10).

Rooney, T. O., Furman, T., Yirgu, G., and Ayalew, D. (2005). Structure of the Ethiopian lithosphere: Xenolith evidence in the Main Ethiopian Rift. *Geochimica et Cosmochimica Acta*, 69(15):3889–3910.

Rooney, T. O., Hanan, B. B., Graham, D. W., Furman, T., Blichert-toft, J., and Schilling, J. G. (2012a). Upper mantle pollution during Afar plume-continental rift interaction. *Journal of Petrology*, 53(2):365–389.

Rooney, T. O., Herzberg, C., and Bastow, I. D. (2012b). Elevated mantle temperature beneath East Africa. *Geology*, 40(1):27–30.

Rooney, T. O., Lavigne, A., Svoboda, C., Girard, G., Yirgu, G., Ayalew, D., and Kappelman, J. (2017). The making of an underplate: Pyroxenites from the Ethiopian lithosphere. *Chemical Geology*, 455:264–281.

Rooney, T. O., Mohr, P., Dosso, L., and Hall, C. (2013). Geochemical evidence of mantle reservoir evolution during progressive rifting along the western Afar margin. *Geochimica et Cosmochimica Acta*, 102:65–88.

Rudnick, R. L. and Fountain, D. M. (1995). Nature and composition of the continental crust: A lower-crustal perspective. *Reviews of Geophysics*, 33(3):267–309.

Russell, J. B., Gaherty, J. B., Lin, P. Y. P., Lizarralde, D., Collins, J. A., Hirth, G., and Evans, R. L. (2019). High-Resolution Constraints on Pacific Upper Mantle Petrofabric Inferred From Surface-Wave Anisotropy. *Journal of Geophysical Research: Solid Earth*, 124(1):631–657.

Rychert, C. A., Hammond, J. O. S., Harmon, N., Kendall, J.-M., Keir, D., Ebinger, C. J., Bastow, I. D., Ayele, A., Belachew, M., and Stuart, G. W. (2012). Volcanism in the Afar Rift sustained by decompression melting with minimal plume influence. *Nature Geoscience*, 5(6):406–409.

Rychert, C. A. and Harmon, N. (2017). Constraints on the anisotropic contributions to velocity discontinuities at 60 km depth beneath the Pacific. *Geochemistry, Geophysics, Geosystems*, 18(8):2855–2871.

Rychert, C. A., Harmon, N., and Armitage, J. J. (2018). Seismic Imaging of Thickened Lithosphere Resulting From Plume Pulsing Beneath Iceland. *Geochemistry, Geophysics, Geosystems*, 19(6):1789–1799.

Rychert, C. A. and Shearer, P. M. (2009). A Global View of the Lithosphere-Asthenosphere Boundary. *Science*, 324:495–498.

Saito, M. (1988). DISPER80: a subroutine package for the calculation of seismic normal-mode solutions. In Doornbos, D. J., editor, *Seismological Algorithms: Computational Methods and Computer Programs*, pages 293–319. Academic Press.

Samrock, F., Grayver, A. V., Eysteinsson, H., and Saar, M. O. (2018). Magnetotelluric Image of Transcrustal Magmatic System Beneath the Tulu Moye Geothermal Prospect in the Ethiopian Rift. *Geophysical Research Letters*, 45(23):12,847–12,855.

Samrock, F., Kuvshinov, A., Bakker, J., Jackson, A., and Fisseha, S. (2015). 3-D analysis and interpretation of magnetotelluric data from the Aluto-Langano geothermal field, Ethiopia. *Geophysical Journal International*, 202(3):1923–1948.

Sánchez-Sesma, F. J., Pérez-Ruiz, J. A., Campillo, M., and Luzón, F. (2006). Elastodynamic 2D Green function retrieval from cross-correlation: Canonical inclusion problem. *Geophysical Research Letters*, 33(13):1–6.

Saria, E., Calais, E., Stamps, D. S., Delvaux, D., and Hartnady, C. (2014). Present-day kinematics of the East African Rift. *Journal of Geophysical Research : Solid Earth*, pages 1–17.

Sawyer, E. W. (1994). Melt Segregation in the Continental-Crust. *Geology*, 22(11):1019–1022.

Schutt, D. L. and Lesher, C. E. (2006). Effects of melt depletion on the density and seismic velocity of garnet and spinel lherzolite. *Journal of Geophysical Research: Solid Earth*, 111(5):1–24.

Sembroni, A., Faccenna, C., Becker, T. W., Molin, P., and Abebe, B. (2016a). Long-term, deep-mantle support of the Ethiopia-Yemen Plateau. *Tectonics*, 35(2):469–488.

Sembroni, A., Molin, P., Pazzaglia, F. J., Faccenna, C., and Abebe, B. (2016b). Evolution of continental-scale drainage in response to mantle dynamics and surface processes: An example from the Ethiopian Highlands. *Geomorphology*, 261:12–29.

Sens-Schönfelder, C. and Wegler, U. (2006). Passive image interferemetry and seasonal variations of seismic velocities at Merapi Volcano, Indonesia. *Geophysical Research Letters*, 33(21):1–5.

Shapiro, N. M. and Campillo, M. (2004). Emergence of broadband Rayleigh waves from correlations of the ambient seismic noise. *Geophysical Research Letters*, 31(7):8–11.

Shapiro, N. M., Campillo, M., Stehly, L., and Ritzwoller, M. H. (2005). High-resolution surface wave tomography from ambient seismic noise. *Science*, 307:1615–1618.

Shapiro, S. S., Hager, B. H., and Jordan, T. H. (1999). Stability and dynamics of the continental tectosphere. *Developments in Geotectonics*, 24(C):115–133.

Shito, A., Suetsugu, D., and Furumura, T. (2015). Evolution of the oceanic lithosphere inferred from Po/So waves traveling in the Philippine Sea Plate. *Journal of Geophysical Research: Solid Earth*, 120:5238–5248.

Siegburg, M., Gernon, T. M., Bull, J. M., Keir, D., Barfod, D. N., Taylor, R. N., Abebe, B., and Ayele, A. (2018). Geological evolution of the Boset-Bericha Volcanic Complex, Main Ethiopian Rift:40Ar/39Ar evidence for episodic Pleistocene to Holocene volcanism. *Journal of Volcanology and Geothermal Research*, 351:115–133.

Sim, S. J., Spiegelman, M., Stegman, D. R., and Wilson, C. (2020). The influence of spreading rate and permeability on melt focusing beneath mid-ocean ridges. *Physics of the Earth and Planetary Interiors*, 304.

Simmons, G. (1964). Velocity of shear waves in rocks to 10 kilobars, 1. *Journal of Geophysical Research*, 69(6):1123.

Simmons, N. A., Myers, S. C., Johannesson, G., and Matzel, E. M. (2012). LLNL-G3Dv3: Global P wave tomography model for improved regional and teleseismic travel time prediction. *Journal of Geophysical Research: Solid Earth*, 117(10):1–28.

Sleep, N. H. (2005). Evolution of the Continental Lithosphere. *Annual Review of Earth and Planetary Sciences*, 33(1):369–393.

Smith, M. L. and Dahlen, F. A. (1973). The azimuthal dependence of Love and Rayleigh wave propagation in a slightly anisotropic medium. *Journal of Geophysical Research*, 78(17):3321–3333.

Sparks, D. W. and Parmentier, E. M. (1991). Melt extraction from the mantle beneath spreading centers. *Earth and Planetary Science Letters*, 105(4):368–377.

Sparks, D. W., Parmentier, E. M., and Phipps Morgan, J. (1993). Three-Dimensional Mantle Convection Beneath a Segmented Spreading Center: Implications for Along-Axis Variations in Crustal Thickness and Gravity. *Journal of Geophysical Research*, 98:21977–21995.

Spiegelman, M. (1996). The sensitivity of trace elements to mantle dynamics. *Earth Planet. Sci. Lett.*, 139:115–132.

Spiegelman, M. and McKenzie, D. (1987). Simple 2-D models for melt extraction at mid-ocean ridges and island arcs. *Earth and Planetary Science Letters*, 83(1-4):137–152.

Splegelman, M. and Reynolds, J. R. (1999). Combined dynamic and geochemical evidence for convergent melt flow beneath the East Pacific Rise. *Nature*, 402(6759):282–285.

Stamps, D. S., Flesch, L. M., Calais, E., and Ghosh, A. (2014). Current kinematics and dynamics of Africa and the East. *Journal of Geophysical Research : Solid Earth*, 119(May):5161–5186.

Stamps, D. S., Iaffaldano, G., and Calais, E. (2015). Role of mantle flow in Nubia-Somalia plate divergence. *Geophysical Research Letters*, 42(2):290–296.

Stamps, D. S., Saria, E., and Kreemer, C. (2018). A Geodetic Strain Rate Model for the East African Rift System. *Scientific Reports*, 8(1):1–8.

Stork, A., Stuart, G. W., Henderson, C. M., Keir, D., and Hammond, J. O. S. (2013). Uppermost mantle (Pn) velocity model for the Afar region, Ethiopia: An insight into rifting processes. *Geophysical Journal International*, 193(1):321–328.

Stuart, G. W., Bastow, I. D., and Ebinger, C. J. (2006). Crustal structure of the northern Main Ethiopian Rift from receiver function studies. *Geological Society, London, Special Publications*, 24(4):623–626.

Takei, Y. (2017). Effects of Partial Melting on Seismic Velocity and Attenuation: A New Insight from Experiments. *Annual Review of Earth and Planetary Sciences*, 45(1):447–470.

Takei, Y. and Holtzman, B. K. (2009). Viscous constitutive relations of solid-liquid composites in terms of grain boundary contiguity: 1. Grain boundary diffusion control model. *Journal of Geophysical Research: Solid Earth*, 114(6):1–19.

Tarantola, A. and Valette, B. (1982). Generalized nonlinear inverse problems solved using the least squares criterion. *Reviews of Geophysics*, 20(2):219–232.

Temtime, T., Biggs, J., Lewi, E., and Ayele, A. (2020). Evidence for Active Rhyolitic Dyke Intrusion in the Northern Main Ethiopian Rift from the 2015 Fentale Seismic Swarm. *Geochemistry, Geophysics, Geosystems*.

Tepp, G., Ebinger, C. J., Zal, H. J., Gallacher, R. J., Accardo, N. J., Shillington, D. J., Gaherty, J. B., Keir, D., Nyblade, A. A., Mbogoni, G., Chindandali, P. R., Ferdinand-Wambura, R., Mulibo, G. D., and Kamihanda, G. (2018). Seismic Anisotropy of the Upper Mantle Below the Western Rift, East Africa. *Journal of Geophysical Research: Solid Earth*, 123(7):5644–5660.

Tesfaye, S., Harding, D. J., and Kusky, T. M. (2003). Early continental breakup boundary and migration of the Afar triple junction, Ethiopia. *Bulletin of the Geological Society of America*, 115(9):1053–1067.

Thybo, H. and Nielsen, C. A. (2009). Magma-compensated crustal thinning in continental rift zones. *Nature*, 457(7231):873–876.

Tiberi, C., Ebinger, C. J., Ballu, V., Stuart, G. W., and Oluma, B. (2005). Inverse models of gravity data from the Red Sea-Aden-East African rifts triple junction zone. *Geophysical Journal International*, 163(2):775–787.

Tolman, H. L. (2009). User manual and system documentation of WAVEWATCH-IIITM version 3.14.

Toomey, D. R., Jousselin, D., Dunn, R. A., Wilcock, W. S., and Detrick, R. S. (2007). Skew of mantle upwelling beneath the East Pacific Rise governs segmentation. *Nature*, 446(7134):409–414.

Traer, J., Gerstoft, P., Bromirski, P. D., and Shearer, P. M. (2012). Microseisms and hum from ocean surface gravity waves. *Journal of Geophysical Research*, 117:1–16.

Tromp, J., Luo, Y., Hanasoge, S. M., and Peter, D. (2010). Noise cross-correlation sensitivity kernels. *Geophysical Journal International*, 183(2):791–819.

Ukstins, I. A., Renne, P. R., Wolfenden, E., Baker, J., Ayalew, D., and Menzies, M. (2002). Matching conjugate volcanic rifted margins: 40Ar/39Ar chrono-stratigraphy of pre- and syn-rift bimodal flood volcanism in Ethiopia and Yemen. *Earth and Planetary Science Letters*, 198(3-4):289–306.

van Wijk, J. W. (2005). Role of weak zone orientation in continental lithosphere extension. *Geophysical Research Letters*, 32(2):1–4.

Varga, R. J., Horst, A. J., Gee, J. S., and Karson, J. A. (2008). Direct evidence from anisotropy of magnetic susceptibility for lateral melt migration at superfast spreading centers. *Geochemistry, Geophysics, Geosystems*, 9(8):1–8.

Vigny, C., Huchon, P., Ruegg, J.-c., Khanbari, K., and Asfaw, L. (2006). Confirmation of Arabia plate slow motion by new GPS data in Yemen. *Journal of Geophysical Research*, 111(April 2005):1–14.

Wadge, G., Biggs, J., Lloyd, R., and Kendall, J.-M. (2016). Historical Volcanism and the State of Stress in the East African Rift System. *Frontiers in Earth Science*, 4(September).

Walker, K. T., Nyblade, A. A., Klemperer, S. L., Bokelmann, G. H., and Owens, T. J. (2004). On the relationship between extension and anisotropy: Constraints from shear wave splitting across the East African Plateau. *Journal of Geophysical Research: Solid Earth*, 109(8).

Wang, Y., Forsyth, D. W., and Savage, B. (2009). Convective upwelling in the mantle beneath the Gulf of California. *Nature*, 462(7272):499–501.

Weaver, R. L. (2005). Information from Seismic Noise. *Science*, 307(5715):1568–1569.

Weeraratne, D. S., Forsyth, D. W., Fischer, K. M., and Nyblade, A. A. (2003). Evidence for an upper mantle plume beneath the Tanzanian craton from Rayleigh wave tomography. *Journal of Geophysical Research: Solid Earth*, 108(B9).

Wei, S. S., Wiens, D. A., Zha, Y., Plank, T., Webb, S. C., Blackman, D. K., Dunn, R. A., and Conder, J. A. (2015). Seismic evidence of effects of water on melt transport in the Lau back-arc mantle. *Nature*, 518(7539):395–398.

Wessel, P. and Smith, W. H. (2013). Generic Mapping Tools : Improved Version Released. 94(45).

Whaler, K. A. and Hautot, S. (2006). The electrical resistivity structure of the crust beneath the northern Main Ethiopian Rift. *Geological Society, London, Special Publications*, 259:293–305.

White, R. S. and Mckenzie, D. (1989). Magmatism at Rift Zones : The Generation of Volcanic Continental Margins. *Journal of Geophysical Research*, 94(B6):7685–7729.

White, R. S., Smith, L. K., Roberts, A. W., Christie, P. A. F., Kusznir, N., Roberts, A. M., Healy, D., Spitzer, R., Chappell, A., Eccles, J. D., Fletcher, R., Hurst, N., Lunnon, Z., Parkin, C. J., and Tymms, V. J. (2008). Lower-crustal intrusion on the North Atlantic continental margin. *Nature*.

Whittington, A. G., Hofmeister, A. M., and Nabelek, P. I. (2009). Temperature-dependent thermal diffusivity of the Earth's crust and implications for magmatism. *Nature*, 458(7236):319–321.

Wilson, J. T. (1963). Hypothesis of earth's behaviour. *Nature*, (4884):925–929.

Wilson, J. T. (1973). Mantle Plumes and Plate Motions. *Tectonophysics*, 19(2):149–164.

WoldeGabriel, G., Aronson, J. L., and Walter, R. C. (1990). Geochronology and rift basin development in the central sector of the Main Ethiopian Rift. *Geological Society of America Bulletin*, 102(August 2009):439–485.

Wolfenden, E., Ebinger, C. J., Yirgu, G., Deino, A., and Ayalew, D. (2004). Evolution of the northern Main Ethiopian rift: birth of a triple junction. *Earth and Planetary Science Letters*, 224(1-2):213–228.

Wolfenden, E., Ebinger, C. J., Yirgu, G., Renne, P. R., and Kelley, S. P. (2005). Evolution of a volcanic rifted margin: Southern Red Sea, Ethiopia. *Bulletin of the Geological Society of America*, 117(7-8):846–864.

Wright, T. J., Ebinger, C. J., Biggs, J., Ayele, A., Yirgu, G., Keir, D., and Stork, A. (2006). Magma-maintained rift segmentation at continental rupture in the 2005 Afar dyking episode. *Nature*, 442(7100):291–294.

Wright, T. J., Sigmundsson, F., Pagli, C., Belachew, M., Hamling, I. J., Brandsdóttir, B., Keir, D., Pedersen, R., Ayele, A., Ebinger, C., Einarsson, P., Lewi, E., and Calais, E. (2012). Geophysical constraints on the dynamics of spreading centres from rifting episodes on land. *Nature Geoscience*, 5(4):242–250.

Xu, W., Rivalta, E., and Li, X. (2017). Magmatic architecture within a rift segment : Articulate axial magma storage at Erta Ale volcano , Ethiopia. *Earth and Planetary Science Letters*, 476:79–86.

Yang, Y. and Forsyth, D. W. (2006). Regional tomographic inversion of the amplitude and phase of Rayleigh waves with 2-D sensitivity kernels. *Geophysical Journal International*, 166(3):1148–1160.

Zhou, Y., Dahlen, F. A., and Nolet, G. (2004). Three-dimensional sensitivity kernels for surface wave observables. *Geophysical Journal International*, 158(1):142–168.

Zwaan, F. and Schreurs, G. (2017). How oblique extension and structural inheritance influence rift segment interaction: Insights from 4D analog models. *Interpretation*, 5(1):SD119–SD138.